UNIVERSITÉ SORBONNE PARIS NORD

École doctorale Sciences, Technologies, Santé Galilée

Multiphysics tritium transport simulations of the WCLL breeding blanket for DEMO

THÈSE DE DOCTORAT
présentée par

James DARK

pour l'obtention du grade de
DOCTEUR EN SCIENCE DES MATÉRIAUX

soutenue le 14 octobre 2024 devant le jury composé de :

BARTHE Marie-France, CNRS	Présidente
TESTONI Raffaella, Politecnico di Torino	Rapportrice
CHRISTIEN Frédéric, Mines Saint-Etienne	Rapporteur
FERRY Sara, Massachusetts Institute of Technology	Examinatrice
VAN BOXEL Steven, UKAEA	Examinateur
WAUTERS Tom, ITER Organization	Invité
HODILLE Etienne, CEA IRFM	Co-encadrant
MOUGENOT Jonathan, Univ. Sorbonne Paris Nord	Co-directeur
CHARLES Yann, Univ. Sorbonne Paris Nord	Directeur de thèse

Abstract

This work presents the development of a multiphysics tritium transport model in the Water-Cooled Lithium Lead (WCLL) breeding blanket, designed using FESTIM to evaluate tritium retention and permeation influenced by heat transfer and fluid mechanics. The developed model aims to estimate inventory buildups within structural materials and quantify permeation into cooling channels. Utilising the Finite Element Method (FEM), the model integrates data from neutronics simulations and accounts for complex fluid flow and heat transfer. Parametric studies assess the influence of heat transfer coefficients, tritium sources, and solubility in PbLi. The work emphasises the impact of tritium trapping mechanisms, increasing tritium inventories in the breeding zone pipes by 80 % and in the first wall by tenfold. A new model, parameterised for tungsten, accounts for the temporal evolution of trap concentrations due to self-damage and thermal annealing, which can be used to estimate the impact of neutron damage on tritium transport in plasma-facing components. Results suggest the tritium inventory in the first wall could increase 700 times after six days of exposure compared to the undamaged case. Methodologies are outlined to modes tritium permeation barriers implicitly for component scale FEM modelling. The developed models and methodologies provide valuable insights for designing and optimising future fusion reactors, ensuring more efficient and sustainable tritium management in breeding blanket systems.

Résumé

Cette étude présente le développement d'un modèle multiphysique dont l'objectif et la simulation du transport du tritium dans la couverture tritigène de DEMO WCLL (Water Cooled Lithium Lead). Le code FESTIM est utilisé pour évaluer la rétention et la permeation du tritium influencé par la thermique et la mécanique des fluides. Le modèle développé à pour objectif d'estimer les accumulations d'inventaire dans les matériaux de structures et à quantifier la perméation dans les canaux de refroidissement. Utilisant la méthode des éléments finis (FEM), le modèle intègre des données provenant de simulations neutroniques et tient compte de la dynamique des fluides et du transport de la chaleur. Des études paramétriques évaluent l'influence des coefficients de transfert de chaleur, des sources de tritium et de la solubilité du tritium dans le PbLi. Les travaux mettent l'accent sur l'impact des mécanismes de piégeage du tritium, qui augmentent de 80 % les stocks de tritium dans les tubes de la zone tritigène et multiplient dix dans la première paroi. Un nouveau modèle, paramétré pour le tungstène, tient compte de l'évolution temporelle des concentrations de pièges dues à l'endommagement et au recuit thermique, qui peut être utilisé pour estimer l'impact de l'endommagement neutronique sur le transport du tritium dans les composants face au plasma. Les résultats suggèrent que l'inventaire de tritium dans la première paroi en tungstène pourrait être multiplié par 700 après six jours d'exposition par rapport au cas non endommagé. Des méthodologies sont décrites pour modéliser les barrières de perméation du tritium de manière implicite pour la modélisation FEM à l'échelle des composants. Les modèles et méthodologies développés fournissent des indications précieuses pour la conception et l'optimisation des futurs réacteurs de fusion, en assurant une gestion plus efficace et durable du tritium dans les systèmes de couverture tritigènes.

Acknowledgements

I want to express my deepest gratitude to exceptional individuals whose support has been indispensable throughout my doctoral journey.

Firstly, my sincere thanks go to my thesis committee members, Dr Raffaella Testoni, Dr Frédéric Christien, Dr Sara Ferry, Dr Steven Van Boxel, Dr Tom Wauters and Dr Marie-France Barthe. Your willingness to engage with my work and provide insightful feedback has enhanced my research. The dedication required to read this lengthy manuscript did not go unnoticed; I am genuinely thankful for this.

The warm welcome and continued support provided by the GCFPM team at IRFM have been pillars of my experience abroad. Marianne, Marc, and the rest of the team not only introduced me to the nuances of French culture, cuisine, and customs during our cherished coffee breaks but also supported my professional growth by facilitating numerous opportunities to attend conferences and workshops and helping to secure a visiting position at MIT. These experiences have been invaluable in expanding my academic network and sharing my work within the community.

To my friends and fellow doctoral candidates at the IRFM: Matthieu, Virginia, Samy, Yann, Ricardo, Luca, Loic, and David, to name a few, and especially Maxime, thank you for the camaraderie and memorable times we shared, whether over beers or during late nights in Bat 507. Each moment spent with you has made this academic pursuit all the more enjoyable.

My time in Aix-en-Provence was enriched by the friends I made through the polyglot language exchange. Hicham, Melodie, Raphael, Jamie, James, Tamara, Lakeshia, and many others, your friendship has been a treasured part of my life in Aix.

Laura and Massoud, I am indebted to you for your hospitality and friendship when I first arrived in Paris. Watching you grow from a couple to a family while exploring Paris's hidden gems through your eyes has been a profound joy.

Back home, Dec, Hamoud, Lucille, and Brandon have been my rock. Despite the physical distance, our friendships have strengthened, and we have been supported by countless online gaming sessions, catch-ups, memorable trips to Oxford, the Netherlands, and times I had the pleasure of hosting you in Aix. Thank you for always making me feel at home in your company; I value your friendship more than I can express.

I am grateful to the LSPM team, particularly my supervisors, Dr Jonathan Mougenot and Dr Yann Charles. Thank you for taking me under your wing for that initial CDD position, setting the stage for my PhD journey. Your guidance, mentorship, and support have been crucial in my academic growth over the past three and a half years.

To Dr Etienne Hodille, being your first PhD student has been an honour and a journey of mutual growth. Your meticulous attention to detail and vast knowledge have profoundly shaped my development as a researcher.

To Remi and Steph, thank you for welcoming me with open arms upon my arrival in France. Rémi, you have demonstrated what it means to adhere to the highest standards in research and have pushed me to strive for excellence in every aspect of my professional life. For this, I will always be thankful.

And finally, I am deeply grateful to my family for their unwavering support, patience, and encouragement throughout this journey. Their belief in me has been a constant source of strength, and I could not have reached this milestone without their love and understanding.

Contents

Abstract i

Acknowledgements iii

List of Figures vii

List of Tables xiii

List of Acronyms xvii

Introduction 1

1 Nuclear fusion and the role of tritium breeding blankets 5
- 1.1 Nuclear Fusion 6
  - 1.1.1 Nuclear energy 6
  - 1.1.2 Nuclear fusion reactions 7
  - 1.1.3 Plasma confinement 9
  - 1.1.4 Fusion Power 10
  - 1.1.5 DEMO 13
- 1.2 The tritium issue 14
  - 1.2.1 Safety 14
  - 1.2.2 Fusion reactor fuel cycle 16
  - 1.2.3 Breeding 18
  - 1.2.4 Hydrogen in materials 21
- 1.3 WCLL 25
  - 1.3.1 Design 25
  - 1.3.2 Neutronic performance 27
  - 1.3.3 Thermal-Hydraulic performance 29
  - 1.3.4 Tritium generation and permeation 31
- 1.4 Problem definition 32

2 Model definition and implementation 35
- 2.1 Multiphysics framework 36
  - 2.1.1 Heat transfer 37
  - 2.1.2 Fluid mechanics 38
  - 2.1.3 Hydrogen transport 39
  - 2.1.4 Summary: Governing equations 40
- 2.2 Finite element methods 41
  - 2.2.1 Problem definition 44
  - 2.2.2 Weak formulation 44
  - 2.2.3 Discretisation 45
  - 2.2.4 Function spaces 46

2.2.5 Assembly of the system of equations . . . 48
2.2.6 Solving . . . 49
2.2.7 Fluid mechanics solver application . . . 50
2.3 FESTIM . . . 52
2.3.1 FEniCS . . . 52
2.3.2 Features . . . 53
2.3.3 Model construction . . . 53
2.3.4 Validation & Verification . . . 55
2.4 Summary . . . 57

3 WCLL model 59
3.1 WCLL Geometry . . . 60
3.2 Model parameters . . . 61
3.2.1 Thermophysical material properties . . . 62
3.2.2 Hydrogen transport material properties . . . 64
3.2.3 Sources due to neutrons . . . 67
3.2.4 Boundary conditions . . . 68
3.3 Standard case . . . 71
3.4 Parametric studies . . . 76
3.4.1 Influence of coolant heat transfer coefficient . . . 77
3.4.2 Influence of tritium sources . . . 85
3.4.3 Influence of PbLi solubility . . . 87
3.4.4 Summary . . . 89

4 Influence of trapping 91
4.1 Damage-induced trap creation model . . . 92
4.1.1 Model definition . . . 92
4.1.2 Model parametrisation . . . 93
4.1.3 1D parametric study . . . 101
4.2 WCLL application . . . 105
4.2.1 Influence of intrinsic traps . . . 105
4.2.2 Influence of neutron damage . . . 108

5 Permeation mitigation strategies 113
5.1 Influence of a tritium extraction system . . . 113
5.2 Influence of permeation barriers . . . 118
5.2.1 Cartesian analytical model . . . 119
5.2.2 Cylindrical analytical model . . . 121
5.2.3 Macroscopic interface condition implementation . . . 123
5.2.4 WCLL application . . . 129

Conclusions 133

Appendices 137

A CFD verification: Lid driven cavity 139

B Mesh convergence study 141

C Influence of magnetic field 149
- C.1 Model Description . . . 149
  - C.1.1 Weak form evaluation . . . 149
- C.2 Benchmark case . . . 151

D Damaged tungsten TDS fittings 155

E Analytical model: Cylindrical permeation barrier 161

F Macroscopic boundary condition for permeation barriers 163

Bibliography 167

List of Figures

1.1 Binding energy per nucleon . . . 7
1.2 Fusion reaction cross-sections . . . 8
1.3 Tokamak reactors (left) and related designs known as stellarator reactors (right) both confine the plasma (yellow) with magnetic fields (purple) that are generated by electromagnetic coils (blue and red) . . . 10
1.4 Artistic rendering of the DEMO reactor . . . 13
1.5 A schematic process diagram for a simplified fuel cycle . . . 17
1.6 Tritium inventory changes over time in the TES, storage and breeder . . . 18
1.7 Cross-section of neutron capture reactions in barns with Li-7 Li-6 and H2 producing tritium . . . 19
1.8 cross-section of neutron capture reactions with Pb and Be compared to lithium isotopes . . . 20
1.9 Interactions of solute hydrogen isotopes in metals . . . 21
1.10 Potential energy vs reaction coordinate, showing the influence surface effects and two different types of defect . . . 22
1.11 WCLL v0.6B COB equatorial elementary cell in isometric and poloidal views 26
1.12 A cross-sectional view of a collision cascade in gold, induced by a 10 keV primary knock-on atom . . . 28
1.13 Nuclear heating radial profile evaluated in W armour, Eurofer, PbLi and SS316 L for the outboard WCLL . . . 29
1.14 WCLL v0.6B thermal field . . . 30
1.15 The multiphysics issue in modelling breeding blankets . . . 33

2.1 2D WCLL domain showing W 🟥, Eurofer ◼, PbLi 🟩 . . . 36
2.2 Representation of the mathematical problem . . . 44
2.3 Line, triangle and tetrahedral element types . . . 45
2.4 First, second and third order 2D Lagrange elements . . . 46
2.5 The function u (solid blue line) is approximated with u_h (dashed red line), which is a linear combination of linear basis functions (the solid black lines represent ψ_i). The DOFs are denoted by u_0 through u_9 . . . 47
2.6 Verification case 1: multi-material . . . 56
2.7 Verification case 2: heat transfer . . . 57
2.8 Verification case 3: trapping . . . 58

3.1 Simulation workflow for multiphysics modelling of the WCLL, highlighting in dashed lines which physics is solved by FESTIM and FEnicS . . . 60
3.2 3D geometry of WCLL v0.6b geometry showing the position of the 2D domain considered . . . 61
3.3 Thermophysical properties of density, ρ (top), thermal conductivity, λ (middle) and specific heat capacity, c_p (bottom) of the materials in the WCLL: tungsten, Eurofer and PbLi over a temperature range found within the operational conditions of the WCLL and beyond . . . 63

3.4 Diffusivities and solubilities for hydrogen isotopes H, D and T in tungsten, Eurofer and PbLi. Values obtained from HTM, experimental points in dot and interpolations in lines . . . 65

3.5 Hydrogen transport properties of diffusivity (top) and solubility (bottom) of the materials in the WCLL: tungsten, Eurofer and PbLi over a temperature range found within the operational conditions of the WCLL and beyond . . . 66

3.6 Nuclear heating in the PbLi and Eurofer by radial length, r . . . 67

3.7 Front end of 2D WCLL geometry showing tungsten 🟥, Eurofer ⬛, LiPb 🟩. Γ represents a defined surface, PFS is the Plasma Facing Surface, FW is the First Wall, and BZ is the Breeding Zone . . . 69

3.8 Rear end of 2D geometry showing Eurofer ⬛, LiPb 🟩. Γ represents a defined surface, Γ_{walls} applies to all LiPb/Eurofer interfaces. . . . 69

3.9 3D steady-state temperature field . . . 72

3.10 2D toroidal mid-plane slice . . . 72

3.11 Steady state velocity field with associated profile A across the PbLi 🟩 channels and Eurofer ⬜ structure . . . 73

3.12 Tritium mobile concentration, c_{m}, field after 7200 s . . . 74

3.13 Tritium mobile concentration, c_{m}, field at steady-state . . . 74

3.14 Temporal evolution of the tritium inventories in the PbLi, structure, BZ pipes and first wall . . . 75

3.15 Temporal evolution of the tritium permeation rate at the cooling surfaces for the first wall cooling channels and breeding zone pipes at the front, middle and rear position relative to the plasma facing surface . . . 76

3.16 BZ cooling pipe (left) and FW cooling channel (right) dimensions . . . 78

3.17 Variation of density, viscosity, specific heat capacity and thermal conductivity of water in the temperature range observed in the WCLL . . . 79

3.18 Temperature field in the WCLL comparing the reference solution (left) to this work (right). The temperature colour bar range on the left applies to both cases 80

3.19 Heat transfer coefficient values across the WCLL unit in the BZ pipes (left) and the FW channels (right) . . . 80

3.20 Variation in heat transfer coefficient in the FW system (top) and the BZ system (bottom) varying bulk coolant temperature and mass flow rate, value of standard case highlighted with white star . . . 82

3.21 Maximum temperature observed in the Eurofer in the structure (top) and BZ pipes (bottom) as a result of varying the heat transfer coefficient as a function of bulk coolant temperature and mass flow rate. Values from the standard case are highlighted in the centre with a white star . . . 83

3.22 Relative tritium surface flux to the average case (white star) in the FW channels (left) and BZ pipes (right) as a result of varying the heat transfer coefficient as a function of bulk coolant temperature and mass flow rate. Values from the standard case are highlighted with a black star. . . . 84

3.23 Surface flux at the first wall cooling channels divided into contributions from the plasma 🟥, from the breeder 🟩, and both together ⬛ . . . 85

3.24 Temporal evolution of the tritium inventory in the PbLi, FW, BZ pipes and structure divided into contributions from the plasma 🟥 and the breeder 🟩 . . . 86

3.25 Solubilities for hydrogen isotopes H, D and T in PbLi. Values obtained from HTM, experimental points in dot and interpolations in lines 87

3.26 Evolution of the steady state tritium inventories as a function of hydrogen solubility, K_S, in PbLi normalised to the standard case solubility, $K_\mathrm{S-SC}$ . . . 88

3.27 Influence of the solubility of hydrogen in PbLi on the temporal evolution of tritium inventory (top) and surface flux (bottom). The solubility at 600 K varies from 1.5×10^{20} to $3.0 \times 10^{22}\,\mathrm{m^{-3}\,Pa^{-0.5}}$. 89

4.1 Process diagram for evaluating variables in Eq.(4.1). Work completed by M Pečovnik *et al* is highlighted in the dashed box. 94

4.2 Trap densities evolution with annealing temperature fitted using Eq. (4.4). Experimental data points 95

4.3 Trapping site density Fermi-Dirac-like distribution described by Eq. (4.6) . . 96

4.4 Results of TDS analysis from tungsten samples damaged to various levels (0.001 - 2.5 dpa at 800 K and decorated with D at 370 K 98

4.5 TDS data for tungsten sample damaged to 0.1 dpa, fitted using one intrinsic trap and five extrinsic traps 99

4.6 Trap concentrations with increasing damage dose from the fitted TDS, then fitted using the current model. 100

4.7 Total trap densities at 295 K and 800 K with variation in the damage rate after one FPY. 101

4.8 Tritium inventory over 1 FPY (top) and the retention distribution after 24 h (bottom) from simultaneous damage exposure and tritium implantation, at 700 K varying the damage rate. 103

4.9 Tritium retention in tungsten in varying damaged cases, relative to an undamaged case, after 1 FPY varying temperature. 104

4.10 Temporal evolution of the tritium inventory in the PbLi, FW, BZ pipes and structure. Dashed lines correspond to a case without traps. 105

4.11 Temporal evolution of the tritium fluxes at the cooling surfaces for the first wall cooling channels and breeding zone pipes at the front, middle and rear position relative to the plasma facing surface. Dashed lines correspond to the standard case without trapping effects 106

4.12 Tritium repartition in Eurofer structure and BZ pipe 107

4.13 Temporal evolution of trap concentration of damaged induced traps D1-D5 as a result of a damage at 5 dpa/fpy, using an average temperature of 684 K, compared to intrinsic traps concentrations 109

4.14 Temporal evolution of tritium retention in tungsten FW as a result of damage at 5 dpa/fpy, relative to an undamaged case 110

4.15 Tritium retention profile across the tungsten FW comparing the standard case against one considering trap creation after 2 h and 6 days of exposure to a damage rate of 5 dpa/fpy 111

5.1 Tritium cycle between breeder and extraction system 114

5.2 Tritium concentration of the inlet, $c_{\mathrm{m,inlet}}$, with resulting evaluation for contraction to use in next iteration, $((1-\eta)\ \varphi_{\mathrm{outlet}})/(\mathbf{u}_{\mathrm{inlet}}\ A)$, converging to a max difference of 1%, for each case of $(1-\eta)$ 115
5.3 Tritium inventories in the PbLi, structure, BZ pipes and FW as a function of tritium re-entering the WCLL. Standard case at $\eta = 1.0$ 116
5.4 Tritium surface flux entering the different regions of BZ pipes and FW cooling channels as a function of tritium re-entering the WCLL 117
5.5 2D representation of the 1D cartesian geometry for permeation barrier analytical solution 119
5.6 2D representation of the 1D cylindrical (polar) geometry for permeation barrier analytical solution 122
5.7 Cartesian 1D model of a domain of 2 mm PbLi 🟩 and 2 mm Eurofer ■ with and without a 5 μm Al_2O_3 □ permeation barrier 124
5.8 Mobile concentration of tritium across a domain with a permeation barrier modelled explicitly, without a barrier and with modification condition 125
5.9 Measured PRF compared to a standard material interface condition against modification factor for Eurofer solubility 127
5.10 Measured PRF compared to a standard material interface condition against modification factor for Eurofer solubility, varying the length of the PbLi . . . 128
5.11 Measured PRF compared to a standard material interface condition against modification factor for Eurofer solubility, varying the temperature of the domain 128
5.12 Tritium surface flux entering the different regions of BZ pipes at steady state varying the modification factor applied to the solubility value of the Eurofer in the BZ pipes. For colours, see figure 5.4a 129
5.13 The measured PRF of the total BZ pipe surface flux against the standard flux, against respective modification factor, with quadratic fitting 130
5.14 Steady-state tritium inventories in the BZ pipes (top) and surface flux at the BZ pipes coolant interfaces (bottom), varying the enforced PRF 131

A.1 Lid driven cavity problem 139
A.2 Re = 400 (a), Re = 1000 (c), Re = 5000 (e), Re = 10000 (g), compared to its respective counterpart reference solution (b), (d), (f) and (h) 140

B.1 Simulation workflow for multiphysics modelling of the WCLL 141
B.2 Mesh domains considered in the mesh refinement 143
B.3 Time to run steady state simulation with increasing mesh size 144
B.4 Tritium inventories with increasing mesh size in the PbLi subdomain 144
B.5 Tritium inventories with increasing mesh size in the eurofer subdomains . . . 145
B.6 Tritium inventories with increasing mesh size in the FW domain 146

C.1 Rectangular duct geometry 151
C.2 Fully conductive case ($\Phi = 0$ on Γ_{HW}) compared to analytical solutions . . . 152
C.3 Fully insulated case ($\frac{\partial \Phi}{\partial x} = 0$ on Γ_{HW}) compared to analytical solutions 153

D.1 TDS data for tungsten sample damaged to 0 dpa, fitted using one intrinsic trap 155

D.2 TDS data for tungsten sample damaged to 0.001 dpa, fitted using one intrinsic trap and five extrinsic traps . . . 156
D.3 TDS data for tungsten sample damaged to 0.005 dpa, fitted using one intrinsic trap and five extrinsic traps . . . 156
D.4 TDS data for tungsten sample damaged to 0.023 dpa, fitted using one intrinsic trap and five extrinsic traps . . . 157
D.5 TDS data for tungsten sample damaged to 0.1 dpa, fitted using one intrinsic trap and five extrinsic traps . . . 157
D.6 TDS data for tungsten sample damaged to 0.23 dpa, fitted using one intrinsic trap and five extrinsic traps . . . 158
D.7 TDS data for tungsten sample damaged to 0.5 dpa, fitted using one intrinsic trap and five extrinsic traps . . . 158
D.8 TDS data for tungsten sample damaged to 2.5 dpa, fitted using one intrinsic trap and five extrinsic traps . . . 159

F.1 2D pipe geometry comprised of a 13.5 mm outer diameter Eurofer pipe (8 mm inner diameter) ■ within a 20 mm^2 PbLi 🟩 domain . . . 164
F.2 Measured PRF compared to a recombination flux boundary condition against an enforced PRF value . . . 164

List of Tables

2.1 Comparison of some hydrogen transport modelling tools 42

3.1 Geometric dimensions for the 3D WCLL geometry 61
3.2 Density values, ρ [$\mathrm{kg\,m^{-3}}$], $T_0 = 273.15\,\mathrm{K}$ 63
3.3 Specific isobaric heat capacity values, C_p [$\mathrm{J\,kg^{-1}\,K^{-1}}$] 64
3.4 Thermal conductivity values, λ [$\mathrm{W\,m^{-1}\,K^{-1}}$] 64
3.5 PbLi fluid property values 64
3.6 H transport properties of W, Eurofer and PbLi 66
3.7 Trap properties for tungsten and Eurofer 67
3.8 Nuclear heating, Q [$\mathrm{MW\,m^{-3}}$] 68
3.9 Tritium generation, S [$\mathrm{T\,m^{-3}\,s^{-1}}$] 68
3.10 Boundary conditions parameter values 71
3.11 Cooling water parameters 77
3.12 Water thermophysical properties 78

4.1 Annealing parameter values for each defect type 95
4.2 TDS simulation parameters 97
4.3 Fitted intrinsic trap properties 97
4.4 Results of the model parametrisation for the damage-induced traps 100

5.1 H transport properties of Al_2O_3 124

B.1 Optimised maximum cell size values for each domain in the WCLL geometry 147

List of Acronyms

BB	Breeding Blanket	16
BZ	Breeding Zone	26
DEMO	DEMOnstration power plant	2
DFT	Density Functional Theory	21
DOF	Degrees of Freedom	46
DT	deuterium-tritium	9
DWT	Double-Walled Tubes	60
FEM	Finite Element Method	2
FW	First Wall	26
ITER	International Thermonuclear Experimental Reactor	1
MD	Molecular Dynamics	21
MHD	Magnetohydrodynamics	16
PDE	Partial Differential Equation	41
PKA	Primary Knock-on Atom	27
PP	proton-proton	7
PRF	Permeation Reduction Factor	118
PWR	Pressurised Water Reactor	26
TBM	Tritium Breeding Module	2
TBR	Tritium Breeding Ratio	28
TDS	Thermal Desorption Spectroscopy	23
TES	Tritium Extraction System	16
WCLL	Water Cooled Lead Lithium	2

Introduction

Advancements in energy generation technology form a cornerstone for modern societal progress, driving economic growth and environmental sustainability. Meanwhile, reliance on legacy fossil fuel technologies from the Industrial Revolution has led to significant CO_2 release in Earth's atmosphere, accelerating climate change and emphasising the critical need for transitioning to sustainable energy practices. The shift from fossil fuels to renewable sources mitigates ecological impact and fosters new industries and job opportunities. These energy advancements are integral to supporting and enhancing digital communication networks and eco-friendly transportation systems, facilitating a more interconnected and efficient society in which improvements in energy infrastructure catalyse broader technological and social advancements.

Nuclear fusion, a proposed energy generation technology, promises safe, reliable, and sustainable power. Despite its vast potential to revolutionise energy systems, nuclear fusion remains primarily in the research phase and is not yet ready to serve as an immediate solution for climate change. The challenges of achieving and maintaining the conditions necessary for fusion require significant scientific breakthroughs and technological advancements. However, if these hurdles can be overcome, nuclear fusion could significantly strengthen society's foundational pillars, enabling unprecedented advancements across various sectors by offering a substantial and clean energy source.

Several significant technological limitations must be addressed to make nuclear fusion energy viable. Among the potential fuelling options, the most favourable is a combination of deuterium and tritium hydrogen isotopes. However, reliance on tritium presents several critical challenges. Tritium is a radioactive hydrogen isotope and, therefore, is scarce due to its rapid decay into helium. Another significant issue is tritium's radiotoxicity, posing severe health risks if ingested, for instance, through contaminated water. This toxicity requires strict limits on the amount of tritium in reactors to minimise potential environmental and health impacts in case of accidents or leaks. Furthermore, tritium's small atomic size allows it to penetrate and become trapped within the reactor's material structures, complicating the fuel cycle. Over time, this retention increases the internal radioactivity of reactor components, complicating maintenance and eventual decommissioning due to heightened radioactive waste concerns. These challenges highlight the complexities of managing tritium in fusion reactors, impacting everything from safety protocols to long-term waste management and the feasibility of fusion as a sustainable energy source. There are methods available to produce tritium; however, the most viable method will be to use neutrons produced in the plasma. Thus, to produce the tritium fuel, a component called a breeding blanket will surround the reactor vessel, producing tritium on-site in a complex and demanding process.

The breeding blanket in fusion reactors is crucial for the production of tritium fuel, heat removal from the system and plasma, and providing neutron shielding to the reactor's external components. Second only to the fusion plasma regarding its critical role in the success of the technology. Despite its significance, a breeding blanket has yet to be constructed or tested. As part of the Eurofusion roadmap, the International Thermonuclear Experimental Reactor

(ITER) test reactor is currently under construction in Cadarache, France, the results of which will inform the design of the DEMOnstration power plant (DEMO) reactor. Within the ITER Tritium Breeding Module (TBM) program, two breeding concepts will be tested: the Helium-Cooled Pebble Bed (HCPB) and the Water Cooled Lead Lithium (WCLL) designs. This research focuses on the WCLL concept. This work aims to develop sophisticated multiphysics models of the WCLL to explore impacting factors on tritium transport. Critical concerns include characterising the creation and transport of tritium within the system, its recovery efficiency, and whether tritium will permeate and remain within local structures. FESTIM is employed to analyse and predict tritium behaviour in the WCLL to address these queries, providing essential insights into its dynamics within the breeding blanket.

The following chapters will provide in-depth analyses and methodologies for developing sophisticated models of the WCLL to aid in determining the success of this technology.

Chapter 1: Nuclear fusion and the role of tritium breeding blankets

This chapter delves into the basics of nuclear fusion and the critical role of tritium as a fuel. It highlights the potential of fusion energy to replace conventional fossil fuels, offering a minimal carbon footprint alternative. The chapter also discusses the challenges of tritium's limited natural availability and the necessity of breeding it within fusion reactors. The WCLL breeding blanket is introduced as a solution for tritium breeding. It is also reviewed, along with the tritium transport complexities that must be addressed.

Chapter 2: Model definition and implementation

Accurate modelling of the WCLL requires an integrated approach considering various interacting physical phenomena, including heat transfer, fluid mechanics, and hydrogen transport. This chapter provides an overview of the multiphysics framework employed, detailing the application of the Finite Element Method (FEM) for solving partial differential equations. It emphasises using FEniCS software for efficient finite element analysis and introduces a fluid mechanics solver tailored for PbLi flow within the WCLL. The chapter concludes with an introduction to FESTIM, this work's primary software for hydrogen transport modelling.

Chapter 3: WCLL model

Building on the foundational context and methodologies discussed in previous chapters, this chapter presents the parameters and results of the multiphysics tritium transport model for the WCLL. It starts with the geometry and simulation parameters, followed by a benchmark standard simulation case. The chapter includes parametric studies covering sensitivity analyses of critical model components, such as the convective heat transfer boundary condition and tritium sources. It finally examines the influence of hydrogen's solubility in PbLi.

Chapter 4: Influence of trapping

This chapter explores the impact of tritium trapping mechanisms on transport behaviour. It introduces a new model parameterised for tungsten that accounts for the temporal evolution of trap concentrations due to self-damage and thermal annealing. The chapter investigates intrinsic traps within WCLL materials. It also estimates the influence of neutron damage on tritium transport, providing an understanding of trapping effects in the WCLL breeding blanket.

Chapter 5: Permeation mitigation strategies

The final chapter focuses on methods to reduce tritium permeation into cooling channels and structural components of the WCLL. It begins with a study on the influence and effectiveness of tritium extraction systems in controlling permeation. The chapter then presents a methodology for modelling permeation barriers, addressing the challenges of scale disparity. It demonstrates the application of implicit modelling techniques for permeation barriers in large-scale simulations, exploring their impact on tritium transport dynamics.

CHAPTER 1

Nuclear fusion and the role of tritium breeding blankets

Contents

1.1 Nuclear Fusion 6
  1.1.1 Nuclear energy 6
  1.1.2 Nuclear fusion reactions 7
  1.1.3 Plasma confinement 9
  1.1.4 Fusion Power 10
  1.1.5 DEMO 13
1.2 The tritium issue 14
  1.2.1 Safety 14
  1.2.2 Fusion reactor fuel cycle 16
  1.2.3 Breeding 18
  1.2.4 Hydrogen in materials 21
1.3 WCLL 25
  1.3.1 Design 25
  1.3.2 Neutronic performance 27
  1.3.3 Thermal-Hydraulic performance 29
  1.3.4 Tritium generation and permeation 31
1.4 Problem definition 32

Fusion research aims to develop the necessary scientific and engineering expertise to establish fusion power as a dependable and sustainable energy solution for the future. Among various approaches, magnetically confined fusion appears to be the most promising for realising practical fusion power plants. The potential of fusion extends to global energy transition, with the prospect of replacing conventional coal, oil, and gas-fired power plants. Unlike these traditional sources, fusion power generation has a minimal carbon footprint, primarily limited to emissions associated with constructing and manufacturing the plant [1]. Due to their advantageous characteristics, hydrogen isotopes have been identified as potential fusion fuels. However, achieving desirable reaction rates and maximising power output necessitates using the hydrogen isotope tritium. Tritium, being radioactive with a half-life of 12.3 years, is not naturally abundant, posing a challenge to the fusion fuel supply [2]. This chapter covers the process of nuclear fusion and the rationale behind incorporating tritium as a fuel. Additionally, it delves into the complexities surrounding tritium availability and transport behaviour before introducing a proposed concept for tritium breeding: the Water-Cooled Lead Lithium breeder.

1.1 Nuclear Fusion

Energy release in chemical or nuclear reactions is a fundamental process which can be harnessed to produce electricity, marking a pivotal aspect of modern energy systems. In chemical reactions, energy is released through rearranging electrons in atoms and molecules, often while breaking bonds and forming new ones. This release can take various forms, such as heat, which can then be converted into electrical energy through generators. For instance, burning fossil fuels is a chemical reaction where the combustion of carbon-based materials in the presence of oxygen releases a significant amount of heat. This heat is then used to produce steam that drives turbines, generating electricity. However, despite its prevalence, this method has notable drawbacks, including the emission of greenhouse gases and limited fuel resources, prompting the search for cleaner, more sustainable alternatives.

1.1.1 Nuclear energy

Nuclear reactions distinguish themselves from chemical reactions by releasing vast amounts of energy, a phenomenon fundamentally tied to differences in nuclear binding energy and resultant mass changes. This release occurs because the mass of the nuclear reaction's products differs from that of the reactants, with the excess mass liberated in the form of energy, ΔE, where a slight mass difference, Δm, translates into a significant energy output [3]:

$$\Delta E = \Delta m c^2 \tag{1.1}$$

where m is in units kg and c is the speed of light in a vacuum in units $\mathrm{m\,s^{-1}}$. The crux of this mass-energy conversion lies in nuclear binding energy, the energy required to keep a nucleus together. Nickel has the highest binding energy per nucleon, making it the most stable; therefore, all nuclear reactions naturally tend towards nickel [4]. This means lighter elements tend to undergo fusion, combining to form heavier, more stable nuclei up to nickel, releasing the excess binding energy. Conversely, elements heavier than nickel can release energy through fission, splitting into lighter, more stable elements, releasing excess binding energy (See Figure 1.1).

Nuclear fission and fusion both come with distinct advantages and disadvantages. Fission is currently more technologically mature and powers all nuclear reactors today, whereas fusion remains an area of research. Both forms of nuclear power can generate large amounts of energy from relatively small amounts of fuel. However, current fission reactors use established technologies and infrastructure. Furthermore, fission technology has some inherent critical issues, such as the production of more high-level radioactive waste that requires long-term management [6] and carries a higher risk of more severe nuclear accidents, as seen in historical incidents like Three Mile Island, Chornobyl and Fukushima. On the other hand, fusion offers the potential for a highly efficient and long-term energy source, leveraging abundant fuel supplies and producing minimal radioactive waste compared to current nuclear fission technologies. However, achieving controlled and sustained fusion reactions remains a significant

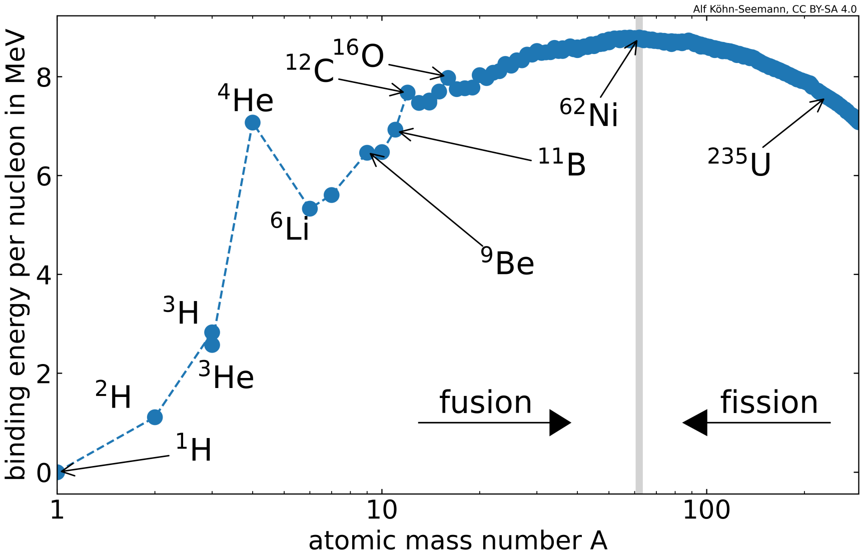

Figure 1.1: Binding energy per nucleon [5]

technological challenge. No operational fusion power plants have yet been realised, making it a potential future rather than a present solution.

1.1.2 Nuclear fusion reactions

Nuclei carry a positive charge, and for fusion to occur, they must overcome the electric repulsion from the Coulomb barrier, which arises from the charged state of the particles. The strength of this barrier is directly proportional to the nuclear charge (or the number of protons). Therefore, the colliding nuclei need energy to overcome the barrier and fuse. This energy is typically in the form of kinetic energy. On the atomic scale, this velocity denoted as v_{th} [7]:

$$v_{\text{th}} = \sqrt{\frac{k_B T}{m}} \tag{1.2}$$

where $k_B = 1.38 \times 10^{-23}\,\text{J}\,\text{K}^{-1}$ is the Boltzmann constant, T is the temperature in K and m is the nucleus mass in kg.

As hydrogen has the fewest protons, it requires the least energy to overcome the forces of its Coulomb barrier. The primary source of solar energy, and that of similar-sized stars, is hydrogen fusion, with the proton-proton (PP) chain being the primary fusion process in the Sun [8]. In more massive stars, the Carbon–Nitrogen–Oxygen (CNO) cycle dominates. It uses carbon, nitrogen, and oxygen as catalysts to convert hydrogen into helium, producing energy. In these cycles, hydrogen nuclei fuse under extreme temperatures and pressures to form helium, releasing immense energy. The overall reaction for the PP chain [8] can be represented as:

$$4\,{}^{1}\text{H}^{+} + 2e^{-} \;\rightarrow\; {}^{4}\text{He}^{2+} + \nu_e \tag{1.3}$$

A nuclear fusion reaction's probability depends on three critical factors: temperature, density, and confinement time. Due to its immense mass, gravitational effects, and very high confinement time, the Sun's environment features relatively low temperatures but high density. Replicating the Sun's core density levels on Earth is impractical, but higher temperatures can compensate for this offset. The environment's temperature determines the energy of the reacting particles. However, the probability of a reaction, or the cross-section, does not vary linearly with temperature, and each fusion reaction has specific cross-section data. In particle physics, the cross-section is a measure of the probability of a specific interaction or scattering event occurring between two particles, often expressed in units of area, either barns (b), which has an equivalent area of $10^{-28}\,\mathrm{m}^2$. It quantifies how likely it is that the particles will interact in a particular way when they encounter each other. Some reactions exhibit cross-sections that are orders of magnitude higher than others [9]. In the Sun, the PP chain reactions and the CNO cycle have relatively low cross-sections, but the large quantity of reactants compensates for this. For terrestrial fusion, leveraging reactions with higher cross-sections is crucial for achieving a more efficient reaction and a net energy gain. The cross-section increases significantly by utilising isotopes of hydrogen, such as deuterium and tritium, enhancing the feasibility of fusion reactors (see Figure 1.2).

$$
\begin{aligned}
{}^{2}\mathrm{D} + {}^{2}\mathrm{D} &\rightarrow {}^{3}\mathrm{He}(0.82\,\mathrm{MeV}) + n(2.45\,\mathrm{MeV}) && \text{(1.4a)}\\
{}^{2}\mathrm{D} + {}^{2}\mathrm{D} &\rightarrow {}^{3}\mathrm{T}(1.01\,\mathrm{MeV}) + p(3.02\,\mathrm{MeV}) && \text{(1.4b)}\\
{}^{2}\mathrm{D} + {}^{3}\mathrm{T} &\rightarrow {}^{4}\mathrm{He}(3.52\,\mathrm{MeV}) + n(14.06\,\mathrm{MeV}) && \text{(1.4c)}\\
{}^{2}\mathrm{D} + {}^{3}\mathrm{He} &\rightarrow {}^{4}\mathrm{He}(3.60\,\mathrm{MeV}) + p(14.7\,\mathrm{MeV}) && \text{(1.4d)}
\end{aligned}
$$

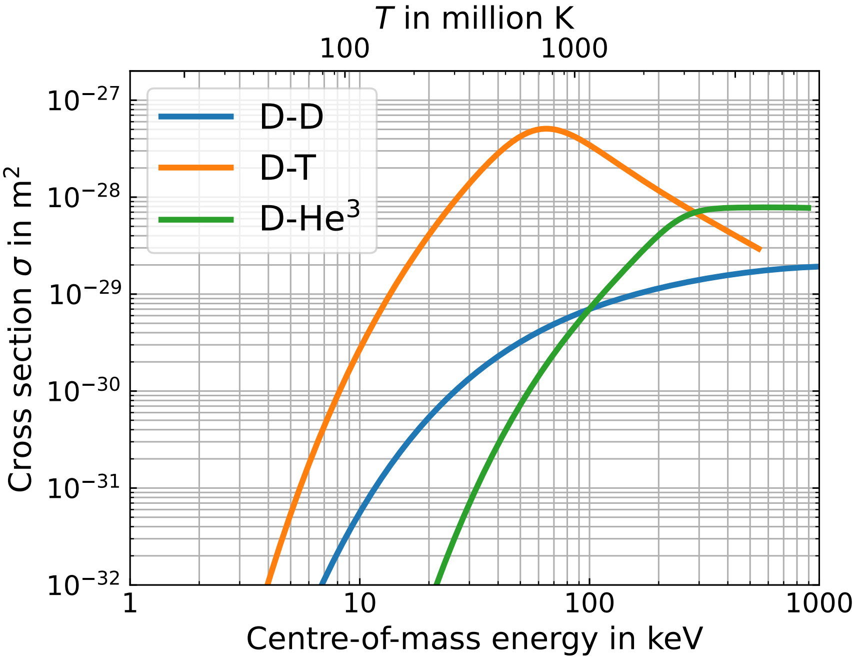

Figure 1.2: Fusion reaction cross-sections [5]

Reactions in (1.4) describe the most promising fusion sections proposed for reactors on Earth using combinations of hydrogen isotopes or helium. Deuterium-deuterium (DD) reactions could be valuable due to the natural abundance of deuterium, making it cost-effective. However, the cross-section for these reactions is relatively low (see Figure 1.2), and the reaction has multiple outcomes, either creating tritium and a proton or ^{3}He and a low-energy neutron. This variability complicates energy recovery, as the lower-energy neutrons make harnessing significant energy from the reaction challenging. Alternatively, deuterium-tritium (DT) fusion creates neutral helium and a high-energy neutron, from which the energy can be harnessed to produce electricity. This reaction has a higher cross-section at achievable temperatures, making it the most feasible option for current fusion reactor designs. Another favourable reaction is D-^{3}He fusion, as it produces no neutrons, reducing damage to the reactor. Furthermore, the high-energy proton's energy can be harnessed as its charged state will allow it to remain within the plasma, contributing to its heating. However, this reaction requires much higher temperatures to initiate (see Figure 1.2), and ^{3}He is an extremely rare isotope with no method for mass production. Suggestions to mine ^{3}He from the moon's surface may offer a solution in the distant future. Thus, the most favourable solution remains the DT reaction. While tritium is not naturally abundant, it can be manufactured by reacting high-energy neutrons with lithium, making it a more practical choice for sustainable fusion energy production.

1.1.3 Plasma confinement

The fusion fuel must be heated to hundreds of millions of degrees to initiate nuclear fusion. At this point, the DT gas transforms into a plasma in which electrons are separated from their nuclei. Magnetic confinement reactors operate on the principle of encasing these electrically charged particles within a "magnetic cage". The electrons and ions then gyrate around the magnetic field lines, characterised by the gyroradius [9]:

$$R = \frac{\sqrt{2mT}}{eB} \tag{1.5}$$

where e is its charge, and B is the magnetic field. In the environment of hot plasma, characterised by a temperature around 10 keV and subjected to a robust magnetic field of strength 3 T, the gyroradius of ions is ≈ 1 mm. This radius is significantly small relative to the reactor's dimensions $\approx> 10$ m, making magnetic confinement viable. The gyroradius radius for electrons is smaller due to their lesser mass, facilitating their confinement by straight magnetic lines perpendicular to the field lines. However, this system does not confine particles in a direction parallel to the magnetic lines. This challenge is overcome by transforming the magnetic field into a toroidal (doughnut-shaped) configuration, which, while effective, introduces a new issue. Bending the magnetic lines generates a gradient in the magnetic field along the radial direction, causing particles to drift and eventually escape the magnetic confinement.

Two solutions have been developed to counteract this drift. The first involves adding a central solenoid magnet, which induces a current within the plasma, twisting the magnetic field lines [11]. This setup is a Tokamak, a Russian acronym for "toroidal chamber with magnetic coils". The alternative approach is the stellarator, which achieves the necessary twist in the magnetic field through the toroidal coils' physical shaping [12]. This eliminates

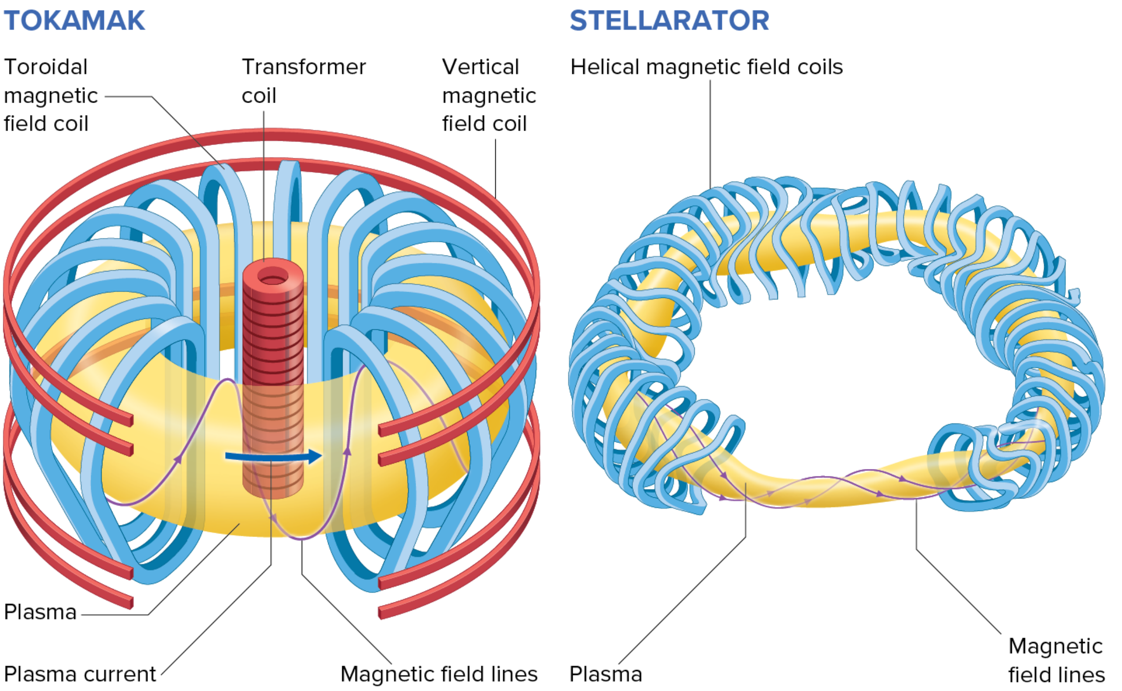
TOKAMAK
Toroidal magnetic field coil
Transformer coil
Vertical magnetic field coil
Plasma
Plasma current
Magnetic field lines
STELLARATOR
Helical magnetic field coils
Plasma
Magnetic field lines

Figure 1.3: Tokamak reactors (left) and related designs known as stellarator reactors (right) both confine the plasma (yellow) with magnetic fields (purple) that are generated by electromagnetic coils (blue and red) [10]

the need for an induced current and enables continuous, steady-state operation (see Figure 1.3). While tokamaks operate on a pulsed basis due to the central solenoid's limited capacity, their design is simple and scalable, allowing for the serial production of their components. On the contrary, the stellarator's main disadvantage is the complexity and uniqueness of its coil designs, which drives up the costs and technical challenges associated with its construction [13]. Despite these differences, each approach seeks to effectively maintain the conditions necessary for nuclear fusion, with tokamaks being the choice for international collaborative projects such as the ITER and the DEMO.

1.1.4 Fusion Power

A fundamental equation that tracks the change in thermal energy density, W, in units $\mathrm{J\,m^{-3}}$, stored in the plasma over time, can encapsulate the energy dynamics within a fusion reactor using DT fuel [14, 15].

$$\frac{\partial W}{\partial t} = P_{\text{fusion}} + P_{\text{heating}} - P_{\text{losses}} \tag{1.6}$$

This equation balances three primary elements: the density of power produced from fusion reactions, P_{fusion}, the external density of power applied to heat the plasma, P_{heating}, and the energy density losses the system experiences, P_{losses}. All three components are in units $\mathrm{W\,m^{-3}}$. The thermal energy density, W, is calculated by multiplying the plasma's density ,

n, in units m^{-3}, by its temperature, T, in units K:

$$W = 3nk_{\mathrm{B}}T \tag{1.7}$$

where the factor of 3 in Eq (1.7) arises because each particle in a three-dimensional plasma has three translational degrees of freedom, each contributing $\frac{1}{2}k_BT$ to the kinetic energy, resulting in a total thermal energy density of $\frac{3}{2}nk_BT$ for each particle species (ions and electrons), and when considering both species with equal densities and temperatures, this simplifies to $3nk_{\mathrm{B}}T$.

Fusion power density, P_{fusion}, generated directly from fusion reactions, depends on the densities of deuterium, n_D, and tritium, n_T, the DT reaction rate in units $\mathrm{m}^3\,\mathrm{s}^{-1}$, $\langle\sigma\rangle$, and the energy released by these reactions, E (see Eq. (1.8)). Though high energy, the neutrons born in DT fusion reactions don't contribute to the fusion power as they interact little with the plasma. Thus, for a reaction primarily producing energy through alpha particles, in the context of the plasma, $E = E_\alpha$, the relevant energy is around 3.56 MeV per reaction. Furthermore, assuming an equal mix of deuterium and tritium densities of D and T, $n_{\mathrm{D}} = n_{\mathrm{T}} = \frac{1}{2}n$. Therefore, the fusion power density formula simplifies to [14]:

$$P_{\mathrm{fusion}} = \frac{1}{4}n^2\langle\sigma\rangle E_\alpha \tag{1.8}$$

The ratio of fusion power density to heating power density is known as the amplification factor, Q. The heating power density (P_{heating}) then can be expressed in terms of Q as:

$$P_{\mathrm{heating}} = \frac{P_{\mathrm{fusion}}}{Q} \tag{1.9}$$

Power density losses, P_{losses}, resulting from both mass loss and radiation, are determined by the plasma confinement time, τ_E, leading to:

$$P_{\mathrm{losses}} = \frac{W}{\tau_E} = \frac{3nk_{\mathrm{B}}T}{\tau_E} \tag{1.10}$$

Assuming the reactor operates in an energy equilibrium state (where the total change in thermal energy over time equals zero), the equation balances out as follows:

$$\frac{1}{4}n^2\langle\sigma\rangle E_\alpha + \frac{P_{\mathrm{fusion}}}{Q} - \frac{3nk_{\mathrm{B}}T}{\tau_E} = 0 \tag{1.11}$$

Rearranging terms yields an equation for the triple product, $nT\tau_E$, a key metric for reactor performance, indicating the conditions needed to achieve a specific amplification factor, Q at a given temperature, T, in units eV [15]:

$$nT\tau_E = \frac{12T^2}{\langle\sigma\rangle E_\alpha} \cdot \frac{1}{1+Q^{-1}} \tag{1.12}$$

This triple product quantifies the conditions for a fusion reactor to achieve a designated energy amplification, encapsulating the interplay between plasma density, temperature, and energy confinement time.

When the external heating power density, P_{heating}, is reduced to nearly zero (meaning the reactor's auxiliary heating systems are turned off), the amplification factor, Q, tends to become infinitely large. Under these conditions, the equation for the triple product ($nT\tau_E$), which measures the plasma density, temperature, and energy confinement time, simplifies to [15]:

$$nT\tau_E \xrightarrow[Q\to\infty]{} \frac{12T^2}{\langle\sigma\rangle E_\alpha} \tag{1.13}$$

Here, the term $T^2/\langle\sigma\rangle$ reaches its minimum value when the temperature, $T = 14\,\text{keV}$ [15]. Additionally, within the temperature range, $10\,\text{keV} < T < 20\,\text{keV}$, the reaction reactivity, $\langle\sigma\rangle$, can be approximated as $\langle\sigma\rangle \approx 1.1 \times 10^{-24}\,\text{T}^2$ [15]. Thus, the simplified equation under these conditions can be expressed as:

$$nT\tau_E \geq 3 \times 10^{21}\,\text{keV}\,\text{s}\,\text{m}^{-3}$$

This equation is referred to as the Lawson criterion [16]. This fundamental threshold must be surpassed for a fusion reactor to achieve ignition (where $Q = \infty$), indicating a state of self-sustaining fusion reactions without needing external heating.

Fusion energy systems can be categorised into three main types based on how they achieve the necessary conditions for fusion:

- Stellar Fusion: Stars, such as the Sun, naturally meet the Lawson criterion through extremely long confinement times and high densities, though they operate at relatively low temperatures (2 keV in the Sun's core).
- Magnetic Confinement Devices: Tokamaks and stellarators, designed to contain hot plasma using magnetic fields, achieve temperatures significantly higher than those found in stars (an order of magnitude higher), but their energy confinement times are much shorter, typically on the order of seconds, and have lower densities.
- Inertial Confinement Devices: These devices aim to rapidly heat and compress a target fuel using lasers (like the NIF [17] or Laser Mega Joule [18]), pistons (as with General Fusion), or high-speed projectiles (as explored by First Light Fusion). They are characterised by extremely high densities, high temperatures, and brief confinement times, aiming to momentarily achieve the conditions necessary for fusion before the fuel disperses.

These diverse approaches to achieving fusion energy illustrate the explored strategies, each presenting unique challenges and advantages. While natural stellar fusion operates continuously within stars, technological solutions on Earth—whether through magnetic or inertial confinement—aim to replicate the conditions necessary for sustained fusion in a controlled environment. Among these, magnetic confinement devices, particularly tokamaks, are the leading candidates for scalable fusion power production.

The development of the DEMO power plant under the EUROfusion roadmap marks a critical step forward in ongoing efforts to bring magnetic confinement fusion closer to commercial viability. DEMO is designed to demonstrate the continuous operation of a fusion reactor and integrate essential technologies, such as the tritium breeding blanket, that will enable a self-sufficient fuel cycle. The following section will introduce the concept of DEMO and explore the role of these technologies in facilitating the transition from experimental devices to practical fusion power plants.

1.1.5 DEMO

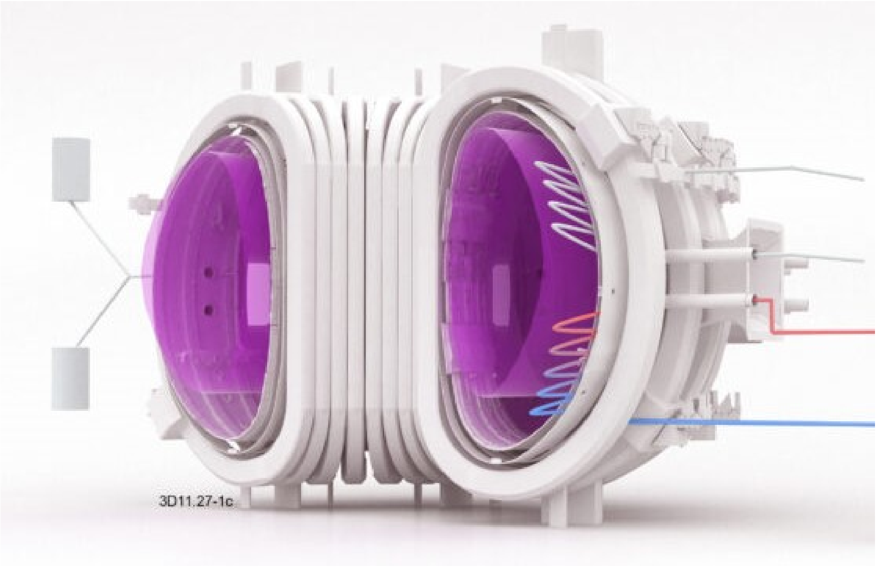

Figure 1.4: Artistic impression of the DEMO reactor [19]

The DEMOnstration fusion power plant represents an ambitious step forward in harnessing fusion energy, designed to transition from experimental to practical, commercial energy production [20]. It is envisioned as the successor to the ITER, aiming to capitalise on ITER 's technological and scientific breakthroughs. While ITER's mission is to prove that nuclear fusion can be a viable energy source, DEMO 's goal is to demonstrate that this energy can be converted into electricity and supplied to the power grid, marking a significant leap towards commercialising fusion power. DEMO is planned to operate with a self-sustaining fusion plasma in long pulses to maximise the plant availability. Additionally, it will serve as a testing ground for advanced technologies essential for a commercial fusion reactor, including tritium breeding to generate its fuel, materials capable of withstanding the reactor's extreme conditions, and efficient systems for converting fusion energy into electricity. An artistic impression of the DEMO reactor's design is shown in Figure 1.4.

As the conceptual and planning phases of DEMO continue, the project aims to build upon the foundation laid by ITER and address the technological, operational, and economic challenges of bringing fusion energy to the market. The international fusion research community views DEMO as a critical step towards realising the dream of clean, sustainable, and abundant energy from fusion [19]. The development timeline for DEMO is ambitious. Construction is anticipated to begin several years after ITER achieves full-power operation.

1.2 The tritium issue

As described previously, tritium will be a vital component of the fusion fuel. However, the handling of this radioactive hydrogen isotope presents several challenges. Tritium's unstable nature makes it a hazard to human health and leads to the natural depletion of its stored reserves. To harness tritium effectively as a fuel, it is crucial to understand its interactions with living tissues, establish safety protocols for handling, determine its role within the global fuel cycle and explore methods for its production. Additionally, a detailed grasp of how hydrogen isotopes interact with various components of the fuel cycle is essential. This includes understanding tritium's behaviour when in contact with metals, its transportation within the system, and the mechanisms of its interactions.

1.2.1 Safety

Given tritium's radioactive nature, safe handling is paramount to protect local working personnel, the public, and the environment. This section delves into the safety considerations associated with tritium, examining its radioactive characteristics and the methods used to evaluate radiation doses. Subsequently, regulatory frameworks and safety protocols that govern tritium activities are explored, highlighting the stringent measures to mitigate potential risks in handling tritium.

The becquerel (Bq) is the standard unit for measuring radiation. A becquerel represents one radioactive disintegration per second, making it a minimal measure of radiation. Conversely, one curie is roughly equivalent to the radiation emitted by 1 gram of radium, making it a much larger measure.

$$1\,\mathrm{Ci} = 3.7 \times 10^{10}\,\mathrm{Bq} \tag{1.14}$$

However, the becquerel (Bq) measures only the activity level of a radioactive source. It does not provide information about the quantity or energy of the rays or particles released with each disintegration. A material's radioactivity refers to the rate at which it emits radiation and can be characterised by its activity. The activity of an isotope is given by [21]:

$$A = \lambda N_\mathrm{A} \frac{m}{M} e^{-\lambda t} \tag{1.15}$$

where m is the mass of the sample in kg, $N_\mathrm{A} = 6.022 \times 10^{23}\,\mathrm{mol}^{-1}$ is Avogadro's constant, M is the molar mass in $\mathrm{kg\,mol}^{-1}$, t is time in s and λ is the decay constant, in units s^{-1}, is defined as [21]:

$$\lambda = \frac{\ln(2)}{T_{1/2}} \tag{1.16}$$

where $T_{1/2}$ is the isotope's half-life and is defined as the time required for the activity to half. Tritium has a half-life of 12.32 years and undergoes beta decay [2], producing ^{3}He in the process:

$$^3\mathrm{H} \;\rightarrow\; ^3\mathrm{He} + e^- \;(18.6\,\mathrm{keV}) \tag{1.17}$$

thus, the initial activity of 1g tritium is equivalent to 355 TBq.

The effect of ionising radiation on matter is expressed in energy deposited per unit mass (D). The SI unit of absorbed dose is the gray (Gy). A further factor is considered as different types of radiation have different effects on living tissue. This is called the radiation weighting factor (W_R) and gives rise to a measure of radiation dose called the equivalent dose (H_T). The SI unit is the sievert (Sv).

$$1\,\text{Sv} = 1\,\text{Jkg}^{-1} \tag{1.18}$$

hence:

$$H_T = W_R D \tag{1.19}$$

The equivalent dose is a point source quantity. It is further weighted by a tissue or organ weighting factor (W_T) to account for the fact that some body parts are more susceptible to radiation damage than others. The final result is an effective dose E (also measured in Sv) given by:

$$E = \sum_{\text{organs}} W_T H_T \tag{1.20}$$

Values of radiation weighting factor (W_R) for different types of radiation and organ weighting factors (W_T) can be taken from the latest International Commission on Radiological Protection (ICRP) recommendations [22, 23].

Due to tritium's radioactive properties and potential health hazards, the management and handling of this isotope are governed by stringent regulations at both international and national levels [24]. ITER is being built in France and is subject to French nuclear regulation. French regulations specify a maximum allowable effective dose of 20 mSv for 20 consecutive months for radiation workers, excluding natural radioactivity and medical exposures. This standard applies to the "whole body dose." When specific organs or tissues are exposed, equivalent dose limits are applied, such as 15 mSv/year for the eye's crystalline lens and 50 mSv/year for the skin (average value for any 1 cm^2 of skin). A 1 mSv/year limit is prescribed for the general public. To put this into perspective, the average exposure in France from sources other than medical treatments and natural radioactivity is 0.060 mSv/year, a portion of this coming from nuclear activities that affect the public. For professionals working with ionising radiation, the exposure limit is set at 100 mSv over five years, with no year exceeding 50 mSv [25].

To minimise the risk of environmental contamination from a vacuum loss accident, limiting the amount of tritium kept in fusion reactors is necessary [26]. For example, the ITER project restricts its tritium inventory to 1 kg, which includes 120 g stored in cryo-pumps and an additional 180 g allocated for measurement uncertainties [27, 28]. This limitation aims to prevent the need to evacuate nearby populations in case of such an accident. Tritium, which can permeate through materials, renders components it contacts as contaminated waste requiring special handling. The permeation of tritium into cooling systems can contaminate coolants and, therefore, requires coolants to undergo detritiation (tritium removal) [29, 30].

Efforts are underway to develop detritiation techniques that reduce radioactive waste volume in future fusion reactors. These methods primarily involve heating tritiated materials to release and then recapture tritium gas, which can be recycled as fuel [31]. Additional strategies to minimise tritium levels include laser-induced desorption and "baking" plasma-facing components in between reactor operations [28].

Research also focuses on creating permeation barriers to significantly lower tritium permeation into cooling fluids [32, 33, 34]. These barriers might include coatings made from alumina, Al_2O_3, or other ceramics like Cr_2O_3 and Er_2O_3 on the inner or outer surfaces of cooling pipes. Naturally occurring oxides are also being considered. These coatings could serve multiple purposes, such as reducing corrosion or providing electrical insulation to mitigate Magnetohydrodynamics (MHD) effects.

Given the stringent safety protocols and regulatory frameworks governing tritium handling, its role within a fusion reactor extends beyond mere fuel supply. The radioactive nature of tritium necessitates careful management throughout its lifecycle, from storage and transport to its integration within the reactor system. In a typical fusion plant, this management is embedded within the broader concept of the fuel cycle, where tritium is handled as a hazardous substance and actively produced and recycled to sustain the fusion process. The following section will delve into the intricacies of this fuel cycle, highlighting how tritium is bred, extracted, and recirculated. This ensures a self-sufficient and continuous operation within the fusion reactor while maintaining strict safety standards.

1.2.2 Fusion reactor fuel cycle

The fuel cycle in a fusion reactor, particularly in deuterium-tritium (DT) fusion, encompasses several key components designed to sustain the fusion process and harness its energy. Initially, the cycle involves preparing and injecting deuterium and tritium as fuel into the reactor's core. Deuterium and tritium nuclei fuse within the plasma to form helium, releasing a neutron and significant energy. The released neutrons are captured by a blanket surrounding the plasma, where their kinetic energy is transformed into heat for electricity generation. Importantly, this blanket also contains lithium or lithiated compounds that, upon neutron capture, undergo nuclear reactions to breed tritium. The bred tritium is then extracted, purified, and recycled back into the reactor as fuel. This cycle is pivotal for maintaining the fusion reaction and ensuring a self-sufficient supply of tritium, given its scarcity and the challenges associated with its procurement and handling due to its radioactive nature.

In this work, the fuel cycle is presented in a simplified form, as seen in Figure 1.5, comprised of four core components: the plasma, tritium fuel storage, the Breeding Blanket (BB), and the Tritium Extraction System (TES). This basic model illustrates fundamental concepts such as start-up inventory requirements, the inflexion point in storage quantities, and the dynamic interplay between the production and consumption of tritium. However, it should be noted that this simplified cycle makes certain assumptions, such as no losses from permeation out of the loop or decay, which are not fully representative of real reactor conditions.

In practice, fusion fuel cycles are far more intricate, involving many subsystems and processes that interact in complex ways. Realistic models must account for additional components such as tritium processing and separation units, various subsystems for coolant management, and safety measures to handle permeation, trapping, and radioactive decay. Furthermore, one critical challenge in accurately modelling tritium behaviour is accounting for phenomena like tritium trapping within materials, which can significantly affect the dynamics of the fuel cycle. Many advanced system codes used for fuel cycle modelling often simplify or overlook these effects, leading to potential discrepancies between simulated and actual tritium inventories.

While this work does not explore the complexities of a fully developed fuel cycle model, the simplified approach highlights essential features and the potential limitations of current modelling practices. The focus is to provide a conceptual understanding rather than a detailed simulation, emphasizing critical factors for effective tritium management in future fusion reactors.

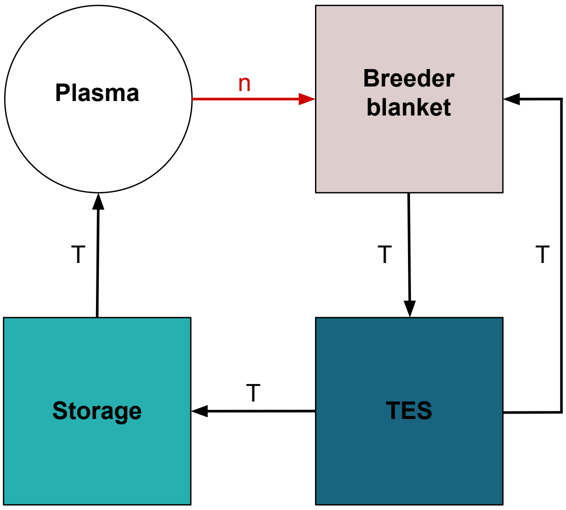

Figure 1.5: A schematic process diagram for a simplified fuel cycle

One can model the dynamics of the tritium inventory for each component in such a simplified fuel cycle model with a set of ODE's:

$$\frac{\partial I_{\mathrm{BB}}}{\partial t} = \dot{N} \cdot \mathrm{TBR} - \frac{I_{\mathrm{BB}}}{\tau_{\mathrm{BB}}} + f_{\mathrm{TES} \to \mathrm{BB}} \frac{I_{\mathrm{TES}}}{\tau_{\mathrm{TES}}} \tag{1.21a}$$

$$\frac{\partial I_{\mathrm{TES}}}{\partial t} = -\frac{I_{\mathrm{TES}}}{\tau_{\mathrm{TES}}} + \frac{I_{\mathrm{BB}}}{\tau_{\mathrm{BB}}} \tag{1.21b}$$

$$\frac{\partial I_{\mathrm{S}}}{\partial t} = -\dot{N} + f_{\mathrm{TES} \to \mathrm{Storage}} \frac{I_{\mathrm{TES}}}{\tau_{\mathrm{TES}}} \tag{1.21c}$$

where I_{BB}, I_{TES} and I_{S} are the tritium inventories in the BB, tritium extraction system and storage respectively. τ is the residency time, f is the flow fraction and $\dot{N}$ is the neutron flux from the plasma interacting with the BB. With these, using arbitrary values, one can model a simplified version of a fusion reactor fuel cycle and examine how the tritium inventories for each component change with time.

In the complex ecosystem of a fusion reactor's fuel cycle, the management and tracking of tritium inventories embody a critical and intricate challenge. At the heart of this challenge is the nuanced journey of tritium from its initial storage as start-up inventory to its vital role in generating fusion plasmas. This journey is punctuated by a significant temporal delay, marking the time it takes for newly produced tritium within the breeders to be moved to an extraction system, where it is then extracted and processed into a usable form for plasma generation. This inherent delay introduces a dynamic flux within the tritium inventory landscape, revealing distinct phases in the inventory's life cycle within the fuel storage system.

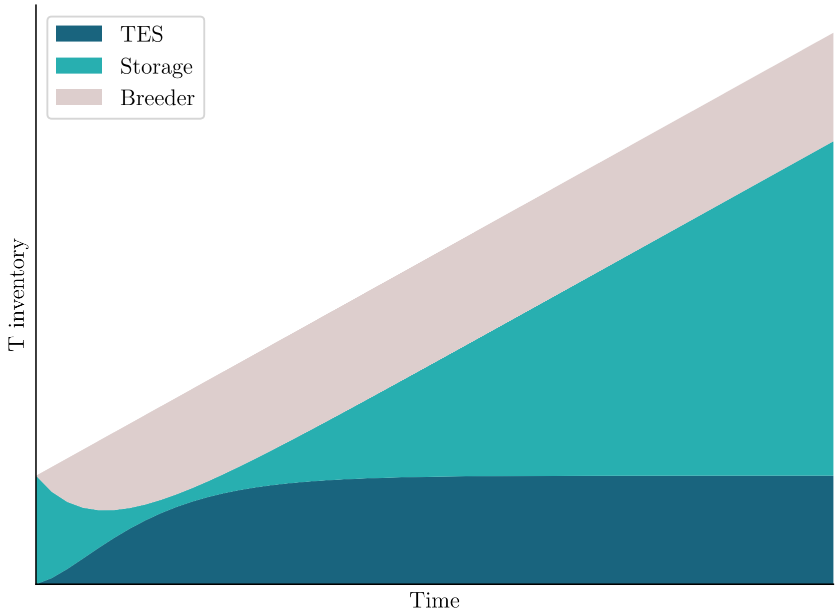

Figure 1.6: Tritium inventory changes over time in the TES, storage and breeder

As the fusion reactor commences operations, the tritium inventory depletes rapidly (see Figure 1.6), drawing down the start-up reserves to fuel the plasma generation processes. This phase is characterised by a marked decrease in tritium levels, culminating in an inflexion point. This pivotal moment occurs when tritium, newly generated and processed through the internal fuel cycle, begins to arrive for use, mitigating the initial rapid decline in inventory. This inflexion point heralds a shift in the dynamics of tritium management, underscoring the critical interplay between tritium production, extraction, and replenishment within the fusion fuel cycle. However, modelling tritium inventories within this cycle often encompasses simplifications and assumptions that gloss over the complexities of tritium behaviour in reactor components. A notable simplification is the assumption of an arbitrary value for tritium extraction efficiency, which does not account for the nuances of tritium trapping and local inventory buildup within reactor components. Tritium can be trapped in materials, leading to localised concentrations not readily accounted for in standard fuel cycle models. To address this discrepancy, models frequently adjust a component's residency time, intending to mimic the effect of trapping on tritium diffusion. Thus, this approach falls short of capturing the true essence of local inventory buildup, presenting a simplified view of the fundamentally complex processes involved in hydrogen transport [35, 36, 37, 38]. Furthermore, this model neglects the permeation of tritium out of the cycle components or radioactive decay.

1.2.3 Breeding

Current methods of industrial tritium production are limited to the transmutation of D_2O or irradiation of lithiated compounds. Deuterium can absorb a neutron through capture to form tritium [14]:

$$n + {}^{2}D \rightarrow {}^{3}T \tag{1.22}$$

Thus, tritium is a natural by-product in CANDU fission reactors, which use D_2O as a neutron moderator [39]. Alternatively, lithiated compounds undergo neutron capture to produce tritium, where the products depend on the isotope of lithium [14]:

$$n + {}^{6}Li \rightarrow {}^{3}T + \alpha + 4.8\ \text{MeV} \tag{1.23}$$

$$n + {}^{7}Li + 2.5\ \text{MeV} \rightarrow {}^{3}T + \alpha + n' \tag{1.24}$$

The neutron capture cross-section for each reaction is shown in units barns (b), a unit of area equivalent to $10^{-28}\,m^{-2}$. Neutron cross-sections depend on the incident energy, shown in Figure 1.7.

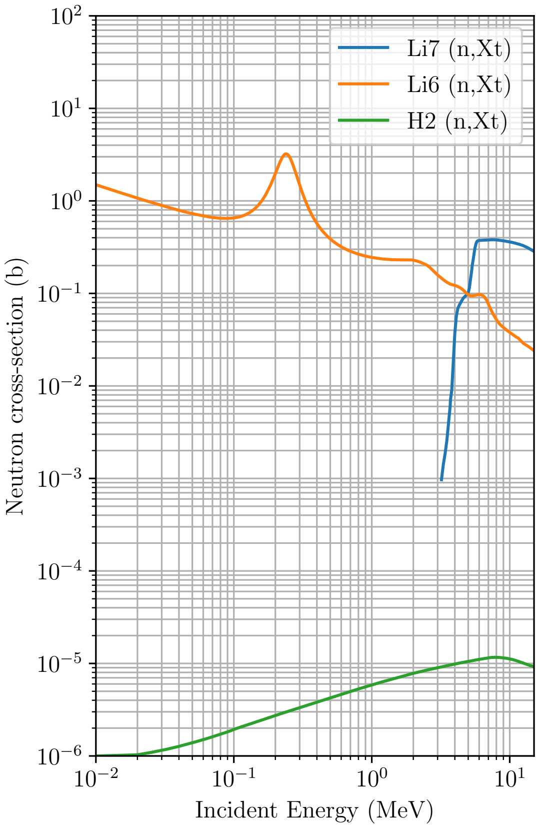

Figure 1.7: Cross-section of neutron capture reactions in barns with Li-7 Li-6 and H2 producing tritium [40]

Figure 1.7 illustrates that the probability of tritium production from deuterium is significantly lower, by several orders of magnitude, than from lithium isotopes. Despite this, CANDU reactors generate approximately 130 g of tritium annually due to the extensive quantity of D_2O as a moderator, which increases the likelihood of tritium production [41]. Therefore, lithium compounds are more suitable for tritium production in breeder blankets. Although ${}^{6}Li$ has a higher neutron capture cross-section at lower energies than ^{7}Li, it naturally occurs at only 7.59% abundance. Lithium compounds can be enriched to increase the ^{6}Li concentration, but this process can be costly [42]. Optimisations such as ^{6}Li enrichment, adjusting the ^{6}Li/^{7}Li ratio, or employing neutron multipliers can improve the efficiency of a tritium BB. Furthermore, using liquid tritium breeders can increase the area that reacts with neutrons. Another method uses distribution techniques, placing ^{7}Li nearer to the first wall where neutron energies are higher and ^{6}Li further back. However, this approach is impossible for liquid breeders like PbLi. An alternative strategy involves neutron multiplication using materials with large cross-sections for (n, 2n) or (n, 3n) reactions, thereby increasing the neutron population and the likelihood of interactions with lithium to produce more tritium (see Figure 1.8). Examples of such materials include beryllium and lead [14].

$$\mathrm{n} + {}^{9}\mathrm{Be} + 3\ \mathrm{MeV} \rightarrow 2\alpha + \mathrm{n}' + \mathrm{n}'' \tag{1.25}$$

$$\mathrm{n} + {}^{208}\mathrm{Pb} + 10\ \mathrm{MeV} \rightarrow {}^{207}\mathrm{Pb} + \mathrm{n}' + \mathrm{n}'' \tag{1.26}$$

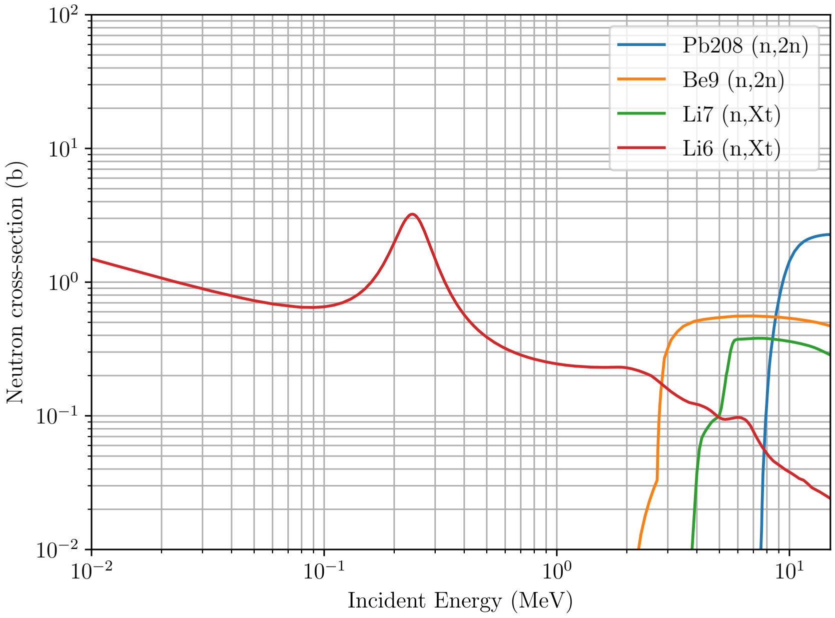

Figure 1.8: cross-section of neutron capture reactions with Pb and Be compared to lithium isotopes [40]

Furthermore, a suggested liquid breeder material, PbLi, has a neutron multiplier within the compound and thus would not require additional material for multiplication. However, for materials without internal neutron multiplying materials, it has been suggested small pellets could be used within the blanket [43].

1.2.4 Hydrogen in materials

In addition to the tritium generated within a breeder, hydrogen particles bombard the inner surface of a fusion reactor, including plasma-facing components such as the first wall and divertor. Due to their small size, these particles can infiltrate the metal structure and embed themselves within the material. Hydrogen transport in metals involves various mechanisms and processes (see Figure 1.9). Such processes can be broadly divided into four main categories: diffusion, trapping, boundary physics, and interface conditions.

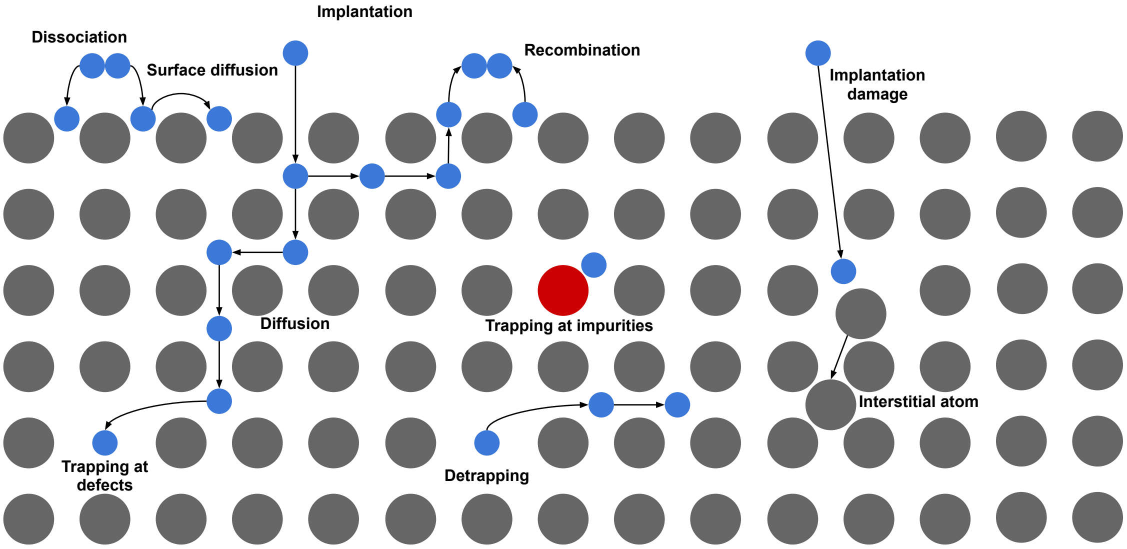

Figure 1.9: Interactions of solute hydrogen isotopes in metals [44]

Hydrogen transport in metals can be complex, depending on the type of metal lattice (e.g., face-centred cubic, body-centred cubic, hexagonal close-packed). Hydrogen atoms diffuse through a metal lattice by jumping from one interstitial site to another. Each interstitial site provides a potential energy well, and a hydrogen atom can move from one site to another if it has enough energy E_D (see Figure 1.10). At the atomistic scale, particles move around a lattice in what is described as Brownian motion [45]. However, the chemical potential gradient governs hydrogen transport diffusion at a macroscopic scale, encompassing gradients of concentration, temperature (Soret effect or thermophoresis [46, 47]), and mechanical hydrostatic pressure [48]. The concentration gradient can be described by Fick's laws of diffusion to model the movement of hydrogen atoms [49]. Higher temperatures generally increase the diffusion rate by providing the energy necessary for hydrogen atoms to overcome energy barriers between interstitial sites and can be described by an Arrhenius law:

$$D = D_0 \cdot \exp\left(\frac{-E_D}{k_B T}\right) \tag{1.27}$$

where D_0 is a pre-exponential factor expressed in terms $\mathrm{m^2\,s^{-1}}$, E_D is the diffusion activation energy expressed in units eV. Atomistic modelling techniques like Density Functional Theory (DFT) and Molecular Dynamics (MD) are valuable tools for estimating hydrogen diffusion coefficients in metals. They can model the fundamental atomic processes of diffusion and can be used to derive macroscopic diffusion coefficients [50, 51, 52, 53].

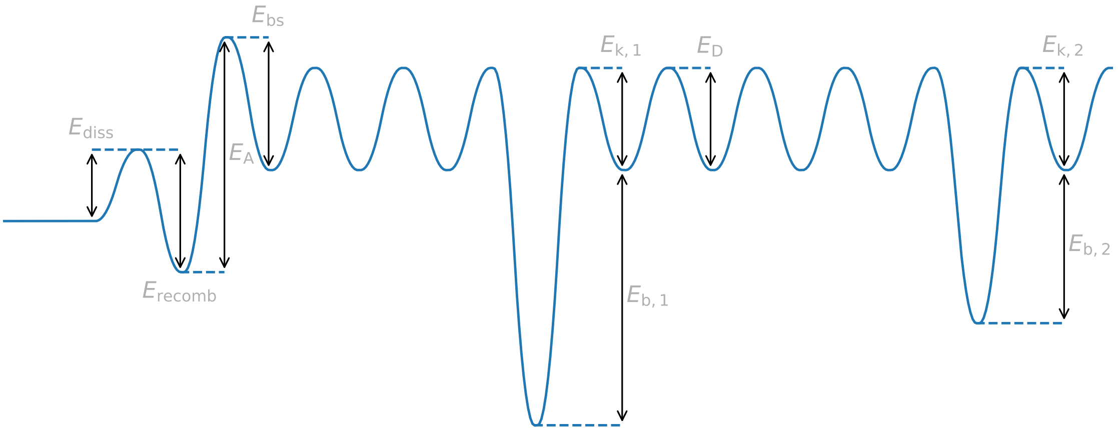

Figure 1.10: Potential energy vs reaction coordinate, showing the influence surface effects and two different types of defect [44]

Alternatively, the diffusion coefficient of H in metals can be evaluated experimentally. In permeation experimental platforms, hydrogen is introduced on one side of a thin metal membrane, and the hydrogen flux at which it appears on the opposite side is measured. The time lag and steady-state flux methods are used to calculate the effective diffusion coefficient, $D_{\rm eff}$. $D_{\rm eff}$ includes the effects of microstructural features like grain boundaries and traps. In contrast, the actual diffusion coefficient (D) represents hydrogen diffusion in a perfect, homogeneous crystal lattice [54].

Temperature gradients may also facilitate diffusion, known as the Soret effect or thermophoresis [46, 47].

Defects within a metal's lattice, such as vacancies, impurities, dislocations or voids, create potential energy wells, more profound than those for interstitial sites, trapping diffusing species, and require further energy in the form of temperature to escape. The trapping process can be described as [55]:

$$[\quad] + (\mathrm{H}) \underset{\nu_{\rm dt}}{\overset{\nu_{\rm t}}{\rightleftarrows}} [\mathrm{H}] + (\quad) \tag{1.28}$$

where H is the mobile diffusing hydrogen within an interstitial site, [ ] is an empty trap site, [H] represents a trapped hydrogen particle, and ( ) represents an empty interstitial site. The rates of trapping and detrapping, $\nu_{\rm t}$ and $\nu_{\rm dt}$, can be expressed respectively as [56]:

$$\nu_{\rm t} = \nu_{\rm t,0} \cdot \exp\left(\frac{-E_{\rm t}}{k_B T}\right) \tag{1.29}$$

$$\nu_{\rm dt} = \nu_{\rm dt,0} \cdot \exp\left(\frac{-E_{\rm dt}}{k_B T}\right) \tag{1.30}$$

where $\nu_{\mathrm{t},0}$ is the trapping pre-exponential factor in $\mathrm{m^3\,s^{-1}}$, E_t is the trapping energy in eV. Typically, it is assumed that $E_t = E_D$. $\nu_{\mathrm{dt},0}$ is the detrapping pre-exponential factor in $\mathrm{s^{-1}}$, E_dt is the detrapping energy in eV, where $E_\mathrm{dt} = E_\mathrm{b} + E_\mathrm{k}$ (see Figure 1.10). These parameters can be determined experimentally from Thermal Desorption Spectroscopy (TDS) data [54]. TDS experiments involve loading a metal sample with the element being examined (for instance, deuterium) and then gradually heating it at specific rates, all while monitoring the rate at which these elements are released from the sample. This process generates a spectrum often characterised by one or a series of peaks, each indicative of various binding sites within the metal. Peaks that emerge at higher temperatures are sometimes associated with "irreversible" binding sites, which require more energy or time to release the trapped elements. These parameters can also be obtained from atomistic calculations [57, 58, 59, 60, 61, 62]

Defects in a material can be categorised into two types. The first type, often referred to as intrinsic defects (or native defects), are inherent to the material, such as impurities and grain boundaries. The second type, extrinsic defects, result from external influences, including damage from particle bombardment (such as ions and neutrons) [63] or mechanical stress [64], and may evolve temporally and spatially. Extrinsic defects are crucial to characterising fusion reactors due to the high neutron fluxes with which components near the plasma are likely to interact. The intense neutron bombardment in these environments can lead to significant damage, creating a high density of extrinsic defects that can affect the material properties and performance. Understanding the formation and evolution of these defects is essential for predicting the lifespan and reliability of reactor components. Despite their importance, the dynamics of extrinsic trap formation due to neutron interactions have not been extensively explored in the literature.

When a surface is in contact with a gas, molecules like $\mathrm{H_2}$, $\mathrm{T_2}$, and HD can dissociate into individual atoms, which may then be adsorbed onto the surface's adsorption sites [65]. At steady-state, this dissociation follows a sticking probability described by the Arrhenius law: $s = s_0 \exp\left(-E_s/k_B T\right)$. While DFT calculations can determine energy barriers for adsorption and migration on surfaces [61], studies indicate that the process isn't only thermally activated (i.e., $E_s = 0$) but can also depend on the surface coverage, θ, which is the ratio of the surface concentration of the species to the concentration of adsorption sites [66, 67]. Surface coverage, θ, ranges from 0 (all sites available) to 1 (fully saturated). Impurities on adsorption sites can lower the sticking probability of a species. Adsorbed particles can be absorbed into the bulk, a thermally activated process with an absorption coefficient following an Arrhenius law. DFT models this absorption, allowing the determination of absorption activation energies E_A for various surface orientations [68, 69]. From these detailed processes, simpler macroscopic models can be designed. An absorption flux can describe all these processes (dissociation, adsorption and absorption) [56]:

$$\phi_\mathrm{abs} = n K_\mathrm{abs} P \tag{1.31}$$

where n is the absorption order, K_abs is the absorption coefficient in units $\mathrm{m^{-2}\,s^{-1}\,Pa^{-1}}$ and P is the partial pressure of hydrogen in Pa. The desorption of a solute species can be expressed with a desorption flux [70]:

$$\phi_\mathrm{des} = n K_\mathrm{des} c_\mathrm{surface}^n \tag{1.32}$$

where n is the order of desorption (1 if monoatomic, two if diatomic), K_{des} is the rate constant for desorption in units $\mathrm{m}^{-2+3n}\,\mathrm{s}^{-1}$ (units depending on order n) and c_{surface} is the sub-surface concentration, in units m^{-3}. When the equilibrium between absorption and desorption is reached, $\phi_{\mathrm{abs}} = \phi_{\mathrm{des}}$, resulting in:

$$nK_{\mathrm{abs}}P = K_{\mathrm{des}}c_{\mathrm{surface}}^{n} \tag{1.33}$$

thus, the concentration on the surface can be expressed as:

$$c_{\mathrm{surface}} = \sqrt[n]{\frac{nK_{\mathrm{abs}}}{nK_{\mathrm{des}}}}\sqrt[n]{P} \tag{1.34}$$

When the absorbing/desorbing gas is monoatomic (order n=1):

$$c_{\mathrm{surface}} = K_{\mathrm{S}}P \tag{1.35}$$

This relationship is known as Henry's law of solubility [71] where $K_{\mathrm{S}} = K_{\mathrm{abs}}/K_{\mathrm{des}}$ and is in units $\mathrm{m}^{-3}\,\mathrm{Pa}^{-1}$. K_{S} is also describe by an Arhenius Law:

$$K_{\mathrm{S}} = K_{\mathrm{S},0} \cdot \exp\left(\frac{-E_S}{k_B T}\right) \tag{1.36}$$

where $K_{\mathrm{S},0}$ is a pre-exponential factor expressed in terms $\mathrm{m}^{-3}\,\mathrm{Pa}^{-1}$, E_S is the solubility activation energy expressed in units eV. Alternatively, when the absorbing/desorbing gas is diatomic (order n=2):

$$c_{\mathrm{surface}} = K_{\mathrm{S}}\sqrt{P} \tag{1.37}$$

This relationship is known as Sievert's law [72], where in this case, $K_{\mathrm{S}} = \sqrt{K_{\mathrm{abs}}/K_{\mathrm{des}}}$ and in units $\mathrm{m}^{-3}\,\mathrm{Pa}^{-0.5}$.

The continuity of chemical potential must be ensured at the interface between materials. The continuity of the local partial pressure of hydrogen at equilibrium can convey this continuity at equilibrium [73]. In the case of an interface between two metallic surfaces, the partial pressure, P, can be derived from Sievert's law of solubility (Eq. (1.37)):

$$P = \left(\frac{c_{\mathrm{m}}}{K_{\mathrm{S}}}\right)^2 \tag{1.38}$$

thus, for two sides of a metallic interface (- and +), this is expressed as:

$$\left(\frac{c_m^-}{K_{\mathrm{S}}^-}\right)^2 = \left(\frac{c_m^+}{K_{\mathrm{S}}^+}\right)^2 \tag{1.39}$$

In the case of an interface between a metallic surface (where hydrogen transports monoatomically) and a non-metallic liquid (where hydrogen can transport diatomically), the behaviour changes according to Henry's law of solubility:

$$\left(\frac{c_m^-}{K_{\mathrm{S}}^-}\right)^2 = \frac{c_m^-}{K_{\mathrm{S}}^-} \tag{1.40}$$

Typically, hydrogen solubility in materials varies significantly. This results in a concentration jump between materials at the interface [74, 75].

Hydrogen transport within liquids and gases involves the combined effects of advection and diffusion. Advection happens as the hydrogen, acting as a mobile species, is carried along by the flow of the liquid, with its transport rate closely tied to the liquid's velocity. This advective movement is complemented by diffusive transport, where hydrogen moves from areas of higher concentration to lower concentration, independent of the liquid flow. The relative significance of advection versus diffusion in governing hydrogen's mass transport within the liquid is determined by the liquid's velocity and hydrogen diffusivity in that specific liquid. The Péclet number (Pe), a dimensionless value, is used to quantify which phenomenon predominates [76].

$$\mathrm{Pe} = \frac{\text{advective transport rate}}{\text{diffusive transport rate}} = \frac{Lu}{D} \tag{1.41}$$

where L is the characteristic length of a domain in units m, u is the fluid velocity in units $\mathrm{m\,s^{-1}}$, and D is the mobile species diffusivity within the fluid in units $\mathrm{m^2\,s^{-1}}$. A higher Péclet number suggests advection dominance, while a lower value indicates diffusion is the primary transport mechanism.

In the context of hydrogen interaction with materials, hydrogen embrittlement is a widely known issue in high-strength materials, where the absorption and diffusion of hydrogen cause subcritical crack growth, fracture initiation, and catastrophic failure, leading to significant loss of ductility, toughness, and strength [77, 78]. Preventive measures encompass material selection, hydrogen exposure control, process modifications, and hydrogen removal through post-processing treatments [79].

1.3 WCLL

The Water-Cooled Lead-Lithium (WCLL) breeding blanket is one of two concepts planned to be tested in the ITER TBM program [80] (see Figure 1.11). The performance of each concept will determine which will be used for the European DEMO. One of the BB 's primary functions is to recover the thermal power from the first wall and the breeding zone and drive it to the Primary Heat Transfer System. Moreover, due to the DEMO pulsed operation, an energy storage system is foreseen to ensure thermal energy availability and reduce cycling loading during dwell time. The blanket design must interface with the primary and intermediate heat transfer systems in an integrated solution to deliver a feasible power plant with high conversion efficiency [81]. However, the heart of the WCLL BB concept lies in its ability to produce tritium efficiently. It will be required to demonstrate an ability to produce more tritium than used by the reactor.

1.3.1 Design

The design of the BB is significantly affected by the layout of the DEMO reactor [82]. The DEMO reactor is divided into 16 sectors by 16 Toroidal Field Coils (TFCs), each spanning an angle of 22.5°. These sectors are further divided into five BB segments. The inboard region of each sector has two segments: the Left Inboard Blanket (LIB) and the Right Inboard Blanket (RIB). The outboard region contains three segments: the Left Outboard Blanket (LOB), the Central Outboard Blanket (COB), and the Right Outboard Blanket (ROB). During Horizon 2020, or European Framework Program 8 (FP8), the WCLL BB design underwent significant revisions [83], transitioning from a multi-module segment (MMS) concept based on small, ITER-like modules to a single-module segment (SMS) approach in 2017 [82, 84, 85]. This change enhanced shielding performance, tritium breeding ratio, and segment robustness against electromagnetic loads from plasma disruptions [86] while simplifying the distribution of breeder and coolant materials.

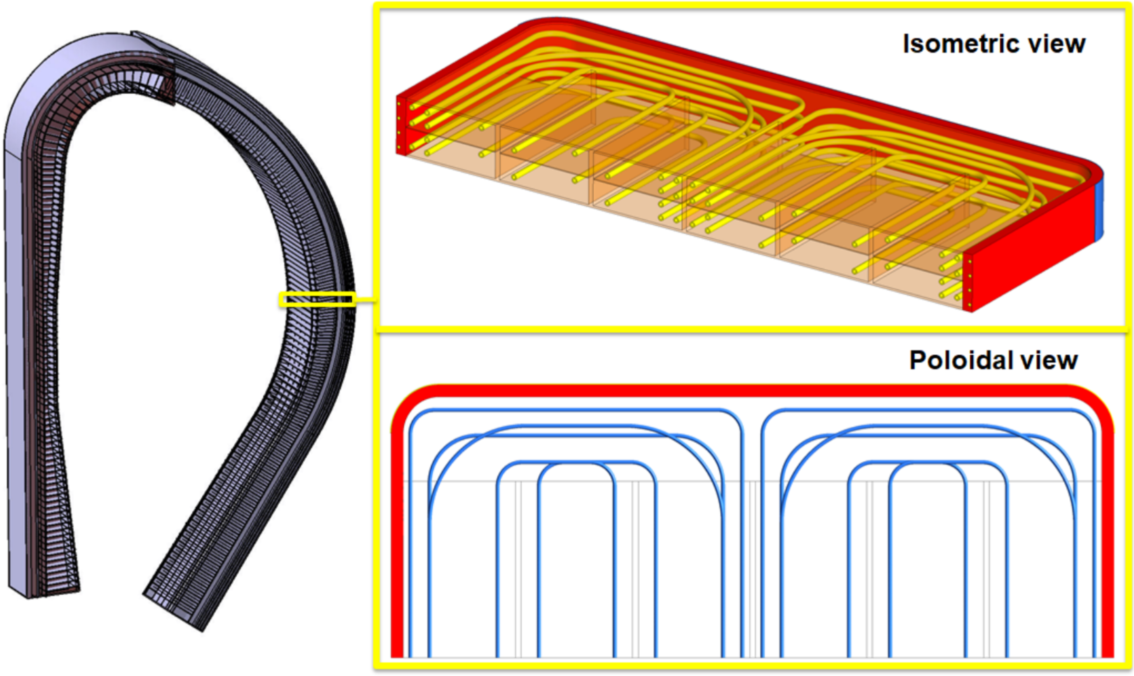

Figure 1.11: WCLL v0.6B COB equatorial elementary cell in isometric and poloidal views [87]

The cooling system for the process fluids consists of three independent circuits: one for circulating the PbLi eutectic alloy and two for directing the water coolant. Both the First Wall (FW) structure and the Breeding Zone (BZ) are cooled by water through two distinct systems operating under the same Pressurised Water Reactor (PWR) conditions, specifically at a pressure of 15.5 MPa and temperatures ranging from 571 K to 601 K [81]. The PbLi alloy, maintained isothermally at approximately 603 K, does not contribute to thermal power removal and experiences an average pressure of 0.5 MPa, which varies significantly along the poloidal direction due to the liquid metal's pressure head. Fluid distribution within the BB is managed through feeding pipes at lower and upper ports. The PbLi alloy is introduced at the lower port and removed at the upper while cooling water is supplied and discharged at the upper port for efficient thermal management [81].

1.3.2 Neutronic performance

The irradiation environment in a DT fusion reactor will be characterised by the 14 MeV neutron radiation field produced by the reactions in the plasma [88]. The fast neutrons generated serve as a critical source of energy to be harnessed for power generation. Yet, they pose a significant threat by causing structural damage to reactor components through neutron irradiation and displacement damage.

Neutron interactions with atoms can occur in two primary ways: scattering or absorption. In scattering, neutrons collide with atoms, and this collision can be elastic or inelastic [89]. During elastic scattering, a portion of the neutron's kinetic energy is transferred to the atom it strikes, with the amount of energy transferred depending on the angle of collision; the most energy is transferred in a direct head-on collision:

$$\frac{E_1}{E_2} = \left[\frac{A-1}{A+1}\right]^2 \tag{1.42}$$

where E_1 and E_2 are the kinetic energies of the atom and neutron, respectively, $A = M/m$ where M is the atom's mass and m is the mass of the neutron, both in units kg. When a fast neutron first collides with an atom in a lattice, it imparts a significant amount of its kinetic energy to the atom, displacing it from its position in the lattice and creating a vacancy site and an interstitial. This displaced atom becomes known as the Primary Knock-on Atom (PKA) [90]. The PKA then collides with surrounding atoms, which react with additional neighbouring atoms, resulting in a ballistic cascade. The total number of displaced atoms resulting from the cascade is quantified by the unit Displacement Per Atom (DPA). This cascade stretches the lattice and can cause localised melting. However, this process occurs over a very short period, typically on the order of picoseconds (see Figure 1.12). Afterwards, the lattice relaxes, but some vacancies and interstitials may remain.

In contrast, if the atom absorbs the neutron, the result can vary depending on the material and the neutron's energy. Absorption can lead to the formation of an unstable compound, which may subsequently transmutate into a different element or isotope. In some cases, particularly with certain heavy elements, neutron absorption can cause the nucleus to undergo fission, splitting into smaller nuclei and releasing additional neutrons and energy. These interactions are quantified by the material's neutron cross-section, which characterises the likelihood of scattering or absorption events under specific conditions.

The characteristics of hydrogen traps in materials are governed by the density and distribution of microstructural defects [92, 93, 94]. However, neutron damage will significantly change the microstructural defect landscape in fusion reactor components close to the plasma. It's anticipated that neutron damage to components in DEMO reactor projects will occur at rates of 5 dpa/FPY and 20 dpa/FPY, respectively [20, 95]. FPY denotes the exposure during a full year of full-power operation. Detailed analysis and measurement of the degradation in materials facing the plasma due to neutron damage are crucial for future fusion devices' safe and reliable operation. Many current studies on materials facing the plasma and experiencing damage use ion irradiation to simulate neutron damage because it can deliver significant doses of damage more quickly and without the safety concerns associated with transmutation

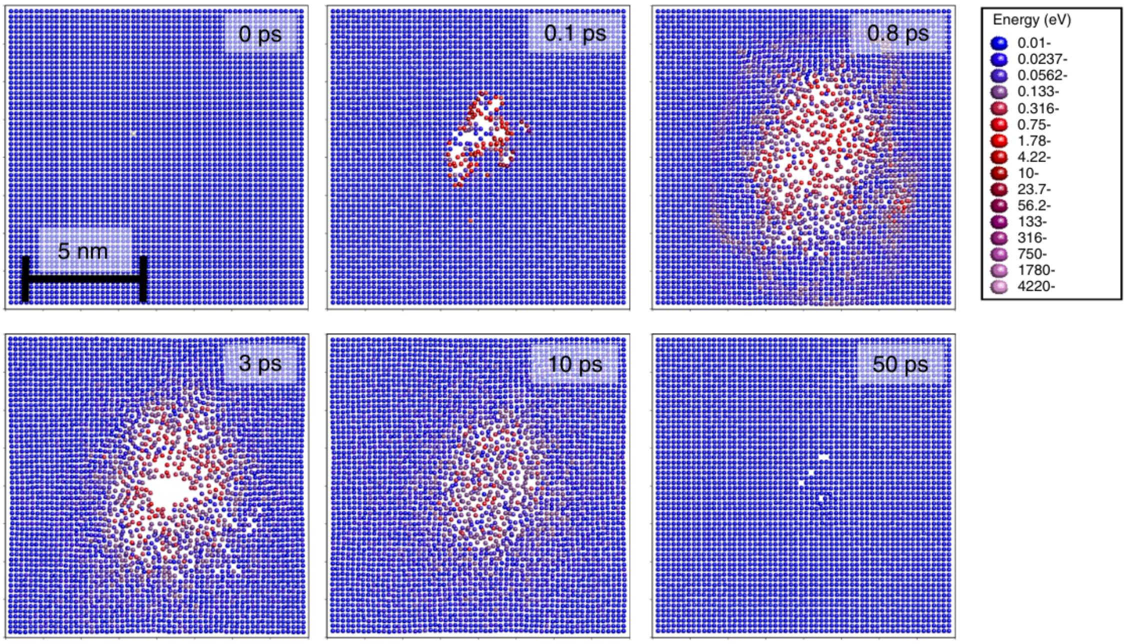

Figure 1.12: A cross-sectional view of a collision cascade in gold, induced by a 10 keV primary knock-on atom [91]

[96, 97]. As irradiation damage alters the landscape of microstructural defects, the characteristics of traps used for modelling must also evolve. Moreover, increased tritium retention will result in more helium production due to decay [98]. Although it might seem logical that more neutron damage and the subsequent increase in defects would increase the density of hydrogen trapping sites, research shows that hydrogen retention saturates after reaching a certain amount of damage [99, 100, 101, 102]. Further doses of damage do not influence the levels of hydrogen retention saturation [103, 94]. Typically, the depth to which hydrogen can penetrate a surface facing the plasma can be predicted from the material's trapping characteristics [94]. However, the formation of traps can restrict migration, causing higher hydrogen concentrations near the surface facing the plasma. This interaction between different mechanisms has been the subject of prior investigation [104]. Additionally, it has been discovered that including hydrogen isotopes in materials while being damaged by ions raises the saturation ceiling and reduces the annealing of the traps created [105].

To assess the neutronic performance of the WCLL, three-dimensional neutron and gamma transport simulations were conducted using the MCNP5v1.6 Monte Carlo code and JEFF 3.3 nuclear data libraries [106]. These analyses employ a fully heterogeneous DEMO WCLL model focused on the Tritium Breeding Ratio (TBR) and shielding performance. Where TBR is defined as the ratio of tritium produced to the amount consumed within the reactor. The target TBR of at least 1.15 ensures sufficient tritium generation despite in-vessel component impacts and tritium decay losses [107]. The blanket must also limit damage to vacuum vessel steel below 2.75 dpa over 6 FPY and keep He concentration in re-weldable zones below 1 appm. Protecting the superconductive TFC requires evaluating the fast neutron flux and

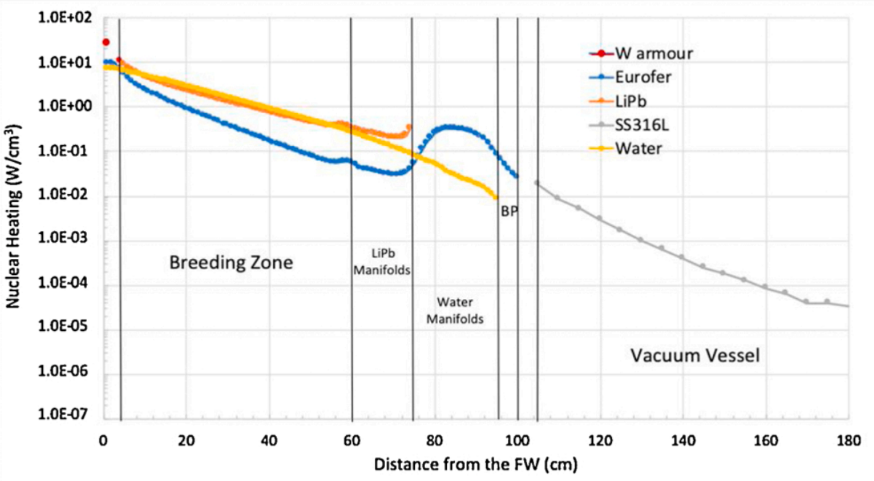

Figure 1.13: Nuclear heating radial profile evaluated in W armour, Eurofer, PbLi and SS316 L for the outboard WCLL [106]

nuclear heating, with targets of $<10^9\,\mathrm{n\,cm^{-2}\,s^{-1}}$ and $<5 \times 10^{-5}\,\mathrm{W\,cm^{-3}}$ respectively. The MCNP WCLL model with the WCLL blanket normalised to 1998 MW fusion power showed maximum neutron wall loading at $1.33\,\mathrm{MW\,m^{-2}}$ in the outboard and $1.1\,\mathrm{MW\,m^{-2}}$ in the inboard equatorial zones, with a poloidal average of $0.93\,\mathrm{MW\,m^{-2}}$ [108].

In addition to evaluating the neutron wall loading, this neutronics study also determined the neutron heating volumetric terms for all WCLL materials as a function of radius from the plasma (see Figure 1.13). The radial distribution of nuclear heating density in the outboard region shows that the heating density remains within acceptable limits. The dotted horizontal line in the figure highlights that the limit on TFC nuclear heating $5\,\mathrm{MW\,cm^{-3}}$ was fulfilled. The results included detailed tritium creation rates and damage levels across the WCLL outboard. These findings provide crucial data for optimising the blanket's design and ensuring its performance and safety, contributing to the WCLL reactor's overall feasibility and efficiency.

1.3.3 Thermal-Hydraulic performance

Over several years, extensive thermal-hydraulic calculations have been conducted to refine the WCLL BB design, either validating its performance or suggesting modifications [109, 110, 84, 85]. These efforts culminated in establishing a consolidated geometry for the WCLL elementary cell, reflecting continuous improvements in its overall performance. Numerous configurations with varying numbers and layouts of Double-Walled Tubes (DWTs) and FW channels have been assessed. Additionally, the impact of different thermophysical property correlations on thermal performance has been thoroughly investigated, resulting in adopting the WCLL v0.6B configuration as the reference design [87]. The thermodynamic analysis has significantly influenced the design of the WCLL, setting critical parameters such as ensuring the maximum temperature of Eurofer does not exceed 823 K. Beyond this point, the Eurofer experiences significant microstructural changes, such as the coarsening of precipitates and recovery, degrading its mechanical properties [111, 112, 113]. The material's strength and creep resistance decrease substantially at higher temperatures, and undesirable phase transformations can occur, compromising its integrity and longevity in reactor environments. Additionally, the WCLL BB is designed with planned input and output water temperatures and fixed mass flow rates to maximise heat removal efficiency [87]. By maintaining specific temperatures and flow rates, the cooling system can effectively transfer the heat generated in the reactor to the coolant, ensuring optimal thermal management and preventing overheating. This controlled environment ensures consistent and efficient heat removal, crucial for the reactor's safety, performance, and longevity.

Computational Fluid Dynamics (CFD) analyses of the WCLLv0.6B model indicated an acceptable temperature field for the structural material Eurofer. The maximum temperature of 816 K was observed in the lower and upper stiffening plates, while a slightly higher temperature of 825 K was recorded in the baffle plate domain, which is acceptable due to the non-structural function of this component (see Figure 1.14). Recirculation in the BZ system increased the average water velocity, thereby reducing temperature values and preventing thermal crises, contributing to a uniform average outlet temperature [114].

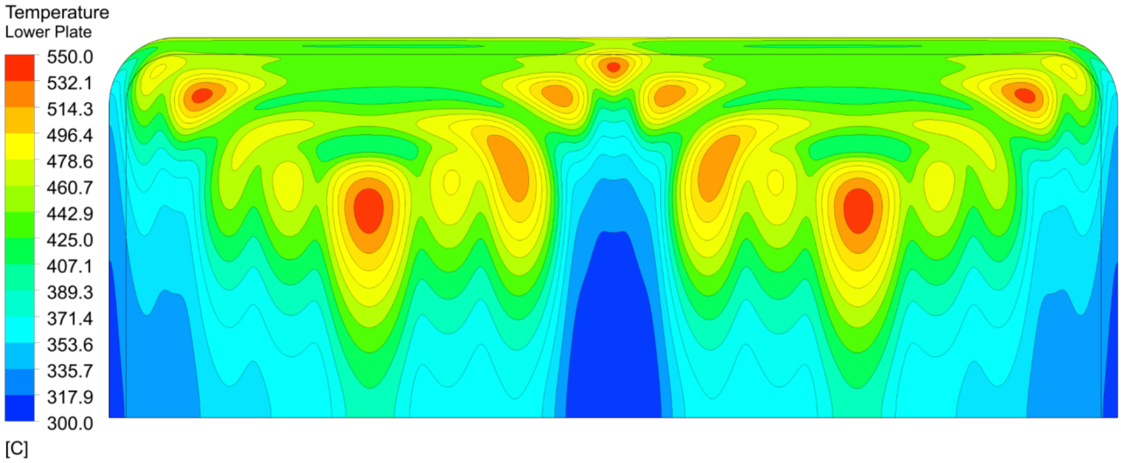

Figure 1.14: WCLL v0.6B thermal field [87]

Given that DEMO is planned to operate with pulses lasting 1000 s, transient analysis for the WCLL considered the same time frame for evaluating peaks in thermodynamic effects [115]. A 1000 s transient analysis was conducted to study the dwell-pulse transition and assess the thermal performance of Eurofer structures under a 15% over-power condition. Results showed that the maximum temperature of Eurofer structures remained below 823 K, with a notable thermal drop of about 200 K in the first 150 s. The PbLi temperature trend closely followed that of the stiffening plates. Transient analysis of the BZ system revealed it did not achieve a steady-state condition, while the FW system reached steady-state conditions after about 300 s [114]. These findings underscore the importance of ongoing thermal-hydraulic evaluations in optimising the WCLL design for efficiency and safety.

1.3.4 Tritium generation and permeation

Tritium is an essential fuel component for fusion reactors, yet it does not naturally occur in significant quantities. To address this, fusion reactors employ BB 's, such as the WCLL system, which utilises lithiated compounds that react with neutrons to produce tritium. This process forms an elegant and self-sustaining fuel cycle crucial for the continuous operation of fusion reactors. However, tritium production in nuclear fusion devices presents several significant challenges. Tritium's ability to permeate through materials and its radioactive nature necessitates precise monitoring and handling. Tritium can permeate the reactor's structure and cooling channels during reactor operation, requiring efficient removal systems. Furthermore, tritium's presence in structural components complicates the decommissioning process of fusion devices [116]. Therefore, accurately assessing tritium retention levels and permeation into the coolant is critical for BB 's' design and safe functioning.

Research into tritium breeding in the WCLL is advancing rapidly to ensure the tritium self-sufficiency of the WCLL reactor, a critical milestone in the EUROfusion roadmap [117]. The TBR must be accurately estimated using validated neutronic calculations cross-checked against integral experiments. To account for uncertainties in these simulations and the anticipated tritium losses during fuel cycle processing, it is essential to demonstrate a global TBR with a margin exceeding unity. This ensures that the fuel cycle can compensate for the natural radioactive decay of tritium, approximately 5.5% per year, and generate a surplus. This surplus is crucial for maintaining operational availability, especially after interruptions, and supplying tritium to future power plants [108] (see section 1.2.2). Current TBR estimates have evolved to address the limitations of earlier models. Initial estimates set at 1.05 were found inadequate as they did not consider the radioactive decay of tritium, leading to a revised estimate of 1.15 [107].

However, these estimates assume no permeation losses out of the loop and view tritium trapping as a delay in permeation rather than a localised buildup in concentration. Addressing these factors is fundamental to developing a BB system that guarantees tritium self-sufficiency for the DEMO reactor, ensuring the long-term viability and sustainability of fusion energy.

There has been extensive modelling work at the sub-component level [118, 119, 120, 121, 122], supported by material testing [54, 123, 124, 125, 126, 127]. However, complete experimental data for BB 's will not be available until the TBM in ITER is operational, meaning current design plans for DEMO rely on computational models. Modelling work on BB's for DEMO in existing literature, focuses mainly on neutronics [128, 106, 129], additionally looking MHD effects [130, 131], mechanical fields [132], and some initial studies on tritium transport [130, 133, 92]. Nonetheless, past studies estimating the amounts of tritium in the structure and its movement did not consider tritium trapping, despite trapping mechanisms significantly influencing inventory levels in materials like tungsten (W) [94] and Eurofer [134, 54]. Furthermore, a study showed hydrogen transport models may better predict hydrogen distribution in materials by including the effects of mobile hydrogen traps [135].

Most efforts to confirm tritium self-sufficiency in the DEMO reactor rely heavily on computational models. However, the accuracy of these models depends critically on the material properties they incorporate. For instance, hydrogen diffusion rates vary among the materials used in the WCLL, such as tungsten, Eurofer, and PbLi. Most of these diffusion values have been determined experimentally and are valid only within limited temperature ranges, which do not encompass the full range expected within the WCLL.

Recent developments in atomistic scale modelling for single-element materials like tungsten have provided more reliable estimates for diffusion parameters [136]. Nevertheless, the models' largest uncertainty source is the hydrogen solubility values in the WCLL materials. As established in a previous section on interface conditions, solubility plays a crucial role in tritium transport in multi-material systems.

In particular, the solubility values for hydrogen in PbLi vary over several orders of magnitude, making it the most uncertain parameter in WCLL system modelling. Depending on the solubility value chosen from the literature, the dynamics of tritium transport can change dramatically. Some solubility values for PbLi are significantly higher than those for Eurofer, which is in direct contact with PbLi, while others are lower. This discrepancy can cause the estimated tritium inventories in the Eurofer structure to vary by order of magnitude [130]. Therefore, this thesis thoroughly investigates the solubility parameter to address this critical uncertainty in tritium transport modelling for the WCLL system.

1.4 Problem definition

The TBR is a pivotal parameter in fusion reactor design, derived from neutronics simulations, the results of which are integrated into system-level models, assuming all tritium generated within the breeding blanket is transported through the PbLi outlet and extracted and processed into fuel. Existing models account for tritium losses only as arbitrary 5% losses and radioactive decay [107]. However, experimental evidence demonstrates significant permeability of hydrogen isotopes through materials used in the WCLL, necessitating a more comprehensive and accurate modelling approach.

A multiphysics model is needed as various physics influence hydrogen transport behaviour in a breeding blanket, which in turn are influenced by other physics, creating a complex interplay necessary for accurately modelling a WCLL; however, it is not feasible to develop a complete direct, strongly coupled multiphysics model, as some physics operate on different time scales and may only need to be weakly coupled (see Figure 1.15) Thus, computational effort can be saved by carefully considering the interaction of the different physics within the WCLL.

The primary objective of this work is to develop a multiphysics model to accurately evaluate tritium transport behaviour within the WCLL. This involves estimating inventory buildups within structural materials and quantifying permeation into cooling channels. To achieve this, the work will utilise established, published literature on neutronics simulations for the WCLL, providing essential data on tritium generation through lithium reactions in PbLi, heat generation through neutron energy deposition, and mechanical damage through defect production. In addition to neutronics, it is crucial to model the fluid flow of the liquid metal breeder (PbLi), considering the strong coupling between fluid mechanics and heat transfer through density changes and advection effects. MHD forces can also be considered as they

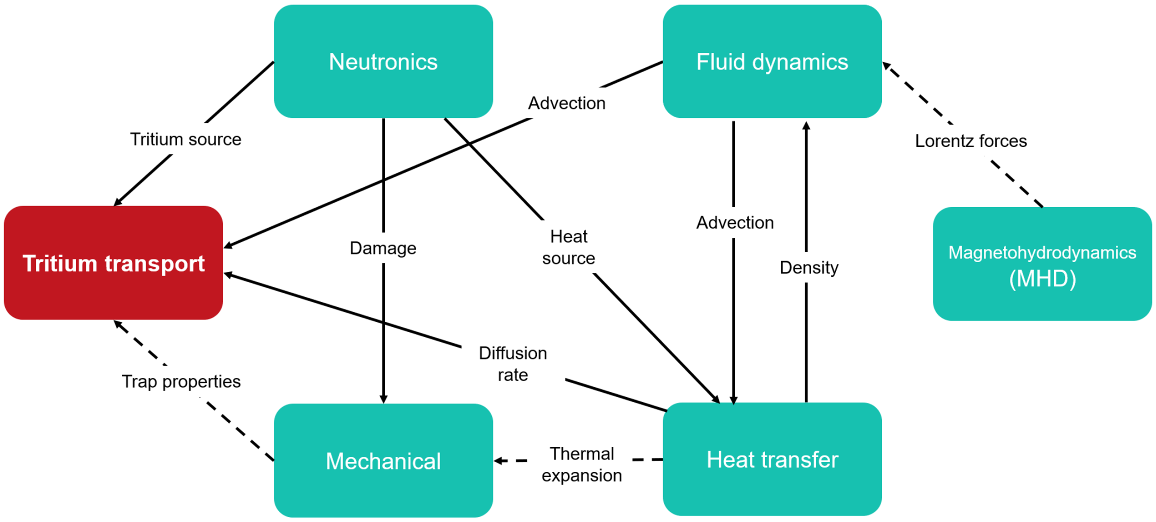

Figure 1.15: The multiphysics issue in modelling breeding blankets

directly impact the fluid flow of the PbLi and, therefore, tritium transport. Hydrogen isotope transport mechanisms must be modelled, considering advection effects from fluid flow and temperature-sensitive Arrhenius laws. Integrating lower-length scale hydrogen transport concepts such as trapping, particularly in materials like Eurofer and tungsten, into macroscopic WCLL models will provide a more accurate depiction of tritium behaviour. A series of parametric studies will investigate the influence of uncertain parameters on the WCLL model. Additionally, the effects of neutron damage on hydrogen trapping and the potential role of permeation barriers will be examined. These investigations aim to enhance the understanding of tritium transport within the WCLL, leading to improved predictions of tritium retention levels in structural materials and permeation into cooling channels.

Modelling tritium transport in the WCLL presents several challenges. The complexity of the task arises from the need to simultaneously consider multiple physics domains: heat transfer, neutronics, fluid mechanics, and MHD. Each domain affects tritium transport and is interdependent, requiring varying degrees of coupling in the simulations. Material permeability is another significant challenge. The high permeability of hydrogen isotopes in WCLL materials complicates the accurate tritium transport and retention prediction. This issue requires detailed material characterisation and the integration of experimental data into the models to enhance their accuracy. Additionally, uncertain parameters, particularly those related to material properties and boundary conditions, can significantly impact model accuracy. Addressing this challenge involves extensive parametric studies to quantify these uncertainties and their effects on tritium transport predictions.

The ultimate goal is to better understand tritium transport behaviour within the WCLL, providing better predictions of tritium retention levels in structural materials and permeation into cooling channels. The intricacies of tritium management in fusion reactors underscore the need for nuanced and accurate modelling techniques to account for tritium behaviour's dynamic and multifaceted nature. Fuel cycle models can achieve a closer approximation of reality by moving beyond simplistic assumptions and incorporating a more detailed understanding of tritium extraction, trapping, and diffusion processes. This, in turn, enhances tritium inventory management strategies, paving the way for more efficient and sustainable fusion energy production.

Chapter 2

Model definition and implementation

Contents

2.1 Multiphysics framework . . . 36
2.1.1 Heat transfer . . . 37
2.1.2 Fluid mechanics . . . 38
2.1.3 Hydrogen transport . . . 39
2.1.4 Summary: Governing equations . . . 40
2.2 Finite element methods . . . 41
2.2.1 Problem definition . . . 44
2.2.2 Weak formulation . . . 44
2.2.3 Discretisation . . . 45
2.2.4 Function spaces . . . 46
2.2.5 Assembly of the system of equations . . . 48
2.2.6 Solving . . . 49
2.2.7 Fluid mechanics solver application . . . 50
2.3 FESTIM . . . 52
2.3.1 FEniCS . . . 52
2.3.2 Features . . . 53
2.3.3 Model construction . . . 53
2.3.4 Validation & Verification . . . 55
2.4 Summary . . . 57

To accurately model the operation of the WCLL, it is essential to consider multiple interacting physical phenomena, including heat transfer, fluid mechanics, and hydrogen transport. This chapter provides a comprehensive overview of the multiphysics framework employed in the current model, detailing the intricate interplay between the various physics considered.

This chapter delves into the detailed application of FEM for solving partial differential equations, using the Poisson equation as a practical example to display the fundamental concepts of FEM. The process of setting up a FEM problem is discussed, from the discretisation of a domain to the construction of a variational formulation and the ultimate solving of the problem. In addition to the general FEM framework, the development of a fluid mechanics solver specifically tailored to model the flow of PbLi within the WCLL is discussed. It highlights the use of FEniCS software, which automates the finite element analysis process and demonstrates its effectiveness in efficiently managing complex mathematical formulations and computations. The steps in defining and verifying this solver are outlined before introducing FESTIM, the primary software utilised for modelling hydrogen transport research presented in this work. By merging the theoretical aspects of multiphysics modelling with practical implementation details, this chapter provides a holistic view of the methodologies and tools essential for advancing the understanding and simulation of WCLL operations.

Specific material properties and parameter values used within the model will be detailed in the following chapter 3.

2.1 Multiphysics framework

In this section, we delve into the equations and physical principles that underpin the multiphysics modelling of the WCLL BB. To model the WCLL, a 2D model was initially considered. This 2D domain, Ω, is taken from a central plane of the outboard module, aiming to simplify the complex geometry and computational demands of a complete 3D analysis (see Figure 2.1).

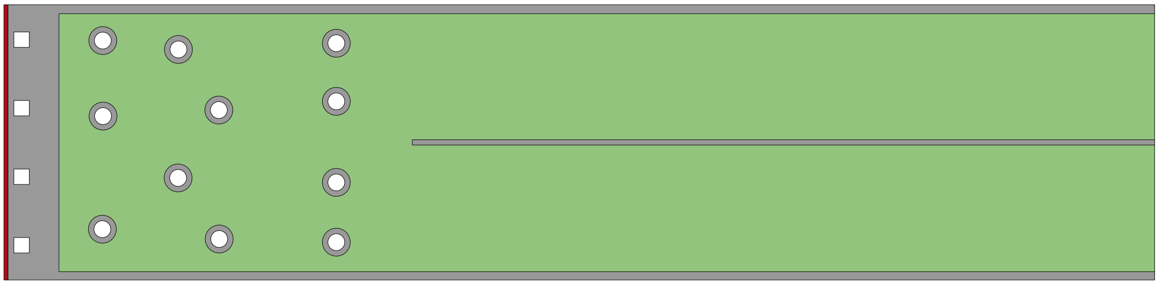

Figure 2.1: 2D WCLL domain showing W 🟥, Eurofer ◼, PbLi 🟩

The 2D domain Ω is defined as the union of the solid domain Ω_{solid} and the fluid domain Ω_{fluid}:

$$\Omega = \Omega_{\text{solid}} \cup \Omega_{\text{fluid}} \tag{2.1}$$

where Ω_{solid} is comprised of the tungsten 🟥 and Eurofer ◼ (see Figure 2.1), and the Ω_{fluid} is comprised of the PbLi 🟩.

Boundary conditions are required to address the physics considered thoroughly. Boundary conditions are separated into three categories:

- Enforcing the value of the solution at a boundary (Dirichlet's condition)
- Enforcing the value of the gradient of the solution (Neumann's condition)
- Enforcing the value of the gradient as a function of the solution itself (Robin's condition)

In this section, the boundary of the domain, Ω, is denoted by $\partial\Omega$. This notation does not imply that all the detailed boundary conditions are to be applied simultaneously on the same boundary; rather, it indicates that these conditions can be defined on the domain's boundary. Specific boundary condition location applications and parameter values are discussed in the following chapter.

2.1.1 Heat transfer

The various processes involving hydrogen transport that depend on temperature changes require precise knowledge of how temperature is distributed. The WCLL will face intense heat flux from plasma and additional heat generated by neutron bombardment. Water actively cools the first wall and breeding zone to manage this heat. Given the WCLL's intricate design, the different areas where heat is produced or removed create significant temperature variations, leading to an uneven temperature distribution. Thus, accurately modelling heat transfer is essential.

The equation describing heat conduction, accounting for heat generation, is described as:

$$\rho c_p \frac{\partial T}{\partial t} = \boldsymbol{\nabla} \cdot (k \boldsymbol{\nabla} T) + \rho c_p \mathbf{u} \boldsymbol{\nabla} T + Q \quad \text{in } \Omega \tag{2.2}$$

where T is the temperature in units K, c_p is the specific heat capacity in units $\mathrm{J\,kg^{-1}\,K^{-1}}$, ρ is the material's density in units $\mathrm{kg\,m^{-3}}$, k is the thermal conductivity in units $\mathrm{W\,m^{-1}\,K^{-1}}$ and Q is a volumetric heat source in units $\mathrm{W\,m^{-3}}$. Eq. (2.2) does not have an advection term coupling the fluid dynamics to the heat transfer within the PbLi liquid domain. Advection effects in this capacity have been considered with the term $\rho c_p \mathbf{u} \boldsymbol{\nabla} T$. Where $\mathbf{u}$ is the velocity of the PbLi in units $\mathrm{m\,s^{-1}}$. However, the significance of this term can be evaluated using the Péclet.

Heat sources $Q(r, t)$, due to neutron interaction with the materials in the WCLL have been evaluated from nuclear heating data [106] in the literature, and fitted with exponential and power-law piece-wise functions where r is the distance from the plasma facing wall expressed in m.

Heat transfer boundary physics

The temperature value can be fixed at the boundaries, $\partial\Omega$ (Dirichlet), such as at the PbLi inlet:

$$T = f(x, y, z, t) \quad \text{on } \partial\Omega \tag{2.3}$$

where f is an arbitrary function of spatial coordinates x, y, z and time t. Alternatively, fluxes can be imposed at the boundaries (Neumann) to account for a heat flux on the first wall, for instance:

$$-k \boldsymbol{\nabla} T \cdot \mathbf{n} = \varphi_{\text{heat}} \quad \text{on } \partial\Omega \tag{2.4}$$

where $\mathbf{n}$ is the outgoing normal vector on $\partial\Omega$ and φ_{heat} is the normal heat flux value in units $\mathrm{W\,m^{-2}}$. Robin boundary conditions can be used to model convective heat fluxes:

$$-k \boldsymbol{\nabla} T \cdot \mathbf{n} = h\ (T - T_{\text{ext}}) \quad \text{on } \partial\Omega \tag{2.5}$$

where h is the heat transfer coefficient in units $\mathrm{W\,m^{-2}\,K^{-1}}$ and T_{ext} is the fluid's external (bulk) temperature in units K. The heat transfer coefficient can be evaluated as a function of the coolant water properties [87]:

$$h = \mathrm{Nu} \cdot \frac{k}{d_w} \tag{2.6}$$

where Nu is the Nusselt number, k is the thermal conductivity of the water in units $\mathrm{W\,m^{-1}\,K^{-1}}$, and d_w is the whetted perimeter of the pipe in units m. The whetted perimeter is defined as the perimeter of the cross-sectional area that is "wet" [137]. The Nusselt number has been evaluated using the Gnielinski correlation:

$$\mathrm{Nu} = \frac{(f_\mathrm{D}/8) \cdot (\mathrm{Re} - 1000) \cdot \mathrm{Pr}}{1 + 12.7 \cdot (f/8)^{1/2} \cdot (\mathrm{Pr}^{2/3} - 1)} \tag{2.7}$$

where f_D is the Darcy friction factor that can either be obtained from a Moody chart [138] or can be obtained from a predefined correlation for smooth tubes [76]:

$$f_\mathrm{D} \ = (0.79 \cdot \ln(\mathrm{Re}) - 1.64)^{-2} \tag{2.8}$$

Re is the Reynolds number, defined as:

$$\mathrm{Re} = \frac{\rho u L}{\mu} \tag{2.9}$$

where ρ is the average water density in units $\mathrm{kg\,m^{-3}}$, u is the water velocity in units $\mathrm{m\,s^{-1}}$, L is the characteristic length of the pipes in units m and μ is the water viscosity in units Pa s. Pr is the Prandtl number and is defined as:

$$\mathrm{Pr} = \frac{c_p \mu}{k} \tag{2.10}$$

Furthermore, the exact velocity of the water in the tubing is not defined, but the mass flow rate, $\dot{m}$, in units $\mathrm{kg\,s^{-1}}$, is constrained. Therefore, the average velocity, u, can be evaluated as:

$$u = \frac{\dot{m}}{\rho A} \tag{2.11}$$

where A is the cross-sectional area of the pipe in units $\mathrm{m^2}$.

2.1.2 Fluid mechanics

The WCLL utilises a liquid metal breeder, PbLi; thus, the breeder's flow needs to be considered to accurately model tritium generation and transport in the breeder. The flow of the PbLi breeder will be of velocity $1.8\,\mathrm{mm\,s^{-1}}$ at the inlet [139]. Using published thermophysical properties for PbLi [140] at the constrained inlet temperature of 598 K [139], the Reynolds number can be approximated ≈ 600 (see Eq. 2.9); thus the flow will not be turbulent and can be modelled using the standard steady-state incompressible Navier-Stokes equations:

$$\rho \frac{\partial \mathbf{u}}{\partial t} + \rho(\mathbf{u} \cdot \boldsymbol{\nabla})\mathbf{u} = -\boldsymbol{\nabla} p + \mu \boldsymbol{\nabla}^2 \mathbf{u} \quad \text{in } \Omega_\text{fluid} \tag{2.12}$$

$$\boldsymbol{\nabla} \cdot \mathbf{u} = 0 \quad \text{in } \Omega_\text{fluid} \tag{2.13}$$

where p is the pressure in units Pa. Eq. (2.13) is the continuity equation. It is noted that as the density and viscosity changes for temperatures within the WCLL, are $> 1\%$, it is assumed that the continuity equation holds [141]. Buoyancy effects and the influence of the magnetic field in the DEMO tokamak have not been considered in this work as they are outside the scope.

2.1.3 Hydrogen transport

A model based on equations developed by McNabb & Foster [142] can be used to model hydrogen transport in materials. The principle is to separate mobile hydrogen c_m and trapped hydrogen c_t, in units m^{-3}. The diffusion of mobile particles is governed by Fick's law of diffusion, where the hydrogen flux is

$$\mathbf{J} = -D \boldsymbol{\nabla} c_\mathrm{m} \tag{2.14}$$

where $\mathbf{J}$ is the hydrogen flux and D is the diffusion coefficient. Each trap i is associated with a trapping and a detrapping rate $\nu_\mathrm{t,i}$ and $\nu_\mathrm{dt,i}$ (see Eqs. (1.29) and (1.30)), and a trap density n_i in units m^{-3}. The temporal evolution of c_m and $c_{\mathrm{t},i}$, both in units m^{-3} are then given by:

$$\frac{\partial c_\mathrm{m}}{\partial t} = \boldsymbol{\nabla} \cdot (D \boldsymbol{\nabla} c_\mathrm{m}) + S - \sum \frac{\partial c_{\mathrm{t},i}}{\partial t} \quad \text{in } \Omega \tag{2.15}$$

$$\frac{\partial c_{\mathrm{t},i}}{\partial t} = \nu_\mathrm{t,i} \; c_\mathrm{m} \; (n_\mathrm{i} - c_{\mathrm{t},i}) - \nu_\mathrm{dt,i} \; c_{\mathrm{t},i} \quad \text{in } \Omega_\mathrm{solid} \tag{2.16}$$

where S is a volumetric source of mobile hydrogen in units $\mathrm{m}^{-3}\,\mathrm{s}^{-1}$, accounting for the tritium generation within the PbLi breeder. These equations can simulate hydrogen implantation in materials, tritium generation from neutron interactions and general transport.

Advection effects

The flow of the breeder is likely to influence tritium transport within the breeder significantly. To account for the advection effects, an additional term, $\mathbf{u} \boldsymbol{\nabla} c_\mathrm{m}$, is amended to Eq. (2.15):

$$\frac{\partial c_\mathrm{m}}{\partial t} = \boldsymbol{\nabla} \cdot (D \boldsymbol{\nabla} c_\mathrm{m}) + S + \mathbf{u} \boldsymbol{\nabla} c_\mathrm{m} - \sum \frac{\partial c_{\mathrm{t},i}}{\partial t} \tag{2.17}$$

Hydrogen transport boundary physics

The mobile hydrogen concentration c_m can be fixed at the boundaries:

$$c_\mathrm{m} = f(x, y, z, t) \quad \text{on } \partial\Omega \tag{2.18}$$

where f is an arbitrary function of spatial coordinates x, y, z and time t. The value of the concentration at the boundary can be determined by Sievert's condition (see Equation 2.19).

$$c_\mathrm{m} = K_\mathrm{S} \, \sqrt{P} \quad \text{on } \partial\Omega \tag{2.19}$$

Dirichlet boundary conditions can also approximate plasma implantation in near-surface regions to be more computationally efficient [44].

$$c_\mathrm{m} = \frac{\varphi_\mathrm{imp} \, R_p}{D} \quad \text{on } \partial\Omega \tag{2.20}$$

where φ_imp is the implanted flux in units $\mathrm{m}^{-2}\,\mathrm{s}^{-1}$ and R_p is the implantation range in units m. However, it should be noted that $\varphi_\mathrm{imp} \neq \varphi$ where φ is the flux of incoming particles from the plasma. A certain fraction of the incoming particles reflect from the surface, never penetrating into the bulk:

$$\varphi_{\mathrm{imp}} = (1 - R)\varphi \tag{2.21}$$

where R is the reflection coefficient. Molecular recombination is modelled by:

$$c_{\mathrm{m}} = \frac{\varphi_{\mathrm{imp}}\ R_p}{D} + \sqrt{\frac{\varphi_{\mathrm{imp}}}{K_{\mathrm{r}}}} \quad \text{on } \partial\Omega \tag{2.22}$$

where K_{r} is the recombination coefficient in units $\mathrm{m}^4\,\mathrm{s}^{-1}$. Moreover, dissociation can also be accounted for:

$$c_{\mathrm{m}} = \frac{\varphi_{\mathrm{imp}}\ R_p}{D} + \sqrt{\frac{\varphi_{\mathrm{imp}} + K_{\mathrm{d}}\ P}{2K_{\mathrm{r}}}} \quad \text{on } \partial\Omega \tag{2.23}$$

where K_{d} is the dissociation coefficient in units $\mathrm{m}^{-2}\,\mathrm{s}^{-1}\,\mathrm{Pa}^{-1}$ and P is the partial pressure of hydrogen, in units Pa. A normal hydrogen flux can also be imposed at boundaries.

$$-D\boldsymbol{\nabla} c_{\mathrm{m}} \cdot \mathbf{n} = f(x, y, z, t) \quad \text{on } \partial\Omega \tag{2.24}$$

where $\mathbf{n}$ is the normal vector of the boundary. This flux application can be used to describe the recombination and dissociation fluxes at the surface:

$$-D\boldsymbol{\nabla} c_{\mathrm{m}} \cdot \mathbf{n} = K_{\mathrm{d}}\ P \quad \text{on } \partial\Omega \tag{2.25}$$

$$-D\boldsymbol{\nabla} c_{\mathrm{m}} \cdot \mathbf{n} = -K_{\mathrm{r}}\ c_{\mathrm{m}}^n \quad \text{on } \partial\Omega \tag{2.26}$$

In Equation 2.26, the exponent of c_{m} is either 1 or 2, depending if the gas is diatomic or monoatomic respectively.

Interface condition

The continuity of chemical potential is ensured by ensuring the continuity of local partial hydrogen pressure at the interfaces between materials. As the WCLL only concerns metal-metal interfaces, the chemical potential continuity can be described using Sieverts law (see section 1.2.4, Eq. (1.39)), the interface condition yields:

$$\frac{c_{\mathrm{m}}^+}{K_{\mathrm{S}}^+} = \frac{c_{\mathrm{m}}^-}{K_{\mathrm{S}}^-} \tag{2.27}$$

where the exponents + and − denote either side of an interface.

2.1.4 Summary: Governing equations

A multifaceted model incorporating various physics to accurately simulate the operation of the WCLL system has been presented. The modelling of heat transfer, fluid mechanics, and hydrogen transport and their interactions within the WCLL is crucial to evaluate its performance thoroughly. The importance of understanding the temperature distribution within the WCLL due to the intense heat flux from plasma and neutron bombardment was discussed, emphasising the role of water cooling in managing this heat. The heat transfer model includes detailed conduction, convective boundary conditions, and the heat transfer coefficient derivation. Fluid mechanics were explored through the flow of the PbLi breeder within the WCLL, using the steady-state incompressible Navier-Stokes equations to model flow. The discussion extends to hydrogen transport within the WCLL, detailing hydrogen diffusion and its interaction with traps in materials influenced by temperature and irradiation. This section introduced a set of macroscopic rate equations based on the McNabb & Foster model for hydrogen transport, emphasising the separation of mobile and trapped hydrogen and the role of various boundary conditions in modelling hydrogen fluxes.

In summary, the chapter outlines a multifaceted approach to modelling the WCLL system, integrating heat transfer, fluid dynamics, and hydrogen transport mechanisms to provide a thorough understanding of the physical processes governing the WCLL's operation. The governing equations for the model are as follows:

for steady-state heat transfer:

$$\boldsymbol{\nabla} \cdot (k\boldsymbol{\nabla} T) + \rho c_p \mathbf{u}\boldsymbol{\nabla} T + Q = 0 \tag{2.28}$$

for steady-state fluid mechanics:

$$\rho(\mathbf{u} \cdot \boldsymbol{\nabla})\mathbf{u} = -\boldsymbol{\nabla} p + \mu \boldsymbol{\nabla}^2 \mathbf{u} \tag{2.29}$$

$$\boldsymbol{\nabla} \cdot \mathbf{u} = 0 \tag{2.30}$$

for hydrogen transport:

$$\frac{\partial c_\mathrm{m}}{\partial t} = \boldsymbol{\nabla} \cdot (D\boldsymbol{\nabla} c_\mathrm{m}) + S + \mathbf{u}\boldsymbol{\nabla} c_\mathrm{m} + \sum \frac{\partial c_{\mathrm{t},i}}{\partial t} \tag{2.31}$$

$$\frac{\partial c_{\mathrm{t},i}}{\partial t} = \nu_\mathrm{t} \cdot c_\mathrm{m} \cdot (n_i - c_{\mathrm{t},i}) - \nu_\mathrm{dt} \cdot c_{\mathrm{t},i} \tag{2.32}$$

However, some models and interface conditions developed within this work are outlined in chapters 4 and 5 to account for neutron damage and permeation barrier influences.

2.2 Finite element methods

Given the complex geometry of the WCLL and the relevant physics that can be described using Partial Differential Equation (PDE)'s, the FEM emerged as the ideal candidate for constructing a multiphysics model. Finite element methods are well-suited for handling the complexities of WCLL's geometry and the interactions between different physical processes.

In modelling the WCLL, it was crucial to have heat transfer simulation capabilities, support for modelling material interface conditions, and the flexibility to operate in both 2D and 3D. Additionally, the tool needed to be adaptable for incorporating new models. Specifically, the PbLi fluid domain needs to be modelled, and the resulting velocity field needs to be in a format readable by the prospective hydrogen transport modelling tool. This narrowed the choices to three primary options: COMSOL (mHIT), ABAQUS, and FESTIM. Given its open-source nature, Python interface, and FEniCS back-end, FESTIM was selected as the primary modelling tool for this work.

Most of the codes detailed in Table 2.1 use macroscopic rate equations based on the McNabb and Foster equations at their core to simulate hydrogen transport and trapping with varying complexity. Depending on their specific objectives, different codes employ various numerical approaches, such as Finite Element Methods or Finite Difference Methods. The diversity in programming languages used across these tools reflects a wide range of design philosophies, programming backgrounds, and priorities regarding performance and usability.

Table 2.1: Comparison of some hydrogen transport modelling tools

	Heat-transfer	Multi-material	Multi-dimensional	Multi-species	Multi-level trapping	Programming language
TMAP7 [143]	✓	✓		✓		Fortran
CRDS [144]				✓	✓	Mathematica
MHIMS [145]				✓	✓	Fortran
TESSIM [146]		✓		✓	✓	Mathematica
mHIT [147]	✓	✓	✓			COMSOL interface
ABAQUS [148]	✓	✓	✓			Fortran subroutines
ACHLYS [149]	✓		✓			C++ (MOOSE)
FESTIM [150]	✓	✓	✓			Python

The feature sets offered by these codes can vary significantly:

- Some are equipped to simulate heat transfer, essential for accurately modelling hydrogen transport in complex geometries with complex temperature fields that significantly impact coefficients within the McNabb and Foster equations.
- Multi-material modelling is supported in some codes, which allow the implementation of specific interface conditions like chemical potential conservation.

- Dimensional modelling varies, with some tools offering 1D, 2D, and 3D capabilities, though 1D is often the default.
- Certain codes can handle multiple diffusing species, such as deuterium and tritium, while also simulating isotopic exchanges and multi-level trapping, which allows for the simulation of different hydrogen retention levels.
- Some emphasise surface interactions, providing detailed models for these effects.

Each code has been developed with specific goals and applications in mind, typically aiming to model different aspects of plasma-facing components. This results in some tools offering detailed physical models but limited scalability, while others can be used for large-scale component simulations but may lack certain physics implementations. Table 2.1 compares each code's key features, showing how their varied capabilities align with different research needs and modelling philosophies. This comparison highlights the nuances and trade-offs in hydrogen transport simulation, emphasising the importance of choosing the right tool based on the specific requirements of the research or application.

Numerous code comparisons have been published in the literature to ensure that each code is verified and validated and produces the same result. Comparisons have been performed between FESTIM, TMAP7, and ABAQUS [151]. In the reference paper for FESTIM, a further comparison was realised between FESTIM, TMAP8 and COMSOL [150]. Within the scope of the TITANS project [152], a study aimed to compare hydrogen transport codes used within its constituent members, within which a comparison was made between FESTIM, MHIMS, and mHIT [153]. All the comparison studies concluded that FESTIM agreed well with the other codes.

In modelling the WCLL, it was crucial to have heat transfer simulation capabilities, support for modelling material interface conditions, and the flexibility to operate in both 2D and 3D. Additionally, the tool needed to be adaptable for incorporating new models. Specifically, the PbLi fluid domain needed to be modelled, and the resulting velocity field had to be in a format readable by the prospective hydrogen transport modelling tool. This narrowed the choices to three primary options: COMSOL (mHIT), ABAQUS, and FESTIM.

Given its open-source nature, Python interface, and FEniCS back-end, FESTIM was selected as the primary modelling tool for this work. Three key factors drove this choice:

1. Open-Source Flexibility: Unlike proprietary solutions, FESTIM's open-source license allows for greater flexibility in extending and customizing the code to incorporate additional models or physics as the research requires.
2. Python Interface: The Python-based interface makes FESTIM easy to integrate with other tools, facilitates automation, and enables straightforward scripting for running simulations. This is particularly useful when dealing with complex workflows or batch processing.
3. Prior Experience: Previous experience with FESTIM provided a foundation for efficient development and troubleshooting, enabling quicker iteration during the research process.

2.2.1 Problem definition

The FEM is a numerical technique used for solving PDE's in engineering and physics. The fundamental premise of FEM is to approximate the solution of a complex problem by dividing it into smaller, simpler subdomains or elements. Within each element, a set of basis functions is chosen to represent the variation of the unknown quantity (e.g., displacement, temperature). FEM finds wide applications in various branches of physics and engineering, providing a versatile and powerful tool for simulating and analysing complex systems where analytical solutions may be difficult or impossible to obtain.

This section outlines the key components of posing a mathematical problem using FEM. The Poisson equation will be used as an example over a domain, Ω, constrained by Dirichlet and Neumann boundary conditions (See Fig. 2.2).

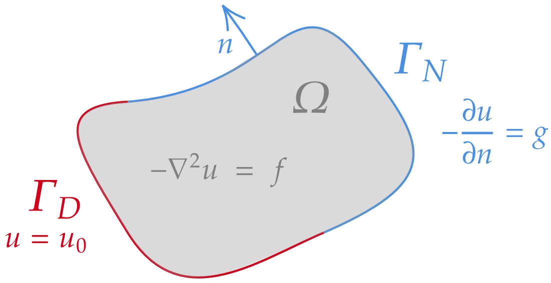

Figure 2.2: Representation of the mathematical problem [44]

$$-\nabla^2 u = f \text{ on } \Omega \tag{2.33}$$

$$u = u_0 \text{ on } \Gamma_D \subset \partial\Omega \tag{2.34}$$

$$-\frac{\partial u}{\partial n} = g \text{ on } \Gamma_N \subset \partial\Omega \tag{2.35}$$

where:

$$\partial\Omega = \Gamma_D \cup \Gamma_N \tag{2.36}$$

$$\Gamma_D \cap \Gamma_N = \emptyset \tag{2.37}$$

This problem is subject to boundary conditions specified on $\partial\Omega$, the boundary of the domain Ω. u is prescribed on a subset of the boundary, Γ_D. On the other boundary segment, Γ_N, the value of u's normal flux is specified. Eq. (2.33) is the Poisson equation represented in its strong form. However, it must be converted into a weak form for FEM to accommodate solutions that may lack smoothness and to enable more straightforward incorporation of boundary conditions and numerical implementation.

2.2.2 Weak formulation

The first step in obtaining the weak formulations of a governing equation is to multiply by a test function, v, such that $v = 0$ on Γ_D, and then integrate over the domain Ω.

$$\int_\Omega -\nabla^2 u \; v \; dx = \int_\Omega f \; v \; dx \tag{2.38}$$

In FEM, reducing the weak formulation to first order is crucial for several reasons. It lowers the differentiability requirements of the solution, allowing it to accommodate functions with lower regularity and discontinuities. This broadens the function space to include more general solutions and simplifies the numerical implementation. First-order derivatives enhance computational efficiency and stability, making incorporating boundary conditions easier. Overall, this reduction increases FEM's flexibility and applicability to complex problems. Thus, Eq. (2.38) can be reduced by using the Gauss-Green theorem and integration by parts:

$$\int_{\Omega} -\boldsymbol{\nabla}^2 u \ v \ dx = \int_{\Omega} \boldsymbol{\nabla} u \cdot \boldsymbol{\nabla} v \ dx - \int_{\Gamma_N} g \ v \ ds \tag{2.39}$$

Thus:

$$\int_{\Omega} \boldsymbol{\nabla} u \cdot \boldsymbol{\nabla} v \ dx - \int_{\Gamma_N} g \ v \ ds = \int_{\Omega} f \ v \ dx \tag{2.40}$$

2.2.3 Discretisation

In FEM, domains must be discretised to simplify complex geometries and problems into smaller, manageable pieces that can be mathematically and computationally handled. This discretisation process involves dividing the entire domain into smaller sections called cells. These cells come in several forms, including lines in 1D domains, triangles or quadrilaterals in 2D, or tetrahedrons and hexahedrons in 3D (See Fig. 2.3).

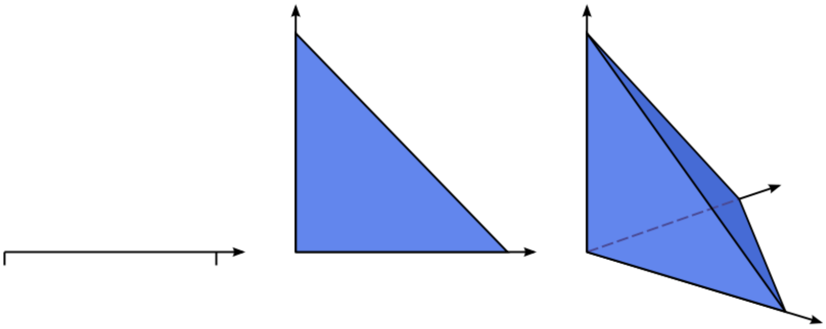

Figure 2.3: Line, triangle and tetrahedral element types [154]

The Ciarlet definition [155] defines a finite element by a triple $(R, \mathcal{V}, \mathcal{L})$, where:

- $R \subset \mathbb{R}^d$ is the reference element, usually a polygon or polyhedron
- $\mathcal{V}$ is a finite dimensional polynomial space on R of dimension n
- $\mathcal{L} = \{l_0, ...l_{n-1}\}$ is the basis of the dual space $\mathcal{V}* = \{f : \mathcal{V} \to \mathbb{R} | f \text{ is linear}\}$. Each functional l_i is associated with a subentity of the reference element R.

In FEM, cells serve as the basic units of the mesh geometry, defining the partition of the computational domain. While isoparametric elements use the same shape functions for geometry and field approximation, they are not mandatory. Instead, the mesh geometry can be described using lower-order finite elements, ensuring the domain is accurately represented. At the same time, the unknown field can be approximated using higher-order finite elements, allowing for more accurate solution approximations. This flexibility enables better control over the mesh quality and solution accuracy, leveraging different polynomial geometry and field interpolation orders.

Each element is then comprised of nodes where the solution, u is evaluated (called Degrees of Freedom (DOF)). The number of nodes and distribution depend on the element type and order. In the case of the most common element, a first-order Lagrangian element consists of nodes on the corners of the triangle, in the case of 2D. When increasing the degree to two or three, the number of nodes increases (See Figure 2.4), offering a higher discretisation level for the same number of elements.

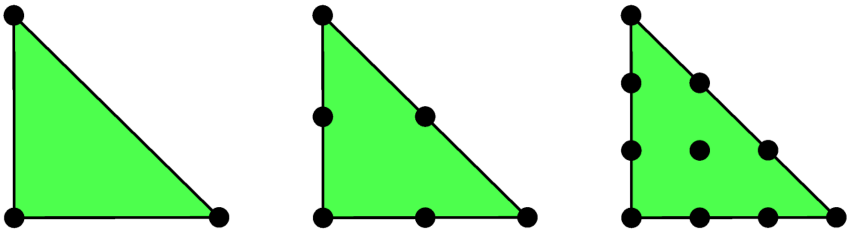

Figure 2.4: First, second and third order 2D Lagrange elements [154]

Increasing the number of elements raises computational costs due to more nodes and larger global matrices. Increasing the order of elements increases the complexity of the matrices but can potentially achieve higher accuracy with fewer elements. Higher-order polynomials can better capture complex behaviours within each element, enhancing solution smoothness and continuity, which is crucial for resolving derivatives in structural mechanics. While this approach enables accuracy improvements in specific scenarios, it can also introduce complexities, such as more intricate numerical integrations and the potential for numerical instabilities. Therefore, the decision to use higher-order elements over more elements should be based on the specific problem requirements, including desired precision and available computational resources. The level of discretisation and integration required in a domain is closely tied to the complexity of the solution; for instance, areas with high gradients within the solution necessitate a denser concentration of nodes to better capture these sharp changes and ensure a smooth and correct solution. This targeted approach allows for more precise modelling in regions where the solution's behaviour is more dynamic and potentially critical (See Fig. 2.5).

In Figure 2.5, ψ is a representation of the basis functions in a FEM problem (see section 2.2.6). Discretising a domain into a series of finite elements creates what is subsequently referred to as a mesh.

2.2.4 Function spaces

In FEM, a function space is a mathematical space consisting of functions that have specific properties and structure, such as continuity or differentiability, suitable for analysis within that context. Typical forms of functions in function spaces include polynomials, piecewise polynomials, trigonometric functions, exponential functions, splines, wavelets, continuous

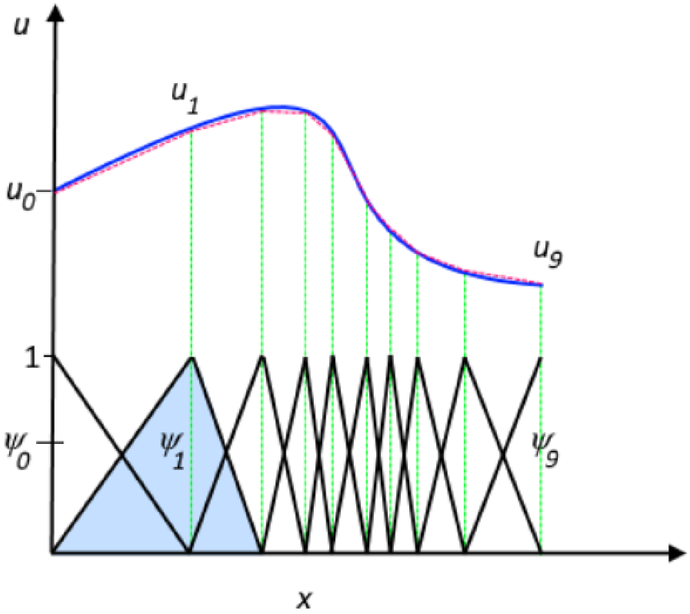

Figure 2.5: The function u (solid blue line) is approximated with u_h (dashed red line), which is a linear combination of linear basis functions (the solid black lines represent ψ_i). The DOFs are denoted by u_0 through u_9 [156]

functions, and differentiable functions. By requiring that the test function v be zero on the Dirichlet boundary Γ_D, where the solution u is already specified, we formulate the following classical variational problem: find u in the space V such that

$$\int_\Omega \nabla u \cdot \nabla v \; dx = \int_\Omega f \; v \; dx - \int_{\Gamma_N} g \; v \; ds \quad \forall v \in \hat{V} \tag{2.41}$$

The test space $\hat{V}$ is defined by:

$$\hat{V} = \{v \in H^1(\Omega) : v = 0 \text{ on } \Gamma_D\} \tag{2.42}$$

where H^1 is the space of functions whose values and first derivatives are square-integrable, ensuring they do not become infinitely large and are suitable for solving first-order partial differential equations in the domain Ω. The trial space V contains members of $\hat{V}$ shifted by the Dirichlet condition:

$$V = \{v \in H^1(\Omega) : v = u_0 \text{ on } \Gamma_D\} \tag{2.43}$$

The test space and trial space differ because the trial space consists of functions that approximate the solution and must satisfy the boundary conditions. In contrast, the test space contains functions used to validate the equation formed by the trial functions, and these do not need to adhere to the boundary conditions. Although often the same in many FEM applications, the trial and test spaces can differ in specialised methods to enhance aspects like stability or accuracy [157]. We can now discretise Poisson's equation by limiting the variational problem (2.41) to a set of discrete spaces: find $u_h \in V_h \subset V$, such that:

$$\int_\Omega \boldsymbol{\nabla} u_h \cdot \boldsymbol{\nabla} v \, dx = \int_\Omega f \; v \, dx - \int_{\Gamma_N} g \; v \, ds \quad \forall v \in \hat{V}_h \subset \hat{V} \tag{2.44}$$

We observe that the Dirichlet condition $u = u_0$ on Γ_D is directly incorporated into the definition of the trial space V_h as an essential boundary condition, while the Neumann condition $-\partial u / \partial n = g$ on Γ_N is integrated into the variational problem as a natural boundary condition.

2.2.5 Assembly of the system of equations

To solve the discrete variational problem for the Poisson equation (2.44), piecewise polynomial interpolation functions, $\{\psi_i\}_{i=1}^N$ are defined for V_h, and $\{\hat{\psi}_j\}_{j=1}^N$ for $\hat{V}_h$ (see Figure 2.5). Here N denotes the dimension of the space V_h. The approximated solution u_h, therefore, can be defined in terms of the basis interpolation functions of the trial space,

$$u_h = \sum_{j=1}^{N} U_j \psi_j \tag{2.45}$$

where $\mathbf{U} = (U_j)_{i=1}^N \in \mathrm{I\!R}^{\mathrm{N}}$ is the vector of degrees of freedom to be computed. Inserting this into (2.44) and varying the test function v over the basis functions of the discrete test space $\hat{V}_h$ we obtain:

$$\sum_{j=1}^{N} U_j \int_\Omega \boldsymbol{\nabla} \psi_j \cdot \boldsymbol{\nabla} \hat{\psi}_i \, dx = \int_\Omega f \; \hat{\psi}_i \, dx - \int_{\Gamma_N} g \; \hat{\psi}_i \, ds \quad i = 1, 2, ..., N \tag{2.46}$$

We may thus compute the finite element solution u_h by showing the linear system

$$\mathbf{AU} = \mathbf{b} \tag{2.47}$$

where:

$$A_{ij} = \int_\Omega \boldsymbol{\nabla} \psi_j \cdot \boldsymbol{\nabla} \hat{\psi}_i \, dx \tag{2.48}$$

$$b_i = \int_\Omega f \; \hat{\psi}_i \, dx - \int_{\Gamma_N} g \; \hat{\psi}_i \, ds \tag{2.49}$$

In the FEM, numerical integration is crucial for evaluating the integrals of basis functions and their derivatives over finite elements during the assembly of the system of equations. This ensures accurate computation of element stiffness matrices and load vectors. Gaussian Integration (Gauss Quadrature) is a highly efficient method that approximates integrals using specific points (Gauss points) and weights [158]. It is particularly effective for polynomial functions, integrating polynomials of degree $2n - 1$ exactly with n points. Considering a generalised PDE in its weak form:

$$\int_\Omega f(x) d\Omega \tag{2.50}$$

where $f(x)$ could be the product of basis functions, their derivatives, or other functions defined over the domain Ω, the formula for Gauss Quadrature over the interval $[-1, 1]$ is:

$$\int_{-1}^{1} f(x)\,dx \approx \sum_{i=1}^{n} w_i f(x_i) \tag{2.51}$$

where x_i are the Gauss points, and w_i are the corresponding weights. This method is preferred in FEM due to its accuracy and efficiency. In contrast, Newton-Cotes formulas use evenly spaced points and weights derived from polynomial interpolation [159]. Common Newton-Cotes methods include the Trapezoidal Rule and Simpson's Rule. The Trapezoidal Rule is given by:

$$\int_{a}^{b} f(x)\,dx \approx \frac{b-a}{2}\left[f(a) + f(b)\right] \tag{2.52}$$

Simpson's Rule, which is more accurate for higher-degree polynomials, is:

$$\int_{a}^{b} f(x)\,dx \approx \frac{b-a}{6}\left[f(a) + 4f\left(\frac{a+b}{2}\right) + f(b)\right] \tag{2.53}$$

In general, the Newton-Cotes formula for $n+1$ evenly spaced points over $[a, b]$ is:

$$\int_{a}^{b} f(x)\,dx \approx \sum_{i=0}^{n} w_i f(x_i) \tag{2.54}$$

where x_i are the uniformly spaced points, and w_i are the weights. Although simpler to implement, Newton-Cotes methods are typically less accurate and efficient than Gauss Quadrature, especially for higher-degree polynomials. Gauss Quadrature is favoured in FEM due to its optimal point selection and higher accuracy for polynomial functions, making it more efficient than Newton-Cotes methods, which use uniformly spaced points and generally achieve lower accuracy [160].

In FEM, quadrature rules or discrete integration techniques are used to evaluate integrals over each finite element accurately. These rules approximate the integrals by summing the contributions at specific points within the elements, known as quadrature points. The sparsity of the arising global stiffness matrix $\mathbf{A}$ is a direct consequence of the localised support of the finite element basis functions, which are non-zero only over their respective elements and immediate neighbours. As a result, each entry in the global matrix $\mathbf{A}$ corresponds to interactions between basis functions of neighbouring elements, leading to a matrix with mostly zero entries. This sparsity is crucial because it significantly reduces the computational cost and memory requirements associated with storing and solving the system of linear equations $\mathbf{AU} = \mathbf{b}$. Sparse matrix storage schemes and solvers exploit this sparsity to perform efficient matrix operations and solve large-scale problems more effectively, making FEM practical for complex, real-world applications.

2.2.6 Solving

The linear system arising from a finite element solution is typically solved using computational methods rather than manual algebraic manipulations. In FEM, discretisation and linear interpolation within elements result in a system of linear equations that can be represented as a matrix equation. As the problem size grows to include many degrees of freedom, the matrix equations become large and complex, making manual solutions impractical. Computational software is essential for efficiently solving these systems, particularly in applications involving thousands or millions of degrees of freedom.

Moreover, when the function f depends on the solution u, the problem becomes nonlinear. An example is heat transfer problems, where the material's thermophysical properties vary with temperature. In such cases, the resulting system of equations requires iterative methods to solve. Newton's method is commonly used for these nonlinear systems because it iteratively linearises the problem and solves a sequence of linear approximations to converge to the solution [161]. The iterative nature of Newton's method and the need to update the system matrix at each iteration further emphasise the necessity of robust computational tools for solving complex FEM problems. While direct solvers based on LU decomposition can be effective for small to moderately-sized problems, iterative methods are crucial for large-scale applications due to their ability to efficiently handle vast amounts of data and leverage the sparsity of the matrix, thereby significantly reducing both computational time and memory usage [162].

Software tools like FEniCS [163] are essential for efficiently constructing and solving finite element problems, automating the creation of matrices, and handling complex computations and optimisations that arise in large-scale applications.

2.2.7 Fluid mechanics solver application

The strong form of the steady state incompressible Navier-Stokes equation and the continuity equation can be expressed as:

$$\rho(\mathbf{u} \cdot \boldsymbol{\nabla})\mathbf{u} = -\boldsymbol{\nabla} p + \mu \boldsymbol{\nabla}^2 \mathbf{u} \tag{2.55}$$

$$\boldsymbol{\nabla} \cdot \mathbf{u} = 0 \tag{2.56}$$

A mixed-element strategy is frequently employed in modelling using the Navier-Stokes equations. This method uses different elements for different variables to enhance stability and accuracy. A popular choice in this category is the Taylor-Hood element, which pairs P2 elements (second-order polynomials) for modelling velocity with P1 elements (linear polynomials) for pressure. This pairing is critical as it helps prevent stability problems, such as the checkerboard effect in pressure fields. The checkerboard effect is a numerical artefact in finite element fluid dynamics analysis. It is characterised by spurious oscillations in the computed pressure field that form a grid-like or checkerboard pattern, typically arising from inadequate stabilisation or incompatible element pairings. Constructing the function space for Taylor-Hood elements involves a mixed-function space approach. Here, vector fields (for velocity) and scalar fields (for pressure) are integrated into a unified function space framework. This integrated approach efficiently manages the interdependence between velocity and pressure in fluid dynamics simulations, facilitating the solution of coupled equations within a single coherent computational setup. This method not only streamlines the implementation but also enhances the numerical stability and accuracy of the simulation results.

To find the weak variational form of the momentum equation, it is first multiplied for a test function $\mathbf{v}$, $\mathbf{v} = 0$ where $\mathbf{u} = \mathbf{u_0}$, defined in a suitable function space V and integrated with respect to the domain Ω.

$$\int_\Omega \rho(\mathbf{u} \cdot \boldsymbol{\nabla}\mathbf{u})\ \mathbf{v}\ dx = -\int_\Omega \boldsymbol{\nabla} p\ \mathbf{v}\ dx + \int_\Omega \mu \boldsymbol{\nabla}^2 \mathbf{u}\ \mathbf{v}\ dx \tag{2.57}$$

Counter-integrating by parts and using the vector calculus identities:

$$\boldsymbol{\nabla} \cdot (\mathbf{A} \cdot \boldsymbol{\nabla}\mathbf{B}) = \boldsymbol{\nabla}\mathbf{A} \cdot \boldsymbol{\nabla}\mathbf{B} + \mathbf{B} \cdot \boldsymbol{\nabla}^2 \mathbf{A} \tag{2.58}$$

$$\boldsymbol{\nabla} \cdot (\mathbf{A} \cdot \mathbf{B}) = \boldsymbol{\nabla}\mathbf{A} \cdot \mathbf{B} + \mathbf{A} \cdot (\boldsymbol{\nabla} \cdot \mathbf{B}) \tag{2.59}$$

and Gauss's theorem (if $\partial\Omega$ is sufficiently regular):

$$\int_\Omega \boldsymbol{\nabla} \cdot (\mathbf{A} \cdot \boldsymbol{\nabla}\mathbf{B})\ dx = \int_{\partial\Omega} (\mathbf{A} \cdot \boldsymbol{\nabla}\mathbf{B}) \cdot \mathbf{n}\ ds \tag{2.60}$$

The diffusive and pressure terms can be expressed as:

$$\int_\Omega \mu \boldsymbol{\nabla}^2 \mathbf{u}\ \mathbf{v}\ dx = -\int_\Omega \mu \boldsymbol{\nabla}\mathbf{u} \cdot \boldsymbol{\nabla}\mathbf{v}\ dx + \int_{\partial\Omega} \mu \mathbf{v} \boldsymbol{\nabla}\mathbf{u} \cdot \mathbf{n}\ ds \tag{2.61}$$

$$\int_\Omega \boldsymbol{\nabla} p\ \mathbf{v}\ dx = -\int_\Omega p(\boldsymbol{\nabla} \cdot \mathbf{v})\ dx + \int_{\partial\Omega} p\mathbf{v} \cdot \mathbf{n}\ ds \tag{2.62}$$

For the continuity equation, this is multiplied for a test function q belonging to a suitable function space Q and integrated across the domain Ω:

$$\int_\Omega (\boldsymbol{\nabla} \cdot \mathbf{u})\ q\ dx = 0 \tag{2.63}$$

Thus, the weak formulation for (2.55) is expressed as:

$$\int_\Omega \rho(\mathbf{u} \cdot \boldsymbol{\nabla}\mathbf{u})\ \mathbf{v}\ dx - \int_\Omega p(\boldsymbol{\nabla} \cdot \mathbf{v})\ dx + \int_\Omega \mu \boldsymbol{\nabla}\mathbf{u} \cdot \boldsymbol{\nabla}\mathbf{v}\ dx = 0 \quad \forall\ \mathbf{v} \in V \tag{2.64}$$

For (2.56):

$$\int_\Omega (\boldsymbol{\nabla} \cdot \mathbf{u})\ q\ dx = 0 \quad \forall\ q \in Q \tag{2.65}$$

In solving (2.64) and (2.65), which describe the flow of a fluid at equilibrium, the Newton Solver is a critical tool. This solver applies Newton's method, a root-finding algorithm that iteratively refines guesses until a solution satisfying the equations is found. Starting from an initial guess for the velocity and pressure fields, the Newton Solver linearises the nonlinear Navier-Stokes equations at each iteration, solving the linear system to update the guess. This process continues until the changes in the solution between iterations fall below a predetermined threshold, indicating convergence. The approach is highly effective for dealing with the inherent nonlinearities of the Navier-Stokes equations, especially in complex flow scenarios.

The finite element fluid dynamics solver constructed using the FEM library FEniCS has been verified by applying an established benchmark, the lid-driven cavity flow problem [164]. This verification process ensures the accuracy and reliability of the solver's implementation. Comprehensive details and results of the verification exercise are provided in appendix A.

2.3 FESTIM

FESTIM, short for *Finite Element Simulation of Tritium In Materials* [150], is a powerful and accessible hydrogen transport code that has been developed using the FEniCS library [163]. The open-source framework ensures the code is freely available for modifications and adaptations to fit specific needs. FESTIM is distributed under the permissive Apache-2.0 license, promoting the use and modification of the code. The tool is designed to be user-friendly and capable of handling simple and complex simulation scenarios in 1D, 2D and 3D. It effectively manages heat transfer and interfaces between different materials.

2.3.1 FEniCS

FEniCS is an open-source computational platform designed for solving partial differential equations (PDEs) using the finite element method (FEM) [163], and is the computational platform in FESTIM. It provides a unified interface for specifying and solving various PDE problems, including linear and nonlinear, steady-state and time-dependent, scalar and vectorial problems. Users can express their models in a high-level domain-specific language, facilitating translation into executable code. One of its key features is automated code generation, allowing for efficient and optimised code creation for numerical solutions. FEniCS leverages parallel computing techniques for scalability, efficiently utilising modern computational resources such as distributed computing clusters. It supports adaptive mesh refinement, dynamically adjusting the mesh during the solution process based on error estimates or user-defined criteria, which improves accuracy and efficiency. FEniCS is interoperable with other scientific computing libraries and tools, facilitating integration with existing workflows and enabling data analysis and visualisation of simulation results. Developed and maintained by an active community, FEniCS offers continuous improvement, bug fixes, and support for new features. It provides a rich ecosystem of extensions and plugins for extending its functionality and adapting it to specific application domains.

FEniCS, a comprehensive computational platform, was crucial for research in specialised fields, including hydrogen transport modelling in FESTIM and fluid dynamics simulations for PbLi flow in WCLL. Its ability to generate velocity fields directly usable by FESTIM allowed for accurate inclusion of advection parameters, enhancing simulation realism and precision. FEniCS excels in modelling the Navier-Stokes equations due to its robust finite element method capabilities, automating the discretization of complex differential equations. Users can quickly define variational problems and boundary conditions, making it versatile for various fluid flow scenarios. Its support for complex geometries and high-order elements and the efficient Python-C++ interface ensure the ease of use and computational efficiency of large-scale simulations. FEniCS also supports checkpointing for managing simulation data, enabling regular storage of velocity and pressure fields through the XDMFFile class, which is readable in ParaView [165]. This feature allows for secure data storage and easy access for further analysis or integration into multi-physics simulations like FESTIM.

2.3.2 Features

FESTIM models hydrogen dynamics in materials by distinguishing between mobile and trapped hydrogen, as governed by Fick's laws and associated rate equations for trapping and detrapping. It employs diffusivity coefficients, trap densities, and source terms that can vary spatially and temporally to simulate scenarios like hydrogen implantation and tritium generation. These dynamics and other physics discussed in sections 2.1.1 - 2.1.3 are either fully supported by FESTIM or can be implemented using the software's flexible framework. The code manages the conservation of chemical potential across different material interfaces by utilising Sievert's and Henry's laws to ensure the continuity of partial pressures, which can result in concentration jumps at interfaces. This comprehensive approach allows FESTIM to solve these dynamics in various coordinate systems under steady-state and transient conditions.

The code handles heat transfer via the heat equation, considering temperature-dependent material properties. Boundary conditions are versatile, encompassing Dirichlet, Neumann, and Robin types for hydrogen and heat transport, facilitating detailed simulation of surface interactions and boundary effects. Despite its advanced capabilities, FESTIM offers a high level of abstraction from the finite element implementation details, enabling users to focus on inputs like material properties and trap properties without requiring deep knowledge of finite element methods. However, for those familiar with such methods, FESTIM's object-oriented nature allows customisation of the code to specific needs, such as altering boundary conditions or equations. For complex geometries, FESTIM supports the use of third-party meshing tools like GMSH [166], Cubit [167], or SALOME [168]. Meshes from these tools can be imported (once converted using packages like meshio [169]) in XDMF format and are compatible with FESTIM. FESTIM handles the solving of nonlinear equations through Newton's method and supports a variety of linear and iterative solvers facilitated by PETSc [170], along with various preconditioners Output from FESTIM can be processed using tools like Paraview [165], matplotlib [171], or NumPy [172] due to its compatibility with standard file formats like XDMF, CSV, and TXT. While the default finite elements used are first-order piecewise elements, FESTIM can switch to discontinuous elements to better manage discontinuities in trapped concentrations, thereby avoiding performance issues and loss of accuracy.

Overall, FESTIM simplifies the simulation of multidimensional multi-material transient simulations coupled with heat transfer for non-experts. It also provides robust tools for advanced users to tailor the simulations to their specific requirements.

2.3.3 Model construction

The variational problem defined within FESTIM depends entirely on the type of simulation defined by a given user. In the most simplistic case of a diffusing mobile species, in a 1D domain, the solution function is simply the mobile population of hydrogen c_m function. A corresponding test function, v_m is also created before creating a corresponding function space, V_CG, using linear continuous Lagrangian elements:

$$V_h = \{c_\mathrm{m} \in H^1(\Omega) : c_\mathrm{m}|_T \in \mathbb{P}_1(T) \text{ for all } T \in \mathcal{T}_h\} \tag{2.66}$$

where $\mathbb{P}_1(T)$ denotes the space of polynomials of degree at most 1 on the element T. In finite elements, $\mathbb{P}_1(T)$ typically corresponds to linear polynomials. Following the application of any boundary conditions, in the case of steady state, the final variational form comes to:

$$\int_\Omega D \boldsymbol{\nabla} c_\mathrm{m} \cdot \boldsymbol{\nabla} v_\mathrm{m} \; dx = 0 \quad \forall v_\mathrm{m} \in V_h \tag{2.67}$$

To model transient transport, FESTIM uses the implicit backwards Euler time discretisation:

$$\int_\Omega \frac{\partial c_\mathrm{m}}{\partial t} \; v_\mathrm{m} \; dx \approx \int_\Omega \frac{c_\mathrm{m} - c_\mathrm{m,old}}{\Delta t} \; v_\mathrm{m} \; dx \tag{2.68}$$

which is added into the formulation (2.67). To model trapping, further functions and test functions are created for each trap, where each new function represents a new DOF:

$$\begin{Bmatrix} c_\mathrm{m} \\ c_\mathrm{t,1} \\ c_\mathrm{t,2} \\ \cdots \\ c_{\mathrm{t},n} \end{Bmatrix}, \begin{Bmatrix} v_\mathrm{m} \\ v_\mathrm{t,1} \\ v_\mathrm{t,2} \\ \cdots \\ v_{\mathrm{t},n} \end{Bmatrix}, \tag{2.69}$$

A new function space is needed for each trap, defined the same as in Eq. (2.66). All the function spaces are then multiplied together to form a mixed-function space:

$$\mathcal{V} = V_{h,1} \times V_{h,2} \times \cdots \times V_{h,n} \tag{2.70}$$

where n is the number of traps. To model the traps in steady state, the following terms are added to the variational formulation (2.67) per trap considered:

$$-\int_\Omega (\nu_{\mathrm{t},i} c_\mathrm{m} (n - c_{\mathrm{t},i}) - \nu_\mathrm{dt,i} c_{\mathrm{t},i}) \; v_\mathrm{m} \; dx + \int_\Omega (\nu_{\mathrm{t},i} c_\mathrm{m} (n - c_{\mathrm{t},i}) - \nu_\mathrm{dt,i} c_{\mathrm{t},i}) \; v_{\mathrm{t},i} \; dx \tag{2.71}$$

To model transient transport with trapping, a further implicit backwards Euler time discretisation term is added:

$$\int_\Omega \frac{c_{\mathrm{t},i} - c_{\mathrm{t,old},i}}{\Delta t} \; v_{\mathrm{t},i} \; dx \tag{2.72}$$

When modelling multi-material scenarios, FESTIM handles this by replacing each c_m within the formulation with a new function θ. Where θ comes from the conservation of chemical potential (See Eq. (2.27)), thus c_m is replaced by:

$$c_\mathrm{m} = K_\mathrm{s} \; \theta \tag{2.73}$$

Then, in post-processing, the value of θ in each subdomain is multiplied by the solubility of its constituent material to obtain the value of the mobile concentration c_m, and the solution is projected into a new function space comprising of discontinuous Galerkin elements. This is because traps are often only defined within a specific material, in a particular subdomain, and thus, can result in large instabilities at the edge of the subdomain, known as the Gibbs phenomenon [173] when using continuous Lagrange elements. The discontinuous Galerkin function space is defined as:

$$V_\mathrm{t,i} = \{c_{\mathrm{t},i} \in L^2(\Omega) : c_{\mathrm{t},i}|_T \in \mathbb{P}_1(T) \text{ for all } T \in \mathcal{T}_h\} \tag{2.74}$$

In this definition, $L^2(\Omega)$ is used instead of $H^1(\Omega)$ to indicate that the function needs only to be square-iterable over Ω, not necessarily continuous over element boundaries. A function is square-integrable if the integral of its square over the entire domain is finite, ensuring it doesn't grow too large too often. Although each function $c_{\mathrm{t},i}$, is still linear on each element T, as per $\mathbb{P}$.

2.3.4 Validation & Verification

Models based on the McNabb & Foster equations [142] have long been employed to simulate hydrogen transport. Its effectiveness is evidenced by its ability to replicate thermo-desorption experiments [174, 54, 175, 176, 177, 178, 179, 144, 180, 181, 94, 182] and profilometry measurements [100, 177, 179, 183, 180, 184]. Additionally, permeation experiments have corroborated hydrogen diffusion models [174, 185, 186].

The utility and validity of this mathematical model are well established; hence, it is validated. Exploring scenarios beyond the scope of existing validations would require further experimental data.

The verification of a code must align with its capabilities. For example, suppose a code asserts that it can execute the McNabb & Foster model in three-dimensional spaces, handle multiple materials, and integrate heat transfer. In that case, verification should not be limited to simplistic one-dimensional, single-material, and isothermal scenarios. The FESTIM test suite includes dozens of verification scenarios as part of over 300 tests accessible on the FESTIM repository. A comprehensive report on these cases would be extensive; hence, only three specific cases are discussed here. The Method of Manufactured Solutions (MMS) is employed to ensure the accuracy of numerical simulation codes [187]. In MMS, an exact analytical solution is deliberately crafted. This solution is then used to derive an analytic source term by applying the mathematical model. Symbolic computation is utilised to derive necessary derivatives of the manufactured solution. The manufactured solution and its corresponding source term provide the boundary conditions for the numerical simulation. The difference between the numerical results and the analytical solution quantifies the error, measuring the code's precision and reliability. MMS is an essential verification tool in scientific and engineering computations to confirm the dependability of simulation results.

This section highlights the verification processes for interface discontinuities, the heat transfer module, and the trapping mechanism within FESTIM. Each MMS case is implemented on a unit square grid for simple visualisation, with 100 cells in the x and y directions. Dirichlet boundary conditions that enforce the exact solution are set on all boundaries. Although this discussion focuses on steady-state problems, MMS applies equally to transient scenarios. The L2 norm of the error E is computed across the domain Ω to evaluate each case:

$$E = \sqrt{\int_\Omega (u_{\mathrm{exact}} - u_{\mathrm{computed}})^2 \, dx} \tag{2.75}$$

where u_{exact} and u_{computed} are the exact and computed solutions, respectively.

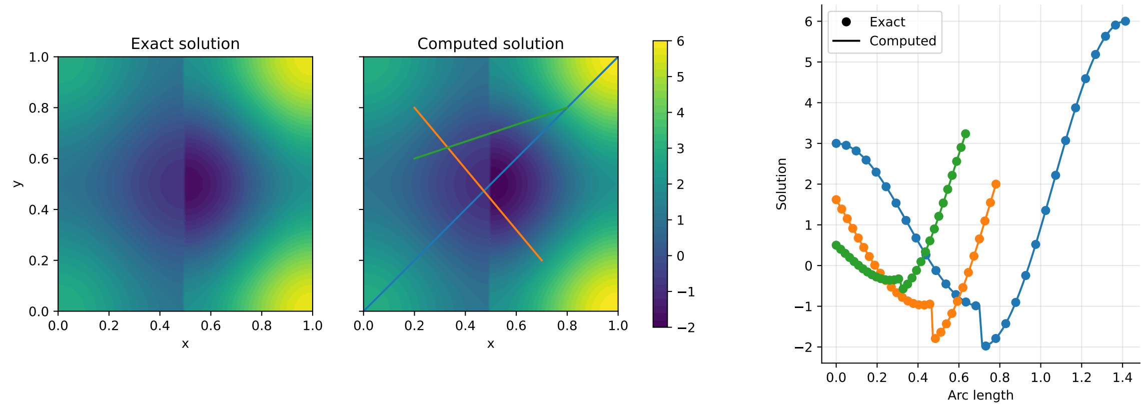

Figure 2.6: Verification case 1: multi-material [150]

Verification case 1: material interface discontinuity

The initial MMS problem involves two distinct materials, the left and right materials. In the left material, the solubility constant is denoted by $K_{S,\mathrm{left}} = 3$, and the diffusivity constant is represented by $D_{\mathrm{left}} = 2$. Conversely, in the right material, the solubility constant is $K_{S,\mathrm{right}} = 6$, and the diffusivity constant is $D_{\mathrm{right}} = 5$. For each material, an exact solution for the mobile hydrogen concentration is specifically crafted, resulting in two separate solutions corresponding to the respective subdomains:

$$c_{\mathrm{left,exact}} = 1 + \sin\left(\pi\left(2x + 0.5\right)\right) + \cos\left(2\pi y\right) \tag{2.76}$$

$$c_{\mathrm{right,exact}} = \frac{K_{S,\mathrm{right}}}{K_{S,\mathrm{left}}}\, c_{\mathrm{left,exact}} \tag{2.77}$$

It is important to note that the manufactured solutions were designed to ensure the continuity of the particle flux, $J = -D\boldsymbol{\nabla} c_{\mathrm{m}} \cdot \mathbf{n}$, across the interface between the materials. Consequently, MMS sources are independently derived for each material:

$$S_{\mathrm{left}} = 8\pi^2\left(\cos\left(2\pi x\right) + \cos\left(2\pi y\right)\right) \tag{2.78}$$

$$S_{\mathrm{right}} = 40\pi^2\left(\cos\left(2\pi x\right) + \cos\left(2\pi y\right)\right) \tag{2.79}$$

The exact solutions established are utilised to define the MMS fluxes and boundary conditions. The agreement between the computed results and the exact solutions is very good, as illustrated in Figure 2.6. The L2 error is quantified at 5.49×10^{-4}.

Verification case 2: heat transfer

This scenario tests the functionality of the heat transfer solver within FESTIM. It involves two materials with differing thermal conductivities: $\lambda_{\mathrm{left}} = 2$ and $\lambda_{\mathrm{right}} = 5$. An exact solution for temperature is established for each material:

$$T_{\mathrm{exact}} = 1 + \sin\left(\pi\left(2x + 0.5\right)\right) + \cos\left(2\pi y\right) \tag{2.80}$$

Like Case 1, the manufactured solution ensures that the thermal flux $-\lambda\boldsymbol{\nabla} T \cdot \mathbf{n}$ remains continuous across the material interface. Distinct MMS sources are defined for each material,

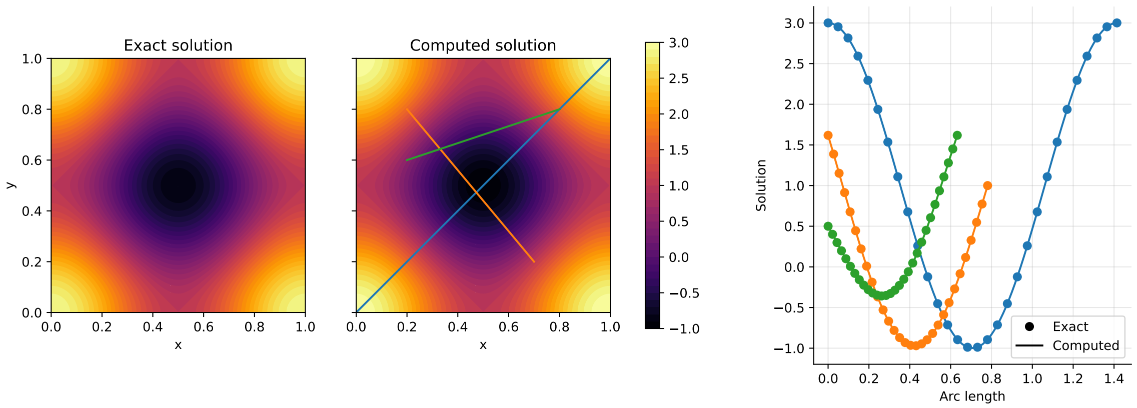

Figure 2.7: Verification case 2: heat transfer [150]

resulting in a computed solution that aligns closely with the exact solution, as shown in Figure 2.7.

$$Q_{\text{left}} = 8\pi^2 \left(\cos\left(2\pi x\right) + \cos\left(2\pi y\right)\right) \tag{2.81}$$

$$Q_{\text{right}} = 20\pi^2 \left(\cos\left(2\pi x\right) + \cos\left(2\pi y\right)\right) \tag{2.82}$$

The L2 error is 3.31×10^{-4}.

Verification case 3: trapping

The final case tests the trapping mechanism within FESTIM. Only one trap is considered for simplicity, although the methodology applies to scenarios with multiple traps. Exact solutions are specified for both the mobile and trapped hydrogen concentrations.

$$c_{\text{m,exact}} = 5 + \sin\left(2\pi x\right) + \cos\left(2\pi y\right) \tag{2.83}$$

$$c_{\text{t,exact}} = 5 + \cos\left(2\pi x\right) + \sin\left(2\pi y\right) \tag{2.84}$$

In this setup, the trap density is defined as $n = 2\ c_{\text{t,exact}}$, with a trapping rate of $k = 0.1$ and a detrapping rate of $p = 0.2$. The diffusivity parameter is set at $D = 5$. MMS sources are calculated for both the mobile and trapped hydrogen concentrations:

$$S_{\text{m}} = -D\boldsymbol{\nabla}^2 c_{\text{m,exact}} + k c_{\text{m,exact}}(n - c_{\text{t,exact}}) - p c_{\text{t,exact}} \tag{2.85}$$

$$S_{\text{t}} = -k c_{\text{m,exact}}(n - c_{\text{t,exact}}) + p c_{\text{t,exact}} \tag{2.86}$$

Once again, the computed solution aligns closely with the exact solution, as Figure 2.8 demonstrates. The L2 error is 1.05×10^{-2} for the mobile concentration and 7.63×10^{-3} for the trapped concentration.

2.4 Summary

This chapter presents a detailed multiphysics model for the WCLL breeding blanket, incorporating heat transfer, fluid mechanics, and hydrogen transport. These physical phenomena

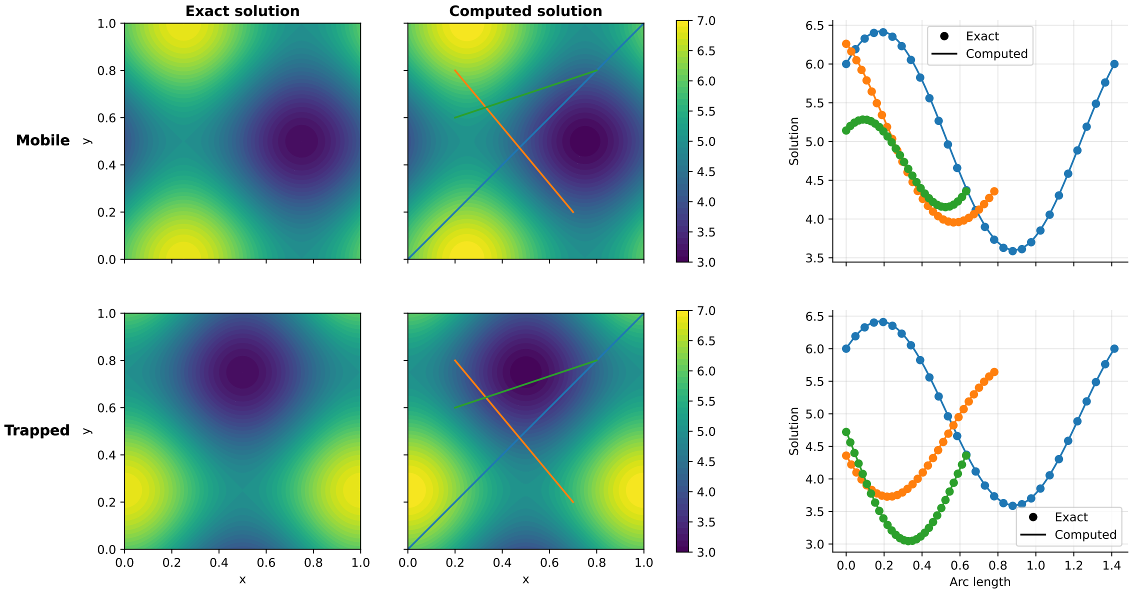

Figure 2.8: Verification case 3: trapping [150]

are critical for accurately simulating WCLL operations. The model uses the Finite Element Method to solve partial differential equations, enabling the simulation of complex geometries and interactions. The use of FEM, mainly through FEniCS software, facilitates efficient management of the intricate mathematical formulations and computations involved. This framework includes a tailored fluid mechanic's solver for PbLi flow and introduces FESTIM as the primary tool for hydrogen transport modelling.

A significant advancement in the presented model includes trapping effects in hydrogen transport within structural materials, a novel contribution to the existing literature. This enhancement addresses the interactions between mobile and trapped hydrogen, considering the influence of temperature and irradiation. By incorporating these trapping effects, the model offers a more comprehensive understanding of hydrogen behaviour, which is crucial for evaluating the performance and safety of the WCLL system.

The development of FESTIM was further advanced to meet the specific needs of modelling the WCLL. Key improvements include transitioning to an object-oriented structure and facilitating more accessible addition of new features. An extrinsic trap class was developed, providing enhanced control over trap density and allowing for temporal evolution. Performance optimisations, such as exporting data at defined time steps, were also implemented to reduce run times. These enhancements ensure that FESTIM can handle the complex, multidimensional, and transient simulations required for WCLL modelling while maintaining user accessibility and flexibility.

Chapter 3

WCLL model

Contents

3.1 WCLL Geometry 60
3.2 Model parameters 61
  3.2.1 Thermophysical material properties 62
  3.2.2 Hydrogen transport material properties 64
  3.2.3 Sources due to neutrons 67
  3.2.4 Boundary conditions 68
3.3 Standard case 71
3.4 Parametric studies 76
  3.4.1 Influence of coolant heat transfer coefficient 77
  3.4.2 Influence of tritium sources 85
  3.4.3 Influence of PbLi solubility 87
  3.4.4 Summary 89

This chapter covers the multiphysics tritium transport model for the WCLL. Following the foundational context, physics, and model implementation methods established in the preceding chapters, this section outlines the specific model parameters and presents the results. First, the geometry of the WCLL and the simulation parameters are presented. The benchmark standard simulation case for subsequent analyses is then presented. The chapter then transitions to a series of parametric studies of critical components within the model. The convective heat transfer boundary condition, which replaces direct modelling of water flow, is examined to understand its impact on the system. This is followed by exploring the impact of the tritium sources within the model and assessing their contributions. The solubility of PbLi, identified as the parameter with the most significant uncertainty, is scrutinised to gauge its influence on the model's outcomes.

For this work, a 2D domain within the 3D WCLL geometry at the central plane was considered for more rapid analysis. This location was chosen as it experiences the most extreme conditions within the WCLL unit cell [87]. However, this 2D approach encounters significant limitations. The WCLL features multiple cooling channels aligned in the radial direction, which are integral to the system's overall heat transfer and thermal management (see Figure 3.2). When these channels are excluded from the 2D model, the intricate 3D heat transfer effects cannot be captured, leading to substantial inaccuracies. To address this critical issue, a transition to a 3D modelling approach for the heat transfer analysis of the WCLL was undertaken. By doing so, the effects of the radial cooling channels are incorporated, ensuring an understanding of the thermal behaviour. From this 3D model, a representative slice is extracted and projected back onto the 2D domain (see Figure 3.1). This method retains the essential 3D characteristics of heat transfer while leveraging the computational efficiency of a 2D analysis.

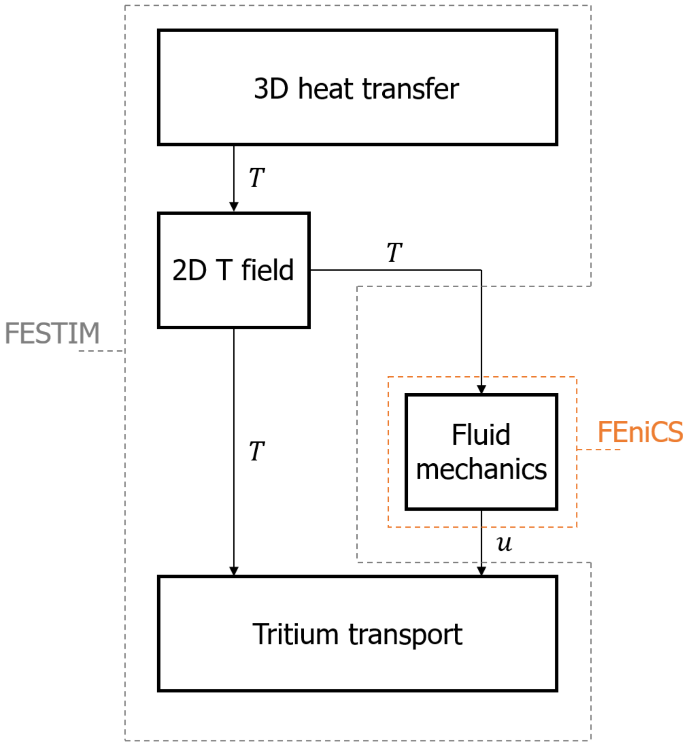

Figure 3.1: Simulation workflow for multiphysics modelling of the WCLL, highlighting in dashed lines which physics is solved by FESTIM and FEnicS

3.1 WCLL Geometry

The WCLL v0.6b unit cell design [81] for the DEMO reactor is geometrically tailored to optimise performance and withstand operational demands. In this work, the geometry considered is a section of the elementary cell from the central outboard position, focusing solely on the First Wall–Side Wal (FW-SW) and the BZ while excluding the manifolds, back supporting structure (BSS), and caps.

The design features a 27 mm thick U-shaped FW-SW plate, actively cooled by water at PWR conditions flowing through square channels with a $7 \times 7\,\text{mm}^2$ cross-section, arranged to manage heat flux variances along the poloidal axis. The BZ, enveloped by the FW-SW and backed by a 20 mm plate, contains PbLi for tritium breeding and heat removal. These cooling processes are facilitated by Double-Walled Tubes (DWT) that prevent exothermic reactions by minimising crack propagation. The BZ is reinforced with 10 mm thick horizontal and 12 mm thick vertical stiffening plates, forming a grid that aids breeder flow and structural integrity. Each elementary cell within the segment is a stack of these reinforced structures, with water-

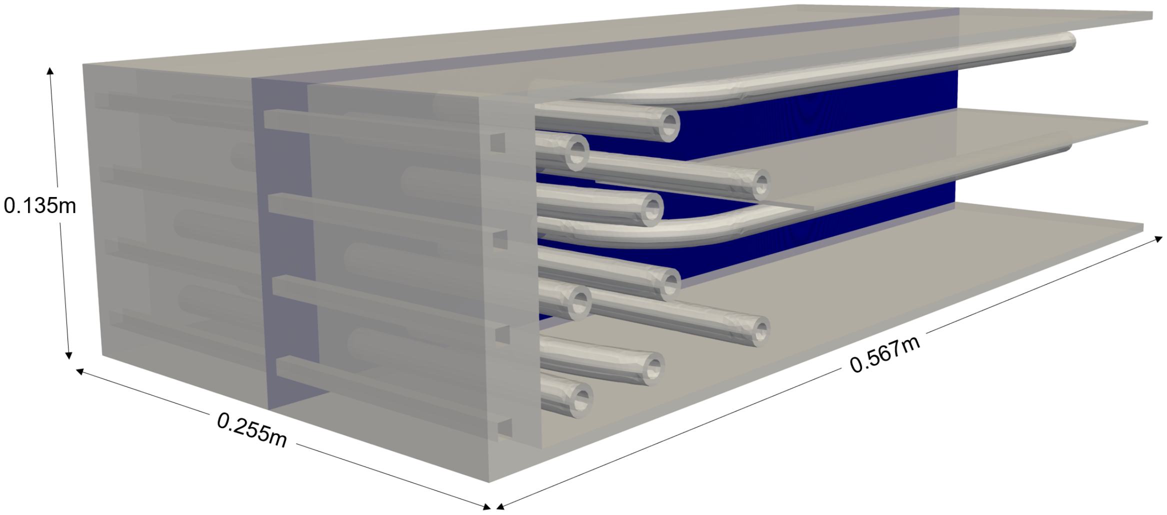

Figure 3.2: 3D geometry of WCLL v0.6b geometry showing the position of the 2D domain considered

Table 3.1: Geometric dimensions for the 3D WCLL geometry [81]

Description	Value [mm]
Radial Length	567
Poloidal length	135
Toroidal length	255
Pipes external diameter	13.5
Pipes internal diameter	8
Baffle Thickness	2
Baffle Length	365
Stiffening plate thickness	5

cooled DWT's ensuring thermal symmetry and maintaining operational temperatures below 550 °C. This robust and optimised geometry supports efficient tritium breeding and effective heat removal, focusing research on the critical processes inside the breeding zone. Details of the 3D geometric dimensions are outlined in Table 3.1.

3.2 Model parameters

The following section details the values for each parameter used in the WCLL model. The values have been carefully selected based on relevant literature, experimental data, and engineering judgments to ensure the model's fidelity and reliability. At the beginning of this work, there was very little work available for comparison other than one notable study [130]. As such, many of the parameter values were chosen from the same references used in this work to enhance comparability.

The multiphysics model of the WCLL BB involves several critical parameters for accurate simulation, including material thermophysical properties like thermal conductivity, specific heat capacity, and density, which predict temperature distributions. Hydrogen transport properties, such as diffusion and solubility coefficients, are essential for tritium management. Source terms account for heat and tritium generation due to neutron interaction with the material within the WCLL. Boundary conditions define temperature, hydrogen surface physics, interface flow conditions, and environmental factors like coolant inlet temperatures and flow rates. Detailed discussions and justifications of these parameters ensure robust and reliable simulations of WCLL BB performance.

3.2.1 Thermophysical material properties

The WCLL comprises three materials: tungsten, Eurofer and PbLi. Each of the materials has unique properties and specific justifications for their inclusion. For instance, Eurofer, a reduced activation ferritic/martensitic steel, has been designed specifically for fusion reactors, balancing mechanical strength and reduced long-term radioactivity [188]. The materials chosen for the WCLL are integral to the success of DEMO and have been subject to rigorous research to have reliable thermophysical properties used within the EUROfusion consortium modelling activities [140, 189].

Tungsten is a critical material for fusion applications, particularly for components exposed to intense plasma-surface interactions. Tungsten is an excellent material for plasma-facing components in fusion reactors due to its high melting point, which allows it to withstand extreme temperatures, and its high density and mechanical strength, providing durability under intense mechanical stresses. Additionally, tungsten's resistance to radiation damage ensures its properties remain stable despite the high neutron fluxes in a fusion environment, making it highly suitable for long-term operation. Tungsten's high thermal conductivity is crucial for plasma-facing components because it allows efficient dissipation of the immense heat generated by the plasma. This property helps prevent localised overheating and thermal fatigue, which are critical issues in maintaining the structural integrity and performance of the components. In contrast, materials like Eurofer or PbLi have lower thermal conductivity (see figure 3.3), making them less effective in managing heat and more prone to thermal stresses and damage under the extreme conditions of a fusion environment.

Eurofer has been developed specifically to address the unique challenges and demands of the fusion reactor environment, including high neutron flux, intense thermal loads, and the need for materials that produce minimal long-lived radioactive isotopes upon irradiation. Eurofer differs from 316 stainless steel, standard steel used in fission reactor vessels, by offering reduced activation, better high-temperature performance, superior thermal conductivity, and enhanced radiation damage resistance, making it more suitable for fusion reactors [188]. Eurofer has been selected as the baseline structural material for the in-vessel components of the EU-DEMO reactor. To support its use and development, the EUROfusion consortium has developed a comprehensive material property handbook [189]. It has been the source reference for all Eurofer thermophysical properties in this work.

PbLi was chosen as the breeder material for its tritium breeding efficiency, thermal conductivity, and compatibility with reactor materials. Comprehensive research on its thermophysical properties has been conducted within the EUROfusion consortium to support modelling activities essential for designing the WCLL [140]. Details for the analytical values of all material thermophysical properties used in this work and their dependence on temperature and quoted range of validity are outlined in Tables 3.2 - 3.5.

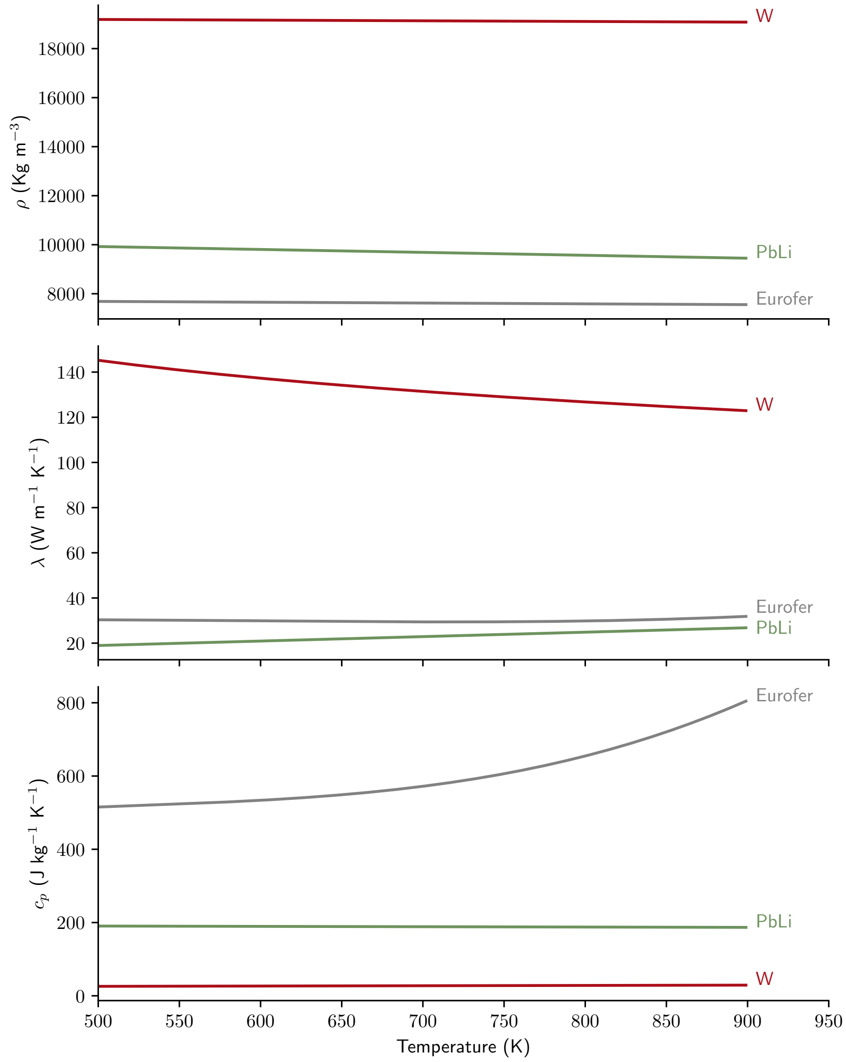

Figure 3.3: Thermophysical properties of density, ρ (top), thermal conductivity, λ (middle) and specific heat capacity, c_p (bottom) of the materials in the WCLL: tungsten [141], Eurofer [189] and PbLi [140] over a temperature range found within the operational conditions of the WCLL and beyond

Table 3.2: Density values, ρ [kg m^{-3}], $T_0 = 273.15\,\mathrm{K}$

Material	Definition	Range
tungsten [141]	$19250 - 2.66207 \times 10^{-1}(T - T_0) - 3.0595 \times 10^{-6}(T - T_0)^2 - 9.5185 \times 10^{-9}(T - T_0)^3$	$300 \leq T(K) \leq 3695$
Eurofer [189]	$7852.1 - 0.331T$	$T(K) \leq 823$
PbLi [140]	$10520 - 1.19T$	$508 \leq T(K) \leq 880$

Table 3.3: Specific isobaric heat capacity values, C_p [$\mathrm{J\,kg^{-1}\,K^{-1}}$]

Material	Definition	Range
tungsten [141]	$21.868372 + 8.068661 \times 10^{-3}T - 3.756196 \times 10^{-6}T^2 + 1.075862 \times 10^{-9}T^3 + 1.406637 \times 10^4 T^{-2}$	$300 \leq T(K) \leq 3695$
Eurofer [189]	$-139.66 + 3.4777T - 0.0063847T^2 + 4.0984 \times 10^{-6}T^3$	$T(K) \leq 823$
PbLi [140]	$195 - 9.116 \times 10^{-6}T$	$508 \leq T(K) \leq 800$

Table 3.4: Thermal conductivity values, λ [$\mathrm{W\,m^{-1}\,K^{-1}}$]

Material	Definition	Range
tungsten [141]	$149.441 - 4.5446 \times 10^{-4}T + 1.3193 \times 10^{-6}T^2 + 1.484 \times 10^{-10}T^3 + 3.866 \times 10^6 T^{-2}$	$300 \leq T(K) \leq 3695$
Eurofer [189]	$5.4308 + 0.13565T - 2.3862 \times 10^{-4}T^2 + 1.3393 \times 10^{-7}T^3$	$T(K) \leq 823$
PbLi [140]	$9.14779235 + 0.019631T$	$508 \leq T(K) \leq 873$

Table 3.5: PbLi fluid property values

Property	Definition	Units
Viscosity, μ [140]	$0.0155 - 4.83 \times 10^5 T + 5.64 \times 10^{-8}T^2 - 2.29 \times 10^{-11}T^3$	Pa s

3.2.2 Hydrogen transport material properties

Tritium transport parameters encompass diffusion, solubility, and trapping, determining the model's fidelity. However, they also contribute significantly to the uncertainties inherent in hydrogen transport property values.

The value published by Frauenfelder [124] is employed to model the diffusion and solubility within tungsten. However, recent publications have been trending towards adopting diffusion values derived from atomistic simulations [136]. Regarding Eurofer, a recent and thorough study by Chen [126] offers a robust evaluation of diffusivity and solubility values. For PbLi, the diffusion parameter exhibits less variability than tungsten and Eurofer (see Figure 3.4). The diffusivity value used in the model is derived from Reiter's work [190], which is the most cited and aligns with comparable studies, such as those by Candido [130]. However, the solubility parameter for PbLi is more contentious. Reiter's solubility value is among the lowest in the literature by orders of magnitude, leading to significant discrepancies in model predictions (see Figure 3.4). Furthermore, the vast distribution of solubility values for PbLi has a significant impact on tritium transport within the WCLL due to the nature of the material interface condition (conservation of chemical potential, see section 2.1.3). Thus, depending on the reference used for solubility in the PbLi, the solubility can be significantly higher or lower than in the Eurofer, which can have severe consequences for tritium transport behaviour. However, more recent studies indicate that the actual solubility value may be much higher, closer to the upper end of the distribution found in the literature [191]. Consequently, the solubility value from Aiello [125] is adopted in this model to represent better the transport behaviour within PbLi and its interaction with Eurofer.

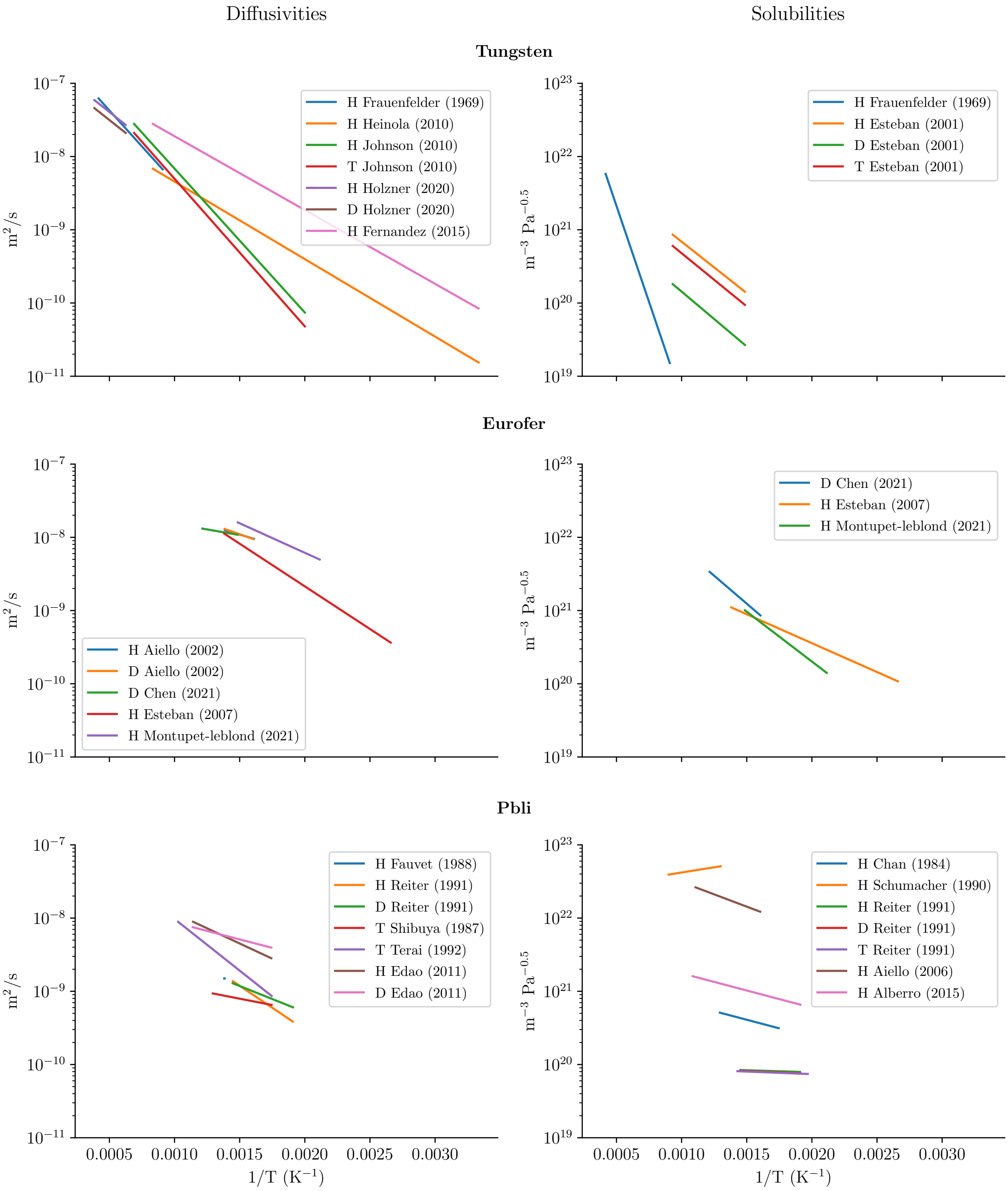

Figure 3.4: Diffusivities and solubilities for hydrogen isotopes H, D and T in tungsten [124, 61, 68, 136, 59, 192], Eurofer 97 [193, 126, 134, 54] and PbLi [194, 190, 195, 196, 197, 198, 199, 125, 200]. Values obtained from HTM [201]

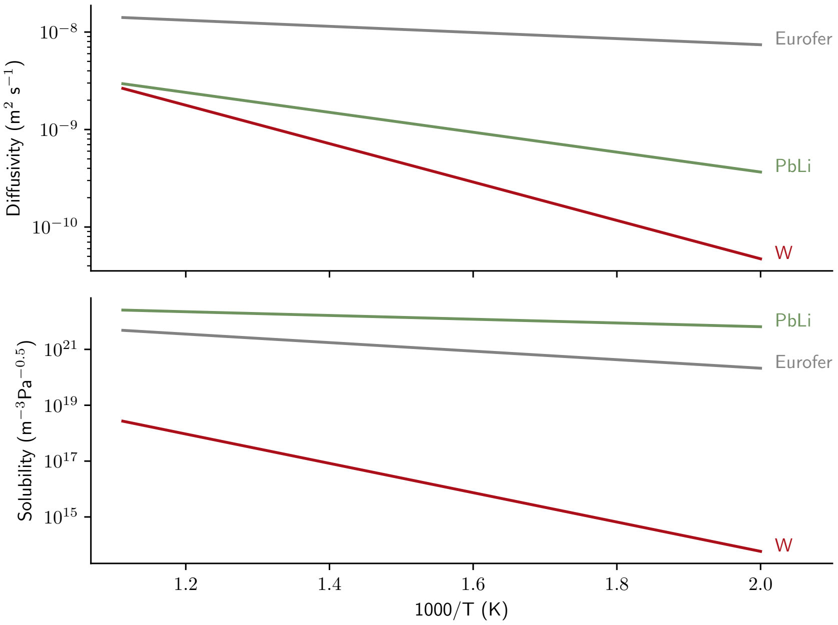

Figure 3.5: Hydrogen transport properties of diffusivity (top) and solubility (bottom) of the materials in the WCLL: tungsten [124], Eurofer [126] and PbLi [190, 125] over a temperature range found within the operational conditions of the WCLL and beyond

Table 3.6: H transport properties of W, Eurofer and PbLi

Material	Solubility $K_{s,0}$ [m^{-3} Pa$^{-0.5}$]	E_{K_s} [eV]	Diffusivity D_0 [m^2 s^{-1}]	E_D [eV]
tungsten [124]	1.87×10^{24}	1.04	2.40×10^{-7}	0.39
Eurofer [126]	2.41×10^{23}	0.30	3.15×10^{-8}	0.06
PbLi [190, 125]	1.43×10^{23}	0.13	4.03×10^{-8}	0.20

The accounting for trapping mechanisms is a significant innovation in this work, distinguishing it from existing literature related to the WCLL [130]. Accounting for trapping mechanisms is typically considered standard practice at small-length scales or in lab-scale experiments. Still, it is not commonly included in component-scale modelling or power plant system-level codes. By incorporating trapping in this model, the goal is to assess their impact on tritium retention within the WCLL. Since PbLi is a liquid, hydrogen cannot get trapped within it. However, the effects of trapping are substantial for structural materials such as tungsten and Eurofer. Tungsten exhibits the most significant trapping effects, with other studies in the literature considering 2-3 traps depending on whether ion irradiation from the plasma is considered [94]. Eurofer, on the other hand, is modelled with a single trap in this work. This trap has a lower detrapping energy and density than tungsten, making it less impactful. Eurofer makes up a significantly more significant portion of the WCLL design than the 2 mm thick tungsten armour, potentially leading to extensive tritium inventories within Eurofer. Recent research [54] suggests a second, more significant heavy trap may be present in Eurofer. However, recent research [54] suggests a second, more significant heavy trap may be present in Eurofer. By exploring the role of trapping at a component scale, this study aims to provide new insights into tritium retention and its implications for the WCLL breeding blanket. Values for the trapping parameters used within the WCLL model are detailed in Table 3.7. Where the atomic densities of tungsten and eurofer used were $6.32 \times 10^{28}\,\mathrm{m}^{-3}$ and $8.41 \times 10^{28}\,\mathrm{m}^{-3}$ respectively.

Table 3.7: Trap properties for tungsten and Eurofer

Material	$E_{t,i}$ [eV]	$\nu_{t,i,0}$ [$\mathrm{m}^3\,\mathrm{s}{-1}$]	$E_{dt,i}$ [eV]	$\nu_{dt,i,0}$ [s^{-1}]	n_i [m^{-3}]
tungsten [94]	0.39	$5.22 \cdot 10^{-17}$	0.87	$1.0 \cdot 10^{13}$	$8.22 \cdot 10^{25}$
	0.39	$8.93 \cdot 10^{-17}$	1.00	$1.0 \cdot 10^{13}$	$2.53 \cdot 10^{25}$
Eurofer [126]	0.06	$2.53 \cdot 10^{-17}$	0.78	$1.0 \cdot 10^{13}$	$4.50 \cdot 10^{23}$

3.2.3 Sources due to neutrons

There are two types of sources to consider in modelling the operation of a WCLL: heat sources and tritium sources. Both sources originate from the same fundamental process: the interaction of neutrons with materials within the WCLL. Neutrons interact with the lithium within the breeder to produce tritium, providing a source for the multiphysics model's tritium transport aspect. As neutrons interact with all materials in the model, they deposit energy with each interaction, resulting in heating across the system, known as nuclear heating. This provides a source in the heat transfer aspect of the multiphysics model.

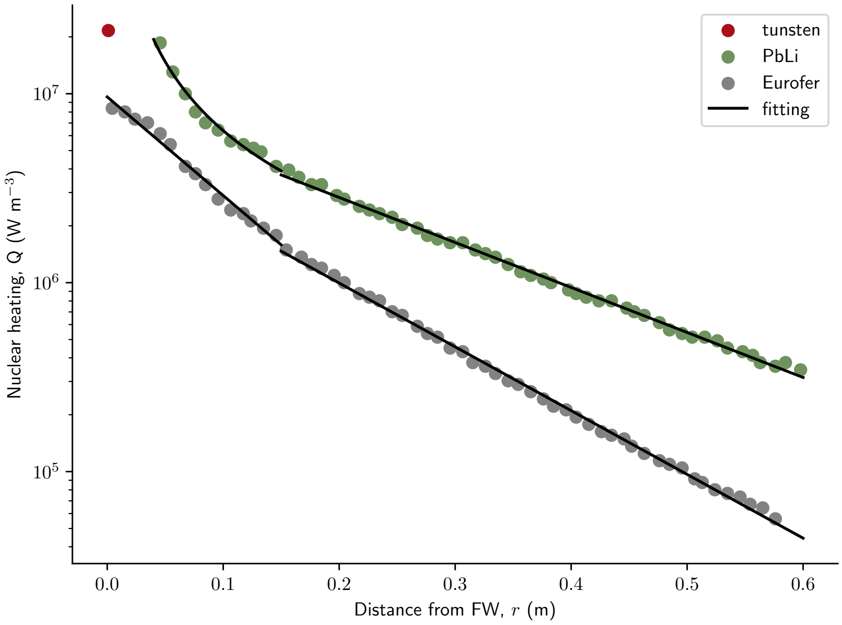

Figure 3.6: Nuclear heating in the PbLi and Eurofer by radial length, r [106]

Table 3.8: Nuclear heating, Q [$\mathrm{MW\,m^{-3}}$]

Material	Definition	Range
tungsten [128]	$23.2 \cdot \exp(-71.74r)$	$\mathrm{r} < 0.002\,\mathrm{m}$
Eurofer [106]	$9.6209 \cdot \exp(-12.02r)$	$\mathrm{r} < 0.15\,\mathrm{m}$
	$4.7109 \cdot \exp(-7.773r)$	$\mathrm{r} \geq 0.15\,\mathrm{m}$
PbLi [106]	$0.391 \cdot \exp(-1.213)$	$\mathrm{r} < 0.15\,\mathrm{m}$
	$8.4629 \cdot \exp(-5.485r)$	$\mathrm{r} \geq 0.15\,\mathrm{m}$

Results from neutronics literature [106] have been fitted to provide source terms for tritium and energy deposition (see Figure 3.6). As a result of the nonlinearity of the nuclear heating data, a series of exponential and power-law piece-wise functions of r, the distance from the FW, in units m, are used to model the heat source (see Table 3.8). The heating is more significant in the PbLi breeder, varying from a factor of 2 to 10 times higher than the Eurofer. The higher heating quantity results from a much larger volume of PbLi in the WCLL than in the Eurofer. Furthermore, the higher density of PbLi than Eurofer steel (see Figure 3.3) results in a shorter neutron mean free path, as more energy is lost with each collision and, consequently, more nuclear heating. Due to the lack of data on energy deposition within the tungsten, a value from the literature has been used [128] (see Table 3.8).

The tritium generation rate term has been taken from the comparable literature [147], which itself has been derived from the same neutronics literature used in this work for the nuclear heating [106]. The value for the tritium generation rate as a function of radial distance from the FW is detailed in Table 3.9.

Table 3.9: Tritium generation, S [$\mathrm{T\,m^{-3}\,s^{-1}}$]

Material	Definition
PbLi [130]	$5.585 \times 10^{18} \cdot \exp(-3.21r)$

3.2.4 Boundary conditions

Positioning for each of the boundary conditions within the 2D WCLL domain are illustrated in Figures 3.7 and 3.8.

In the model's heat transfer aspect, rather than explicitly modelling the coolant water, a convective boundary represents the cooling effect. This approach was chosen due to the complexity of modelling water under PWR conditions, which involve high pressure (155 bar) and high temperature (290-310 °C), with turbulent and often two-phase flow. A convective boundary condition simplifies modelling by eliminating the need to simulate these challenging conditions directly. The convective boundary condition was applied at the coolant interfaces for the first wall and breeding zone, where T_c is the bulk temperature of the coolant in units K (see Eq. (3.1) and (3.2)). A symmetry boundary condition was implemented at the top and bottom surfaces of the model, modelling the influence of the stacking of the WCLL units cells. An imposed temperature was applied at the inlet (see Eq. (3.3)), and a heat flux, φ_{heat}, was imposed on the plasma-facing surface (see Eq. (3.4)). The value for the heat flux has

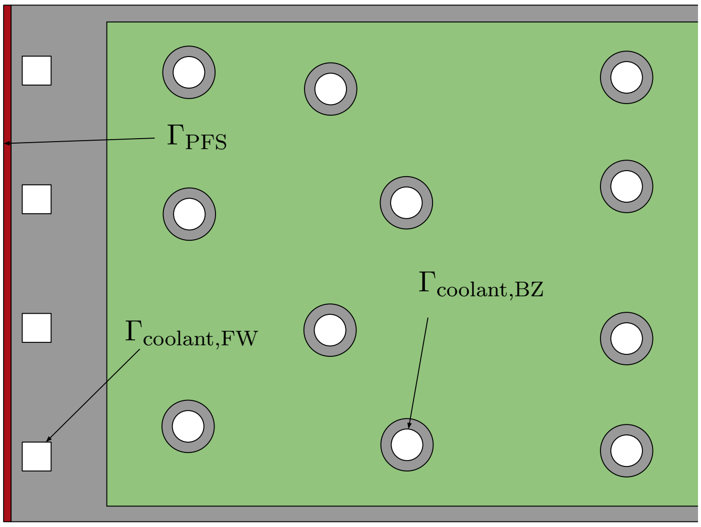
Γ_{PFS}
$\Gamma_{\text{coolant,BZ}}$
$\Gamma_{\text{coolant,FW}}$

Figure 3.7: Front end of 2D WCLL geometry showing tungsten 🟥, Eurofer ■, LiPb 🟩. Γ represents a defined surface, PFS is the Plasma Facing Surface, FW is the First Wall, and BZ is the Breeding Zone

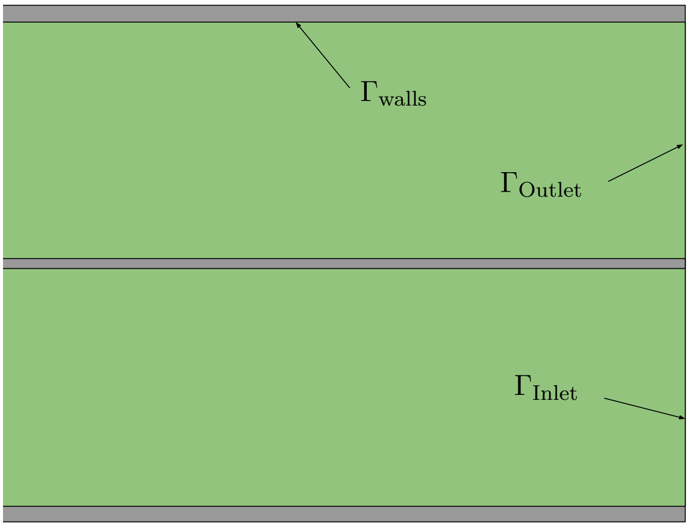
Γ_{walls}
Γ_{Outlet}
Γ_{Inlet}

Figure 3.8: Rear end of 2D geometry showing Eurofer ■, LiPb 🟩. Γ represents a defined surface, Γ_{walls} applies to all LiPb/Eurofer interfaces.

been sourced from similar work in the literature [128].

$$-\lambda \nabla T \cdot \mathbf{n} = h_{\text{FW}} \left(T - T_{\text{c, FW}}\right) \quad \text{on } \Gamma_{\text{Coolant,FW}} \tag{3.1}$$

$$-\lambda \nabla T \cdot \mathbf{n} = h_{\text{BZ}} \left(T - T_{\text{c, BZ}}\right) \quad \text{on } \Gamma_{\text{Coolant,BZ}} \tag{3.2}$$

$$T = T_0 \quad \text{on } \Gamma_{\text{Inlet}} \tag{3.3}$$

$$-\lambda \nabla T \cdot \mathbf{n} = \varphi_{\text{heat}} \quad \text{on } \Gamma_{\text{PFS}} \tag{3.4}$$

The model's fluid mechanics aspect applies a non-slip condition at the fluid domain boundaries (see Eq. (3.5)), where v is in units $\mathrm{m\,s^{-1}}$. The velocity is fixed at the inlet (see Eq. (3.6)). To account for the nonlinearities in the PbLi fluid parameters (density, ρ, and viscosity, μ), the temperature field is interpolated into a function and used to define these properties within the incompressible Navier-Stokes equations (see Eq. (2.29)). This approach facilitates a weak coupling between heat transfer and fluid mechanics, ensuring the fluid flow simulation properly represents temperature-dependent variations in ρ and μ. Table 3.10 describes all fluid dynamics boundary conditions values. The value for the inlet velocity has been sourced from comparative literature on the WCLL [139].

$$\mathbf{v} = (0, 0) \quad \text{on } \Gamma_{\text{walls}} \tag{3.5}$$

$$v = v_0 \quad \text{on } \Gamma_{\text{Inlet}} \tag{3.6}$$

$$P = 0 \quad \text{on } \Gamma_{\text{Outlet}} \tag{3.7}$$

For the tritium transport aspects of the WCLL model, release into the cooling channels was modelled using a recombination flux, which was applied at the cooling surfaces in the BZ pipes and FW cooling channels, where $K_r = 1.41 \cdot 10^{-26} \exp\left(0.257/k_B T\right)$ was the exothermic recombination coefficient expressed in units $\mathrm{m^4\,s^{-1}}$ [202] (see Eq. (3.8)). However, there is uncertainty associated with this value as it has been evaluated experimentally under a vacuum. In this model, recombination occurs at a surface in contact with water. Extensive testing of this surface condition has not yet been completed with Eurofer. Therefore, the potential influence of this uncertainty on tritium transport is unknown. Implantation of tritium from the plasma was modelled (see Eq. (3.9)) where φ_{imp} is the implanted flux in units $\mathrm{m^{-2}\,s^{-1}}$ and R_p is the implantation depth expressed in units m. This boundary condition allows for modelling an implanted source in high flux and high-temperature conditions without needing a nanometre-scale mesh as done in [127]. A homogeneous Dirichlet boundary condition is applied to the inlet, which assumes a perfect purification system (see Eq. (3.10)). The value for implantation flux has been interpreted from plasma-wall interaction modelling data on JET, in which an average value of the implantation flux from the first wall was used [203]. The associated implantation depth of the flux can then be evaluated in SRIM [204], using the corresponding particle energies ($<100\,\mathrm{eV}$) and incident angles, respectively. However, more recently, initial plasma wall interaction simulations expected for DEMO have been undertaken, which suggest the particle fluxes may be lower than anticipated [205].

$$-D \nabla c_{\text{m}} \cdot \mathbf{n} = K_r c_{\text{m}}^2 \quad \text{on } \Gamma_{\text{coolant,FW,BZ}} \tag{3.8}$$

$$c_{\text{m}} = \frac{\varphi_{\text{imp}} R_p}{D} \quad \text{on } \Gamma_{\text{PFS}} \tag{3.9}$$

$$c_{\text{m}} = 0 \quad \text{on } \Gamma_{\text{inlet}} \tag{3.10}$$

Table 3.10: Boundary conditions parameter values

Parameter	Description	Value	Units
φ_{heat}	First wall thermal load	0.5	$\mathrm{MW\,m^{-2}}$
h_{BZ}	BZ pipes heat transfer coefficient	5.03×10^3	$\mathrm{W\,m^{-2}\,K}$
$T_{\text{c,BZ}}$	BZ pipes coolant temperature	585	K
h_{FW}	FW channels heat transfer coefficient	8.87×10^3	$\mathrm{W\,m^{-2}\,K}$
$T_{\text{c,FW}}$	FW channels coolant temperature	585	K
u_0	PbLi inlet velocity	0.18	$\mathrm{mm\,s^{-1}}$
T_0	PbLi inlet temperature	598	K
φ_{imp}	T implantation flux	10^{20}	$\mathrm{m^{-2}s^{-1}}$
R_{p}	T implantation depth	3	nm

3.3 Standard case

This section covers the results of a standard reference case using the governing equations outlined in section 2.1.4 and parameters detailed in section 3.2 on the WCLL geometry detailed in section 3.1. A mesh convergence study was completed, and the resulting mesh used for this standard case and beyond is outlined in appendix B. The simulations presented consider a continuous plasma exposure up to the steady-state point, which for tritium permeation and retention levels was 6 days. Several vital considerations justify modelling a plasma-facing component under continuous exposure up to the point of steady state rather than simulating plasma pulses. The literature has demonstrated that models simulating continuous exposure and those simulating plasma pulses converge towards the same steady-state condition [206]. Studies have shown that deuterium (D) retention dynamics are comparable in both scenarios, particularly during steady-state plasma, where the retention due to D migration deeper into the bulk material remains consistent regardless of whether the plasma is cycled or continuous. This suggests that either modelling approach is valid for long-term exposure for predicting retention and permeation behaviour. Given that DEMO is designed to function as a model power station aiming for either a steady-state plasma or the most extended possible plasma pulses, modelling the continuous condition is a reasonable approach for evaluating tritium permeation and retention levels within the WCLL.

As illustrated in Figure 3.1, the multiphysics simulation workflow begins by modelling the heat transfer at a steady state within the 3D WCLL model. The maximum temperature within the 3D model was found to be 885 K, located explicitly in the central section of the domain where the 2D plane is located (see Figure 3.9). Within the 2D slice, the maximum temperatures in tungsten, Eurofer and PbLi were found to be 885 K, 823 K and 800 K, respectively (see Figure 3.10).

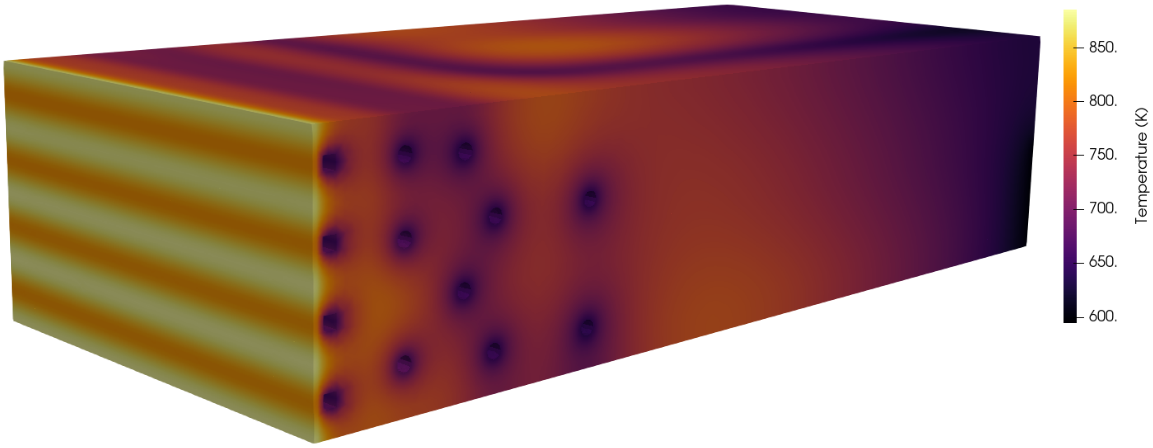

Figure 3.9: 3D steady-state temperature field

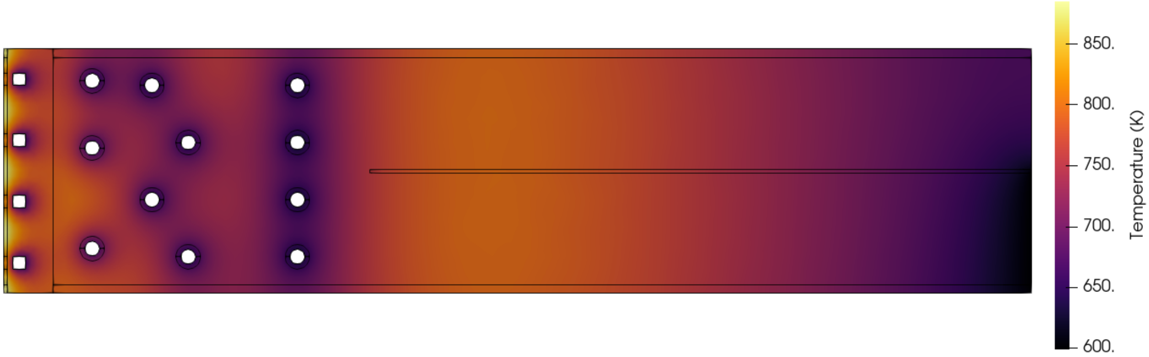

Figure 3.10: 2D toroidal mid-plane slice

Regarding the resulting velocity field of PbLi, two distinct velocity regions were present at the front closest to the first wall and the channels around the baffle plate (see Figure 3.11). The flow is stagnant near the first wall compared to the parabolic profile observed in the channels (see profile A in Figure 3.11). This profile displays the non-slip condition applied at the PbLi/Eurofer interfaces as the velocity approaches zero. This distinction is due to the positioning and length of the baffle plate along the model's centre.

The flow of the PbLi within the WCLL can potentially alter the heat transfer and hydrogen transport by advection effects. However, advection effects were not considered for heat transfer. The average temperature in the Pbli from the heat transfer simulation was 734 K, resulting in a thermal conductivity value of $22.8\,\mathrm{W\,m^{-1}\,K^{-1}}$, a density of $9695\,\mathrm{kg\,m^{-3}}$ and a specific heat capacity of $188\,\mathrm{J\,kg^{-1}\,K^{-1}}$. Additionally, the velocity field has an average magnitude of $1.1 \times 10^{-5}\,\mathrm{m\,s^{-1}}$. The influence of the advection from the PbLi breeder on the thermal simulation can be characterised by the Péclet number:

$$\mathrm{Pe} = \frac{L\ u}{D} \tag{3.11}$$

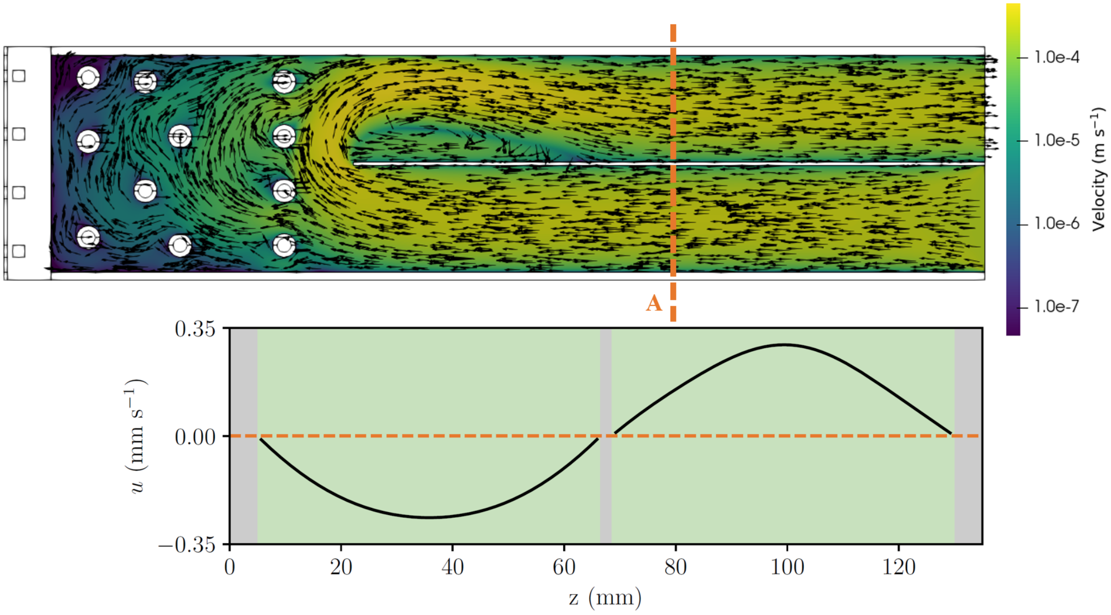

Figure 3.11: Steady state velocity field with associated profile A across the PbLi 🟩 channels and Eurofer ⬜ structure

where:

$$D = \alpha = \frac{k}{\rho\ c_p} \tag{3.12}$$

Thus:

$$\text{Pe} = 0.0586 \tag{3.13}$$

Due to the small size of the Péclet number (Pe « 1), it is unlikely that advection from the flow of the PbLi will significantly impact the thermal field. Therefore, the fact that direct coupling was not considered in this study was justified. However, including buoyancy or MHD effects can significantly alter the characteristics of the resulting velocity field of the PbLi. This decision to neglect these effects was based on the significant complexity of modelling these phenomena within the complex geometry of the WCLL. Despite this, a study into MHD effects on a liquid metal within a rectangular duct has been explored and is attached in the appendices (see appendix C). These considerations can potentially increase local velocities in the field and considerably affect the Péclet number, meaning advection effects must be accounted for.

Regarding the hydrogen transport, the diffusive transport rate is described by D (in Eq. (3.11) $D = \alpha$), the diffusion coefficient of tritium in the PbLi [190]. The average temperature in the PbLi results in a diffusivity value of $1.4 \times 10^{-9}\,\text{m}^{-2}\,\text{s}^{-1}$. The Péclet number can then be characterised as:

$$\text{Pe} = 493 \tag{3.14}$$

As Pe » 1, advection effects from the flow of the PbLi will significantly influence tritium transport behaviour within the WCLL. Therefore, considering the advection term in the hydrogen transport equations is justified.

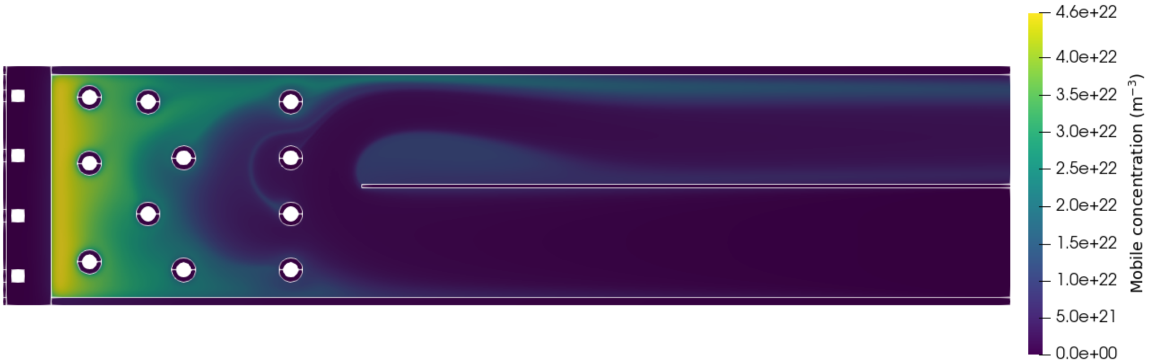

Figure 3.12: Tritium mobile concentration, c_m, field after 7200 s

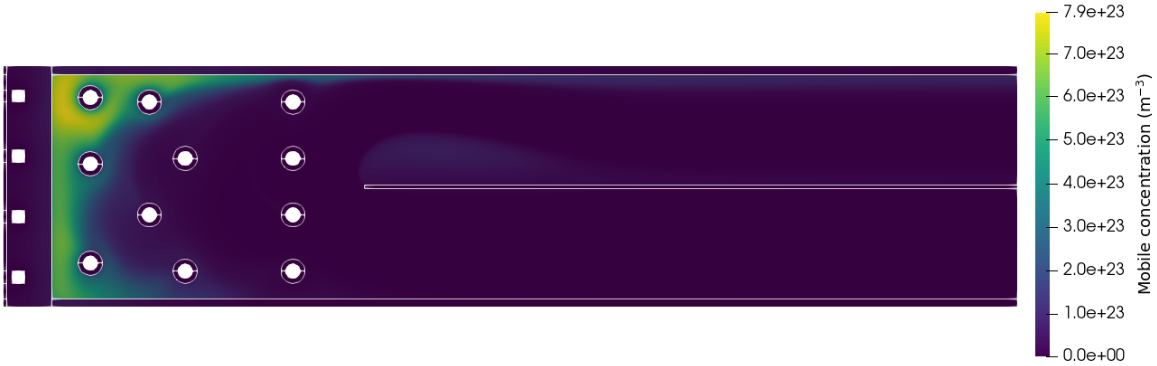

Figure 3.13: Tritium mobile concentration, c_m, field at steady-state

Advection of tritium due to the PbLi flow significantly affects the mobile tritium concentration field (see Figure 3.12); concentrations are highest close to the walls where the velocity is minimised. As the simulation develops to a steady state, a concentration field, as seen in Figure 3.13, is observed, where the PbLi inflow from the inlet of low tritium concentration dominates the flow. Accumulation occurred in the front region due to the higher source term near the front (see Table 3.9) and lack of advection from the breeder flow. Tritium concentrations are shown to reach a maximum of $4.6 \times 10^{22}\,\mathrm{m}^{-3}$ after 7200 s accumulating at the front of the PbLi, increasing to $7.9 \times 10^{23}\,\mathrm{m}^{-3}$ at steady state in the top corner closest to plasma-facing wall as a result of the stagnant flow of the breeder.

Tritium inventory levels peak within the PbLi breeder, reaching a steady-state condition after 6 days (see Figure 3.14). In the first wall, inventory levels reach a maximum of $8 \times 10^{17}\,\mathrm{m}^{-1}$ after just 1 day. Although this is less than the inventory in other parts of the system, it still represents 0.75 % of the total inventory while occupying only 0.35 % of the domain area, highlighting the significant trapping effects in tungsten. Both mobile and intrinsic trap concentrations influence these inventory levels. However, additional traps caused by neutron damage will likely increase inventories significantly in tungsten and Eurofer and extend the time required to reach a steady state. Therefore, it is essential to model the dynamic creation of traps due to the high neutron fluxes that materials within the WCLL will be exposed to [207, 184, 208].

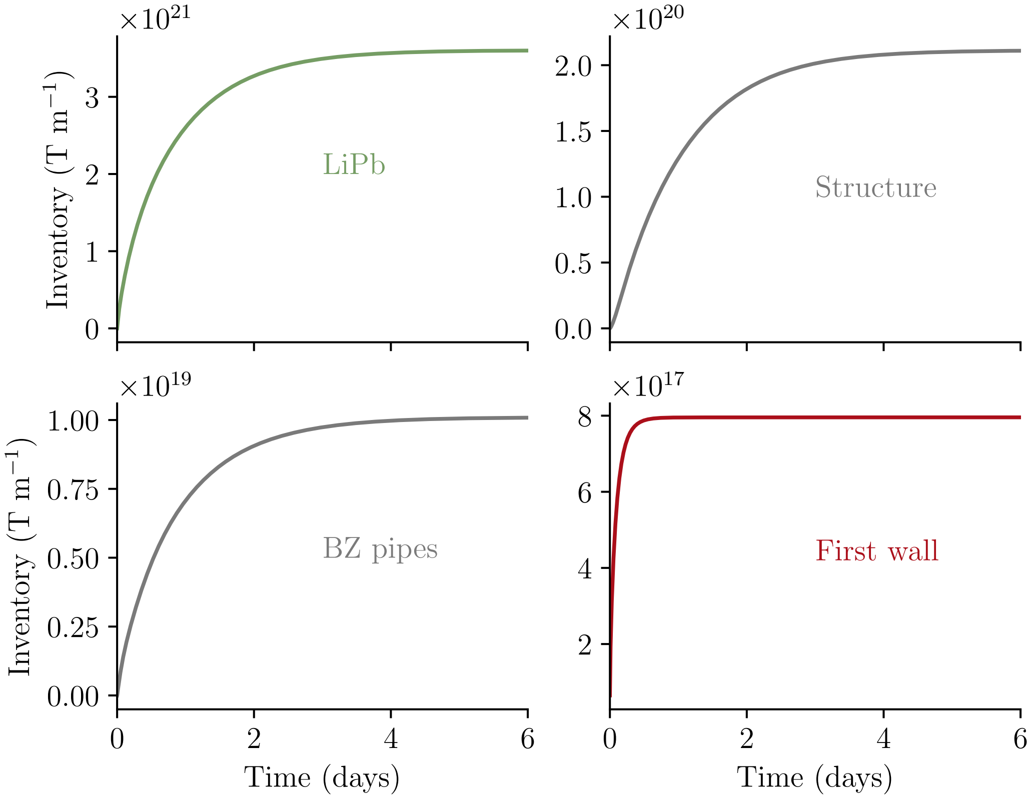

Figure 3.14: Temporal evolution of the tritium inventories in the PbLi, structure, BZ pipes and first wall

A significant delay of 1000 s is observed before any notable amount of tritium permeates the cooling channels at the coolant interfaces. This delay is caused by tritium transport effects within the Eurofer, which mitigates the tritium migration. The highest tritium fluxes are observed in the front breeding zone pipes, followed by the FW channels, then the middle and rear BZ pipes (see Figure 3.15). This pattern is due to the higher tritium generation rates at the front of the breeding zone and the stagnant flow of the breeder, allowing more tritium to diffuse into the front BZ pipes. At steady state, the surface flux for the first wall cooling channels is higher than that of the rear or middle BZ pipes. This is due to several factors:

- The first wall cooling channels are near the region of PbLi with the highest tritium production
- There is an additional contribution from the plasma
- The higher velocity of PbLi surrounding the rear breeding zone pipes (see Figure 3.11) results in more significant advection of tritium produced in this area, thereby reducing the local tritium concentration (see Figure 3.13)

Additionally, the delay in permeation into the FW cooling channels is primarily because most

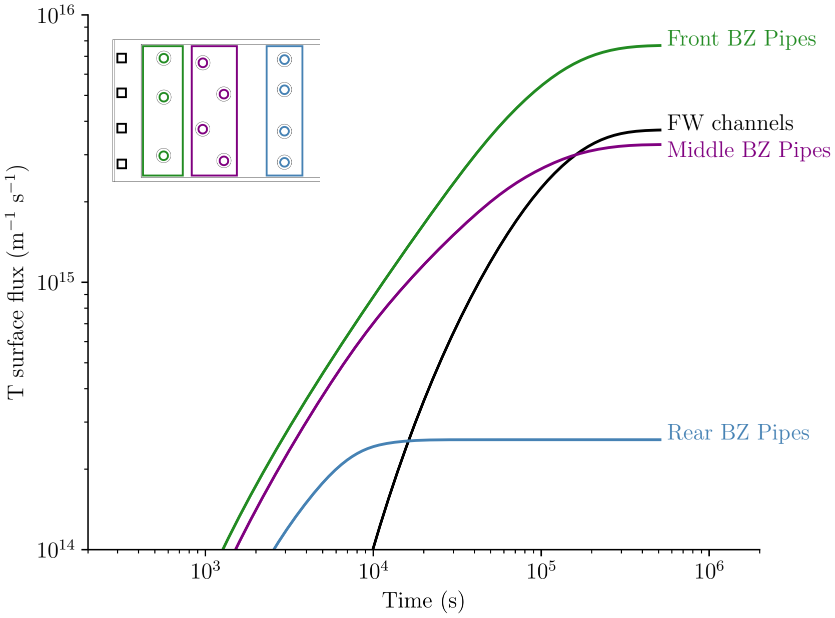

Figure 3.15: Temporal evolution of the tritium permeation rate at the cooling surfaces for the first wall cooling channels and breeding zone pipes at the front, middle and rear position relative to the plasma facing surface

tritium entering these channels comes from the breeder rather than the plasma, despite the plasma source being closer. This delay is due to the time required for tritium to diffuse across the structure to the first wall cooling channels from the breeder source, combined with the significant trapping rate within the FW, which slows tritium diffusion from the plasma. The details of this behaviour are explored in a subsequent parametric study on the influence of tritium sources within the WCLL (see section 3.4.2).

3.4 Parametric studies

This section provides an extensive overview of the parametric studies conducted on the WCLL model, focusing on several critical aspects that influence its performance and operational efficacy.

- The influence of the heat transfer coefficient on the temperature distribution within the WCLL, which in turn affects tritium transport and retention.
- The influence of the two tritium sources, the plasma and the breeder, are analysed to assess their respective contributions to the permeation rates into the cooling channels and inventories within the WCLL
- The uncertainty surrounding the value of hydrogen solubility in the lead-lithium breeder is scrutinised, as this parameter is pivotal in modelling the tritium transport behaviour between the PbLi breeder and the Eurofer structure.

Together, these studies aim to refine the understanding of tritium transport within the WCLL model, identifying how different parameters influence tritium transport dynamics and analysing their impacts on tritium permeation and retention within the WCLL.

3.4.1 Influence of coolant heat transfer coefficient

In the WCLL system's thermal modelling, explicit water simulation in the cooling channels was omitted. Instead, a convective boundary condition was implemented to represent the cooling effect. This methodology was selected due to the complexity of accurately modelling water under PWR conditions. Modelling water under PWR conditions is complex due to the need to accurately simulate multiphase flow, heat transfer, and thermodynamic properties under high pressure and temperature. Additionally, water's behaviour in such conditions involves phase changes (like boiling and condensation), turbulent flow, and interactions with reactor materials, all of which require sophisticated models and high computational resources to capture accurately. A convective boundary condition simplifies the modelling by eliminating the need to simulate these challenging conditions directly in the WCLL's heat transfer simulations. However, given the significant influence of temperature on tritium mobility and trapping, any deviations in the simulated temperature field due to the simplified boundary conditions could potentially impact the distribution of mobile and trapped tritium concentrations. To address this, a parametric study was conducted to explore how these boundary conditions affect hydrogen transport in the WCLL model, drawing on previous thermodynamic analyses of the WCLL for comparative insights [87].

Key design parameters for the cooling systems within the WCLL, such as the outlet water temperature and mass flow rates in the BZ pipes and the FW cooling channels, are constrained [87] and detailed in Table 3.11.

Table 3.11: Cooling water parameters [87]

Parameter	Description	Value	Units
T_{inlet}	Inlet temperature	568	K
T_{outlet}	Outlet temperature	601	K
$\dot{m}_{\text{BZ}}$	BZ pipes mass flow rate	0.85491	$\text{kg}\,\text{s}^{-1}$
$\dot{m}_{\text{FW}}$	FW channels mass flow rate	0.63159	$\text{kg}\,\text{s}^{-1}$

These values for the mass flow rates are divided equally across the 14 pipes in the BZ system and 4 channels in the FW system to determine the mass flow rate per pipe/channel, respectively. The dimensions of these cooling channels are detailed in Figure 3.16. Given these dimensions and the flow rates, the average velocity of water in each pipe or channel can be computed, which is critical for further thermal analysis. The Nusselt number can be calculated using the average velocity to determine the heat transfer coefficient based on equations detailed in section 2.1.1. The parameters, such as the dimensions of the pipes, mass flow rates in each system, and the temperature range across the WCLL, have been carefully selected to maximise the system's Carnot efficiency [209].

Understanding the thermophysical properties of water is essential to determine the heat transfer coefficient at the interface between the water coolant surface and the metal structure

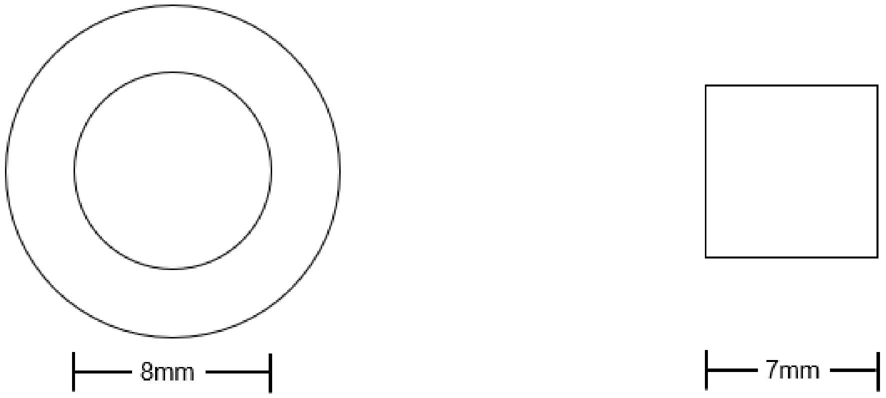

Figure 3.16: BZ cooling pipe (left) and FW cooling channel (right) dimensions

of the WCLL. As detailed in section 2.1.1, specific methodologies and equations are employed to evaluate this coefficient, contingent upon knowing the properties such as density (ρ), viscosity (μ), specific heat capacity (c_p), and thermal conductivity (λ) of water. Under normal conditions, these values can be reliably sourced from steam tables [210]. However, water coolant will be used in the unique conditions of PWR, which are characterised by high pressures and temperatures close to phase changes and demand greater precision. In such scenarios, steam table values may not provide the necessary accuracy due to the proximity to phase changes. Consequently, specific expressions that consider the dependencies of these properties on pressure and temperature are utilised to achieve higher accuracy [87] (see Table 3.12). These refined evaluations allow for the computation of the heat transfer coefficient for the bulk coolant temperatures observed throughout the WCLL. An average value of this coefficient can then be integrated into the thermal model, offering a benchmark for comparison against published references.

Table 3.12: Water thermophysical properties [87]

Parameter	Definition	Units
ρ	$-1.4226 \times 10^{-2}T^2 + 14.122T - 2693$	$\mathrm{kg\,m^{-3}}$
μ	$(-8.095238 \times 10^{-4}T^2 + 0.5722429T + 29.67213) \times 10^{-6}$	$\mathrm{Pa\,s}$
c_p	$9.8485 \times 10^{-3}T^3 + 16.39861T^2 - 9228.681T - 1.6882247 \times 10^6$	$\mathrm{J\,kg^{-1}\,K^{-1}}$
λ	$-1.2024 \times 10^{-4}T^2 + 1.1846 \times 10^{-2}T - 2.2804$	$\mathrm{W\,m^{-1}\,K^{-1}}$

Utilising the predefined constraints, such as the mass flow rates and the number of channels through which these rates are divided, alongside the thermophysical properties of water provided in Table 3.12, calculations of water flow velocities were conducted for the WCLL cooling systems. Specifically, the water flow velocity in the FW cooling channels was determined to be $1.73\,\mathrm{m\,s^{-1}}$, while in the BZ cooling pipes, it was calculated to be $4.60\,\mathrm{m\,s^{-1}}$. Building upon these velocities, the Nusselt numbers, indicative of the convective heat transfer relative to conductive heat transfer within the fluid, were calculated. The Nusselt number was established at 464.2 for the FW cooling channels, whereas for the BZ cooling pipes, it reached 235.8. These Nusselt numbers facilitate the determination of an average heat transfer coefficients for each system, considering an average bulk temperature of 584.65 K:

$$h_{\mathrm{BZ}} = 5.03 \times 10^3\,\mathrm{W\,m^{-2}\,K^{-1}} \tag{3.15}$$

$$h_{\mathrm{FW}} = 8.87 \times 10^3\,\mathrm{W\,m^{-2}\,K^{-1}} \tag{3.16}$$

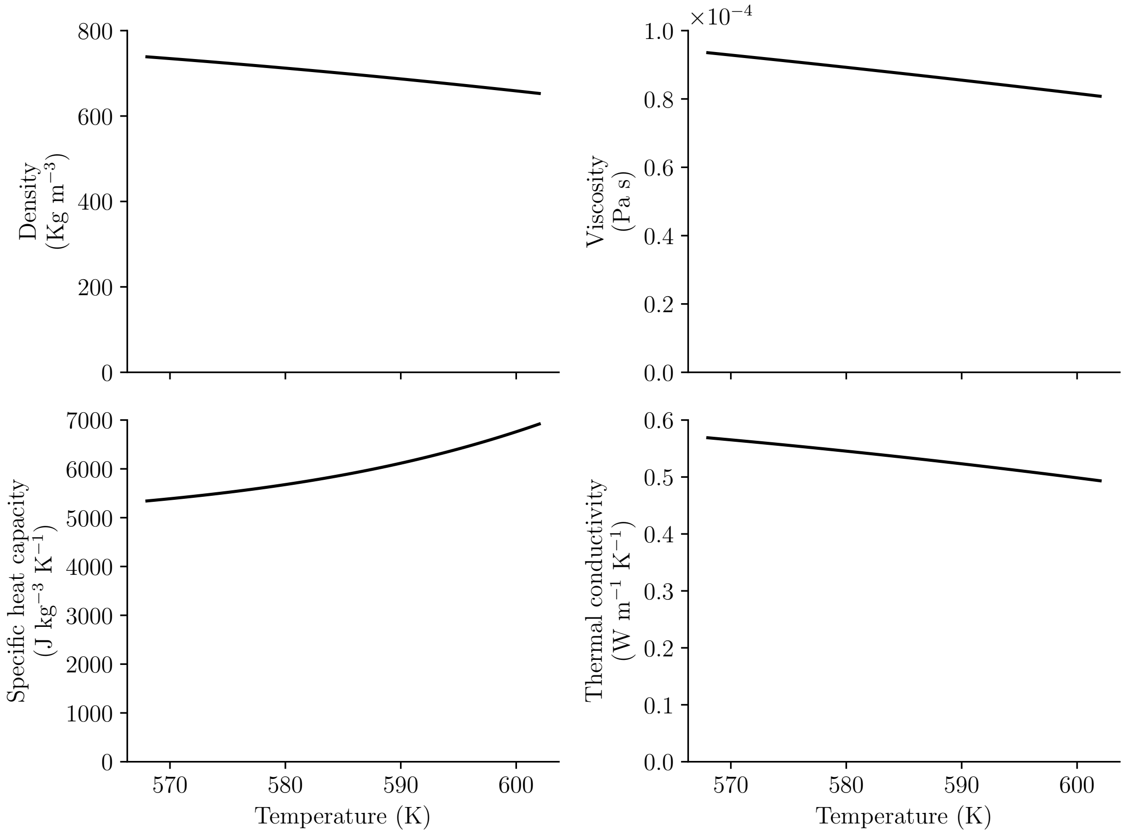

Figure 3.17: Variation of density, viscosity, specific heat capacity and thermal conductivity of water in the temperature range observed in the WCLL

The average heat transfer coefficient values derived from the Nusselt number calculations were subsequently applied in a thermal simulation of the 3D WCLL model. This simulation aimed to validate the thermal management performance by comparing its results against a known published reference [87] (see Fig 3.18). The comparison revealed that the model is in good agreement with the published reference work, confirming the accuracy of the simulation methodologies and the reliability of the thermal performance predictions of the WCLL model.

In the investigation of the WCLL's thermal dynamics, the heat transfer coefficient was analysed across the observed range of bulk coolant temperatures in the breeding blanket system, which spans from 568 K to 601 K. This variation in coolant temperature induced a change in the heat transfer coefficient by approximately 13.7% for the BZ system and 14.8% for the FW system, as illustrated in Figure 3.19. However, despite these changes in the heat transfer coefficient, the resultant impact on the steady-state temperature fields within the WCLL was minimal. This observation indicates that the temperature field within the WCLL is relatively insensitive to fluctuations in the heat transfer coefficient within this specific range of coolant temperatures.

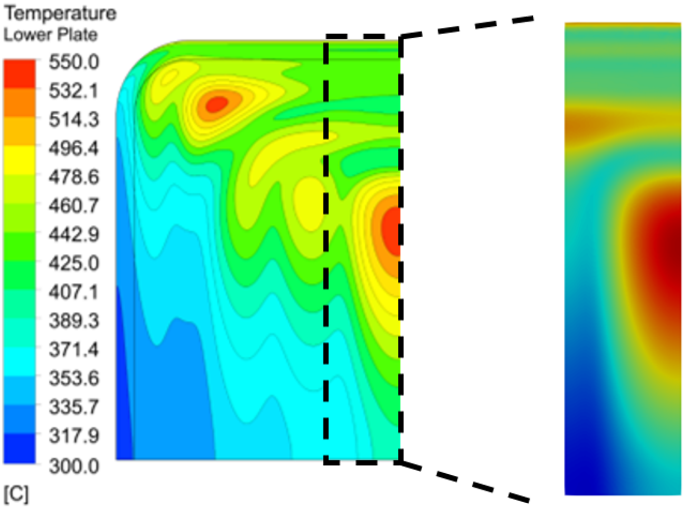
Temperature
Lower Plate
550.0
532.1
514.3
496.4
478.6
460.7
442.9
425.0
407.1
389.3
371.4
353.6
335.7
317.9
300.0
[C]

Figure 3.18: Temperature field in the WCLL comparing the reference solution [87] (left) to this work (right). The temperature colour bar range on the left applies to both cases

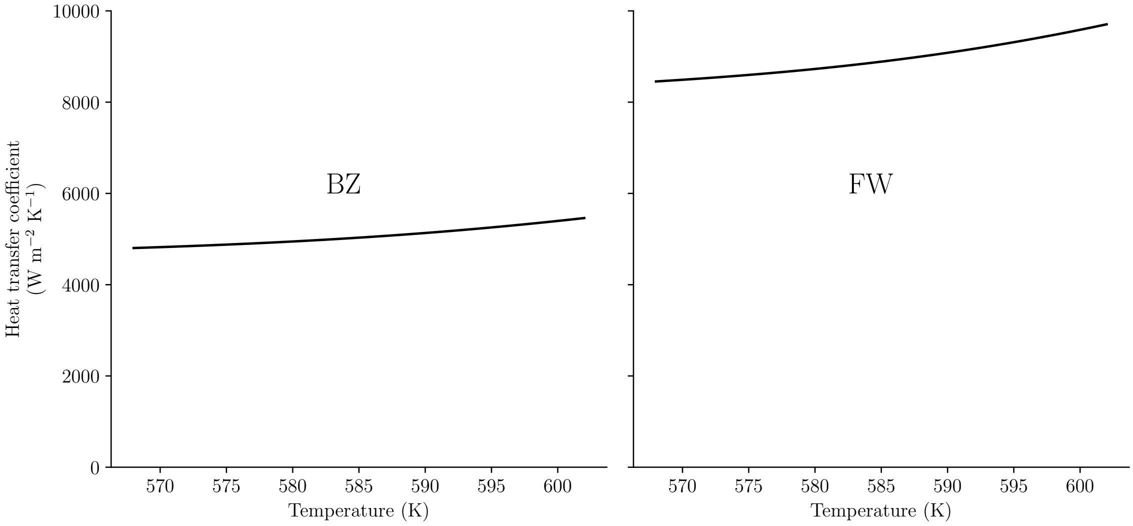

Figure 3.19: Heat transfer coefficient values across the WCLL unit in the BZ pipes (left) and the FW channels (right)

Despite the 33-degree range in the bulk coolant temperature (568-601K) across the WCLL, the corresponding changes in the heat transfer coefficient were relatively modest, with a maximum variation of approximately 15%. This variance had negligible effects on the temperature field within the system. Given the strong dependency of tritium transport on temperature, this slight fluctuation in the heat transfer coefficient resulted in minimal impact on tritium behaviour. Expressly, parametric studies in tritium transport simulations within this temperature range indicated a maximum deviation of 3.7% in tritium permeation into the cooling system for the BZ pipes and a 2.2% difference in the FW channels. These results suggest that the variance in bulk coolant temperature has little effect on tritium transport. However, considering DEMO's breeding blanket system, where the water coolant traverses hundreds of meters of piping, significant pressure drops could likely reduce flow velocity and thus influence the heat transfer coefficient. In light of this, further investigations were conducted, varying the flow velocity or mass flow rate. The mass flow rate for each system was adjusted to 0.1 and 1.9 times the standard value:

$$0.1\dot{m} < \dot{m}_{\mathrm{BZ,FW}} < 1.9\dot{m} \tag{3.17}$$

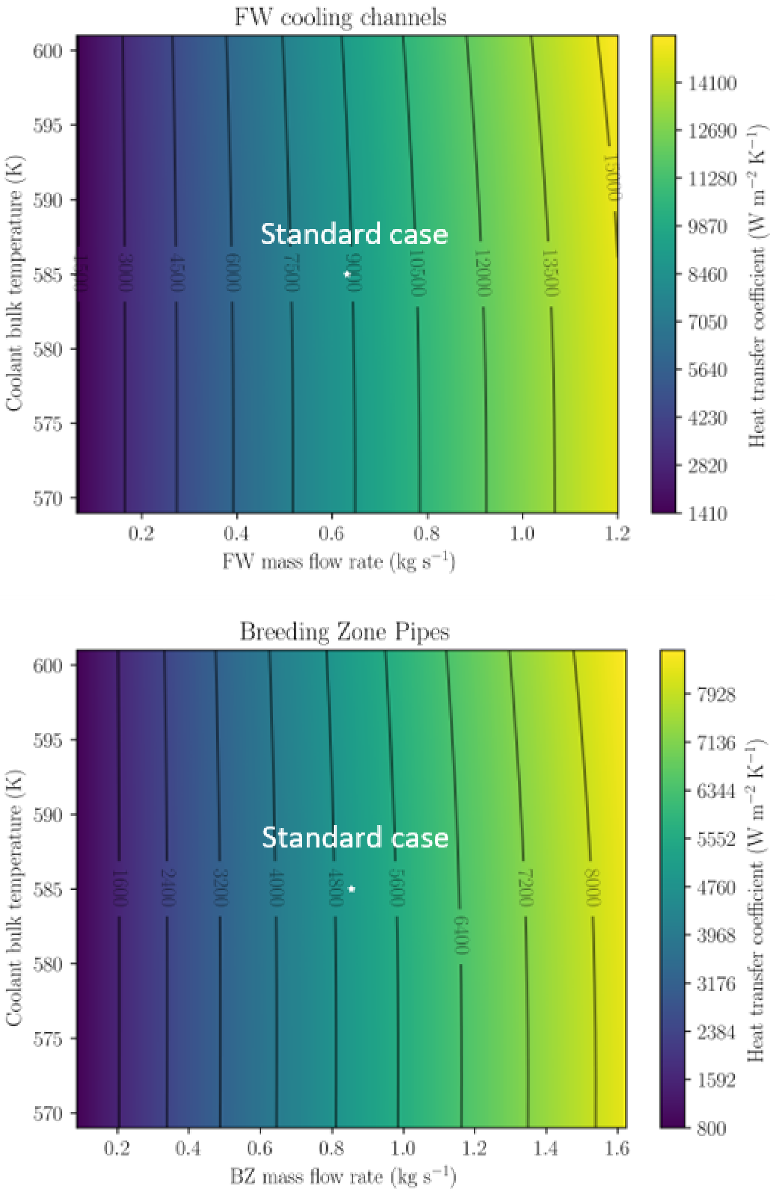

Figure 3.20: Variation in heat transfer coefficient in the FW system (top) and the BZ system (bottom) varying bulk coolant temperature and mass flow rate, value of standard case highlighted with white star

This comprehensive approach allows for assessing the heat transfer dynamics and their influence on tritium transport under realistic operational conditions of a large-scale system.

Varying the mass flow rate has a more significant effect on the heat transfer coefficient than the bulk coolant temperature (see Fig 3.20). This results in an order of magnitude variation between the lowest and highest heat transfer coefficient values. Some cases tested result in temperatures in the structure being over the operational limit of 823 K; thus, they can be ignored and are shadowed in white (see Fig 3.21). Thus, discounting the invalid results, the

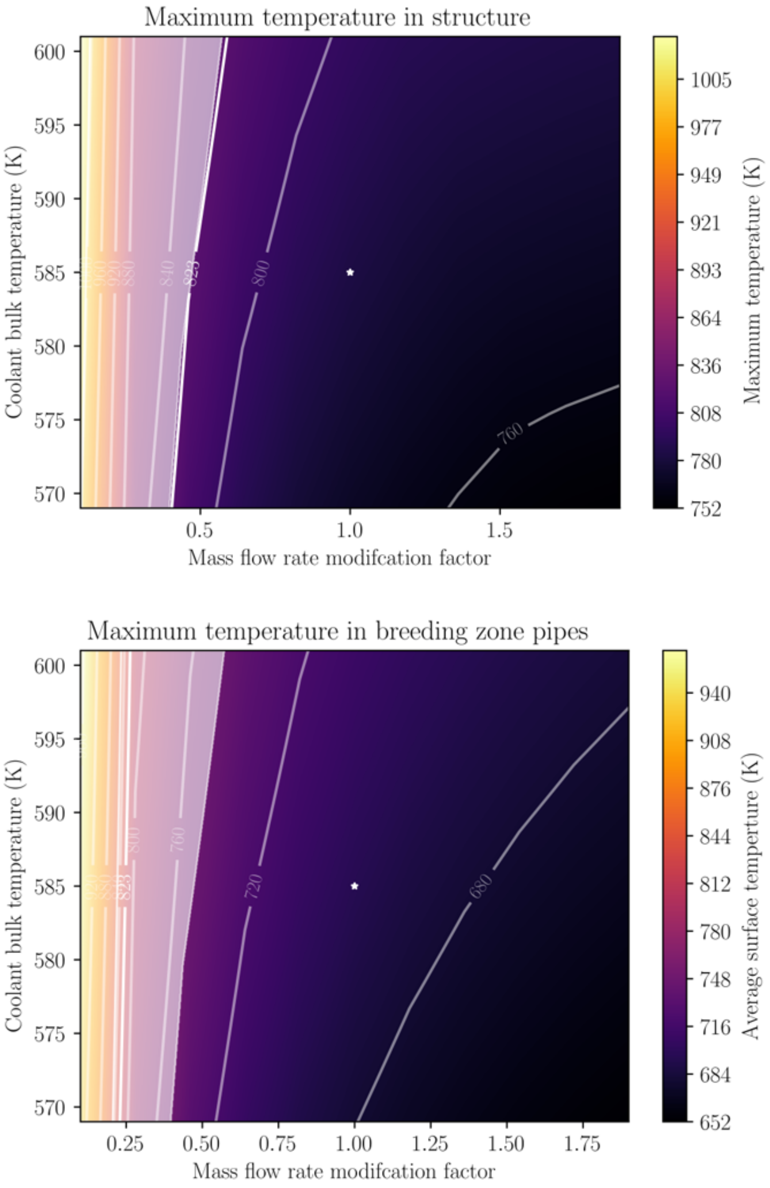

Figure 3.21: Maximum temperature observed in the Eurofer in the structure (top) and BZ pipes (bottom) as a result of varying the heat transfer coefficient as a function of bulk coolant temperature and mass flow rate. Values from the standard case are highlighted in the centre with a white star

total variation in maximum temperatures is observed to be 13 % and 20 % in the structure and BZ pipes at steady-state, respectively, compared to the value from the standard case.

Despite the modification of the heat transfer coefficient in the FW system resulting in a total variation of 13% in maximum temperature, this corresponds to a 7 % difference in steady state surface flux of hydrogen (see Figure 3.22). However, in the BZ system, a more considerable difference in maximum temperature was observed. This was expected as the total surface

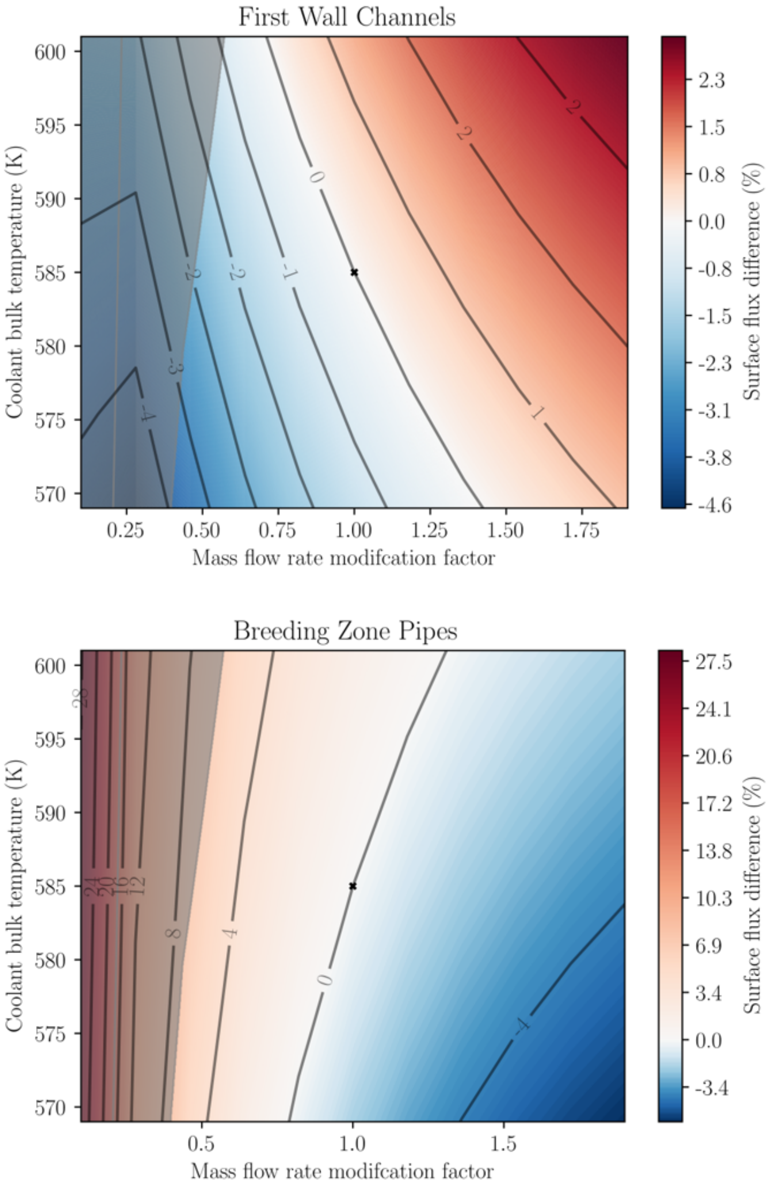

Figure 3.22: Relative tritium surface flux to the average case (white star) in the FW channels (left) and BZ pipes (right) as a result of varying the heat transfer coefficient as a function of bulk coolant temperature and mass flow rate. Values from the standard case are highlighted with a black star.

area of the BZ cooling pipes is much larger than that of the FW system (0.276 m to 0.112 m respectively). Furthermore, more heat is generated in the breeding zone around the BZ cooling pipes, thus changing the coefficient here, which impacts the overall system more. Yet, the higher difference compared to the standard case in the BZ system resulted in a total difference of 11 % in the surface flux of hydrogen.

In summary, a detailed parametric study explored the influence of heat transfer coefficient variations on tritium transport within the WCLL system. Critical parameters such as outlet water temperature and mass flow rates for the BZ pipes and FW cooling channels were derived based on previous thermodynamic analyses, ensuring a comprehensive evaluation. The study revealed that variations in the heat transfer coefficient, driven only by changes in bulk coolant temperature, had minimal impact on the overall temperature field and resulting tritium behaviour within the WCLL. However, variations in the mass flow rate significantly impacted the heat transfer coefficient, resulting in more measurable effects on maximum temperatures observed in the model and consequences on the surface flux of hydrogen into the cooling systems. These findings highlight the WCLL model's robustness to changes in thermal conditions, suggesting that the temperature field and tritium transport remain relatively stable despite significant variations in the heat transfer coefficient. However, the study also emphasised the need for further investigation into pressure drops and flow velocity reductions over extensive piping systems, which could influence thermal dynamics and tritium transport under realistic operational conditions.

3.4.2 Influence of tritium sources

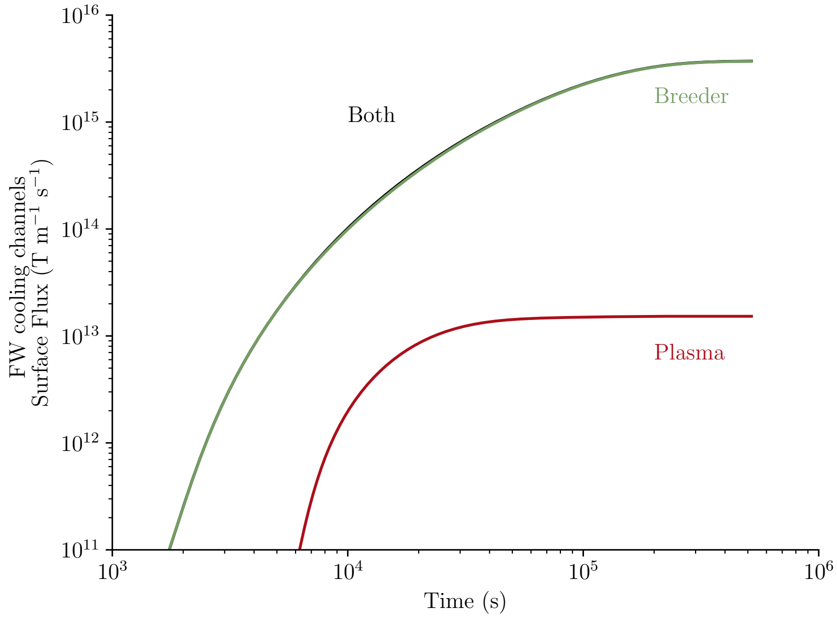

Figure 3.23: Surface flux at the first wall cooling channels divided into contributions from the plasma 🟥, from the breeder 🟩, and both together ⬛

The WCLL model incorporates two primary sources of tritium: the plasma and the breeder. However, the exact contribution of each source to the overall tritium inventory and the surface flux at the coolant interfaces is not explicitly defined. A series of tests were conducted to understand better how each source affects these parameters. These tests involved running 6-day transient simulations under three different conditions: one with only the breeder source term active, one with only the plasma source term (implantation flux) active, and one with both sources active simultaneously (as in the standard case). This parametric study aims to isolate and analyse the influence of each tritium source on the global tritium inventory and their respective permeation behaviour at the coolant interfaces. By doing so, the influence of these tritium sources' individual and combined effects within the WCLL system can be better understood, ultimately informing more effective management and mitigation strategies.

Figure 3.23 illustrates the contributions of tritium from different sources to the surface flux of hydrogen in the FW cooling channels. The breeder is the dominant contributor, providing more than three orders of magnitude higher tritium levels than the plasma source. This is why the breeder case completely overshadows the case concerning both sources in Figure 3.23. Despite the closer proximity to the plasma source, the PbLi breeder remains the most significant contributor to the tritium flux entering the first wall cooling channels. This is primarily because the tritium generation rate in the breeder is substantially higher than that of tritium fuel from plasma. These findings highlight the critical importance of considering the breeder source's effects when modelling the first wall, which is not always considered in the literature [29].

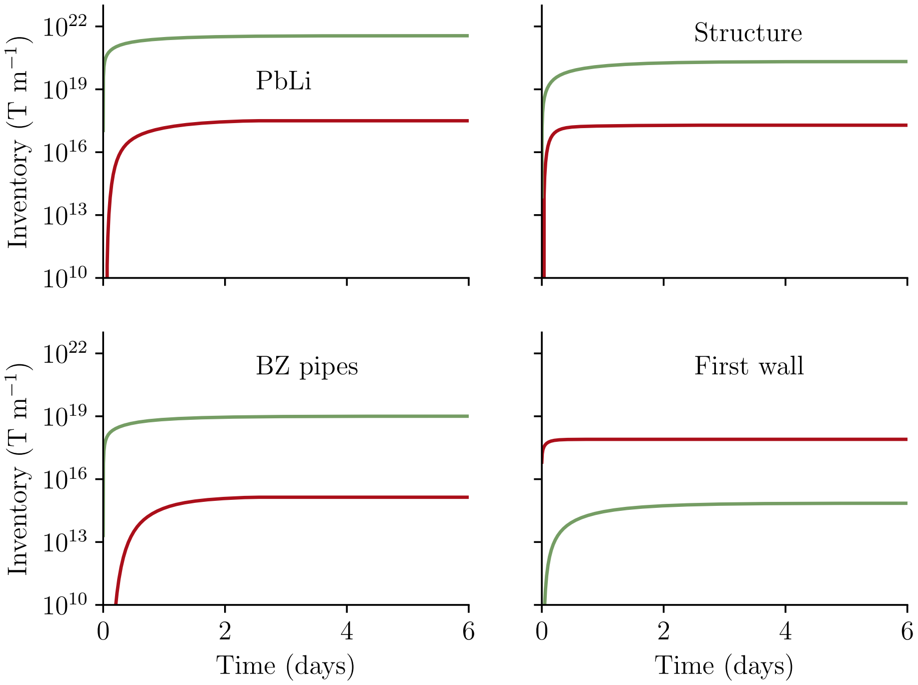

Figure 3.24: Temporal evolution of the tritium inventory in the PbLi, FW, BZ pipes and structure divided into contributions from the plasma 🟥 and the breeder 🟩

Figure 3.24 illustrates the tritium inventories within various components of the WCLL, including the structure, PbLi, and BZ pipes. The results show that the breeding source's tritium overwhelmingly dominates these inventories, except in the tungsten armour. Specifically, the breeder source accounts for 99.97 % of the total tritium inventory within the WCLL system. Even when excluding the PbLi and focusing solely on solid structural materials, Eurofer and tungsten, the plasma source contributes a mere 0.45 % to these inventories. The inventory within the first wall is predominantly influenced by the plasma source, suggesting that very little tritium from the breeder source diffuses past the FW cooling channels.

One significant factor not considered within the current model is the presence of deuterium in the plasma. DEMO will primarily use a DT plasma. However, this work has not considered deuterium implantation from the plasma. Yet, this study's results suggest that deuterium's influence on inventory dynamics is likely negligible. This is because the breeder material remains the dominant tritium source in the system. Nonetheless, deuterium may still play a more significant role in tritium transport behaviour within the tungsten first wall, where the plasma source contributes substantially to the inventory. These findings emphasise the critical need to model the influence of the breeder material in any comprehensive study of the WCLL.

3.4.3 Influence of PbLi solubility

The reliability of material properties significantly influences the quality of numerical results in tritium transport modelling. One critical property is the solubility of tritium in PbLi, denoted as K_S, which has been experimentally evaluated. However, there is considerable uncertainty in the solubility values obtained from different experiments (see Figure 3.25).

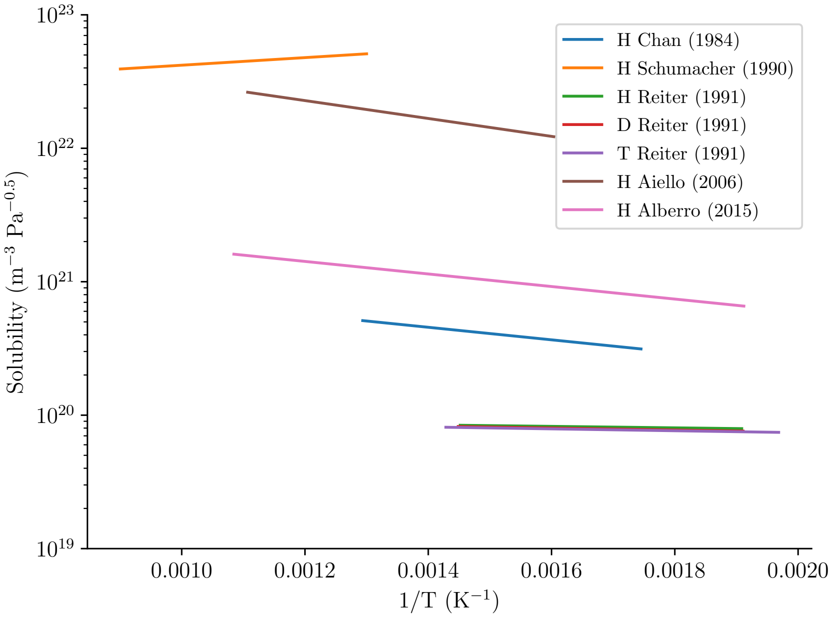

Figure 3.25: Solubilities for hydrogen isotopes H, D and T in PbLi [198, 199, 190, 125, 200]. Values obtained from HTM [201]

This range of solubility values is primarily due to variations in experimental methods and the use of different hydrogen isotopes across experiments. As a result, the solubility values can differ by up to two orders of magnitude at a given temperature. A parametric study was conducted to understand this uncertainty's impact on tritium transport dynamics within the WCLL. In this study, the solubility activation energy E_{Ks} was fixed at 0.13 eV, while the pre-exponential factor $K_{\mathrm{S},0}$ was varied within a range of 2.0×10^{21} to $4.0 \times 10^{23}\,\mathrm{m}^{-3}\,\mathrm{Pa}^{-0.5}$.

This range of parameters encompasses the full spectrum of experimentally measured tritium solubility in PbLi, allowing for an exploration of the solubility's influence on tritium transport while maintaining consistent temperature dependence. By examining these variations, the study aims to quantify the sensitivity of tritium transport dynamics to changes in solubility values. This analysis is crucial for improving the accuracy of predictive models and ensuring reliable tritium management strategies in the WCLL system. Understanding the extent to which solubility affects tritium behaviour can help refine experimental methods and enhance the precision of future measurements.

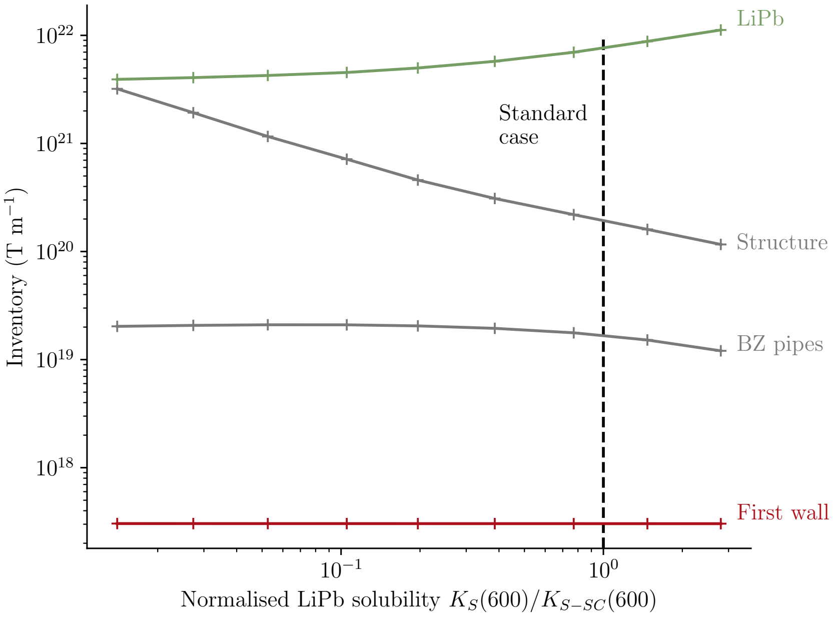

Figure 3.26: Evolution of the steady state tritium inventories as a function of hydrogen solubility, K_S, in PbLi normalised to the standard case solubility, $K_\mathrm{S-SC}$

The conservation of chemical potential dictates that the ratio $c_\mathrm{m}/K_\mathrm{S}$ must remain constant across interfaces. Consequently, altering hydrogen solubility in PbLi directly affects the concentration of mobile particles diffusing into the Eurofer structure. The solubility value used in this work's standard case, by Aiello [125], is among the highest reported in the literature. Utilising lower solubility values from other references would increase the concentration of mobile hydrogen in Eurofer. Over the range of solubility values studied, the tritium inventory in the structure increases by a factor of 25 (see Figure 3.26). In the breeding zone pipes, a factor of 1.5 difference is observed. Moreover, increasing the solubility of tritium in PbLi raises the hydrogen inventory in PbLi itself, as the ratio of mobile concentration, c_m, to solubility changes (see Figure 3.26). Regarding surface fluxes, the values vary significantly, ranging from approximately 2×10^{16} to $3 \times 10^{16}\,\mathrm{m^{-1}\,s^{-1}}$ for the breeding zone pipes and from 3×10^{15} to $1 \times 10^{16}\,\mathrm{m^{-1}\,s^{-1}}$ for the first wall cooling channels (see Figure 3.27). Since the solubility ratio between tungsten and Eurofer remains unchanged, the inventory in the first wall is unaffected and thus not included in the analysis.

However, tritium solubility in PbLi is just one factor that poses significant uncertainty in this

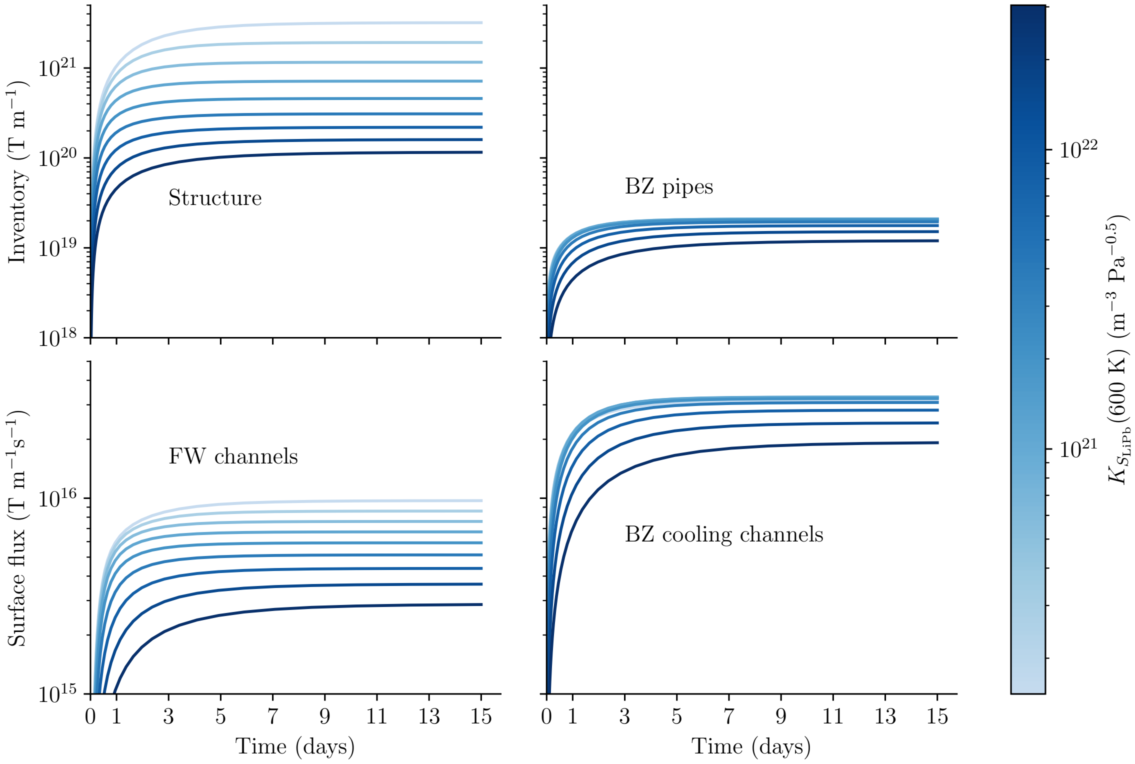

Figure 3.27: Influence of the solubility of hydrogen in PbLi on the temporal evolution of tritium inventory (top) and surface flux (bottom). The solubility at 600 K varies from 1.5×10^{20} to $3.0 \times 10^{22}\,\mathrm{m}^{-3}\,\mathrm{Pa}^{-0.5}$.

work. Many other transport parameters are uncertain, such as the recombination coefficient in tungsten [211]. Additionally, future geometric design updates will significantly impact tritium diffusion and inventories. For instance, a recent update in the WCLL design removed 60 % of the first wall cooling channels [87], affecting neutron moderation, nuclear heating, and tritium production. Furthermore, an optimisation study of the breeding zone cooling pipes introduced an additional pipe, increasing the surface area for tritium diffusion into the coolant. Despite the uncertainty associated with various factors within the model, which complicates the accurate estimation of tritium inventories, measures must be taken to mitigate tritium diffusion into structural materials. Potential methods to reduce inventories include minimising the amount of structural material and introducing neutron shielding. However, the most promising option is tritium permeation barriers [34].

3.4.4 Summary

A series of parametric studies have been undertaken to understand better the sensitivity of various parameters used in the WCLL model and their impact on tritium transport dynamics. The initial study examined the WCLL's thermal dynamics, focusing on how variations in the heat transfer coefficient influenced the system. Despite fluctuations in coolant temperature and mass flow rates leading to a maximum variance of approximately 15% in the heat transfer coefficient, the temperature field within the WCLL showed remarkable stability, demonstrating minimal sensitivity to these changes on subsequent tritium permeation (maximum of 3.7%). The second study assessed the impact of different tritium sources on the system's tritium inventory and surface flux. The breeder source contributed overwhelmingly more than the plasma source, accounting for 99.97 % of the total tritium inventory within the WCLL. Even when focusing solely on solid structural materials, the plasma source's contribution was minimal, only 0.45%. Furthermore, contributions to the tritium permeation into the FW cooling channels are shown to be entirely dominated by the breeder, attributing more than three orders of magnitude levels of permeation into these channels. This dominant role of the breeder highlights its critical importance in modelling and safety assessments for the WCLL. The final study investigated the impact of uncertainties in the solubility of tritium in PbLi. Variations in solubility values, ranging over two orders of magnitude to represent the range found within the literature, significantly affected tritium transport dynamics. Specifically, the structure's tritium inventory increased by 25x, and a factor of 1.5 difference was observed in the breeding zone pipes. Surface flux values varied from approximately 2×10^{16} to $3 \times 10^{16}\,\mathrm{m}^{-1}\,\mathrm{s}^{-1}$ for the breeding zone pipes and from 3×10^{15} to $1 \times 10^{16}\,\mathrm{m}^{-1}\,\mathrm{s}^{-1}$ for the first wall cooling channels. These results highlight the necessity of refining the measurement and modelling of tritium solubility in PbLi to enhance the model's fidelity and estimation of tritium behaviour.

CHAPTER 4

Influence of trapping

Contents

4.1 Damage-induced trap creation model 92
- 4.1.1 Model definition 92
- 4.1.2 Model parametrisation 93
- 4.1.3 1D parametric study 101

4.2 WCLL application 105
- 4.2.1 Influence of intrinsic traps 105
- 4.2.2 Influence of neutron damage 108

The role of tritium trapping mechanisms is examined, highlighting how accounting for trapping dynamics can significantly alter tritium transport behaviour. A new model is introduced that accounts for the temporal evolution of trap concentrations due to neutron damage and thermal annealing. This model is parameterised for tungsten, a key material in the WCLL, and its methodology is thoroughly detailed. Previous studies have utilised similar equations to model the generation of traps in self-damaged tungsten [212, 104]. However, they did not consider the potential annealing of these traps observed in experimental work [105, 213]. The model is then applied to a generic 1D case to explore potential influences on trap concentration and subsequent tritium inventories.

Following this, the influence of trapping within the WCLL is examined. The first study examines the influence of intrinsic traps inherent to the materials used in the WCLL breeding blanket. While considering these types of traps is standard practice in tritium transport modelling at more minor length scales, this study extends the approach to macroscopic cases, marking a novel contribution to the field. By incorporating intrinsic trapping effects at a larger scale, the study aims to provide a more comprehensive understanding of tritium behaviour in more realistic fusion reactor conditions. The influence of neutron damage is then estimated using the new neutron damage-induced trap creation model. The model is applied for the tungsten within the WCLL to provide an initial estimate of how neutron damage might impact tritium transport. Together, these studies enhance our understanding of tritium transport mechanisms in the WCLL breeding blanket and highlight the importance of considering both intrinsic and neutron-induced trapping effects in macroscopic modelling.

4.1 Damage-induced trap creation model

The study of neutron damage and its effects on hydrogen transport within materials is a critical area of research in nuclear fusion. As fusion reactors operate, materials within the reactor environment are subjected to high levels of neutron irradiation, which can significantly alter their structural and transport properties [214, 215]. This section focuses on modelling neutron damage-induced trapping of hydrogen, specifically within tungsten. The model is applied to a 1D model to analyse the potential influences of neutron damage in tungsten at various damage rates and temperatures.

4.1.1 Model definition

As described in section 1.3.2, the Eurofer and tungsten within the WCLL are likely to be severely damaged by the neutron flux originating from the plasma. This increases the number of defects in the materials and, therefore, trapping sites. When modelling hydrogen transport, the trap density, n_i (see Eq. (2.16)), does not typically evolve in time or vary spatially for a given material. However, this work explores the impact of this parameter varying due to irradiation damage and annealing effects.

$$\frac{\partial n_i}{\partial t} = \Phi \cdot K \left[1 - \frac{n_i}{n_{\mathrm{max},\Phi}}\right] - A \cdot n_i \tag{4.1}$$

Equation 4.1 outlines how the density of traps n_i is assumed to change over time. The term $\Phi \cdot K \left[1 - \frac{n_i}{n_{\mathrm{max},\Phi}}\right]$ represents the creation of traps up to a certain saturation level $n_{\mathrm{max},\Phi}$. This saturation aspect was considered due to the extensive experimental literature [102]. Here, $\Phi(x, y, z, t)$ indicates the rate of damage measured in $\mathrm{dpa\,s^{-1}}$, is a function of space and time. K represents the rate at which traps are formed, measured in $\mathrm{traps\,m^{-3}\,dpa^{-1}}$. The term A, representing the rate at which traps heal, is measured in $[\mathrm{s^{-1}}]$ and is assumed to follow an Arrhenius law, $A = A_0 \cdot \exp(-E_A/(k_B \cdot T))$.

Coupling with hydrogen transport

It is assumed when a trap is annihilated, atoms trapped in it are instantaneously released as mobile ones. For a population of traps with a density n_i, the concentration rate of trapped atoms released by annihilation can be expressed as $\dot{c}_{t,i}^{\mathrm{release}} = \theta_{t,i}\dot{n}_i$, where $\theta_{t,i}$ represents the trap occupancy (equal to $c_{t,i}/n_i$) and $\dot{n}_i = -An_i$ the annihilation rate. This release has to be accounted for in the chemical balance equations of both c_m and $c_{\mathrm{t},i}$:

$$\begin{cases} \frac{\partial c_\mathrm{m}}{\partial t} = \nabla \cdot (D \nabla c_\mathrm{m}) + S - \sum \frac{\partial c^r_{\mathrm{t},i}}{\partial t} + \sum \dot{c_{\mathrm{t},i}}^{\mathrm{release}} \\ \\ \frac{\partial c_{\mathrm{t},i}}{\partial t} = \frac{\partial c^r_{\mathrm{t},i}}{\partial t} - \dot{c_{\mathrm{t},i}}^{\mathrm{release}} \\ \\ \frac{\partial c^r_{\mathrm{t},i}}{\partial t} = \nu_{\mathrm{t,i}} \cdot c_\mathrm{m} \cdot (n_i - c_{\mathrm{t},i}) - \nu_{\mathrm{dt,i}} \cdot c_{\mathrm{t},i} \\ \\ \dot{c_{\mathrm{t},i}}^{release} = \theta_{t,i}\dot{n}_i = -Ac_{\mathrm{t},i} \end{cases} \tag{4.2}$$

Thus, to account for the instantaneous hydrogen de-trapping when a trap is annealed, Eq. (2.16) is defined as:

$$\frac{\partial c_{\mathrm{t},i}}{\partial t} = \nu_{\mathrm{t,i}} c_{\mathrm{m}} (n_i - c_{\mathrm{t},i}) - \nu_{\mathrm{dt,i}} c_{\mathrm{t},i} - A c_{\mathrm{t},i} \tag{4.3}$$

The model operates under the assumption that only unoccupied traps are initially formed. Additionally, it is assumed that filled and empty traps both anneal at the same rate, and hydrogen released from traps that have undergone annealing doesn't get instantly captured again. Instead, it adds to the freely moving hydrogen concentration, c_{m}. Additionally, the model presumes that the rate at which damage occurs does not affect the model's kinetics [216].

A method is proposed to determine the values of these parameters through experiments on self-damaged tungsten samples. By analysing TDS data, it is possible to deduce the parameters related to hydrogen trapping within a material and understand how these parameters are influenced by the extent of damage and the temperature at which annealing occurs.

4.1.2 Model parametrisation

In this study, self-damaged and optionally annealed tungsten samples have been subjected to TDS analysis to determine the properties of extrinsic traps formed due to neutron damage.

The parameterisation procedure for these properties is divided into two main parts: parameterisation of the annealing parameters and the trap creation parameters. The procedure focuses on parameters for tungsten, as the same data is unavailable for Eurofer. No new traps form during annealing, allowing for the evaluation of specific parameters like activation energy for trap annihilation and trap density evolution with annealing temperature. This helps understand tungsten's recovery behaviour and predict its long-term stability in fusion reactors. TDS analysis can also characterise new traps in samples with varying damage exposure levels. These parameters are then incorporated into a model predicting trap density and distribution under different irradiation conditions.

A schematic visualises this two-part parameterisation process (see figure 4.1). Self-damaged tungsten samples are initially annealed and analysed to obtain the annealing parameters. These parameters are then used as a baseline in further testing samples subjected to varying levels of self-damage. Combining the annealing and trap creation parameters, a comprehensive model is developed that accurately describes the trapping behaviour of hydrogen isotopes in damaged tungsten. The methodology can be adapted to investigate the effects of neutron damage on materials such as Eurofer and Inconel, contributing to developing more resilient materials for future fusion reactors.

Annealing parameter estimation

In a case in which samples are irradiated and then annealed, one can simplify Eq. (4.1) to model the latter stage, as no damaging takes place; thus, the damage rate Φ is equal to zero and Eq. (4.1) can be reduced to:

$$\frac{\partial n_i}{\partial t} = -A \cdot n_i \tag{4.4}$$

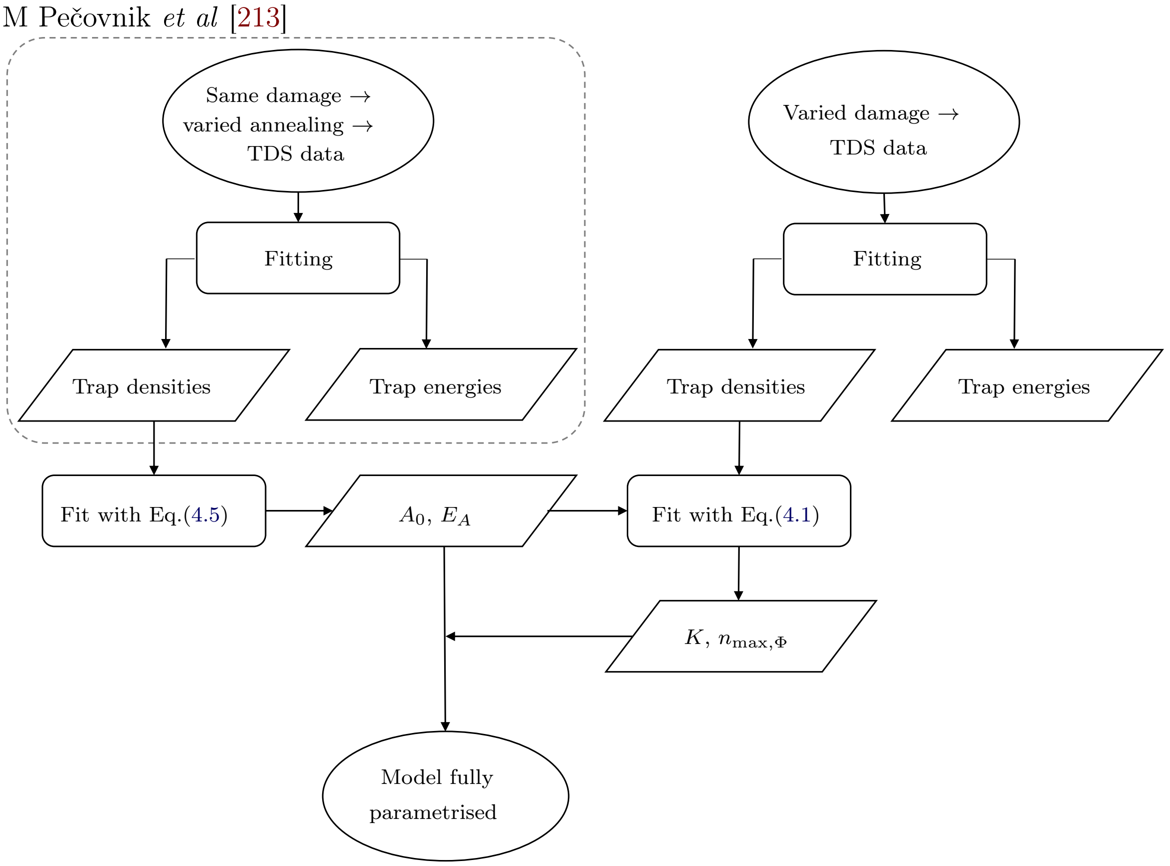
M Pečovnik et al [213]
Same damage → varied annealing → TDS data
Fitting
Trap densities
Trap energies
Varied damage → TDS data
Fitting
Trap densities
Trap energies
Fit with Eq.(4.5)
A_0, E_A
Fit with Eq.(4.1)
K, $n_{\max,\Phi}$
Model fully parametrised

Figure 4.1: Process diagram for evaluating variables in Eq.(4.1). Work completed by M Pečovnik *et al* [213] is highlighted in the dashed box.

Solving this equation analytically for a given temperature, T, the trap density is expressed as:

$$n_i = n_{i,0} \cdot \exp(-A \cdot \Delta t) \tag{4.5}$$

where $n_{i,0}$ is the initial trap concentration (no annealing) and Δt is the annealing time (2 h from the reference). From this, one can fit the results from Pečovnik *et al.* [213] with Eq. (4.5), allowing for the identification of the two unknown parameters (A_0 and E_A) from Eq. (4.1). These values can then identify the remaining unknown trap creation parameters. This is detailed in Section 4.1.2. The first factor evaluated from Eq. (4.1) was the trap annealing factor A. Three types of defects were identified in the work of Pečovnik *et al.* [213], and the trap densities evaluated for each defect type were used. Each trap's density variation with annealing temperature is fitted using Eq. (4.5) (see Figure 4.2). Each trap type was fitted to obtain values of A_0 and E_A, the values of which are outlined in Table 4.1.

Defect type III has been incorporated into the model based on the observation that it is resistant to annealing. This assumption is supported by findings in the experimental literature [217], which suggest that certain defects either cannot undergo annealing or require significantly higher temperatures.

It is important to note that the data for fitting the model was derived from tungsten samples

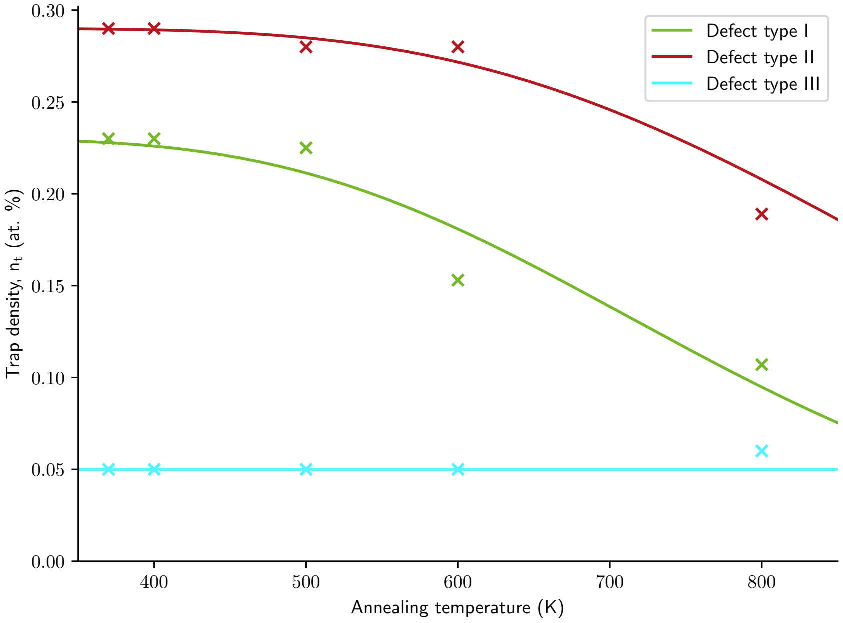

Figure 4.2: Trap densities evolution with annealing temperature fitted using Eq. (4.4). Experimental data points [104]

Table 4.1: Annealing parameter values for each defect type

Defect type	A_0 [s^{-1}]	E_A [eV]
I	6.18×10^{-3}	0.24
II	6.18×10^{-3}	0.30
III	0	-

pre-loaded with deuterium before irradiation. The impact of the presence of deuterium in a sample on defects in tungsten during irradiation is an ongoing area of research [104, 100, 207]. While other studies have explored the influence of annealing temperature on tungsten samples damaged without the presence of deuterium [105, 180], it has been undertaken with low energy atom exposure at high temperature (500 K) preventing defect I from being filled with D. Thus, annealing data for this defect is not available from these studies. In addition, it could be argued that including deuterium during the damaging process better represents components in an operational reactor. Consequently, the pre-loaded damaged samples are employed to analyse annealing parameters.

The values obtained from this parameter estimation procedure are then utilised in the subsequent section to assess trap creation parameters.

Trap creation parameter estimation

To evaluate the trap creation parameters, K and $n_{\mathrm{max},\Phi}$, a similar approach was used as in Section 4.1.2. T. Schwarz-Selinger conducted an experimental campaign in which samples of self-damaged tungsten underwent ion beam analysis and TDS to evaluate how damage affects deuterium retention [102]. In the study, recrystallised Polycrystalline tungsten (PCW) samples (2000K Plansee 99.97 at.%, 10-50 µm grain size), of size 12x15mm and 0 8mm thick, were exposed to 20 MeV W^{6+} ions at 800 K for varying exposure times. Following this, the samples were exposed to a 15 eV/D atom beam with a flux of $6 \times 10^{19}\,\mathrm{D\,m^{-2}\,s^{-1}}$ for a total fluence of $10^{25}\,\mathrm{D\,m^{-2}}$ at a temperature of 370 K. The samples were analysed using TDS with a heating ramp of $0.05\,\mathrm{K\,s^{-1}}$. For the damaging parameters, TDS data from seven damaged tungsten samples (0.001 - 2.5 dpa) were analysed to provide damage-induced trap properties. The TDS data for each sample was fitted to provide the de-trapping energies and densities for traps induced by damage. The fitting was undertaken with the constraint that each TDS spectrum has the same number of traps with the same de-trapping energies. From this, the trap density variance with damage for each induced trap can be evaluated. The results of the TDS data fittings can identify the remaining unknown parameters (K and $n_{\mathrm{max},\Phi}$) from Eq. (4.1). From this, the model is characterised for each damaged-induced trap and can be modelled using FESTIM to investigate the influence of damaged-induced traps on tritium transport in tungsten. Section 4.1.2 outlines the experimental data and parameter fitting details. A diagram is shown in Figure 4.1, which visually outlines the parameter evaluation process. Modelling the experimental set-up using SRIM identified the damage profile produced by the ions and peak levels of damage at 0.001, 0.005, 0.023, 0.1, 0.23, 0.5 and 2.5 dpa, excluding one that was not damaged [204]. The damage occurred within the sample's first 2 µm to 3 µm; thus, damage-induced trap creation would only happen in the same area. To account for this, the induced traps were modelled using a Fermi-Dirac-like density distribution (see Figure 4.3), which can adequately reproduce experimental depth profiles [180, 218]. The deuterium depth profiles measured with ^{3}He nuclear reaction analysis can be well described with a Fermi-Dirac-like distribution.

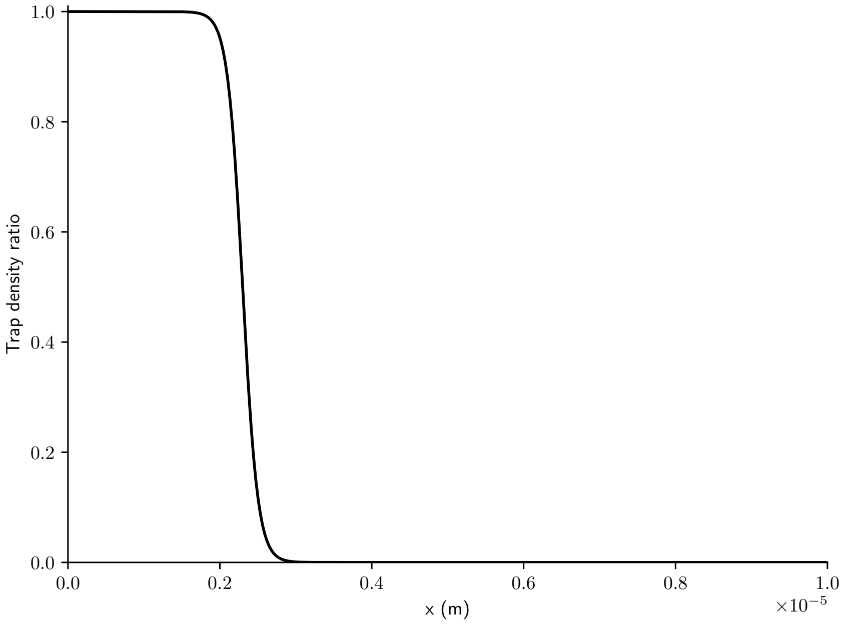

Figure 4.3: Trapping site density Fermi-Dirac-like distribution described by Eq. (4.6)

$$f(x) = \frac{1}{1 + \exp\left(\frac{x - x_0}{\Delta x_0}\right)} \tag{4.6}$$

where $x_0 = 2.3\,\mu\text{m}$ and $\Delta x_0 = 0.1\,\mu\text{m}$.

The pre-exponential factor of the diffusion coefficient of deuterium in tungsten was $D_0 = 1.6 \times 10^{-7}\,\text{m}^2\,\text{s}^{-1}$ and its activation energy $E_D = 0.28\,\text{eV}$ [136]. The procedure consists of three phases: implantation, resting, and desorption. For all phases, $c_\text{m} = 0$ is applied to both boundaries of the 1D model, equivalent to instantaneous recombination. For the implantation phase, the source term in Eq. (2.31) is $S = \Gamma \cdot f(x)$, where Γ is the implanted ion flux, in units $\text{m}^{-2}\,\text{s}^{-1}$ and $f(x)$ is a Gaussian distribution with R_p as its mean value and σ its width, both in units m, the values of which have been determined using SRIM [204] and are outlined in table 4.2. This phase lasts t_imp, in units s, and has a uniform temperature of T_imp, in units K. The second phase is the resting period in which no implantation is occurring and has a uniform temperature of T_rest for t_rest, in units K and s respectively. The final phase models the desorption due to a linear uniform temperature increase with a given ramp β, in units Ks^{-1}. Table 4.2 gives the TDS simulations' parameters. The TDS fitting procedure is the same as used by Delaporte-Mathurin *et al* [219].

Table 4.2: TDS simulation parameters

Property	Value	Unit
T_imp	370	K
T_rest	295	K
Γ	10^{20}	$\text{m}^{-2}\,\text{s}^{-1}$
R_p	0.7	nm
σ	0.5	nm
t_imp	72	h
t_rest	12	h
β	0.05	$\text{K}\,\text{s}^{-1}$

Initially, the data from the un-damaged sample was analysed. This was to identify any intrinsic traps, which can then be used to model the damaged samples. A single trap fits the TDS with an associated de-trapping energy of 1.00 eV (see Table 4.3).

Table 4.3: Fitted intrinsic trap properties

Property	Value	Unit
E_t	0.28	eV
$\nu_{\text{t},0}$	5.22×10^{-17}	$\text{m}^3\,\text{s}{-1}$
E_dt	1.00	eV
$\nu_{\text{dt},0}$	1.0×10^{13}	s^{-1}
n_i	2.0×10^{22}	m^{-3}

The TDS spectra from the damaged samples were then fitted considering the intrinsic trap previously identified in the whole sample and any further extrinsic traps with the distribution described by Eq. (4.6) (see Figure 4.4). A highlight of the 0.1 dpa case is shown in Figure 4.5, displaying the contribution of each trap (shown in a dashed line), respectively.

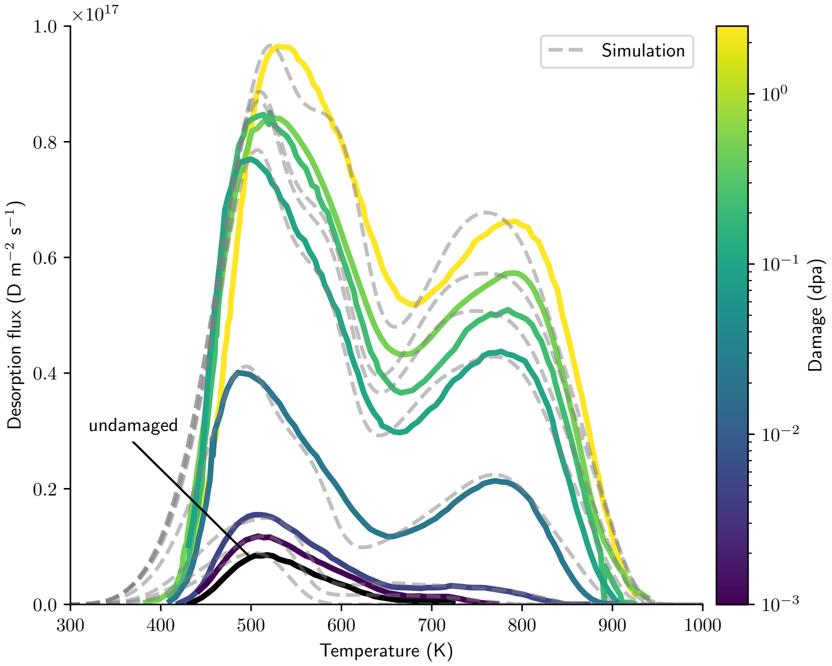

Figure 4.4: Results of TDS analysis from tungsten samples damaged to various levels (0.001 - 2.5 dpa at 800 K and decorated with D at 370 K

Five extrinsic traps were used to fit the TDS data with de-trapping energies of 1.15, 1.35, 1.65, 1.85 and 2.05 eV, and are hereafter referred to as D1, D2, D3, D4 and D5, respectively. Detailed versions of the fitting figures for each dpa case are presented in appendix D.

Resulting trap interpretation

Research on atomistic scale modelling can shed light on specific defect types that could be linked to traps D1-5. Simulations of collision cascades in tungsten reveal that self-interstitial atom (SIA) clusters are the primary defects caused by irradiation, alongside the formation of monovacancies, dislocation loops, and voids [97]. However, DFT calculations indicate that the de-trapping energy of deuterium with SIA clusters is usually below $E_{\mathrm{dt}} = 0.95\,\mathrm{eV}$ [58]. Therefore, since deuterium was implanted at 370 K, these defects are ineffective at retaining the deuterium, as shown by the TDS data. De-trapping energies of deuterium from monovacancies range between 1.0 and 1.4 eV [59, 61], which aligns with traps D1 and D2, characterised by desorption around 500–600 K in Figure 4.5. Monovacancies were also identified as defect type I in [213]. Similarly, de-trapping energies of deuterium from vacancy clusters (up to size 20) are between 1.6 and 1.9 eV [57], corresponding to traps D3 and D4, characterised by desorption around 750-850 K in Figure 4.5. Vacancy clusters were identified as defect type II in [213]. Additionally, DFT calculations suggest that the energy barrier

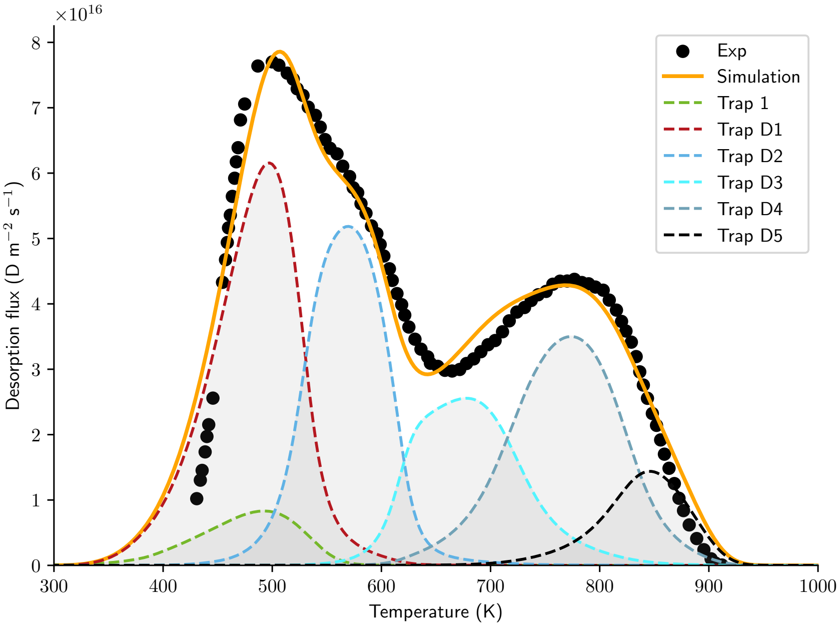

Figure 4.5: TDS data for tungsten sample damaged to 0.1 dpa, fitted using one intrinsic trap and five extrinsic traps

from the surface to bulk, simulating large vacancy clusters, is around 2.0 eV [69, 61, 220], which matches trap D5. Large vacancy clusters were identified as defect type III in [213]. The identified traps are also consistent with previous rate equation simulations on similar systems [213, 184, 63, 97, 221, 222].

By referencing atomistic modelling studies, one can make educated guesses about the characteristics of a trap. However, the energy required to release a trapped particle does not always indicate the trap's size. Large vacancies in a lattice can hold multiple hydrogen atoms. According to atomistic modelling, when multiple atoms are trapped in the same defect, their release dynamics can cause variations, leading to distinct peaks in TDS results associated with different traps [57].

From this analysis, the densities for each trap, in each damage case, are fitted using Eq. (4.1) using each trap's respective annealing parameters depending on its assigned type. The results from the parametrised model for the five traps identified D1-5 are outlined in Table 4.4, and the fitting displayed in Figure 4.6.

Beyond 1300 K, recrystallisation effects become more significant in tungsten, altering the microstructural defect landscape [223, 224]. The increased mobility of vacancy clusters at such high temperatures can result in larger clusters [225, 226]. More experimental data is needed to ensure the model's accuracy beyond 1300 K. Another issue with the presented methodology, similar to other inverse problem-solving methods, is that multiple parameter sets can fit the same TDS data, indicating various solutions to the same optimisation problem [151]. Additionally, the data was collected from self-damaging experiments ($W6^+$ ions), not 14 MeV neutron damage. 14 MeV neutrons will likely have a much longer mean-free

Table 4.4: Results of the model parametrisation for the damage-induced traps

Trap	E_{dt} [eV]	K [traps m^{-3} dpa^{-1}]	$n_{\mathrm{max},\Phi}$ [m^{-3}]	A_0 [s^{-1}]	E_A [eV]
D1	1.15	9.0×10^{26}	6.9×10^{25}	6.2×10^{-3}	0.24
D2	1.35	4.2×10^{26}	7.0×10^{25}	6.2×10^{-3}	0.24
D3	1.65	2.5×10^{26}	6.0×10^{25}	6.2×10^{-3}	0.30
D4	1.85	5.0×10^{26}	4.7×10^{25}	6.2×10^{-3}	0.30
D5	2.05	1.0×10^{26}	2.0×10^{25}	0	-

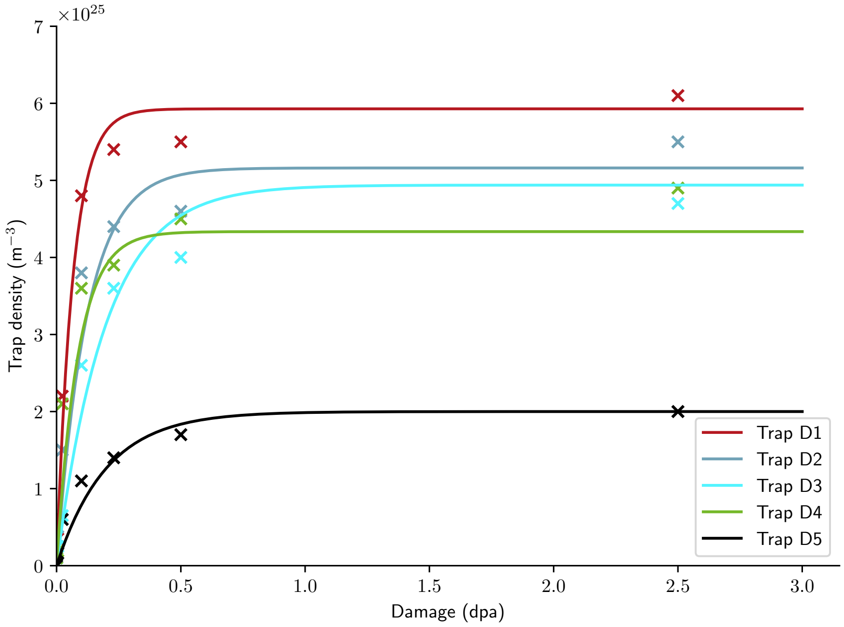

Figure 4.6: Trap concentrations with increasing damage dose from the fitted TDS, then fitted using the current model.

path in the tungsten armour in a fusion reactor compared to the self-damaging ions. This will likely mean that neutron damage will create a more uniform damage profile across the tungsten armour sample than self-damage, and the defects from self-damaging ions likely differ from those caused by 14 MeV neutrons. Thus, TDS analysis might yield different results, altering the parameters for this model. TDS spectra obtained from tungsten damaged with fission-generated neutrons show similar high-temperature peaks to those for self-damaged tungsten. TMAP analyses of these neutron-damaged tungsten samples reveal similar detrapping energies [222]. Hence, the identified defects in self-damaged tungsten are relevant to neutron-damaged tungsten, with differences mainly in the distribution of trap concentration.

Nevertheless, the evaluated trap properties are taken forward to model the influence of damage-induced traps on tritium retention levels in tungsten within tokamak-like environmental conditions.

4.1.3 1D parametric study

To investigate the potential significance of the damage-induced trap densities evaluated in Section 4.1.2, Eq. (4.1) was solved numerically to assess how the total trap density varies with damage rate. A scenario is considered in which 2 mm of tungsten is damaged homogeneously (emulating a likely neutron damage profile in the first wall of a fusion reactor) [106]. It should be noted that the model was parameterised using heavy-ion irradiation data, which affects only the first few micrometres of a sample; it is assumed that similar damage characteristics apply throughout the sample when it is subjected to neutron damage. Primarily, two cases are considered with constant temperatures of 295 K and 800 K, varying the damage rate, Φ, from 10^{-3} to 10^{3} dpa/FPY and ran over a FPY (see figure 4.7).

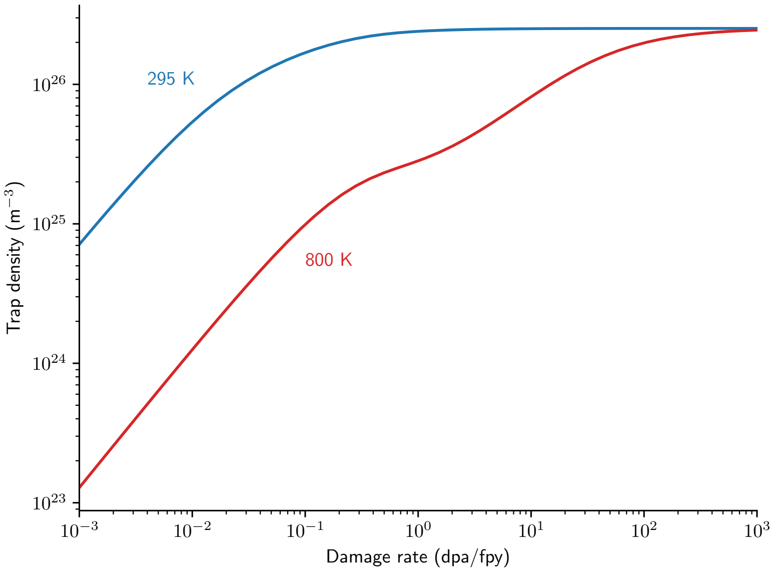

Figure 4.7: Total trap densities at 295 K and 800 K with variation in the damage rate after one FPY.

Including the annealing term A in Eq. (4.1) affects the dynamics of trap creation. Although, as the rate of damage increases, the ratio of $\Phi \cdot K$ to A increases significantly, trap creation becomes independent of annealing (see Figure 4.7). Additionally, when the ratio of $\Phi \cdot K$ to $n_{\max,\Phi}$ exceeds A, the characteristic time is approximately $\frac{n_{\max,\Phi}}{\Phi \cdot K}$. Given that K is large, the characteristic time becomes shorter, which explains why the curves overlap at high damage rates. Notably, in the case of DEMO, where the highest level of damage is anticipated to be 5 dpa/FPY [20], the temperature continues to exert an influence. However, it is crucial to highlight that temperature applies its most substantial and noteworthy effect at the lower levels of damage. For damage rates anticipated in DEMO, the disparity in trap density is approximately a factor of four, contingent upon temperature variations. In particular, at the lowest levels of damage, specifically at 10^{-3} dpa/FPY, the contrast becomes markedly pronounced, escalating to a substantial factor of 50. This exponential increase in the difference underscores the heightened sensitivity of trap density to temperature at lower damage levels, revealing a nuanced relationship that merits careful consideration in analysing materials under irradiation.

Simulations of a 2 mm W slab at a constant temperature of 700 K show the impact of damage-induced traps on tritium retention over time and migration after 24 h (see Figure 4.8). The implantation flux used was $10^{20}\,\mathrm{m^{-2}\,s^{-1}}$ with an assumed implantation depth of 9 mm. The diffusion coefficient of hydrogen [136] has been scaled by a factor $1/\sqrt{3}$ to emulate tritium [227].

The results of the transient simulations are shown in Figure 4.8. The upper figure illustrates how the tritium inventories vary for different levels of damage in the tungsten model. The undamaged case is shown to reach a point of saturation after 10^3 s. Notably, after 24 h, tungsten damaged at a rate of 10^2 dpa/FPY has an inventory four orders of magnitude higher compared to the undamaged case, and after a full power year, this escalation intensifies further to five orders of magnitude after 1 FPY. In cases with a lower damage rate, tritium can migrate from the plasma source on the left side through the entire domain. Despite significantly higher inventories in cases with substantial damage rates, tritium migration is mitigated; this inventory is confined within the initial 0.1 mm of tungsten in scenarios with the most significant damage rate at 10^2 dpa/FPY (see Figure 4.8). Furthermore, it can be seen that even in the lowest damage rate, the tritium inventory is yet to reach a point of saturation after 1 FPY. Moreover, the level of tritium retention in the lowest rate of damage (10^{-5} dpa/FPY) is shown to follow the same behaviour as the undamaged case, up till beyond 10^5 s, at which point the tritium has migrated through the whole sample. Still, the traps continue to be formed; thus, the retention across the whole sample increases. This shows the competition between two regimes at play: trap creation and tritium migration. The tritium migration regime (at a high dpa rate) occurs when the trap concentration saturates quickly, and the tritium inventory is limited by tritium migration from the surface to the bulk (left to right on Figure 4.8). The trap creation regime (low dpa rate) occurs when the tritium quickly migrates through the W slab, and the tritium inventory is limited by the trap creation build-up (the tritium concentration goes from bottom to top in Figure 4.8). Tritium migration has been studied extensively, and work in the literature shows how the migration depth can be predicted depending on the trap properties considered [228]. However, this model does not account for a temporally evolving trap density term. The relation between trap creation and tritium migration has been explored in similar work in the literature, in which the same behaviour is observed [213].

Expanding the scope of the analysis to include variations in both sample temperature and damage rate reveals the impact of damage-induced traps on tritium retention levels after one FPY depends on both factors (see upper Figure 4.9). In the undamaged case, a near-standard Arrhenius law is observed with the tritium retention after one FPY with temperature variation. Two distinct behaviours are observed in tritium retention levels. Below 900 K, the retention levels are shown to be temperature independent, as the tritium implanted gets trapped in the damage-induced defects. However, the tritium has enough energy to escape the traps beyond this temperature. With higher temperatures, more tritium can be de-trapped, reducing the inventory and levels approach the standard undamaged case. The damage rate

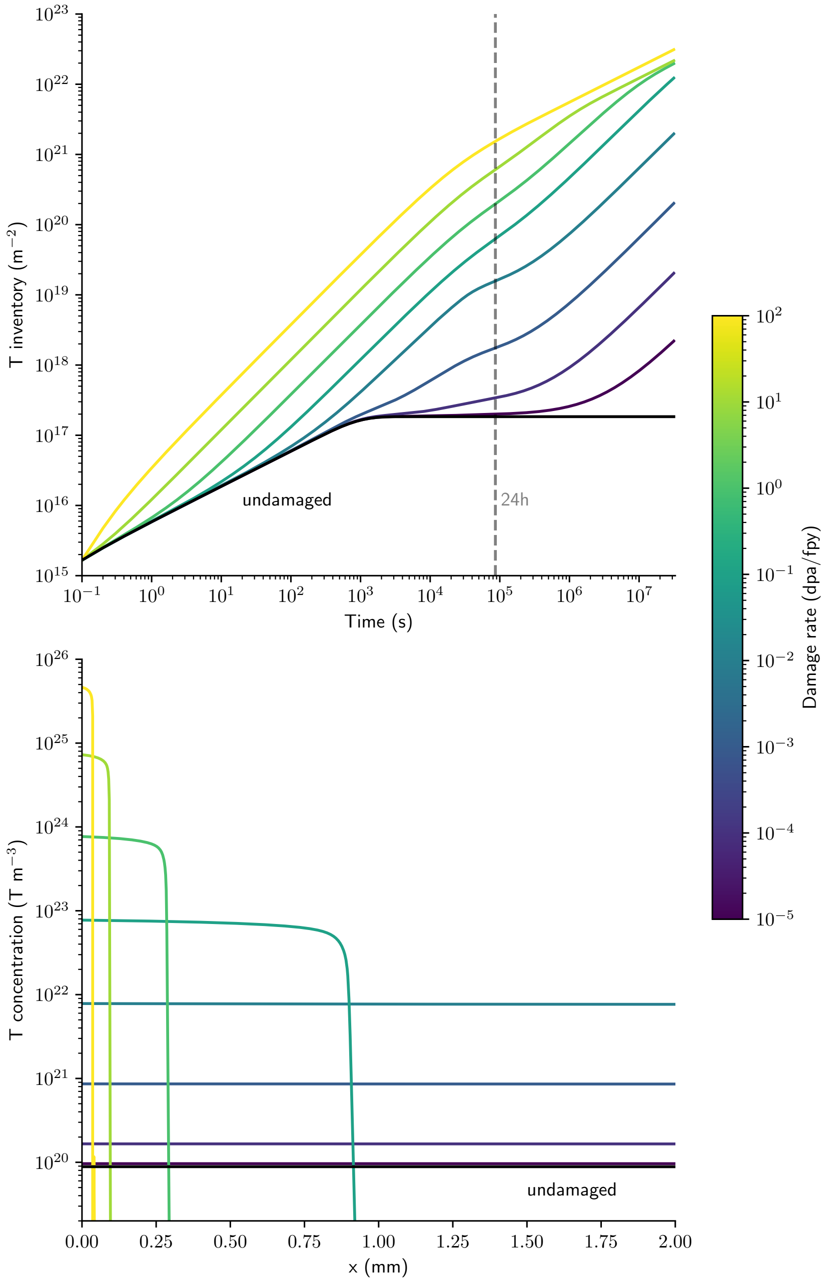

Figure 4.8: Tritium inventory over 1 FPY (top) and the retention distribution after 24 h (bottom) from simultaneous damage exposure and tritium implantation, at 700 K varying the damage rate.

exacerbates the retention level, although following the same two behaviours in each case. Although the highest magnitude of tritium retention occurs at the lowest temperatures, the highest value relative to the undamaged case occurs around 850 K. Around this value, the temperature is high enough to de-trap any tritium within the intrinsic trap of the sample but not high enough to remove any tritium from the damage-induced traps (see lower Figure

4.9). This result could be of particular concern for fusion devices, as this temperature range is within the operational limitations of tungsten.

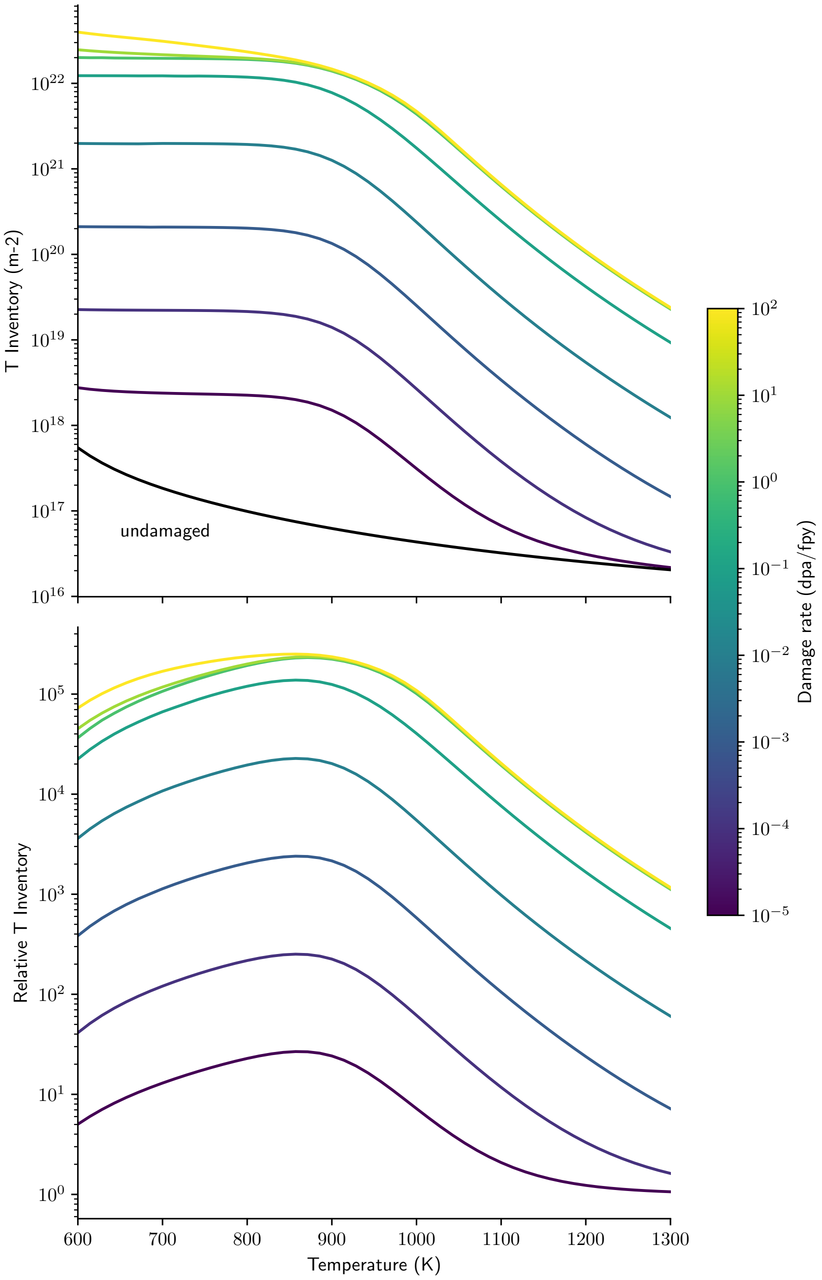

Figure 4.9: Tritium retention in tungsten in varying damaged cases, relative to an undamaged case, after 1 FPY varying temperature.

4.2 WCLL application

A significant differentiator of this work compared to the current published literature is incorporating trapping mechanisms into the WCLL model. Existing models often overlook these traps' complexities, leading to potential inaccuracies in predicting hydrogen behaviour [130]. By accounting for intrinsic and damage-induced trapping mechanisms, this research enhances the fidelity of hydrogen transport predictions within the WCLL. This section begins by examining the influence of intrinsic traps within the WCLL model. Intrinsic traps, inherent to the material's microstructure, play a crucial role in capturing and retaining hydrogen. This work evaluates the impact of these traps on hydrogen transport and demonstrates how their inclusion modifies the transport characteristics within the WCLL. Subsequently, the focus shifts to applying the novel model of damage-induced trap creation, explicitly applied to the tungsten armour of the WCLL. Neutron irradiation in fusion environments can create additional traps within the tungsten, significantly affecting tritium transport. This work estimates the influence of neutron damage in tungsten, how tritium transport is altered, and characterises the resulting local inventories.

4.2.1 Influence of intrinsic traps

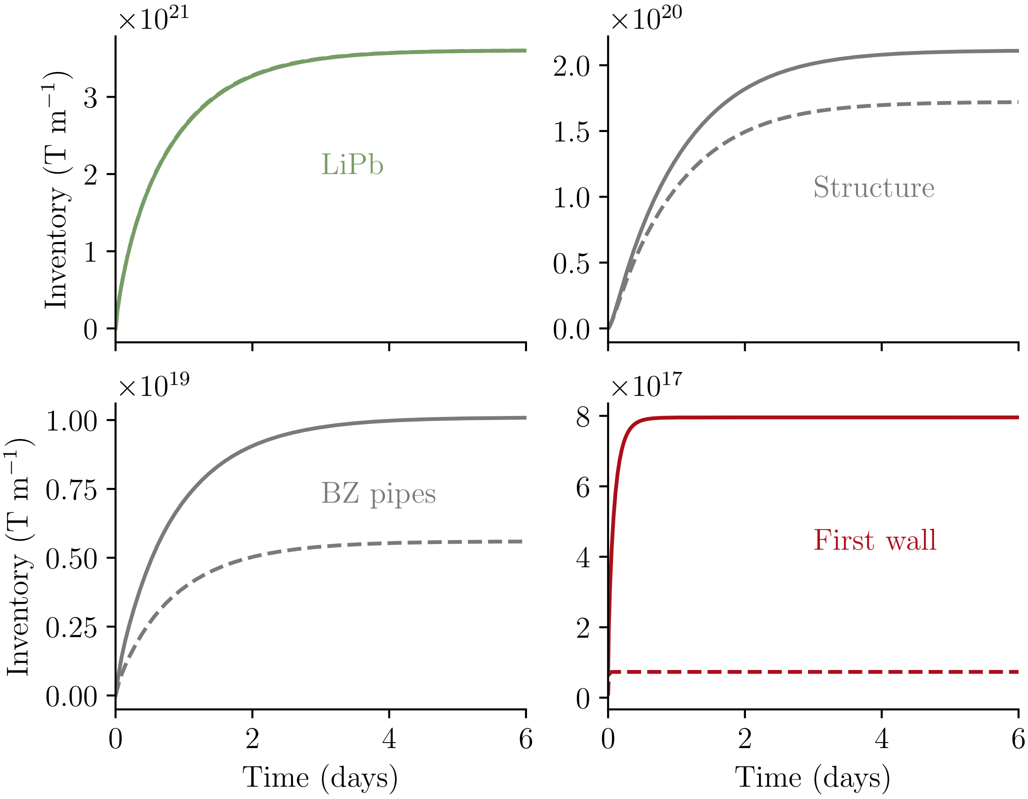

Figure 4.10: Temporal evolution of the tritium inventory in the PbLi, FW, BZ pipes and structure. Dashed lines correspond to a case without traps.

Intrinsic trapping effects significantly increase retention within Eurofer (see Figure 4.10). Specifically, the tritium inventory in the BZ pipes saw an 80% increase, while the structural inventory experienced a 20% rise. The most pronounced effect was observed in the FW, where tritium inventories increased by an order of magnitude (a factor 10.9). This highlights the substantial impact of the higher de-trapping energy and constant density of the traps considered within the tungsten (see Table 3.7). However, the vast majority of tritium within the WCLL system is contained within the PbLi breeder and incorporating trapping mechanisms only increased the total steady-state inventory by 1.3%. Although, considering the solid domains, accounting for trapping led to an average inventory increase of 25.1%. These findings highlight the role of trapping effects in influencing tritium distribution and storage within the WCLL.

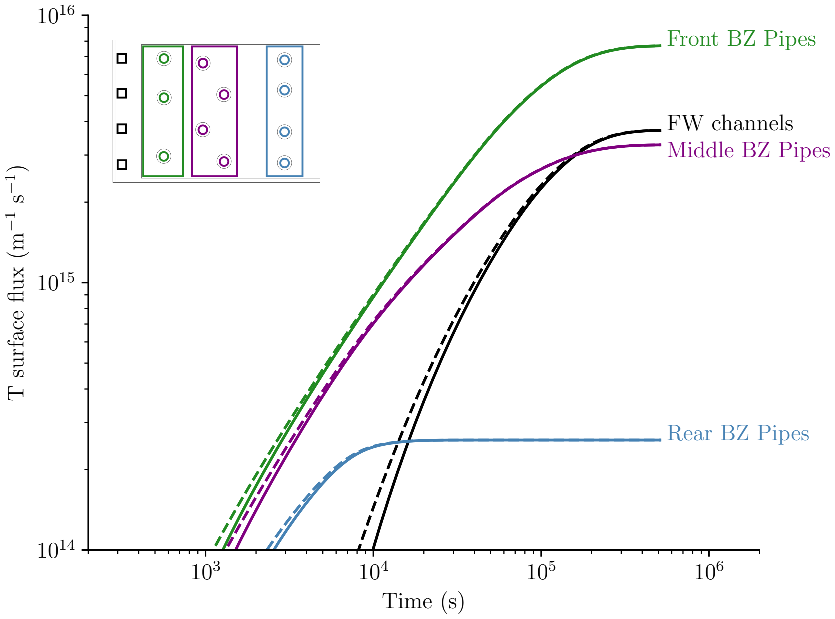

Figure 4.11: Temporal evolution of the tritium fluxes at the cooling surfaces for the first wall cooling channels and breeding zone pipes at the front, middle and rear position relative to the plasma facing surface. Dashed lines correspond to the standard case without trapping effects

Regarding the surface flux of tritium at coolant interfaces, the delay in permeation due to trapping is observed in Figure 4.11. This delay in the transient phase is primarily due to the trapping mechanisms within the structural materials, which temporarily impede the movement of tritium. Trapping causes tritium to be temporarily immobilised, delaying its migration towards the cooling channels. However, this delay is minimal compared to the case without trapping and does not influence the steady-state surface flux.

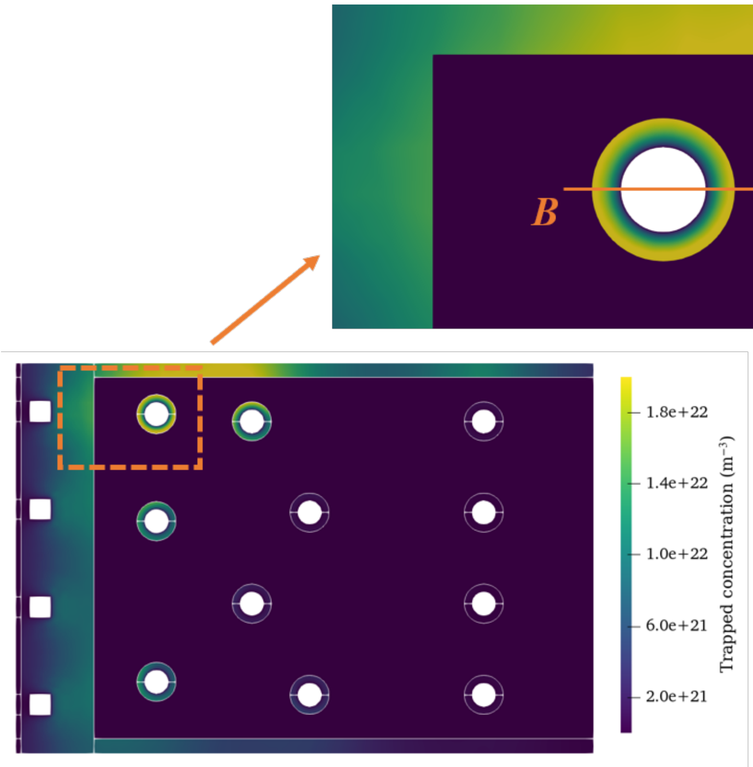

(a) Concentration field of trapped T in Eurofer at steady state and identification of profile B's location

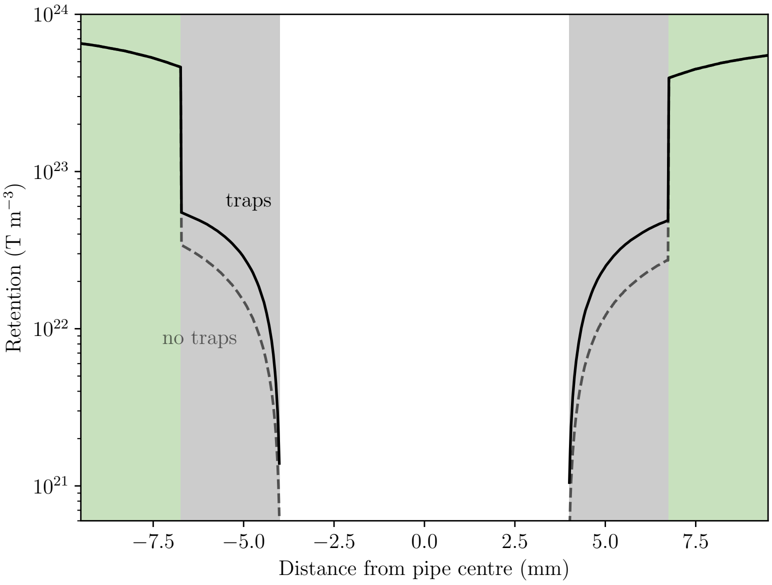

(b) Tritium concentration profile B in Eurofer ■ and PbLi 🟩

Figure 4.12: Tritium repartition in Eurofer structure and BZ pipe

Analysing the trapped concentration field and the retention profile across a BZ pipe reveals several key insights. The trapped population of tritium is most prevalent in the BZ pipe and the structure surrounding the top left of the breeding zone, where mobile concentrations are highest (see Figure 3.13). Due to the nature of the McNabb and Foster-like transport model, with an increase in mobile population, c_{m}, the local trapped population, c_{t}, increases for the same conditions in time. The temperature dependence of trapping is evident in the structure closest to the FW cooling channels. Trapped concentrations build up along the channels in these regions as these areas cool, meaning tritium does not de-trap as quickly (see Figure 3.10). Furthermore, the highest advection of tritium occurs at the rear of the breeding zone, where velocity is highest (see Figure 3.11). This results in lower mobile concentrations and, consequently, much lower trapping levels in this region. Observing the profile of tritium retention across the top left BZ pipe, the interface condition of conservation of chemical potential is evident (see Figure 4.12b). Additionally, accounting for trapping mechanisms in Eurofer nearly doubles the total retention in this region, highlighting the significant impact of trapping on overall tritium retention.

This finding underscores the importance of considering transient and steady-state behaviours in tritium transport models. While trapping can complicate the initial phases of tritium migration, its impact diminishes over time as the system stabilises. Therefore, engineering designs and safety assessments must account for these dynamics to ensure accurate predictions of tritium behaviour under operational conditions.

4.2.2 Influence of neutron damage

This section explores the modelling of damage-induced traps within the WCLL, focusing primarily on the tungsten FW. The trap creation model introduced in this work has been explicitly parameterised for tungsten (see section 4.1.2), as most data on hydrogen isotope retention in damaged materials pertains to tungsten. The parameterised model has been applied to the tungsten FW in the WCLL model to provide an initial approximation of how neutron damage may influence tritium transport dynamics in the FW. The same two intrinsic traps in the tungsten from the standard case are assumed (see Table 3.7), along with the five damage-induced traps identified in the trap creation parameterisation section (see Table 4.4).

To assess the impact of neutron damage, a 6-day transient simulation was conducted, mirroring the standard case but including damage-induced traps. The damage rate was assumed to be 5 dpa/fpy. While this value is representative, it is subject to variation, as different studies on the EU-DEMO project report varying levels of neutron damage distributions in the FW [129, 106, 81]. Furthermore, the damage levels will likely vary poloidally across the reactor [129]. It is assumed that neutron damage occurs homogeneously across the FW.

The results of this simulation provide insights into the effects of neutron-induced damage on tritium retention and transport within the WCLL. Incorporating damage-induced traps into the model enhances its fidelity and understanding of the complexities of tritium behaviour in a fusion reactor environment.

The variation in trap concentrations over time is depicted in Figure 4.13. The results indicate that the concentrations of traps D1-D4 increase rapidly during the initial phase of the transient model. These traps appear to reach a point of equilibrium around 2×10^5 s (approximately 2.31 days). However, trap D5, unaffected by annealing processes, continues

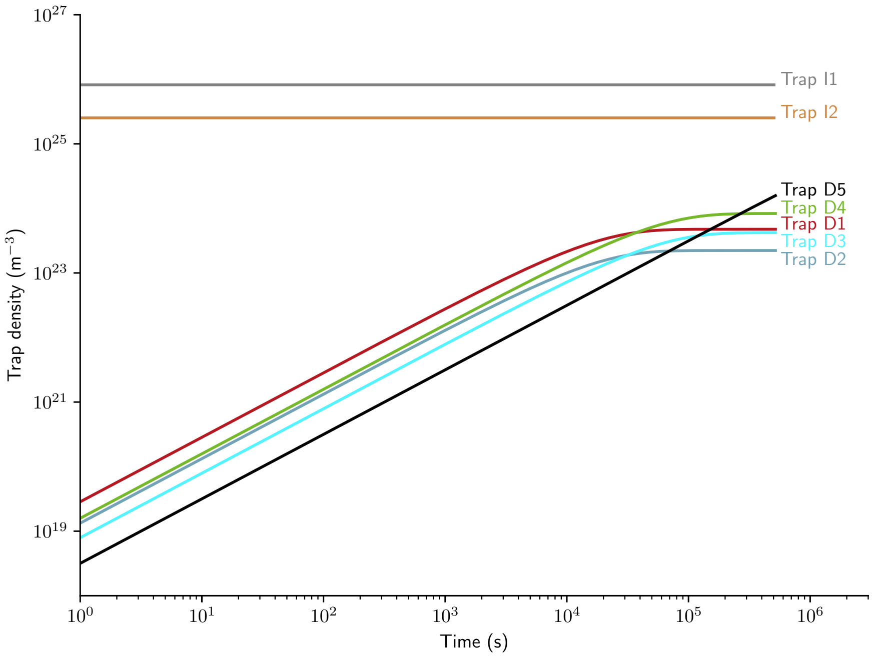

Figure 4.13: Temporal evolution of trap concentration of damaged induced traps D1-D5 as a result of a damage at 5 dpa/fpy, using an average temperature of 684 K, compared to intrinsic traps concentrations

to increase beyond this point, showing no sign of stopping and tending towards D5's $n_{\mathrm{max},\Phi}$ value. Although the concentrations of D1-D4 fall short of reaching equivalent density levels of the intrinsic traps, they still play a significant role in hydrogen trapping due to their high de-trapping energies, which range from 1.15 to 1.85 eV. This ongoing increase in trap D5 concentration underscores its potential impact on tritium retention and transport within the tungsten FW, highlighting the importance of considering these dynamics in the overall modelling of tritium behaviour in the WCLL system.

Figure 4.14 illustrates the evolution of the tritium inventory within the FW and compares the damaged and standard cases. The effect of neutron damage-induced traps on the tritium inventory within the FW is evident almost immediately. Due to these damage-induced traps, the tritium inventory doubles within the first few minutes of exposure. This increase becomes more pronounced over time, with a 50-fold rise observed after 2 h of exposure and an astounding 700-fold increase after 6 days. The inventory continues to grow with the trap concentration, highlighting the severe impact of damage-induced traps on fuel retention within the first wall.

However, this figure lacks critical insights into the dynamics of tritium transport within the FW under the influence of neutron damage. The high number of high-energy traps significantly mitigates tritium diffusion from the plasma. After 2 hours of exposure, despite the tritium inventory being 50 times higher, it is primarily contained within the first 0.3 mm of the tungsten armour (see Figure 4.15). In contrast, tritium permeates the standard case within this time frame through the FW. Furthermore, Figure 4.15 shows that tritium

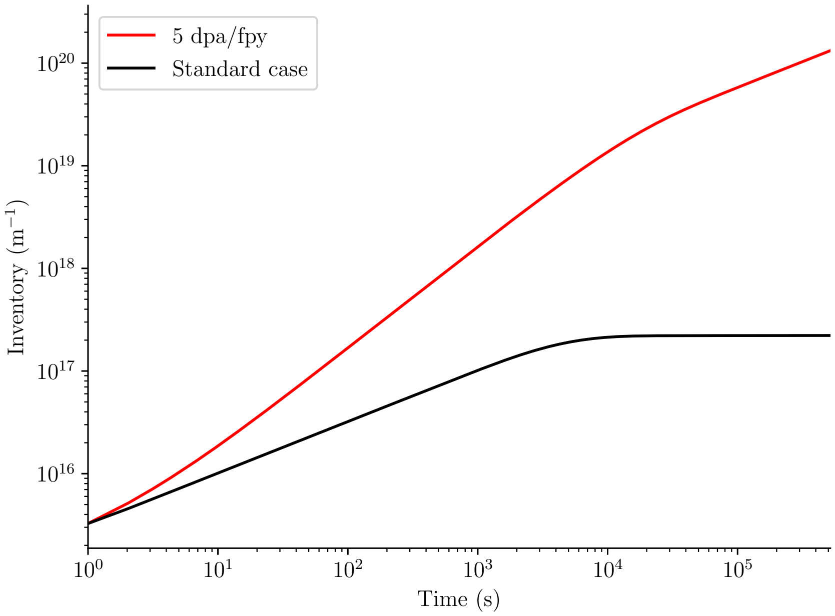

Figure 4.14: Temporal evolution of tritium retention in tungsten FW as a result of damage at 5 dpa/fpy, relative to an undamaged case

from the breeder starts to reach the FW at the 2-hour mark, demonstrated by a sharp peak in concentration at near $x = 2\,\mathrm{mm}$. Beyond this point, most of the tritium filling the FW originates from the breeder. Although the elevated inventories are problematic, the fact that they are confined within the first 0.3 mm could be advantageous for designers.

Tungsten has undergone extensive experimental campaigns examining trap formation resulting from microstructural damage and subsequent annealing effects. However, the tungsten first wall comprises less than 1 % of the structural materials in the WCLL, with the majority being Eurofer. If similar trap-creation effects are proportionately observed in Eurofer, it could have disastrous consequences for tritium transport within the WCLL. A potential increase in tritium inventories within Eurofer by orders of magnitude could severely disrupt the global fuel cycle and complicate decommissioning processes. Furthermore, the data for tungsten was obtained from self-damaged tungsten using W6^{+} ions. Although self-damage can effectively emulate the ballistic effects of neutron damage, the transmutation of tungsten may influence trap creation and annealing dynamics. Further experimentation is essential to comprehensively understand neutron damage effects on tritium transport within the WCLL. Such studies should focus on the factors influencing trap creation in both tungsten and Eurofer, considering damage levels likely to be observed in fusion reactors and utilising high-energy fusion neutrons. Comprehensive experimental data on the Eurofer and a better understanding of the transmutation effects on tungsten are crucial for accurately predicting tritium behaviour in fusion environments. This knowledge will inform the development of effective tritium management strategies and ensure the safe and efficient operation of fusion reactors.

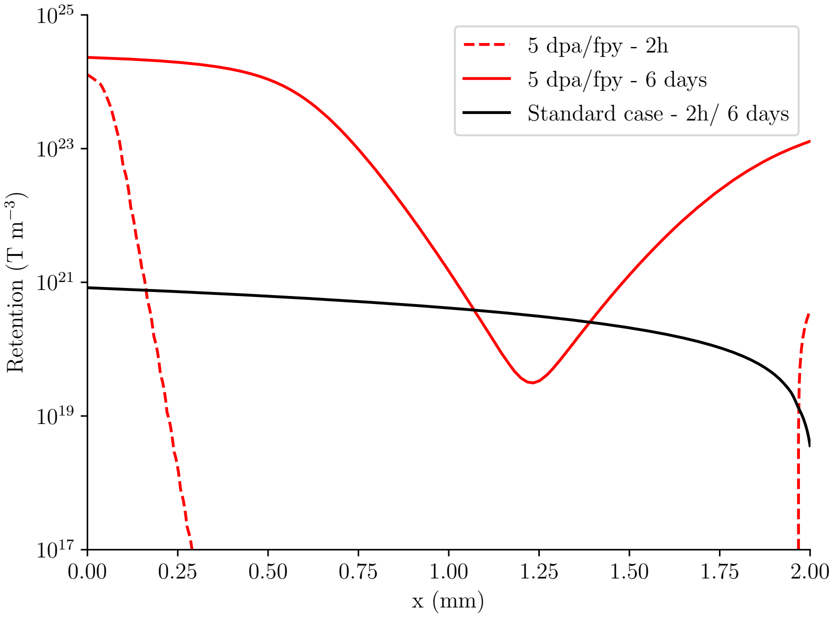

Figure 4.15: Tritium retention profile across the tungsten FW comparing the standard case against one considering trap creation after 2 h and 6 days of exposure to a damage rate of 5 dpa/fpy

These observations underscore the necessity of incorporating dynamic models for trap creation to simulate tritium transport throughout reactor operation. The nuanced profile of tritium retention and transport within the damaged FW emphasises the complex interplay between neutron damage and tritium behaviour, necessitating detailed and adaptive modelling approaches.

Chapter 5

Permeation mitigation strategies

Contents

5.1 Influence of a tritium extraction system 113

5.2 Influence of permeation barriers 118

5.2.1 Cartesian analytical model 119

5.2.2 Cylindrical analytical model 121

5.2.3 Macroscopic interface condition implementation 123

5.2.4 WCLL application 129

This chapter explores various methods to reduce tritium permeation into cooling channels and structural components, thereby minimising tritium inventories in the WCLL. The chapter begins with a study on the potential influence of a tritium extraction system. This study investigates how a tritium flux at the inlet of the WCLL can affect permeation behaviour. This study aims to provide insights into the effectiveness of tritium extraction systems in controlling tritium permeation and maintaining safe operating conditions by analysing different scenarios with varying tritium fluxes. Following this, the chapter introduces a methodology for modelling permeation barriers, which are crucial for mitigating tritium permeation in breeding blankets. Despite the effectiveness of permeation barriers, modelling them presents significant challenges due to the disparity in length scales — the barrier thickness typically ranges from nanometres to micrometres. At the same time, the WCLL operates on a scale of meters. Explicitly modelling these barriers using FEM is technically challenging and computationally intensive. The chapter presents methods for implicitly modelling permeation barriers in macroscopic simulations to address these challenges. These methods simplify the representation of permeation barriers, making it feasible to include their effects in large-scale models. The chapter then demonstrates the application of these implicit modelling techniques to the WCLL, exploring the potential influences of permeation barriers on tritium transport dynamics. By combining studies on tritium extraction systems and permeation barriers, this chapter provides an overview of permeation mitigation strategies for the WCLL breeding blanket.

5.1 Influence of a tritium extraction system

In the standard case (see section 3.3), it is assumed that the WCLL employs a perfect tritium extraction system by fixing the concentration of mobile hydrogen, c_m, at the PbLi inlet to zero. However, this assumption does not reflect the practical realities of a Tritium Extraction

System (TES). Tritium generated in the breeding zone will be transported outside the reactor to a TES. The breeder material, PbLi, flows into the WCLL, becoming enriched with tritium in the breeding zone. This tritiated PbLi is then transported to an external tritium extraction system before returning to the WCLL (illustrated in Figure 5.1). However, the extraction system is unlikely to achieve 100% removal efficiency. Consequently, the returning PbLi will still contain some residual tritium, potentially contributing to inventory build-up within the WCLL and higher permeation rates into the cooling channels. Furthermore, during the transportation of PbLi from the WCLL to the extraction system, it is likely to pass through extensive piping networks spanning 10-100's meters. During this transit, tritium may permeate through the pipe walls, either becoming trapped within the pipe material or diffusing further into the local environment. This permeation results in tritium loss that the extraction system cannot capture. Therefore, the tritium concentration returning to the WCLL depends on extraction efficiencies and the losses in the transportation in between.

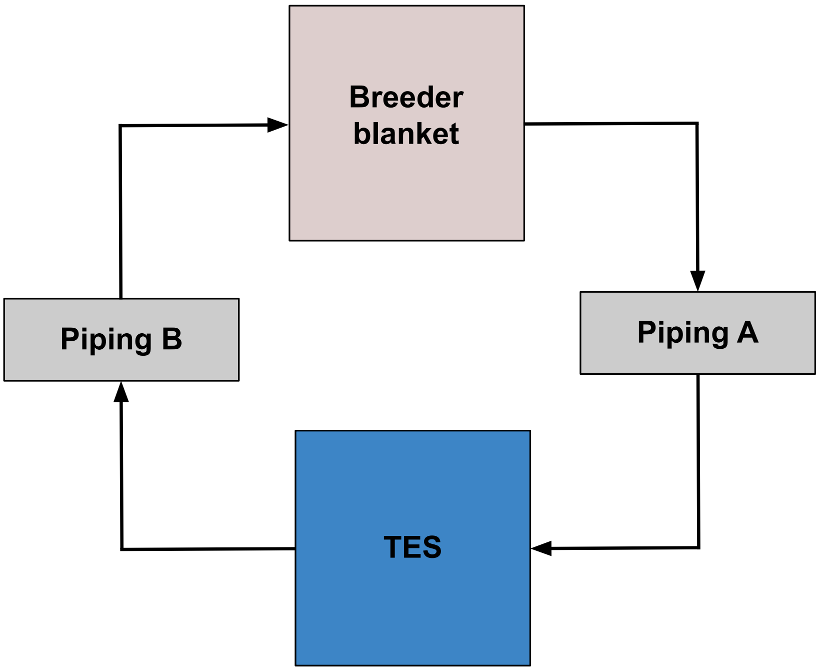

Figure 5.1: Tritium cycle between breeder and extraction system

To this end, a parametric study assessed the potential impacts of extraction and losses within the PbLi loop on tritium transport within the WCLL. This study evaluated the influence of varying tritium concentrations at the inlet of the WCLL, considering a TES's limitations and realistic performance. The flux of tritium entering the WCLL at the PbLi inlet, φ_{inlet}, in units $\mathrm{m}^{-1}\,\mathrm{s}^{-1}$ for a 2D geometry, is a function of the flux that leaves at the outlet, $\varphi_{\mathrm{outlet}}$:

$$\varphi_{\mathrm{inlet}} = (1-\eta)\,\varphi_{\mathrm{outlet}} \tag{5.1}$$

where $\eta \in [0,1]$ is the tritium removal efficiency from the PbLi following the complete cycle to and from the TES, and φ is the advection flux of tritium, in units $\mathrm{H\,m\,s^{-1}}$:

$$\varphi_{\text{outlet}} = \int_{\partial\Omega} (u_{\text{i}}\ c_{\text{m}}) \cdot \mathbf{n}\ ds \tag{5.2}$$

The average concentration at the inlet can then be evaluated as:

$$c_{\text{m}} = (1-\eta)\ \frac{\varphi_{\text{outlet}}}{u_{\text{i}}\ A} \tag{5.3}$$

where u_{i} is the prescribed normal velocity at the inlet ($2\times10^{-4}\,\mathrm{m\,s^{-1}}$) and A is the boundary length of the inlet (0.0615 m). The parameter η can be defined as

$$\eta = 1 - ((1-\alpha)\cdot(1-\beta)\cdot(1-\gamma)) \tag{5.4}$$

where α and γ represent the proportions of tritium losses during the transportation of the PbLi in the piping network to and from the TES, respectively, and β denotes the efficiency of tritium removal by the TES. However, exact values for tritium losses in the piping (α and γ) to the environment cannot be accurately determined until full models of the breeding blanket system are finalised for DEMO. The same can be said for the time required for the PbLi to complete an entire loop (see Figure 5.1). Additionally, there is considerable uncertainty regarding the removal capabilities of tritium extraction systems. Current research indicates that for the tritium extraction system to be economically viable, it must achieve an efficiency of at least 90% [229]. This high efficiency is necessary to minimise tritium losses and ensure the sustainability of the reactor operation.

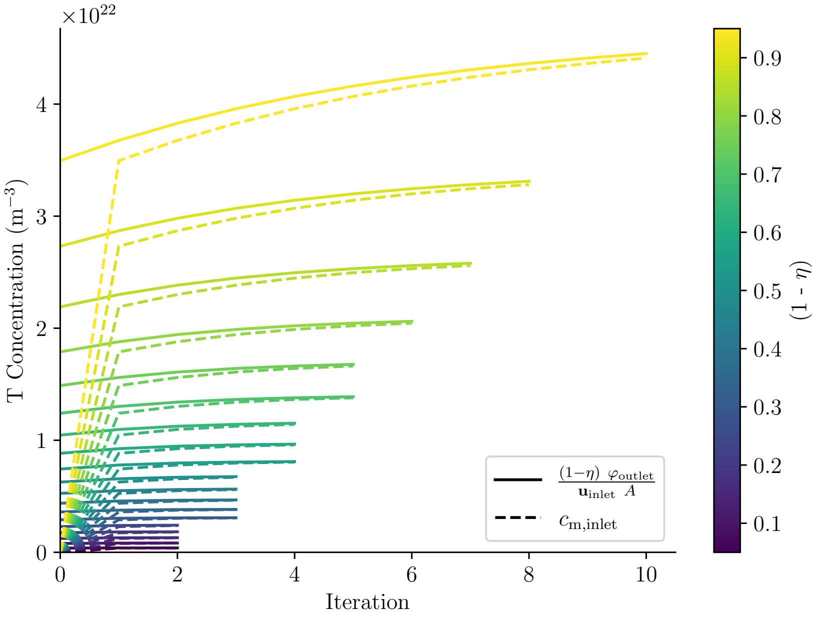

Figure 5.2: Tritium concentration of the inlet, $c_{\text{m,inlet}}$, with resulting evaluation for contraction to use in next iteration, $((1-\eta)\ \varphi_{\text{outlet}})/(\mathbf{u}_{\text{inlet}}\ A)$, converging to a max difference of 1%, for each case of $(1-\eta)$

As the time required for the PbLi to complete an entire loop through the extraction system will likely not be known until the final design stages of DEMO, it is impossible to accurately model a TES's influence in a transient state. Therefore, a steady-state analysis was undertaken. Applying the condition (see Eq. 5.1), if the removal efficiency, η, is not zero, a higher inlet concentration results in a correspondingly higher outlet flux. Steady-state simulations of the WCLL were performed iteratively for each value of η, re-evaluating the required inlet concentration based on the updated outlet flux until convergence was achieved within a 1 % criterion. Values of η tested ranged from 0 to 1. As the η value increases, the number of iterations required to reach convergence increases as the initial guess increases further from the solution (see Figure 5.2). Furthermore, the steady-state outlet flux and inlet concentration would increase exponentially in a system where no tritium is removed but still generated ($\eta = 0$). However, values would not approach infinity as the cooling channels are tritium sinks. By systematically adjusting the inlet concentration based on the PbLi outlet values, the study provides insights into the efficiency of the tritium extraction process and its effect on the performance of the WCLL.

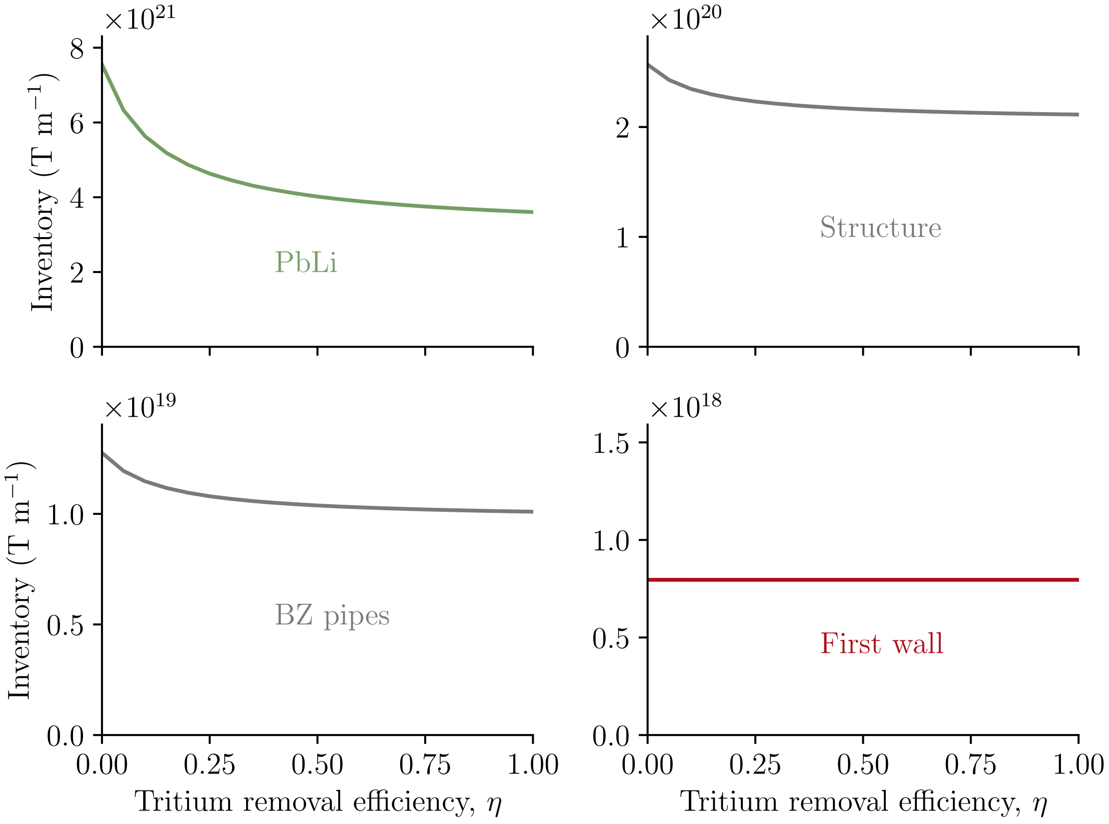

Figure 5.3: Tritium inventories in the PbLi, structure, BZ pipes and FW as a function of tritium re-entering the WCLL. Standard case at $\eta = 1.0$

The analysis of tritium retention levels in different subdomains of the WCLL model indicates that inefficiencies in tritium removal primarily impact the PbLi itself and the Eurofer structure due to their direct contact with the tritiated PbLi. This contact results in increased tritium inventories within these materials. At its worst, with a tritium removal efficiency of 5% ($\eta = 0.05$), tritium retention within the system increases by up to 70%, predominantly within the PbLi (see Figure 5.3). The highest structural increase in tritium retention is observed in the BZ pipes, with a rise of 23%, reflecting the significant interaction between the tritiated PbLi and the structural materials. However, when considering a more desirable range of tritium removal efficiencies ($\eta > 0.9$), the impact on tritium retention is notably less severe. Within this range, the maximum difference in tritium inventory is still observed in the PbLi, but the increase is only 1.5%. This demonstrates that while tritium re-entering the WCLL model has measurable effects on local inventories, the magnitude of these effects is relatively small.

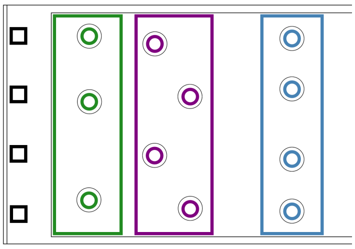

(a) BZ pipe groupings

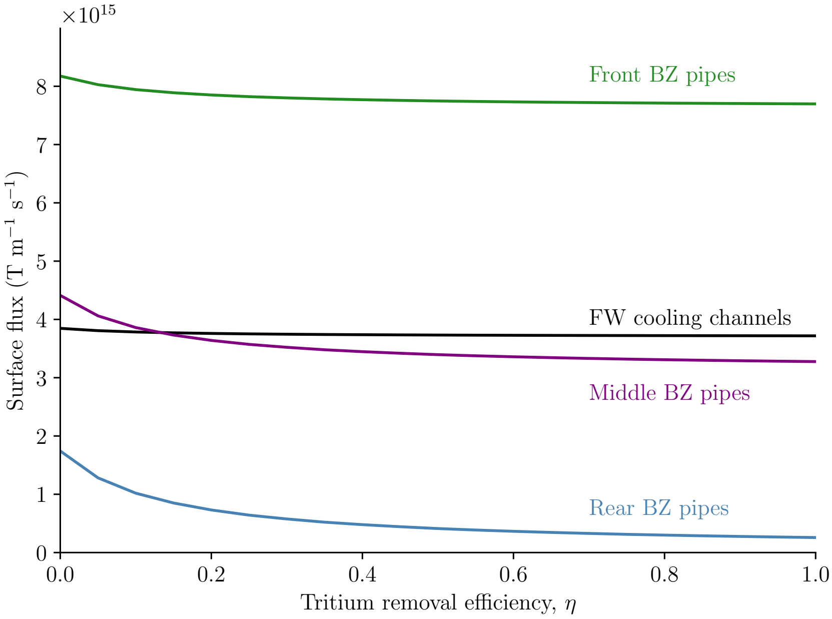

(b) Tritium surface flux

Figure 5.4: Tritium surface flux entering the different regions of BZ pipes and FW cooling channels as a function of tritium re-entering the WCLL

The most pronounced permeation effects are observed in the surface flux levels in the rear BZ pipes (see Figure 5.4b), where permeation rates are shown to vary more than 148% across the range of η values. This is attributed to their positioning within the model, which places them in direct contact with the flow of PbLi. However, once again, considering a more desirable range of tritium removal efficiencies ($\eta > 0.9$) in the rear BZ cooling channels, the difference in permeation drops to 7.5%. This is still a more significant difference than local inventory build-ups. However, it is essential to note that these results may change if buoyancy and MHD effects are considered. Considering these phenomena could result in more significant flow mixing, leading to more advection effects within the PbLi at the front of the model, potentially leading to higher fluxes in the front and middle BZ pipes as the inlet concentration increases.

These results highlight that high proportions of tritium re-entering the WCLL model can increase tritium retention in specific subdomains, particularly in the PbLi and Eurofer structures. Nevertheless, these increases are minimal in the context of typical operational efficiencies, underscoring the effectiveness of the tritium removal system even with less-than-perfect efficiency. The components with the highest sensitivity to TES efficiencies are observed to be the rear BZ cooling channels due to the flow path of PbLi. The tritium extraction system's target efficiency of 90 % mean any results where η falling short of 0.9 may be considered less relevant. However, values lower than 0.9 may be used to model a scenario where the TES becomes dysfunctional. The methodology used in this study is well-suited for steady-state simulations. A thorough analysis of the impact of the PbLi loop on the WCLL would require transient simulations. However, this is not feasible until further details of the loop dynamics and TES system are finalised.

However, the effectiveness of the TES only affected the tritium entering the WCLL system from the PbLi inlet. A far more effective method planned to reduce permeation in the WCLL is using hydrogen permeation barrier coatings.

5.2 Influence of permeation barriers

Tritium permeation barriers, typically consisting of micro-scale layers with low diffusion coefficients, are crucial for preventing tritium release into the environment and maximising recovery. Materials such as Al_2O_3 have shown promise, applying techniques like sputtering onto structural materials [32]. The Permeation Reduction Factor (PRF) quantifies these barriers' effectiveness:

$$\mathrm{PRF} = \frac{\Phi_{\text{uncoated}}}{\Phi_{\text{coated}}} \tag{5.5}$$

where Φ_{uncoated} is the hydrogen flux across an uncoated surface, and Φ_{coated} is the hydrogen flux across a surface covered in a permeation barrier coating, both in units $\mathrm{m^{-2}\,s^{-1}}$, $\mathrm{m^{-1}\,s^{-1}}$ or $\mathrm{s^{-1}}$ depending if the dimension of the domain is 1/2/3D. For the WCLL, it is anticipated that a PRF of at least 200 will be required to minimise permeation into structural materials and cooling channels [230, 231, 232, 233, 32].

Mitigating diffusing medium is not unique to tritium permeation barriers; thermal resistant barriers (TRBs) share core functional similarities [234, 235, 236]. Both are integral to enhancing system efficiency and safety. Several works on TBRs are focused on their mechanical integrity (debonding, fracture, stress...) and the numerical estimation of their efficiency based on FEM modelling of the multi-material components [237]. To our knowledge, no efforts have been made to develop an analytical model of their impact on heat transfer through samples that can be integrated into component-scale simulations.

Analytical models for permeation barriers are presented in cartesian and cylindrical coordinate systems, offering insights into the required barrier thickness to achieve desired PRF conditions based on material hydrogen transport properties.

5.2.1 Cartesian analytical model

Analytical solutions for the steady-state mobile concentration can be derived in simple 1D Cartesian systems, assuming the flux across the system remains constant. This approach allows for evaluating the analytical flux values in both coated and uncoated cases, providing a clear comparison. Solving these scenarios can obtain an analytical expression for PRF.

This section presents a detailed analysis of a cartesian system comprising a substrate of thickness L and coatings of thickness e, constituting this model's three domains (see Fig 5.5). The system is assumed to have a constant homogeneous value for temperature.

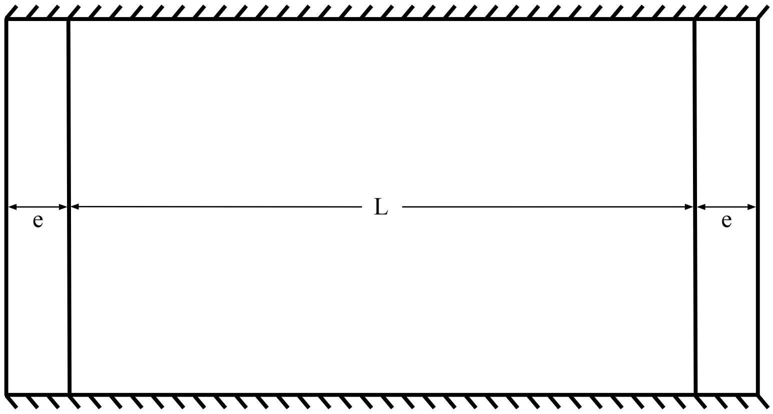

Figure 5.5: 2D representation of the 1D cartesian geometry for permeation barrier analytical solution

The mobile concentration across each domain can be described as follows:

$$0 = \boldsymbol{\nabla} \cdot (D \boldsymbol{\nabla} c_\mathrm{m}) \tag{5.6}$$

The test case considered in this section is made of the three sub-domains Ω_1, Ω_2 and Ω_3. They are described as follows:

$$\Omega = [0, 2e + L] = \Omega_1 \cup \Omega_2 \cup \Omega_3 \tag{5.7}$$

$$\Omega_1 = [0, e] \tag{5.8}$$

$$\Omega_2 = [e, e + L] \tag{5.9}$$

$$\Omega_3 = [e + L, 2e + L] \tag{5.10}$$

Each material within the system is characterised by its diffusion coefficient and hydrogen solubility values.

$$D = \begin{cases} D_1, & \text{in } \Omega_1 \text{ and } \Omega_3 \\ D_2, & \text{in } \Omega_2 \end{cases} \tag{5.11}$$

$$K_\mathrm{S} = \begin{cases} K_{\mathrm{S},1}, & \text{in } \Omega_1 \text{ and } \Omega_3 \\ K_{\mathrm{S},2}, & \text{in } \Omega_2 \end{cases} \tag{5.12}$$

Furthermore, the following quantities are introduced:

$$\alpha = D_2/D_1 \tag{5.13a}$$
$$\beta = K_{\mathrm{S},2}/K_{\mathrm{S},1} \tag{5.13b}$$
$$\gamma = e/L \tag{5.13c}$$

By integrating equation 5.6 and assuming steady-state, one can obtain the following form:

$$c_\mathrm{m} = \begin{cases} a_1 x + b_1, & \text{in } \Omega_1 \\ a_2 x + b_2, & \text{in } \Omega_2 \\ a_3 x + b_3, & \text{in } \Omega_3 \end{cases} \tag{5.14}$$

where a_1, b_1, a_2, b_2, a_3 and b_3 are the unknowns of the problem to be determined. The conservation of chemical potential is assumed at the material interfaces, ensuring a consistent treatment of hydrogen transport across the boundaries. By incorporating additional boundary conditions, the model becomes fully constrained, enabling us to evaluate the solution for the mobile concentration across the entire domain. The boundary conditions and the equilibrium law at the interfaces are defined as:

$$c_\mathrm{m}(x = 0) = c_0 \tag{5.15a}$$
$$c_\mathrm{m}(x = 2e + L) = c_1 \tag{5.15b}$$
$$c_\mathrm{m}^-(x = e) = \frac{1}{\beta} c_\mathrm{m}^+(x = e) \tag{5.15c}$$
$$c_\mathrm{m}^-(x = e + L) = \beta c_\mathrm{m}^+(x = e + L) \tag{5.15d}$$
$$\boldsymbol{\nabla} c_\mathrm{m}^-(x = e) = \frac{1}{\alpha} \boldsymbol{\nabla} c_\mathrm{m}^+(x = e) \tag{5.15e}$$
$$\boldsymbol{\nabla} c_\mathrm{m}^-(x = e + L) = \alpha \boldsymbol{\nabla} c_\mathrm{m}^+(x = e + L) \tag{5.15f}$$

where c_0 and c_1 are fixed concentrations in units m^{-3}. The six equations with six unknowns in 5.15 can be solved using Sympy [238], with these constraints and coefficient describing c_m.

$$a_0 = \frac{c_0\beta(c_1 - 1)}{L(1 + 2\alpha\beta\gamma)} \tag{5.16a}$$

$$a_1 = \alpha a_0 = a_3 \tag{5.16b}$$

$$a_2 = a_0 \tag{5.16c}$$

$$b_1 = c_0 \tag{5.16d}$$

$$b_2 = \frac{\beta c_0(1 + \gamma(1 - c_1 + \alpha\beta))}{1 + 2\alpha\beta\gamma} \tag{5.16e}$$

$$b_3 = \frac{c_0(c_1 + \alpha\beta(1 - c_1 + 2\gamma))}{1 + \alpha\beta\gamma} \tag{5.16f}$$

Assuming the fixed concentration value, $c_0 = K_{\mathrm{S},1}\sqrt{P}$ in the coated case and $c_0 = K_{\mathrm{S},2}\sqrt{P}$ in the uncoated case, and $c_1 = 0$, the coated and uncoated fluxes can be expressed as:

$$\Phi_{\text{coated}} = \frac{D_2 K_{\mathrm{S},2}\sqrt{P}}{L(1 + 2\alpha\beta\gamma)} \tag{5.17}$$

$$\Phi_{\text{uncoated}} = \frac{D_2 K_{\mathrm{S},2}\sqrt{P}}{L} \tag{5.18}$$

Therefore:

$$\mathrm{PRF} = 1 + 2\alpha\beta\gamma \tag{5.19}$$

This analysis shows that the PRF depends on the material properties (diffusivity ratio α and solubility ratio β) and the system geometry (γ). The geometry factor can be investigated further by exploring a differently shaped domain.

5.2.2 Cylindrical analytical model

The following section extends the procedure for evaluating the analytical solution for the PRF to a cylindrical geometry assumed to be axisymmetric. This analysis not only investigates the influence of geometry on the PRF but also holds significant implications for the WCLL, given the numerous cooling pipes that will come into contact with tritium. Understanding the PRF in cylindrical systems is crucial for accurately predicting and mitigating tritium permeation in these complex geometries. The system is assumed to have a constant homogeneous value for temperature. The test case considered in this section is once again made of the three sub-domains Ω_1, Ω_2 and Ω_3 see figure 5.6. They are described as follows:

$$\Omega = [r_0, r_0 + 2e + L] = \Omega_1 \cup \Omega_2 \cup \Omega_3 \tag{5.20}$$

$$\Omega_1 = [r_0, r_0 + e] \tag{5.21}$$

$$\Omega_2 = [r_0 + e, r_0 + e + L] \tag{5.22}$$

$$\Omega_3 = [r_0 + e + L, r_0 + 2e + L] \tag{5.23}$$

Each material within the system is characterised by its diffusion coefficient and hydrogen solubility values.

$$D = \begin{cases} D_1, & \text{in } \Omega_1 \text{ and } \Omega_3 \\ D_2, & \text{in } \Omega_2 \end{cases} \tag{5.24}$$

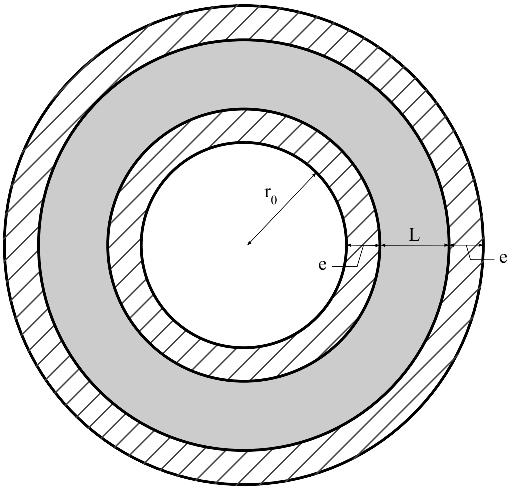

Figure 5.6: 2D representation of the 1D cylindrical (polar) geometry for permeation barrier analytical solution

$$K_{\mathrm{S}} = \begin{cases} K_{\mathrm{S},1}, & \text{in } \Omega_1 \text{ and } \Omega_3 \\ K_{\mathrm{S},2}, & \text{in } \Omega_2 \end{cases} \tag{5.25}$$

We then use the same quantities as outlined previously (see Eq (5.13)) with one addition:

$$\gamma' = r_0/L \tag{5.26}$$

By integrating equation 5.6 and assuming steady-state, one can obtain the following form:

$$c_{\mathrm{m}} = \begin{cases} a_1 \ln(r) + b_1, & \text{in } \Omega_1 \\ a_2 \ln(r) + b_2, & \text{in } \Omega_2 \\ a_3 \ln(r) + b_3, & \text{in } \Omega_3 \end{cases} \tag{5.27}$$

where a_1, b_1, a_2, b_2, a_3 and b_3 are the unknowns of the problem to be determined. The boundary conditions and the equilibrium law at the interfaces are defined as:

$$c_{\mathrm{m}}(r = r_0) = c_0 \tag{5.28a}$$
$$c_{\mathrm{m}}(r = 2e + L) = c_1 \tag{5.28b}$$
$$c_{\mathrm{m}}^{-}(r = e) = \frac{1}{\beta} c_{\mathrm{m}}^{+}(r = e) \tag{5.28c}$$
$$c_{\mathrm{m}}^{-}(r = e + L) = \beta c_{\mathrm{m}}^{+}(r = e + L) \tag{5.28d}$$
$$\boldsymbol{\nabla} c_{\mathrm{m}}^{-}(r = e) = \frac{1}{\alpha} \boldsymbol{\nabla} c_{\mathrm{m}}^{+}(r = e) \tag{5.28e}$$
$$\boldsymbol{\nabla} c_{\mathrm{m}}^{-}(r = e + L) = \alpha \boldsymbol{\nabla} c_{\mathrm{m}}^{+}(r = e + L) \tag{5.28f}$$

Once more, the six equations with six unknowns in Eq. (5.27), constraining the cylindrical domain problem, can be solved using Sympy [238]. Solutions for coefficients a_1-a_3 and b_1-b_3 are detailed in appendix E. With the solutions, assuming the fixed concentration value,

$c_0 = K_{\mathrm{S},1}\sqrt{P}$ in the coated case and $c_0 = K_{\mathrm{S},2}\sqrt{P}$ in the uncoated case, and $c_1 = 0$, the coated and uncoated fluxes can be expressed as:

$$\Phi_{\text{coated}} = \frac{D_2 K_{\mathrm{S},2}\sqrt{P}}{\alpha\beta \ln\left(\frac{\gamma'(\gamma+\gamma'+1)}{(-\gamma+\gamma')(\gamma'+1)}\right) + \ln\left(\frac{\gamma'+1}{\gamma'}\right)} \tag{5.29}$$

$$\Phi_{\text{uncoated}} = \frac{D_2 K_{\mathrm{S},2}\sqrt{P}}{\ln\left(\frac{\gamma'+1}{\gamma'}\right)} \tag{5.30}$$

Thus:

$$\mathrm{PRF} = 1 + \alpha\beta A \tag{5.31}$$

Where:

$$A = \frac{\ln\left(\frac{\gamma'-\gamma}{1+\gamma+\gamma'}\right)}{\ln\left(\frac{\gamma'}{1+\gamma'}\right)} - 1 \tag{5.32}$$

Furthermore, it can be shown that as r_0 grows to infinity, the geometry changes to approach the cartesian system, and this is reflected in the solution.

$$\lim_{r_0 \to \infty} \mathrm{PRF} = 1 + 2\ \alpha\beta\gamma \tag{5.33}$$

5.2.3 Macroscopic interface condition implementation

The lack of comprehensive knowledge regarding the hydrogen transport properties of permeation barriers poses a challenge. Potential alterations in these properties due to the barrier application method compound this. Furthermore, difficulties arise when attempting to model macroscopic components, such as cooling channels, to which permeation barriers may be applied. The vast difference in thickness between the permeation barrier ($\approx$ μm) and the cooling channel ($\approx$ cm) complicates the discretisation of such domains. Further complexity is introduced in 3D scenarios where cooling channels extend for meters.

The influence of a hydrogen permeation barrier at a material interface (such as PbLi-Eurofer) can be modelled by using an effective solubility:

$$\frac{c_{\mathrm{m}}^-}{K_{\mathrm{S}}^-} = \frac{c_{\mathrm{m}}^+}{K_{S,\mathrm{eff}}^+} \tag{5.34}$$

where the $K_{\mathrm{S,eff}}^+$ can be a function of a defined PRF and the original material solubility value:

$$K_{\mathrm{S,eff}}^+ = f(K_{\mathrm{S}}, \mathrm{PRF}) \tag{5.35}$$

This method leverages an analytical derivation of the PRF (see section 5.2.1), allowing one to enforce a PRF on the system through adjustments in material properties rather than explicit barrier modelling. This implicit method provides a streamlined way to account for permeation barriers, potentially reducing computational overhead while maintaining accuracy.

A simple domain is considered comprising 2 mm of lead-lithium (PbLi), and 2 mm of Eurofer steel can be used to validate this approach. This setup emulates a small section within the

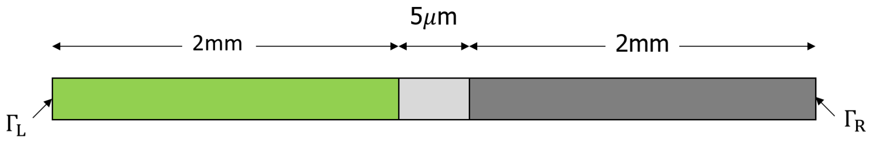

(a) With permeation barrier

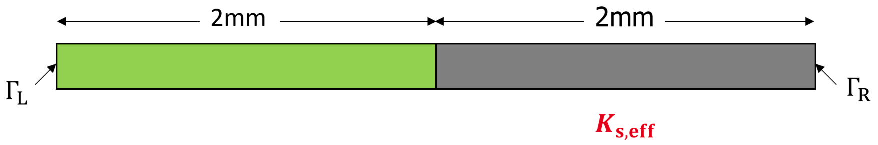

(b) Without permeation barrier

Figure 5.7: Cartesian 1D model of a domain of 2 mm PbLi 🟩 and 2 mm Eurofer ⬛ with and without a 5 μm Al_2O_3 ⬜ permeation barrier

breeding zone of the WCLL blanket. Tests were undertaken modelling the domain with and without a 5 μm Al_2O_3 permeation barrier modelling explicitly (see figure 5.7). No trapping effects were considered in this study. The concentration of tritium was fixed at either end of the domain with the following boundary conditions:

$$c_\mathrm{m} = 10^{20}\,\mathrm{m}^{-3} \quad \text{on } \Gamma_\mathrm{L} \tag{5.36}$$

$$c_\mathrm{m} = 0 \quad \text{on } \Gamma_\mathrm{R} \tag{5.37}$$

The hydrogen transfer problem was solved at steady-state and with a constant temperature of 600 K. The maximum mesh cell size considered was 2.5×10^{-7} m, allowing for the discretisation of 20 cells across the permeation barrier. The same hydrogen transport parameters for solubility and diffusivity for PbLi and Euorfer have been considered from the standard case (see Table 3.6), in addition to the transport parameters for Al_2O_3 have been taken from Serra *et. al* [239].

Table 5.1: H transport properties of Al_2O_3 [239]

Material	Solubility $K_{s,0}$ $[\mathrm{m}^{-3}\,\mathrm{Pa}^{-0.5}]$	E_{K_s} [eV]	Diffusivity D_0 $[\mathrm{m}^2\,\mathrm{s}^{-1}]$	E_D [eV]
Al_2O_3 [239]	3.74×10^{21}	0.245	7.87×10^{-8}	0.807

Modelling the permeation barrier explicitly reveals a significant drop in tritium concentration across the barrier due to its lower solubility, resulting in a markedly lower concentration in the Eurofer compared to the uncoated case (see Figure 5.8). Considering the permeation barrier, results in a PRF at Γ_R of 2.2×10^4, with 5 μm thick alumina. To emulate this effect, the solubility value in the eurofer was modified by a factor 3.9×10^{-4}:

$$K_\mathrm{S,eff} = K_\mathrm{S,eurofer} \cdot 3.9 \times 10^{-4} \tag{5.38}$$

When this effect is replicated using the modified solubility in the implicit model, the concentration profile matches the explicit barrier case well both across the entire domain (see

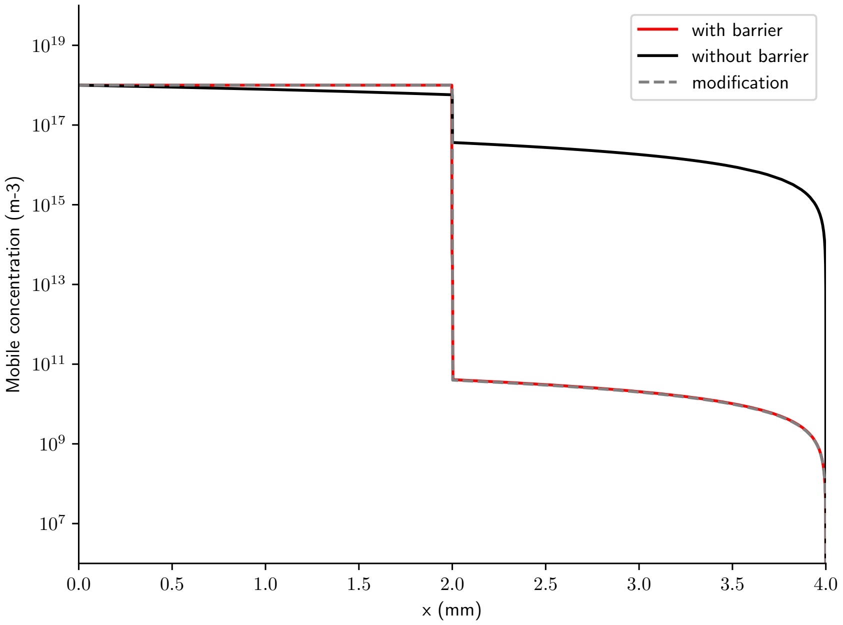

(a) Full domain

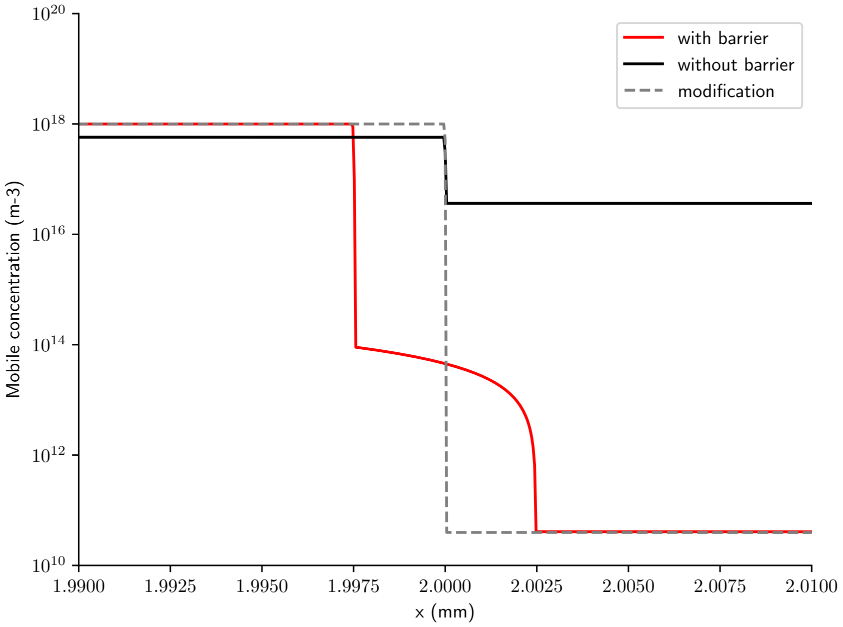

(b) Permeation barrier region highlighted

Figure 5.8: Mobile concentration of tritium across a domain with a permeation barrier modelled explicitly, without a barrier and with modification condition

Figure 5.8a) and across the permeation barrier region (see Figure 5.8a). In this case, the evaluated PRF of 2.2×10^4 is attributable to the permeation barrier's transport properties. This suggests that a thinner alumina layer could be more appropriate for a less conservative

PRF value. Furthermore, the modification of the Eurofer solubility will only emulate the effects of 5 μm thick alumina in this specific case. Varying the geometry of this case will render this modification factor invalid, as shown in section 5.2.1. Plus, the solubility values are temperature dependent, meaning at different temperatures, the ratio of the solubility values between PbLi and eurofer will change, invalidating the current modification factor. Thus, parametric studies can be conducted by varying the geometry and temperature to analyse the influence of these factors on tritium transport to derive a behaviour law to define a required modification factor to enforce a desired PRF.

Behaviour law derivation

This section explores the parametric study conducted to understand the effect of modifying Eurofer's solubility value and its consequential impact on permeation flux. The modification factor derived in the previous section to emulate the effects of 5 μm thick alumina is suitable only for this specific case. Thus, a parametric study was undertaken, systematically altering the solubility of Eurofer using different modification factors. Where the K_{eff} used was evaluated using:

$$K_{\text{eff}} = K_{\text{S}} \times \text{Modification factor} \tag{5.39}$$

The surface flux of hydrogen at Γ_{R} was recorded for each modification. These flux values were then compared against the baseline case, which utilised the standard Eurofer solubility value. The enforced PRF resulting from each modification factor was derived through this comparison. The essence of this study lies in examining how changes in the PRF correlate with the applied modification factors. By analysing these correlations, the aim was to develop a behaviour law that captures the relationship between the modification factor and the resulting PRF. This behaviour law is crucial for predictive simulations, allowing the determination of the necessary modification factor to achieve a desired PRF under varying conditions.

Modification factors from 1 to 10^8 were applied, and the resulting surface flux at Γ_{R} was evaluated to determine the PRF respectively. Analysing the measured PRF against the modification factor reveals a linear correlation (see figure 5.8). From the analysis, the following behaviour law can be derived:

$$K_{\text{eff}} = K_{\text{S}} \cdot \left(\frac{\text{PRF} - 0.4287}{0.6713} \right) \tag{5.40}$$

This analysis demonstrates the implicit method's effectiveness in simplifying the modelling process while providing an accurate and flexible tool for modelling permeation barriers. This can allow for relaxation in the discretisation of a component domain, allowing for larger domains or more discretisation in areas where transport behaviour is more complex.

However, the previous cartesian analytical study (See section 5.15) showed that the system's geometry also influences the PRF value. This influence is illustrated in figure 5.10, where the length of the PbLi domain is varied, and the measured PRF is plotted against the same range of modification factors for each length case. The results show how the behaviour law changes with different length scales of the PbLi subdomain. This variation arises because the concentrations at either side of the domain are fixed. Changing the domain length alters

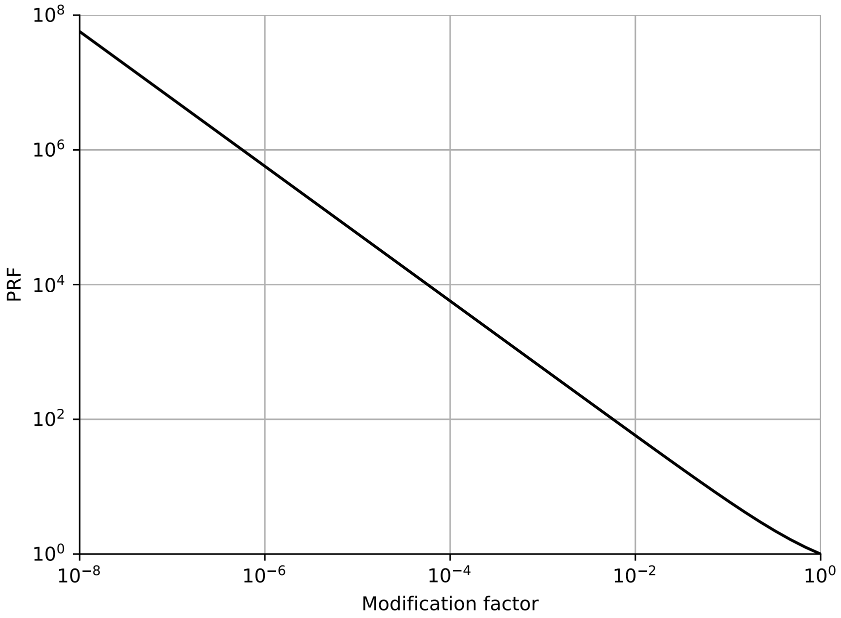

Figure 5.9: Measured PRF compared to a standard material interface condition against modification factor for Eurofer solubility

the tritium flux across the domain, thus impacting the modified fluxes during testing (See figure 5.10). Notably, as the length of the PbLi domain decreases and approaches zero, the behaviour law converges to a perfect linear relationship. This can be deduced from the fact that the permeation barrier's influence in an infinitesimally thin domain is uniformly distributed, leading to a direct proportionality between the modification factor and the PRF.

This linearity occurs because, with minimal length, the resistance to permeation becomes negligible, and the tritium transport is dominated by the solubility modification alone, simplifying the overall transport dynamics to a straightforward linear function. Furthermore, this study demonstrates how the geometry of the material subdomains can significantly affect tritium transport behaviour, thereby altering the PRF. However, geometry is not the only factor influencing the PRF. The interface condition is primarily based on the ratio of solubility values of the materials on either side of the interface. These solubility values follow Arrhenius laws, meaning they change with temperature, and each material's solubility modifies at different rates. Consequently, the solubility ratio varies with temperature, further impacting the PRF.

Despite these variations, the most significant differences in solubility are observed at the lowest temperatures, where at 400 K, the solubility ratio of PbLi to Eurofer maximises at 80. At the highest temperatures, around 1200 K, it minimises to roughly 3. Although these changes alter the properties of the interface condition, they have minimal effects on the measured PRF (see Figure 5.11). Thus, it can be deduced that geometry plays a far more significant role in determining a behaviour law for the PRF, underscoring the importance of geometric considerations in modelling permeation dynamics.

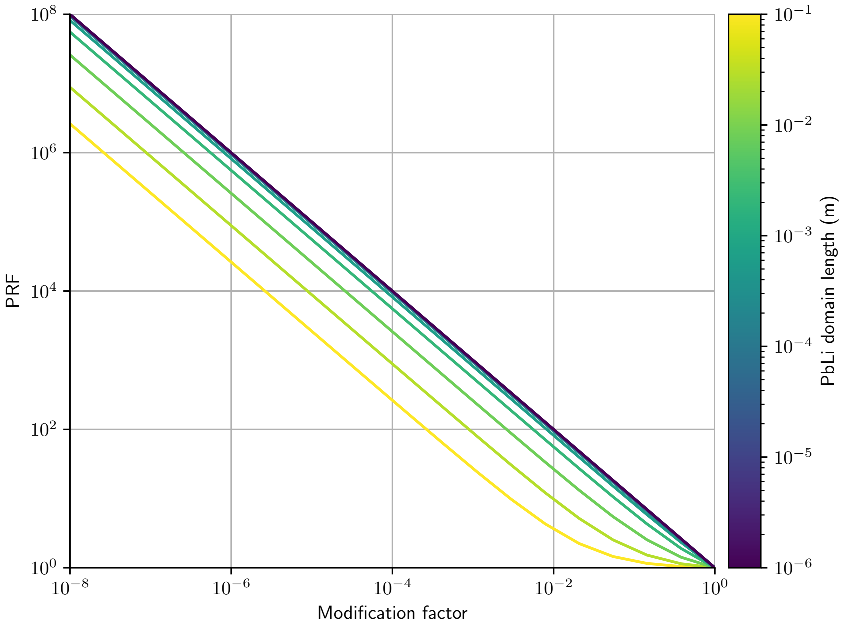

Figure 5.10: Measured PRF compared to a standard material interface condition against modification factor for Eurofer solubility, varying the length of the PbLi

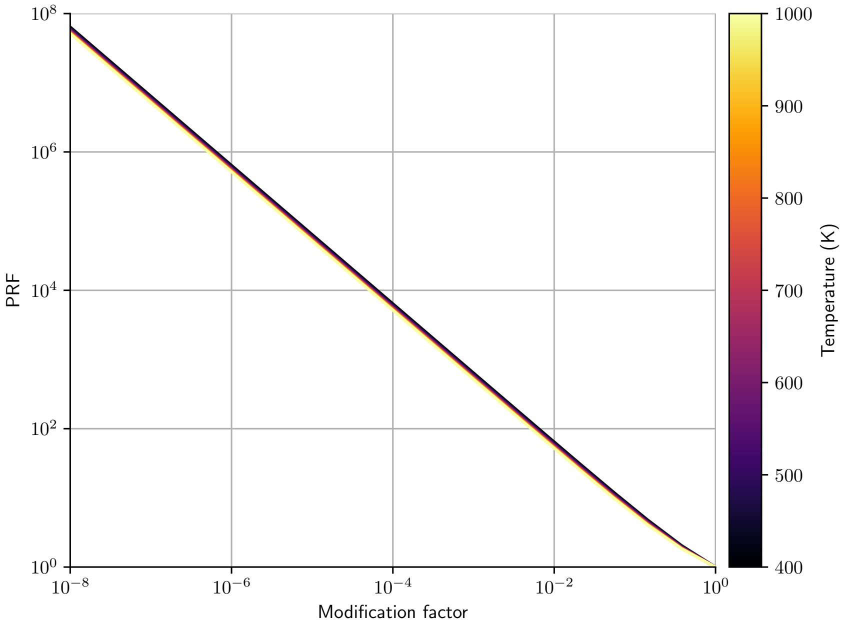

Figure 5.11: Measured PRF compared to a standard material interface condition against modification factor for Eurofer solubility, varying the temperature of the domain

The presented method effectively emulates a permeation barrier between materials by modifying the solubility interface condition, closely replicating the performance of an explicit barrier. However, this approach requires two distinct materials to function correctly and cannot be applied directly as a boundary condition. This limitation suggests that while the method is robust for internal domain applications, alternative approaches are needed for scenarios requiring boundary condition implementations. To address this limitation, a novel method is introduced for implicitly modelling permeation barriers by modifying a previously used boundary condition: the recombination flux (see Appendix F).

5.2.4 WCLL application

This section concerns the application of the implicit permeation barrier model to the BZ pipes within the WCLL breeding blanket. The BZ pipes, critical components within the WCLL, require effective strategies to mitigate challenges, including corrosion and tritium permeation. A coating will likely be used on the outside of the BZ pipe to act as a corrosion barrier [240], to mitigate corrosion effects of the PbLi on the Eurofer; an electrical insulator to reduce pressure drops as a result of MHD effects [241]; and finally to reduce permeation of tritium into the BZ channels and coolant [34, 242]. The interface model presented in section 5.2.3 is applied to the boundary between the PbLi and Eurofer of the BZ channels.

Behaviour law derivation

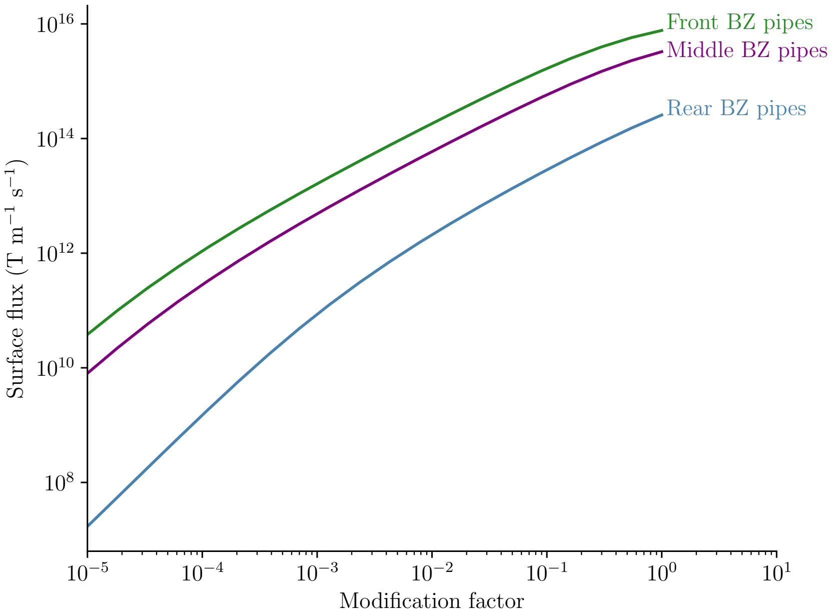

Figure 5.12: Tritium surface flux entering the different regions of BZ pipes at steady state varying the modification factor applied to the solubility value of the Eurofer in the BZ pipes. For colours, see figure 5.4a

Much like the process in section 5.2.3, the solubility of the Eurofer within the BZ pipes is altered by a modification factor over a range, influencing the quantity of tritium entering the BZ pipes as a result of the conservation of chemical potential, the enforced interface condition. Where the K_{eff} used to model the solubility of the Eurofer was evaluated using Eq. (5.39). The tritium permeation flux at the coolant boundary is recorded, providing a detailed visual representation of the impact of these modifications (see Figure 5.12). The steady-state surface flux is observed to vary with the modification factor uniformly across each region of the piping within the WCLL. Specifically, the front BZ pipes contribute the highest levels of surface flux, followed sequentially by the middle and rear sections. This consistent variation in surface flux with the modification factor across different positions of the BZ pipes suggests that a common behaviour law can be established for all BZ pipes within the WCLL.

To further analyse this behaviour, each case of modified flux is normalised against the standard case to obtain a measured PRF value for the steady-state surface flux across the total of the BZ pipes (see Figure 5.13). This normalisation allows for a comparative assessment of the impact of different modification factors.

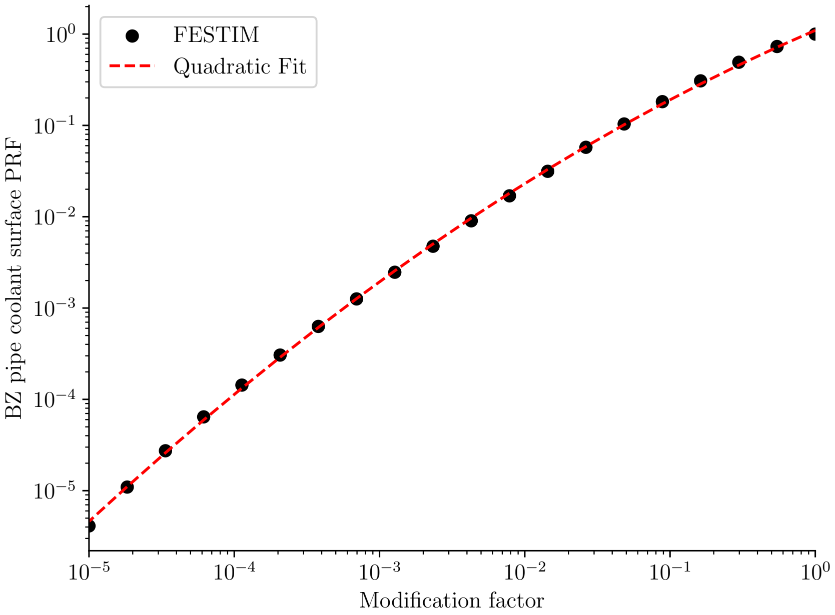

Figure 5.13: The measured PRF of the total BZ pipe surface flux against the standard flux, against respective modification factor, with quadratic fitting

A behaviour law can be derived by applying a log transformation to the data and fitting it using a quadratic polynomial. This law defines the required modification factor to achieve a specific PRF:

$$K_{\mathrm{S,eff}} = K_{\mathrm{S}} \cdot \exp(0.0265 \log^2(\mathrm{PRF}) - 1.23 \log(\mathrm{PRF}) - 0.274) \tag{5.41}$$

where K_{S} is the solubility tritium of Eurofer.

Results

When applying the behaviour law to the solubility of Eurofer in the BZ pipes, subsequent tritium inventories within the BZ pipes are shown to decrease significantly as a result of enforcing the PRF at the PbLi-Eurofer interface (see Figure 5.14).

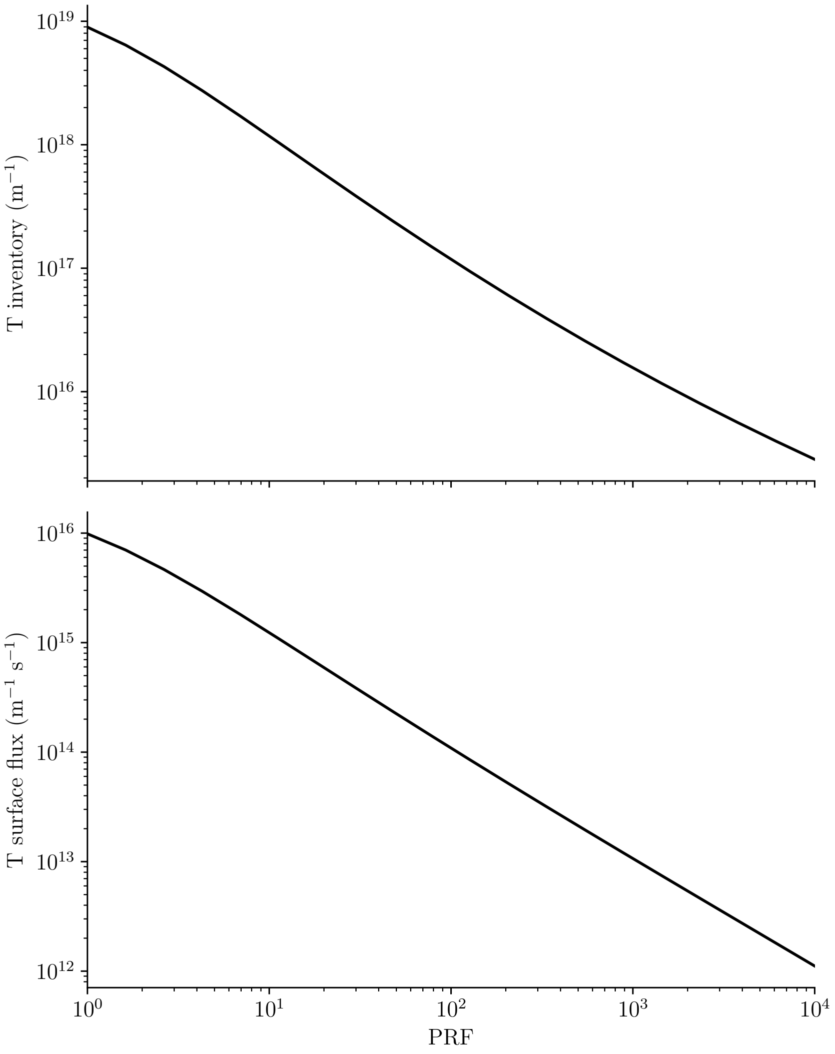

Figure 5.14: Steady-state tritium inventories in the BZ pipes (top) and surface flux at the BZ pipes coolant interfaces (bottom), varying the enforced PRF

The tritium inventory is observed to decrease at a constant rate with the PRF, though not in an entirely proportional manner. Specifically, the tritium inventory decreases from 9.0×10^{18} to $2.8 \times 10^{15}\,\mathrm{m}^{-1}$, a reduction by a factor of approximately 3100, when applying a PRF of 1×10^4. Additionally, the coolant fluxes are shown to reduce proportionally with the PRF, as expected by the derived behaviour law, with the steady-state surface flux decreasing by 4 orders of magnitude when a PRF of 1×10^4 is applied. This demonstrates the significant effect the tritium permeation barrier could have on reducing permeation into the cooling channels and minimising localised inventory build-up within the BZ pipes. Consequently, more tritium can be efficiently extracted from the WCLL system, enhancing overall performance and safety.

Conclusions

The WCLL is one of the proposed breeding blanket concepts for the DEMO fusion reactor. Multiphysics tritium transport simulations have been performed using FEniCS and FESTIM on the WCLL v0.6b geometry to evaluate its performance and investigate factors influencing tritium transport behaviour. Various parameter uncertainties have been tested, and models have been developed to account for the effects of neutron damage and a permeation barrier on tritium transport in the WCLL.

Key findings

A series of parametric studies have been conducted to understand tritium transport dynamics within the WCLL. The final and most critical study investigated the impact of uncertainties in tritium solubility in PbLi. Variations in solubility values, spanning two orders of magnitude, significantly influenced tritium transport. These findings highlight that the uncertainty in PbLi solubility has the most considerable impact on tritium transport behaviour in the WCLL, underscoring the need to refine the measurement and modelling of tritium solubility to improve model accuracy.

This work also introduces a new mathematical model to describe hydrogen traps induced by displacement damage in tungsten, including trap creation and annealing. The parameterisation methodology is detailed for direct application to other materials. TDS data from damaged samples annealed at various temperatures were analysed and fitted to obtain the model's annealing parameters. Additionally, TDS data from deuterium-loaded tungsten samples, damaged at different doses at 800 K, identified five extrinsic traps. The evolution of trap density with damage level provided the trap creation parameters. With the model parameterised, the impact of damage-induced traps on tritium transport within the WCLL was studied, focusing on the tungsten FW. These traps caused the tritium inventory in the FW to double within minutes and increase 700-fold over six days. Despite the elevated inventories, tritium diffusion was primarily confined to the tungsten armour's first 0.3 mm, suggesting that targeted techniques like baking or laser heating could effectively release tritium for recovery. However, there is a lack of experimental data for Eurofer, a critical component that will both experience high levels of neutron damage and interact with the tritium from the PbLi breeder. The study emphasised the potentially severe impact of similar trap-creation effects in Eurofer, which could disrupt the global fuel cycle and complicate decommissioning.

A method for implicitly modelling permeation barriers has been developed to consider their influence in macroscopic or component-scale models. By manipulating the solubility of tritium in the BZ pipes, the permeation into the eurofer from PbLi can be significantly reduced, emulating the effects of a permeation barrier. A study assessed the effectiveness of such a barrier applied to the BZ pipes within the WCLL, focusing on localised inventories and permeation into the cooling channels. The findings highlighted the crucial role of permeation barriers in reducing tritium permeation into cooling channels and minimising localised inventory build-up, thereby enhancing the WCLL system's overall performance and safety.

Contributions to the field

The parameterisation method detailed in Chapter 4 offers a practical approach for approximating how neutron damage may influence hydrogen trapping dynamics in structural materials within fusion reactor components. This method significantly enhances our understanding of material behaviour under neutron irradiation by providing a robust framework for estimating its effects. The approach integrates complex physical phenomena into computational models, allowing for more accurate predictions and informing the design and maintenance of fusion reactor systems. The findings and methodology were published, demonstrating their significance to the field [216]. This contribution is particularly crucial as it addresses a key challenge in fusion technology.

The implicit modelling methods presented in Chapter 5 offer an efficient approach to account for permeation barrier effects in macroscopic FEM models of breeding blanket components. This method streamlines the process of incorporating detailed material behaviours into large-scale simulations, accounting for potential permeation barriers and increasing the accuracy of predictions related to tritium retention and release. The techniques developed provide a valuable tool for engineers and researchers to model the effects of permeation barriers, facilitating more comprehensive analyses of the WCLL's performance.

Another contribution of this research is the development of the FESTIM code, a hydrogen transport code initially in version v0.6 at the commencement of this work. FESTIM has been subsequently developed to model the WCLL and beyond, significantly expanding its capabilities and potential use cases. This development has provided a valuable tool to the hydrogen transport community. Central to the work of this PhD, FESTIM's evolution has enhanced its functionality and versatility. Development began on the most significant update, version v2.0, in October 2023, marking a major milestone in its ongoing enhancement. Integrating the newly released DOLFINx solver from the FEniCS project necessitated substantial modifications to FESTIM's core architecture. The solver's significant improvements in parallel computing and performance have prompted a comprehensive restructuring of FESTIM to eliminate technical debt and fully utilise these enhancements. Extensive consultations with the hydrogen transport modelling community have shaped FESTIM 2.0's development priorities. Critical feedback emphasised the need for advanced features like multi-level trapping and multi-species transport for complex simulations. A dedicated Slack channel and Discourse forum were launched to enhance community engagement and streamline communication. These channels facilitate dynamic interaction, support troubleshooting, and serve as valuable resources for new and experienced users.

Limitations

The work completed relies on certain physical assumptions, some conservative to represent worst-case scenarios, ensuring the robustness of critical findings. However, other assumptions were necessary to manage uncertainties and may impact the model's fidelity.

One significant limitation is the absence of an explicit model for the water coolant. This omission means there was an incomplete representation of non-linear cooling effects across the entire domain. Furthermore, hydrogen isotopes returning from the coolant are not accounted for. Instead, a standard heat transfer coefficient was employed, and a perfect extraction system for the coolant was assumed, simplifying the complex interactions in reality.

Technical limitations also arise from the development issues associated with FESTIM. A notable example is the exclusion of deuterium due to FESTIM's current inability to model more than one diffusing mobile species simultaneously. This restriction limits the study's scope and ability to capture the behaviour of all relevant isotopes fully. Furthermore, the weak coupling of different physical phenomena in the model means that more complex transients, such as ramp-up and ramp-down scenarios, could not be adequately addressed. This limitation reduces the model's applicability to dynamic operational conditions. Aspects of the transport behaviour of tritium have been assumed to be negligible. Yet, thermophoresis and mechanical field phenomena may influence tritium transport in the WCLL.

Notably, the lack of experimental data to validate the multiphysics model presents a significant challenge. Without validation against real-world data, the model's predictions remain theoretical. They may not fully capture the intricacies of tritium transport and behaviour within the WCLL. These limitations collectively highlight the areas where future research and development are needed to enhance the accuracy and reliability of tritium transport models.

Several key assumptions have been made in the design of the introduced trap creation model, including the assumption that values K and A are constant. Furthermore, the damage rate Φ itself is also a function of temperature, yet has not been considered, as dpa represents the whole process of lattice agitation and relaxation, which will change depending on temperature.

Recommendations for future work

In 2023, a significant update to the WCLL design was introduced, primarily affecting the structuring and layout of the BZ cooling pipes. The update maintained the single module segment approach and the dual cooling circuits for the FW and BZ, continuing to use DWT's for BZ cooling. Fundamental changes include modifying the DWT and FW layout to address non-uniform temperature distributions and volumetric nuclear heating. Specifically, the number of FW channels per slice in the lower region of the Outboard Blanket (OB) segments was increased from four to six, and the number of DWTs in the central part of the outboard blanket was increased from 22 to 24. Similar adjustments were made for the inboard blanket (IB). While these changes improve thermal management, they also increase the water content in the WCLL BB, potentially impacting the TBR. Future work on tritium transport modelling in the WCLL would need to account for such design updates. Furthermore, more complex transients such as ramp-up, ramp-down and cycling could be investigated, as well as some nuanced perturbation incidents such as a Loss Of Coolant Accident (LOCA). In addition, as DEMO is still within the pre-conceptual design stage, there is a distant lack of continuity between the data sources required for work such as that completed within this work. In a perfect world, once a design is confirmed for DEMO, a single standard plasma scenario can derive all the relevant parameter values for a multiphysics model of the WCLL.

Alternatively, the ITER TBM WCLL design could be adopted, as this will allow researchers to leverage the comprehensive data gathered during ITER's TBM experimental campaigns, facilitating a validation case for the multiphysics WCLL model. This integration will enhance the robustness of the models and ensure that the findings are directly applicable to real-world fusion reactor scenarios.

The physics within the WCLL model could be extended, accounting for buoyancy and MHD effects on the flow of the PbLi. Incorporating these effects will provide a more comprehensive understanding of fluid dynamics within the WCLL. This extension is critical for accurately predicting the behaviour of the liquid metal breeder under the influence of magnetic fields and temperature gradients.

Including deuterium implantation from the plasma will enhance the fidelity of the transport behaviour within the FW. Additionally, hydrogen coming from the water coolant could be accounted for. These aspects are vital for understanding the full scope of hydrogen isotope behaviour within the reactor environment. Future work could develop sophisticated models that capture the complex dynamics of isotope exchange within the WCLL.

Extending the damage-induced trap creation model to Eurofer will provide valuable insights into its long-term behaviour of tritium transport dynamics and retention levels under neutron irradiation. For tungsten, further development of the model should consider the effects of present hydrogen isotopes in the material while exposed to damage, which has been shown to play a significant role in trap creation and annealing processes. Additionally, validating the model using neutron damage instead of self-damaging ions will ensure that the results are more representative of actual reactor conditions, thereby increasing the reliability and applicability of the findings to real-world scenarios.

Appendices

Appendix A

CFD verification: Lid driven cavity

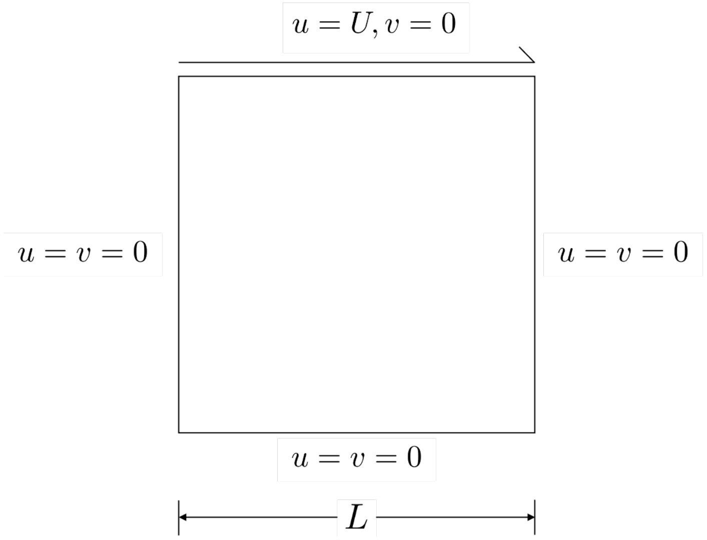

Figure A.1: Lid driven cavity problem

The lid-driven cavity is a classic benchmark problem in computational fluid dynamics (CFD) and fluid mechanics. It is used to study the behaviour of viscous, incompressible fluid flow within a confined domain. The lid-driven cavity setup consists of a square or rectangular container, typically with no-slip boundary conditions on all walls except for one, where the lid (top boundary) moves at a constant velocity, U (See Figure A.1).

$$u(x = 0) = (0, 0) \tag{A.1a}$$
$$u(x = 1) = (U, 0) \tag{A.1b}$$
$$u(y = 0) = (0, 0) \tag{A.1c}$$
$$u(y = 1) = (0, 0) \tag{A.1d}$$

A prescribed velocity profile is imposed on the lid, typically uniform or having a particular profile. The flow within the cavity is assumed to be incompressible (density remains constant) and viscous (governed by the Navier-Stokes equations). The objective of solving the lid-driven cavity problem is to compute the velocity and pressure fields within the cavity, given the boundary conditions, which can then be compared to published benchmark solutions to validate the model. Four cases were considered in which prescribed Reynolds numbers were imposed: 400, 1000, 5000 and 10000. These values were chosen as there are published benchmark solutions for these cases [164]. The agreement between the computed results and the published benchmark solutions is excellent, as illustrated in Figure A.2. A maximum absolute error recorded between the computed values and benchmark was 0.71%.

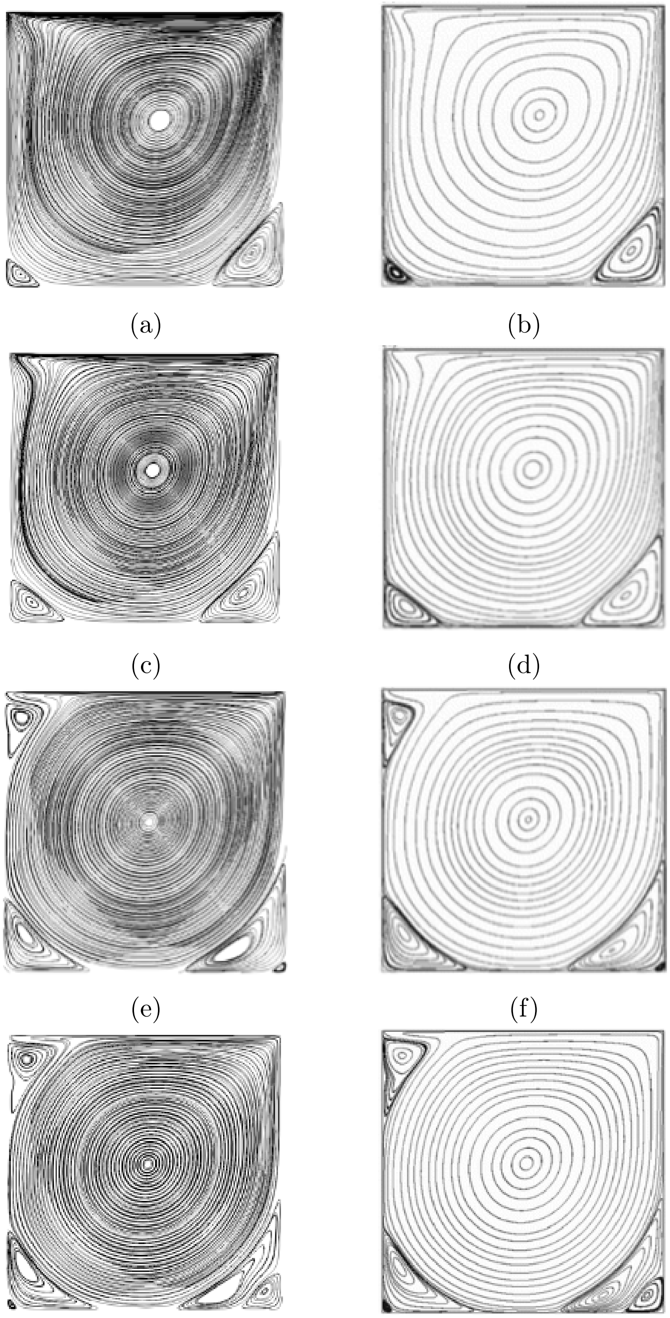
(a) (b)
(c) (d)
(e) (f)
(g) (h)

Figure A.2: Re = 400 (a), Re = 1000 (c), Re = 5000 (e), Re = 10000 (g), compared to its respective counterpart reference solution (b), (d), (f) and (h) [164]

Appendix B

Mesh convergence study

Generally, increasing the number of elements in the mesh enhances the solution's accuracy by better resolving steep gradients and complex geometries. However, this improvement comes at a cost. As the mesh is refined and the number of elements increases, the computational resources required to solve the equations grow respectfully. However, in mesh refinement, there is a point of diminishing returns where further increases in the number of elements yield negligible improvements in accuracy. Beyond this point, the additional computational burden does not justify the minor gains in precision, making it crucial to determine an optimal mesh density. This leads to a trade-off between accuracy and computational efficiency. Therefore, a mesh convergence study was conducted to analyse the impact of mesh density on tritium transport in the WCLL model.

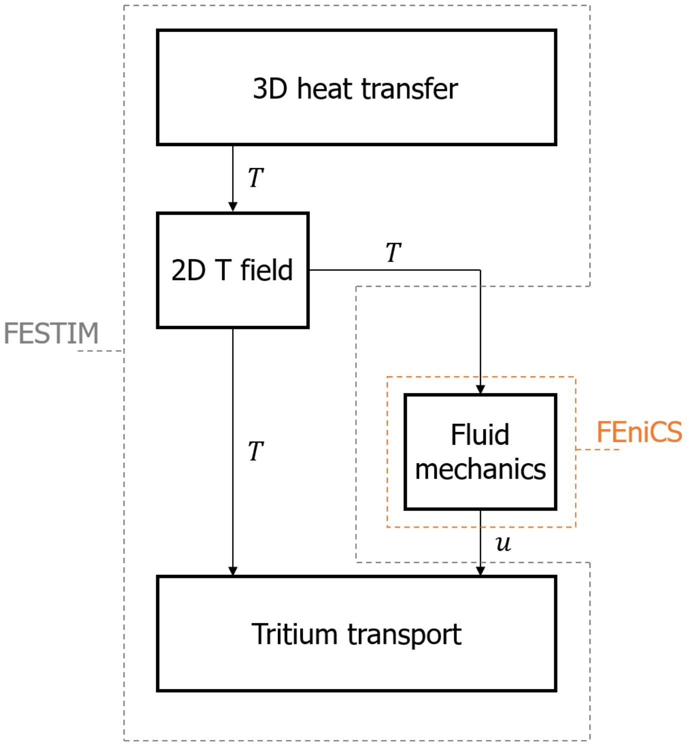

Figure B.1: Simulation workflow for multiphysics modelling of the WCLL

The reference results case for the mesh convergence study focused on the tritium transport simulation of the WCLL in a steady state. However, given the multiphysics nature of the modelling, the full simulation workflow was conducted for each iteration (see Figure B.1).

This workflow began with a 3D heat transfer simulation, where a central slice was taken to obtain the temperature field for the 2D domain. This temperature field was then used in the subsequent fluid mechanics simulation to model the velocity field. Finally, the tritium transport simulation employed both the temperature and velocity fields. This approach ensured that each process step accurately captured all relevant physical phenomena.

The WCLL geometry was divided into five distinct volume subdomains: the breeding zone, first wall, structure, baffle plate, and breeding zone pipes (see Figure B.2). This division was essential as different areas of the model exhibit varying dynamics and gradients, allowing for optimal mesh density specific to each domain. Ideally, this would result in a five-dimensional optimisation problem, with all factors varied until an optimal balance between accuracy and computational efficiency was achieved. However, a pragmatic approach was taken by prioritising the subdomains regarding their influence on the overall tritium transport. The subdomains were prioritised as follows: first, the PbLi fluid subdomain, followed by the structure, breeding zone pipes, and baffle plate, and finally, the tungsten first wall. This prioritisation was based on the fact that the PbLi is the largest tritium source in the system. Optimising the mesh for this subdomain ensures that the velocity field, which significantly influences tritium transport, is accurately resolved. The velocity field resolution was particularly challenging due to its high computational demand, requiring substantial amounts of RAM for larger meshes. Consequently, the mesh refinement that could be achieved with the available computational resources reached a practical limit. Following the PbLi subdomain, attention was given to the eurofer structure and connected subdomains. Although the breeding zone pipes should ideally be further divided to account for differing dynamics and tritium exposure, the approach aimed to balance precision and computational feasibility. Finally, the tungsten first wall region was optimised. This systematic prioritisation ensured that the most critical aspects of the model were accurately represented while maintaining manageable computational costs.

The WCLL geometry was meshed using Salome 9.8.0 [168]. Initially, a mesh with a standard maximum cell size of 0.01 m was created. Following this, heat transfer, fluid dynamics, and tritium transport simulations were performed to record the tritium inventory within the considered subdomains. The maximum cell size was then iteratively reduced by 10%, resulting in an increase in the total number of cells within the mesh until computational resources were exhausted, which occurred at around 1.5 million cells. The tritium inventory evaluated within the respective subdomains using the largest mesh size served as the reference solution, against which the results from smaller mesh sizes were compared. The tritium inventory is defined as the total integrated mobile and trapped concentrations of hydrogen. The solution was considered converged if the mesh size resulted in an inventory value within 0.5 % of the reference solution. As the mesh size increased, the time required to evaluate the steady-state solution rose significantly. For instance, the evaluation time increased from 137 s with the smallest mesh size of 48 970 cells to 4157 s with the largest mesh size of 1.5×10^6 cells. This dramatic increase in computational time illustrates the importance of optimising mesh density to balance accuracy and computational efficiency (see Figure B.3).

For the PbLi subdomain, despite using a series of meshes spanning close to two orders of magnitude in size, the resulting tritium inventories varied by only within 0.5% of the reference

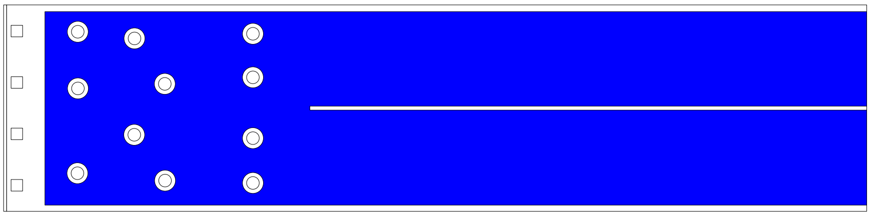

(a) PbLi domain

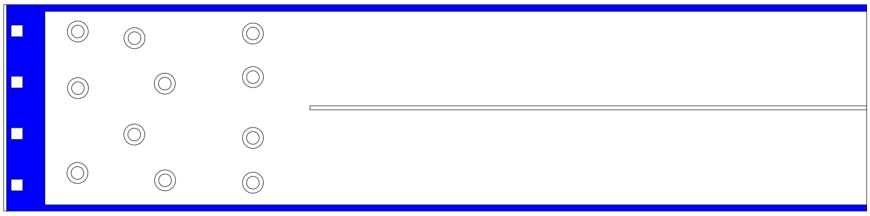

(b) Structure domain

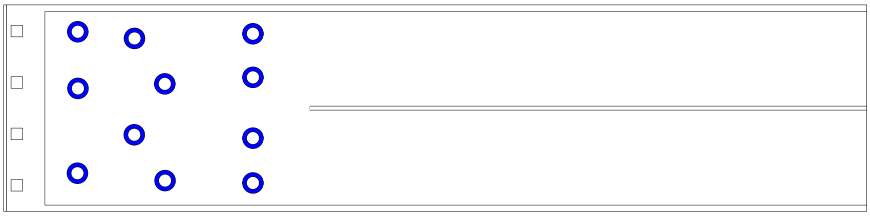

(c) BZ pipes domain

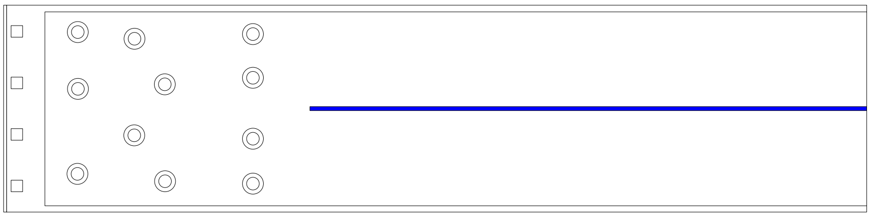

(d) Baffle plate domain

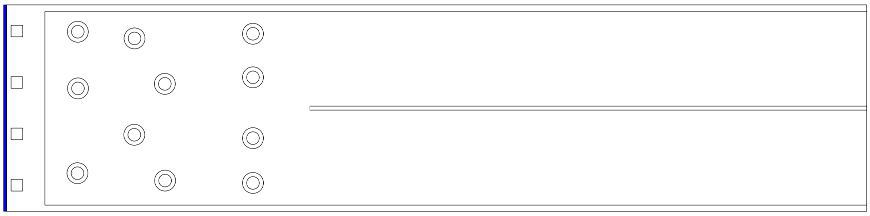

(e) Tungsten FW

Figure B.2: Mesh domains considered in the mesh refinement

solution. This indicates a lack of sensitivity in tritium inventory to the discretisation level (see Figure B.4). This limited sensitivity is likely since only diffusion occurs within the

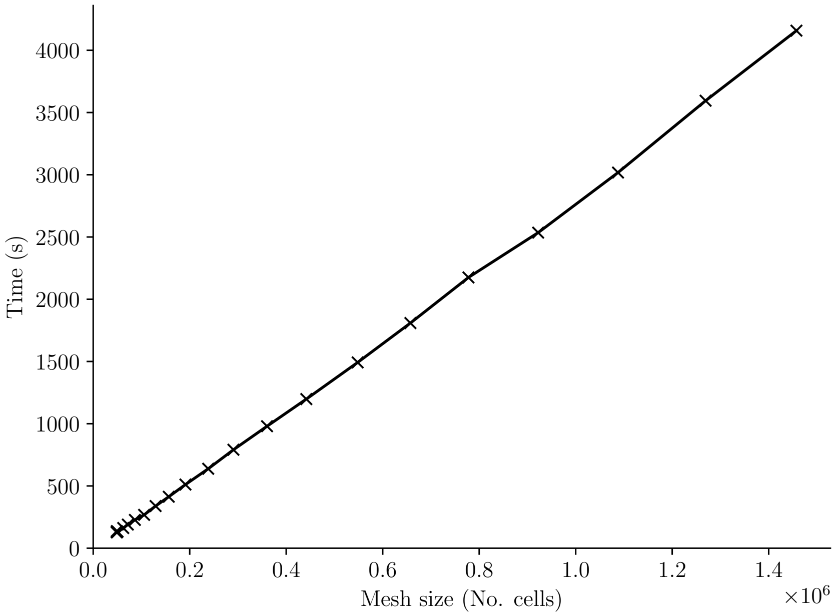

Figure B.3: Time to run steady state simulation with increasing mesh size

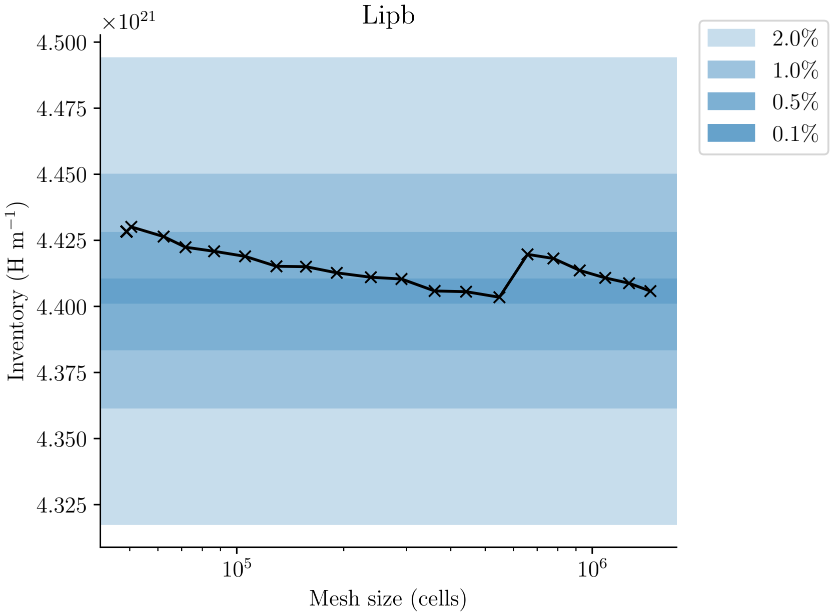

Figure B.4: Tritium inventories with increasing mesh size in the PbLi subdomain

PbLi subdomain, with no trapping mechanisms to mitigate diffusion, thus not inducing large gradients. As a result, even a coarse discretisation is sufficient to achieve tritium inventory levels within 0.5% of the reference solution. This allows for a relaxation in the mesh size requirements for the PbLi subdomain. This finding is particularly significant for the WCLL model, as the PbLi is the largest subdomain considered. Therefore, permitting a coarser discretisation level in this subdomain reduces the mesh size required for an optimal solution. This relaxation in mesh size for the PbLi subdomain contributes significantly to the model's overall computational efficiency, enabling more manageable and cost-effective simulations without compromising accuracy. However, an anomaly is observed in the resulting inventory when the mesh size grows beyond 6×10^5 cells, in which a sudden increase in the inventory is observed (see Figure B.4). This abnormality most likely arises from the meshing algorithm used by SALOME: NETGEN [243]. It is possible that as the mesh becomes more refined, a point was reached where the boundary layer formed by the flowing PbLi is better captured. Yet, the specific reason for this sudden increase in inventory is unknown and requires further investigation.

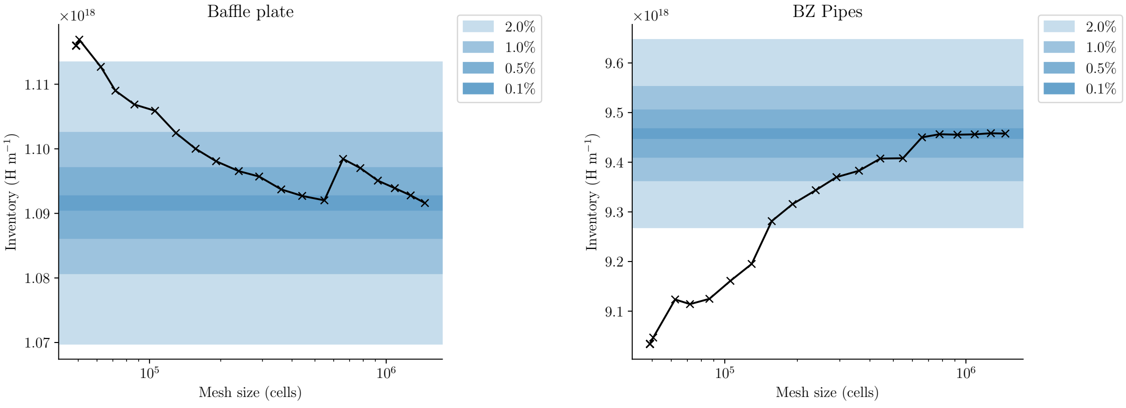

(a) Baffle plate subdomain

(b) BZ pipes subdomain

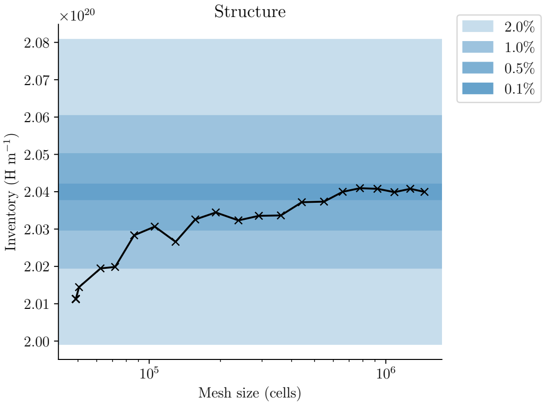

(c) Structure subdomain

Figure B.5: Tritium inventories with increasing mesh size in the eurofer subdomains

For the eurofer subdomains, it can be observed that the baffle plate and BZ pipes domains exhibit the highest sensitivity in tritium inventory to the discretisation level. The BZ pipes, in particular, show a difference of more than 5% with the coarsest mesh compared to the reference solution (see Figures B.5a and B.5b). A significant difference in the inventories is expected in the BZ pipes inventories, given that these pipes are likely to have the largest gradients of tritium concentration. This is due to a tritium source at the PbLi interface and a tritium sink at the coolant interface across the 2.75 mm pipe wall. The gradients are further exacerbated by hydrogen trapping within the eurofer, which mitigates the diffusion process. Therefore, a higher level of refinement in the discretisation is necessary to accurately capture the transport behaviour within the BZ pipes, with inventories within 0.5% of the reference solution. This trend is also observed in the other eurofer domains, such as the structure and baffle plate. However, due to their larger areas, the same level of refinement is not necessarily required to capture all the transport behaviour across these subdomains comprehensively. Nevertheless, to enhance accuracy further, a more specified refinement could be applied at the interfaces of the eurofer with the PbLi.

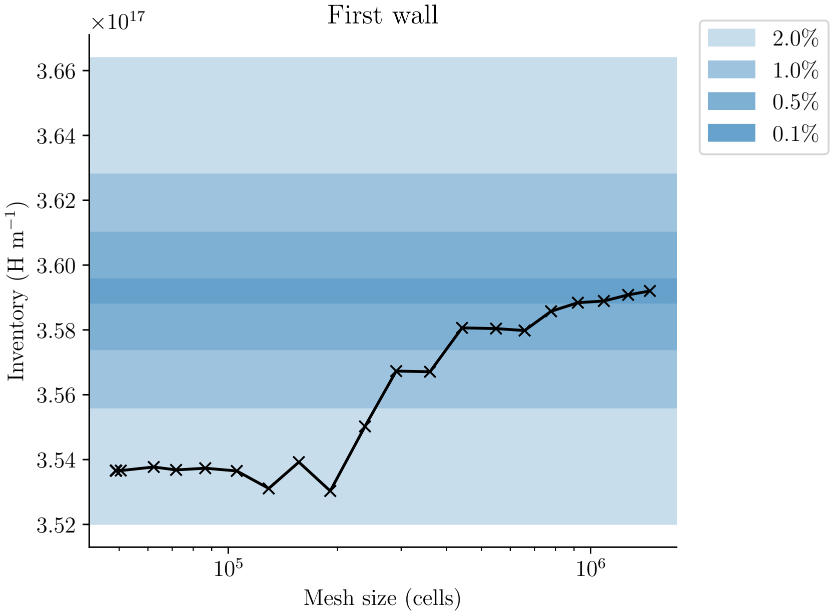

Figure B.6: Tritium inventories with increasing mesh size in the FW domain

The tungsten FW, similar to the BZ pipes, requires a significant level of refinement to fully capture tritium transport behaviour and achieve a measured inventory within 0.5% of the reference solution (see Figure B.6). Although the tritium source from the plasma is not as substantial as the breeder's, the gradients in mobile tritium concentration are consequently less pronounced. However, hydrogen trapping plays a much more significant role in the transport behaviour across the 2 mm tungsten subdomain. The FW subdomain considers two types of traps, which have higher densities and de-trapping energies than the single trap considered within the Eurofer. These traps significantly mitigate tritium diffusion, resulting in larger gradients in both the mobile and trapped concentrations within the FW subdomain. Therefore, a high level of mesh refinement is required in the FW subdomain to capture the transport behaviour and resulting inventory levels accurately. This ensures that the complex interplay between diffusion and trapping mechanisms is well-represented in the simulation results.

In conclusion, the mesh convergence study highlights the varying sensitivity of different sub-

Table B.1: Optimised maximum cell size values for each domain in the WCLL geometry

Subdomain	Max cell size (m)
PbLi	7.70×10^{-4}
Structure	9.00×10^{-4}
Baffle plate	3.23×10^{-4}
First Wall	3.23×10^{-4}
BZ pipes	3.23×10^{-4}

domains within the WCLL model to discretisation levels. Due to its dominant diffusion processes, the PbLi domain allows for coarser discretisation without significant loss of accuracy. In contrast, the eurofer and tungsten subdomains require finer meshes to capture the intricate transport behaviours influenced by hydrogen trapping and steep concentration gradients. The study balances computational efficiency and solution accuracy by optimising the mesh density for each subdomain. The maximum mesh size values for each subdomain in the optimised mesh are detailed in Table B.1, constituting a total mesh size of 245695 cells.

Appendix C

Influence of magnetic field

C.1 Model Description

The strong form of the steady state incompressible Navier-Stokes equation with a Lorentz force term and the continuity equation can be expressed as:

$$\rho(\mathbf{u} \cdot \boldsymbol{\nabla}\mathbf{u}) = -\boldsymbol{\nabla}p + \mu\boldsymbol{\nabla}^2\mathbf{u} + \mathbf{J} \times \mathbf{B} \tag{C.1}$$

$$\boldsymbol{\nabla} \cdot \mathbf{u} = 0 \tag{C.2}$$

Where:

$$\mathbf{J} = \sigma(-\boldsymbol{\nabla}\Phi + \mathbf{u} \times \mathbf{B}) \tag{C.3}$$

Neglecting displacement currents and assuming the fluid is electrically neutral we require that $\boldsymbol{\nabla} \cdot \mathbf{J} = 0$. This leads to an equation for the electric potential Φ:

$$\boldsymbol{\nabla}^2\Phi = \boldsymbol{\nabla} \cdot (\mathbf{u} \times \mathbf{B}) \tag{C.4}$$

for the Lorentz term $\mathbf{J} \times \mathbf{B}$, the definition for $\mathbf{J}$ is used and expanded:

$$\begin{aligned}
\mathbf{J} \times \mathbf{B} &= -\mathbf{B} \times \mathbf{J} \\
&= -\mathbf{B} \times (\sigma(-\boldsymbol{\nabla}\Phi + \mathbf{u} \times \mathbf{B})) \\
&= \sigma[-\mathbf{B} \times (-\boldsymbol{\nabla}\Phi + \mathbf{u} \times \mathbf{B})] \\
&= \sigma[(-\mathbf{B} \times -\boldsymbol{\nabla}\Phi) + (-\mathbf{B} \times (\mathbf{u} \times \mathbf{B})] \\
&= \sigma[(\mathbf{B} \times \boldsymbol{\nabla}\Phi) - (\mathbf{B} \cdot \mathbf{B})\mathbf{u} + (\mathbf{B} \cdot \mathbf{u})\mathbf{B}]
\end{aligned}$$

Thus, Eq. (C.1) can be expressed as:

$$\rho(\mathbf{u} \cdot \boldsymbol{\nabla}\mathbf{u}) = -\boldsymbol{\nabla}p + \mu\boldsymbol{\nabla}^2\mathbf{u} + \sigma[(\mathbf{B} \times \boldsymbol{\nabla}\Phi) - (\mathbf{B} \cdot \mathbf{B})\mathbf{u} + (\mathbf{B} \cdot \mathbf{u})\mathbf{B}] \tag{C.5}$$

C.1.1 Weak form evaluation

To find the weak form of the momentum equation, it is first multiplied for a test function $\mathbf{v}$, defined in a suitable space V, and integrated with respect to the domain Ω.

$$\begin{aligned}
\int_\Omega \rho(\mathbf{u} \cdot \boldsymbol{\nabla}\mathbf{u}) \cdot \mathbf{v} = -\int_\Omega \boldsymbol{\nabla}p \cdot \mathbf{v} + \int_\Omega \mu\boldsymbol{\nabla}^2\mathbf{u} \cdot \mathbf{v} \\
+ \sigma\left(\int_\Omega (\mathbf{B} \times \boldsymbol{\nabla}\Phi) \cdot \mathbf{v} - \int_\Omega (\mathbf{B} \cdot \mathbf{B})\mathbf{u} \cdot \mathbf{v} + \int_\Omega (\mathbf{B} \cdot \mathbf{u})\mathbf{B} \cdot \mathbf{v}\right)
\end{aligned}$$

Counter-integrating by parts and using the vector calculus identities:

$$\boldsymbol{\nabla}\cdot(A\cdot\boldsymbol{\nabla}B)=\boldsymbol{\nabla}A\cdot\boldsymbol{\nabla}B+B\cdot\boldsymbol{\nabla}^2A \tag{C.6}$$

$$\boldsymbol{\nabla}\cdot(A\cdot B)=\boldsymbol{\nabla}A\cdot B+A\cdot(\boldsymbol{\nabla}\cdot B) \tag{C.7}$$

And Gauss's theorem (if $\partial\Omega$ is sufficiently regular):

$$\int_\Omega \boldsymbol{\nabla}\cdot(A\cdot\boldsymbol{\nabla}B)=\int_{\partial\Omega}(A\cdot\boldsymbol{\nabla}B)\cdot\mathbf{n}$$

The diffusive and pressure terms can be expressed as:

$$\int_\Omega \mu\boldsymbol{\nabla}^2\mathbf{u}\cdot\mathbf{v}=-\int_\Omega \mu\boldsymbol{\nabla}\mathbf{u}\cdot\boldsymbol{\nabla}\mathbf{v}+\int_{\partial\Omega}\mu\mathbf{v}\boldsymbol{\nabla}\mathbf{u}\cdot\mathbf{n}$$
$$\int_\Omega \boldsymbol{\nabla}p\cdot\mathbf{v}=-\int_\Omega p\boldsymbol{\nabla}\cdot\mathbf{v}+\int_{\partial\Omega}p\mathbf{v}\cdot\mathbf{n}$$

However, the terms are null because $\mathbf{v}=0$ on $\partial\Omega$. For the continuity equation, this is multiplied for a test function $\mathbf{q}$ belonging to space Q and integrated in the domain Ω:

$$\int_\Omega q(\boldsymbol{\nabla}\cdot\mathbf{u})=0$$

Regarding the electrical potential in Eq. (C.4) the RHS $\boldsymbol{\nabla}\cdot(\mathbf{u}\times\mathbf{B})$ can be expressed as:

$$\boldsymbol{\nabla}\cdot(\mathbf{u}\times\mathbf{B})=(\boldsymbol{\nabla}\times\mathbf{u})\cdot\mathbf{B}-(\boldsymbol{\nabla}\times\mathbf{B})\cdot\mathbf{u}$$

Thus the LHS can be integrated using the same method as the diffusive term in Eq. (C.5). For Eq. (C.4), this is expressed as:

$$\boldsymbol{\nabla}^2\Phi=(\boldsymbol{\nabla}\times\mathbf{u})\cdot\mathbf{B}-(\boldsymbol{\nabla}\times\mathbf{B})\cdot\mathbf{u} \tag{C.8}$$

Eq. (C.6) is then multiplied for test function $\mathbf{q2}$ belonging to space $Q2$ and integrated in the domain Ω

$$\int_\Omega \boldsymbol{\nabla}\phi\cdot\boldsymbol{\nabla}\mathbf{q2}=\int_\Omega((\boldsymbol{\nabla}\times\mathbf{u})\cdot\mathbf{B})\cdot\mathbf{q2}-\int_\Omega((\boldsymbol{\nabla}\times\mathbf{B})\cdot\mathbf{u})\cdot\mathbf{q2}$$

Thus the weak formulation for Eq. (C.5) is expressed as:

$$\int_\Omega \rho(\mathbf{u}\cdot\boldsymbol{\nabla}\mathbf{u})\cdot\mathbf{v}-\int_\Omega p\boldsymbol{\nabla}\cdot\mathbf{v}+\int_\Omega \mu\boldsymbol{\nabla}\mathbf{u}\cdot\boldsymbol{\nabla}\mathbf{v}- \tag{C.9}$$

$$\sigma\left(\int_\Omega(\mathbf{B}\times\boldsymbol{\nabla}\Phi)\cdot\mathbf{v}+\int_\Omega(\mathbf{B}\cdot\mathbf{B})\mathbf{u}\cdot\mathbf{v}-\int_\Omega(\mathbf{B}\cdot\mathbf{u})\mathbf{B}\cdot\mathbf{v}\right)=0\quad\forall\mathbf{v}\in V \tag{C.10}$$

For Eq. (C.2):

$$\int_\Omega q(\boldsymbol{\nabla}\cdot\mathbf{u})=0\quad\forall\mathbf{q}\in Q \tag{C.11}$$

For Eq. (C.4)

$$\int_\Omega \boldsymbol{\nabla}\phi\cdot\boldsymbol{\nabla}\mathbf{q2}-\int_\Omega((\boldsymbol{\nabla}\times\mathbf{u})\cdot\mathbf{B})\cdot\mathbf{q2}+\int_\Omega((\boldsymbol{\nabla}\times\mathbf{B})\cdot\mathbf{u})\cdot\mathbf{q2}=0\quad\forall\mathbf{q2}\in Q2 \tag{C.12}$$

C.2 Benchmark case

The rectangular duct flow problem is a classic benchmark case in MHD used to study the interaction between a conducting fluid and a magnetic field [244]. This scenario is highly relevant in various engineering and physics applications, such as fusion reactors, cooling systems in nuclear reactors, and certain astrophysical phenomena. The primary focus is on understanding how the presence of a magnetic field influences the behaviour of an incompressible, electrically conducting fluid flowing through a duct.

In this problem, the geometry consists of a rectangular duct with dimensions $a \times b$. For this case, $a = b = 2L$ and the length of the duct is equal to $20L$. The fluid flow is driven by a pressure gradient along the x-axis, resulting in a fully developed velocity profile that does not change along the flow direction. A uniform magnetic field is applied perpendicular to the flow along the $-y$-axis (see Figure C.1). The interaction between the fluid and the magnetic field is characterised by the Hartmann number, Ha, which determines the relative significance of the magnetic forces compared to viscous and inertial forces. The Hartmann number is defined as:

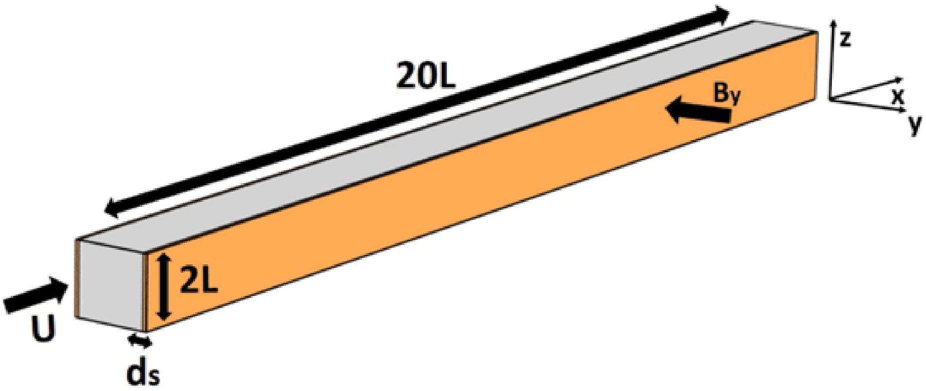

Figure C.1: Rectangular duct geometry [244]

$$\mathrm{Ha} = B \cdot L \cdot \sqrt{\frac{\sigma_{\mathrm{e}}}{\mu}} \tag{C.13}$$

where B is the magnetic field strength in units T, L is the characteristic length scale of the problem in units m, σ_{e} is the electrical conductivity of the fluid in units $\mathrm{S\,m^{-1}}$ and μ is the fluid viscosity in units Pa s.

The geometry consists of an inlet and outlet at either end of the duct

$$\Gamma_{\mathrm{Inlet}} = (z = 0) \tag{C.14}$$

$$\Gamma_{\mathrm{Outlet}} = (z = 20L) \tag{C.15}$$

With walls on all sides of the cross-section. Two of the walls, on the y-axis plane are further defined as the Hartmann walls:

$$\Gamma_{\mathrm{Walls}} = (x = 0), (x = 2L), (y = 0), (y = 2L) \tag{C.16}$$

$$\Gamma_{\mathrm{HW}} = (y = 0), (y = 2L) \tag{C.17}$$

The benchmark can be used to verify two cases, the first of which where the electrical potential, Φ is enforced as zero on the Hartmann walls:

$$\Phi = 0 \quad \text{on } \Gamma_{\text{HW}} \tag{C.18}$$

An additional case is considered in which all the walls are fully insulated, where the gradient of the electrical potential is 0:

$$\frac{\partial \Omega}{\partial x} = 0 \quad \text{on } \Gamma_{\text{HW}} \tag{C.19}$$

Both cases were tested with Hartmann numbers varying from 0 to 100 and compared to published analytical solutions [245, 246]. Results are shown in Figures C.2 and C.3.

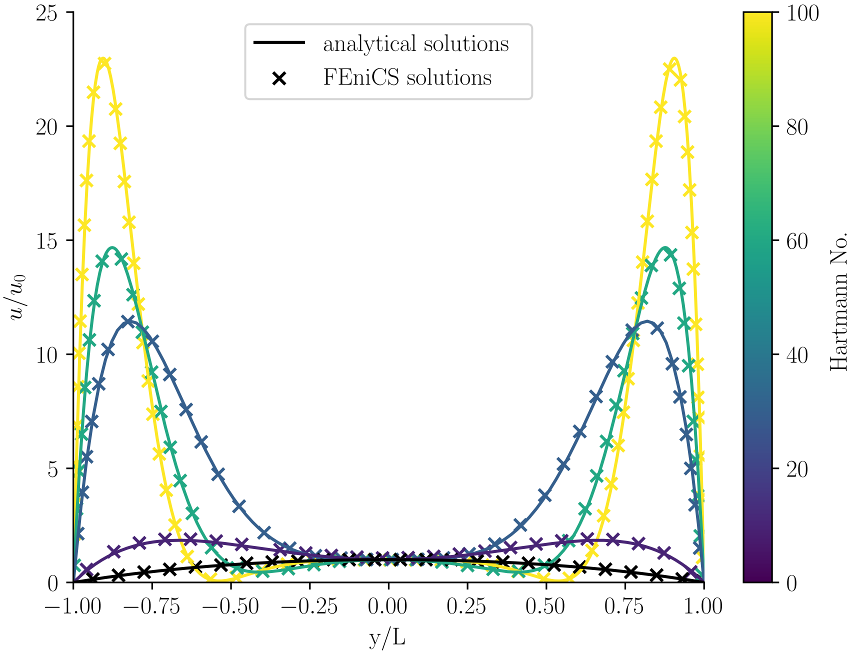

Figure C.2: Fully conductive case ($\Phi = 0$ on Γ_{HW}) compared to analytical solutions [245]

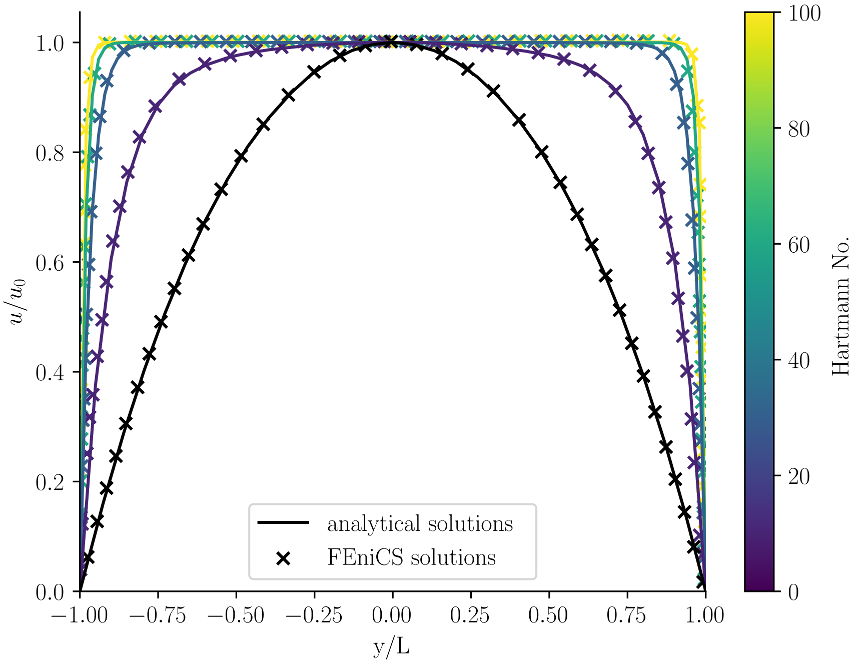

Figure C.3: Fully insulated case ($\frac{\partial \Phi}{\partial x} = 0$ on Γ_{HW}) compared to analytical solutions [246]

Appendix D

Damaged tungsten TDS fittings

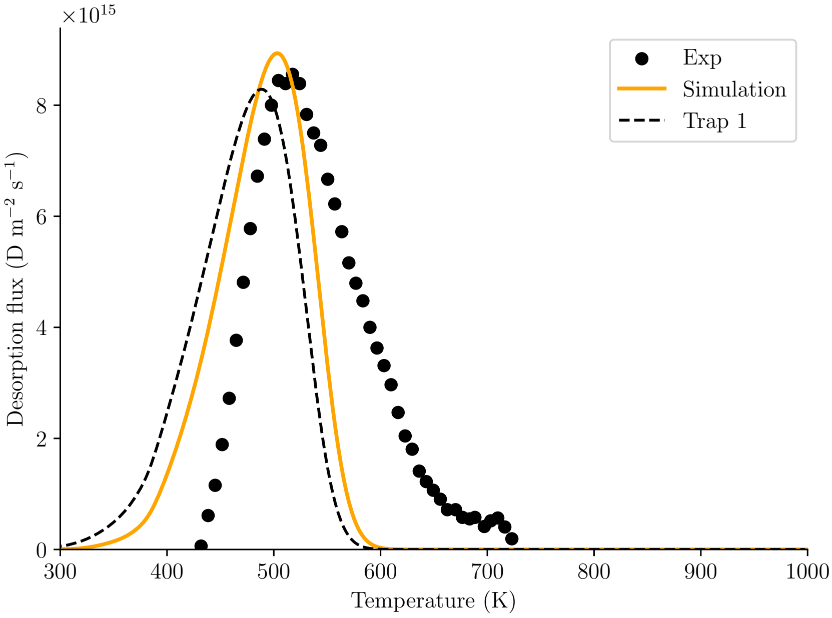

Figure D.1: TDS data for tungsten sample damaged to 0 dpa, fitted using one intrinsic trap

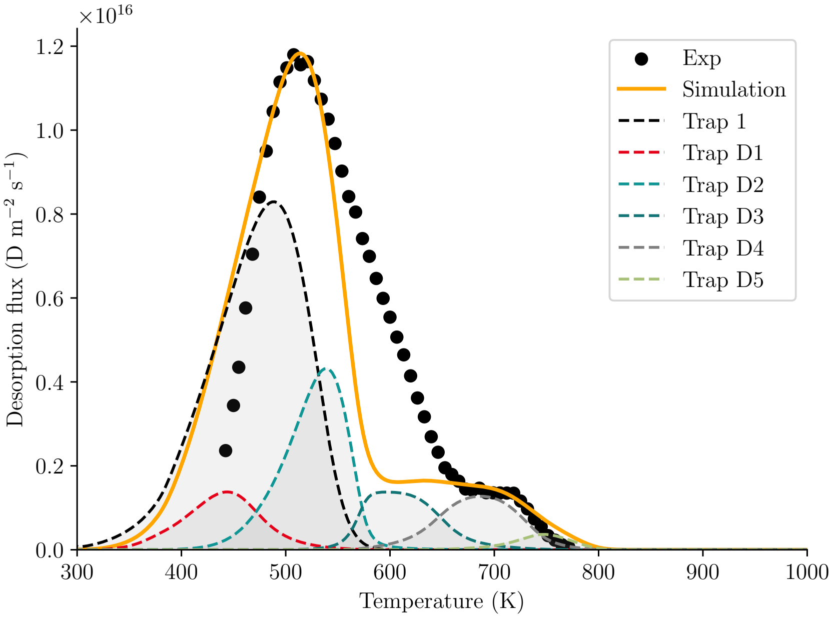

Figure D.2: TDS data for tungsten sample damaged to 0.001 dpa, fitted using one intrinsic trap and five extrinsic traps

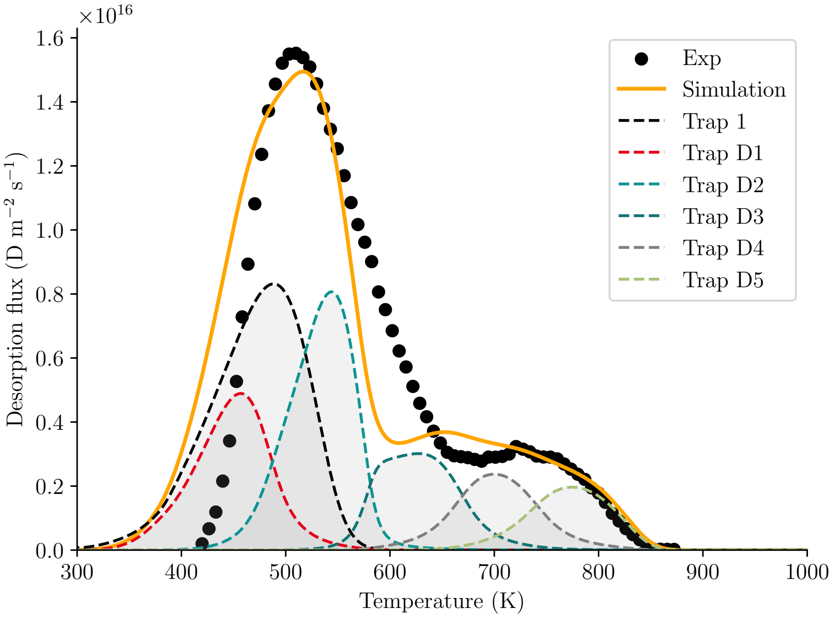

Figure D.3: TDS data for tungsten sample damaged to 0.005 dpa, fitted using one intrinsic trap and five extrinsic traps

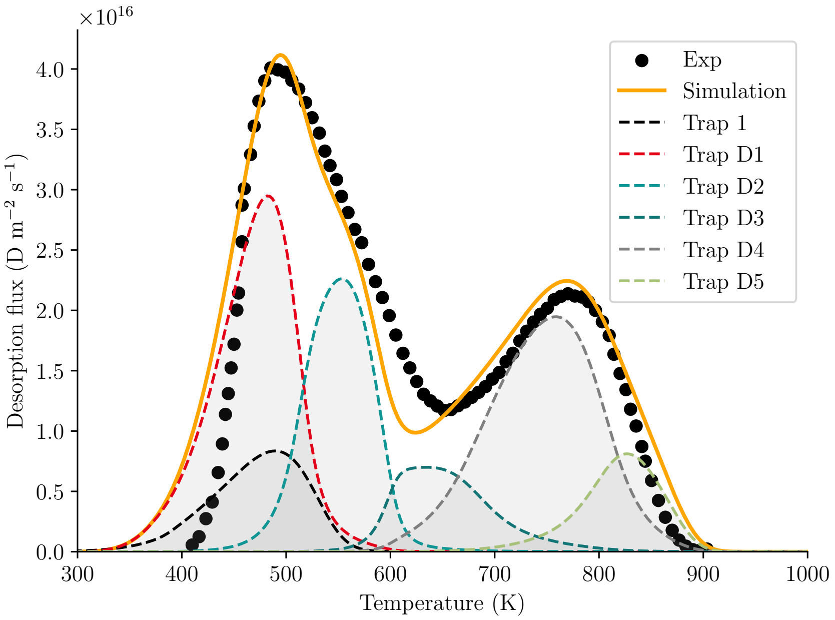

Figure D.4: TDS data for tungsten sample damaged to 0.023 dpa, fitted using one intrinsic trap and five extrinsic traps

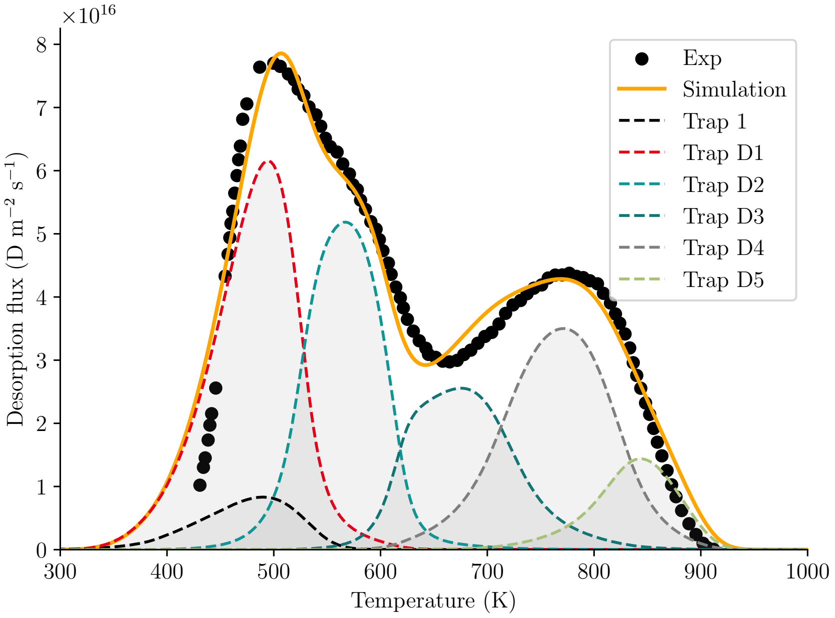

Figure D.5: TDS data for tungsten sample damaged to 0.1 dpa, fitted using one intrinsic trap and five extrinsic traps

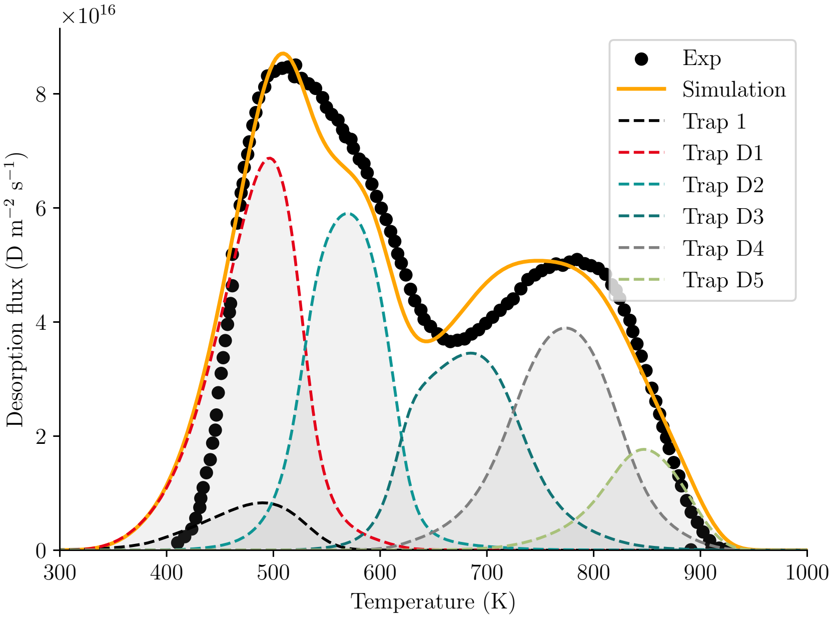

Figure D.6: TDS data for tungsten sample damaged to 0.23 dpa, fitted using one intrinsic trap and five extrinsic traps

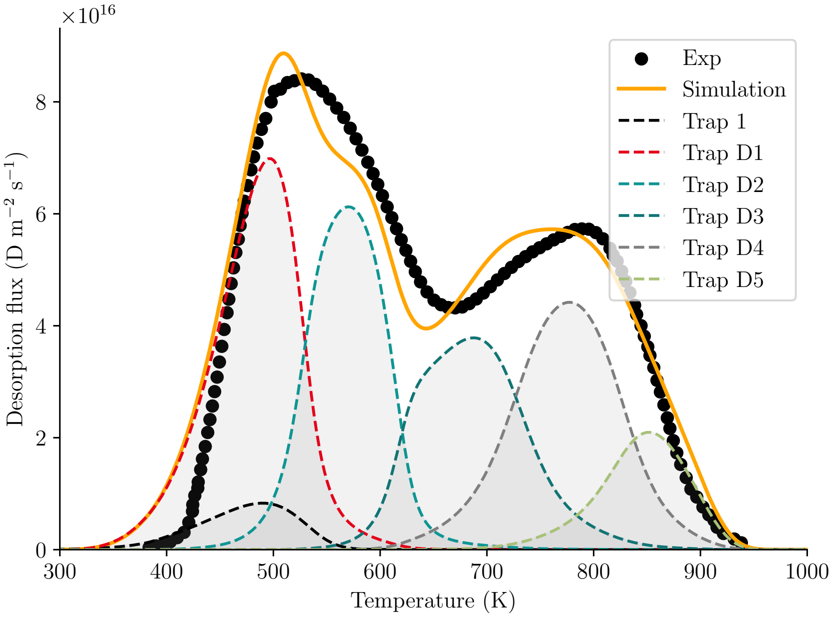

Figure D.7: TDS data for tungsten sample damaged to 0.5 dpa, fitted using one intrinsic trap and five extrinsic traps

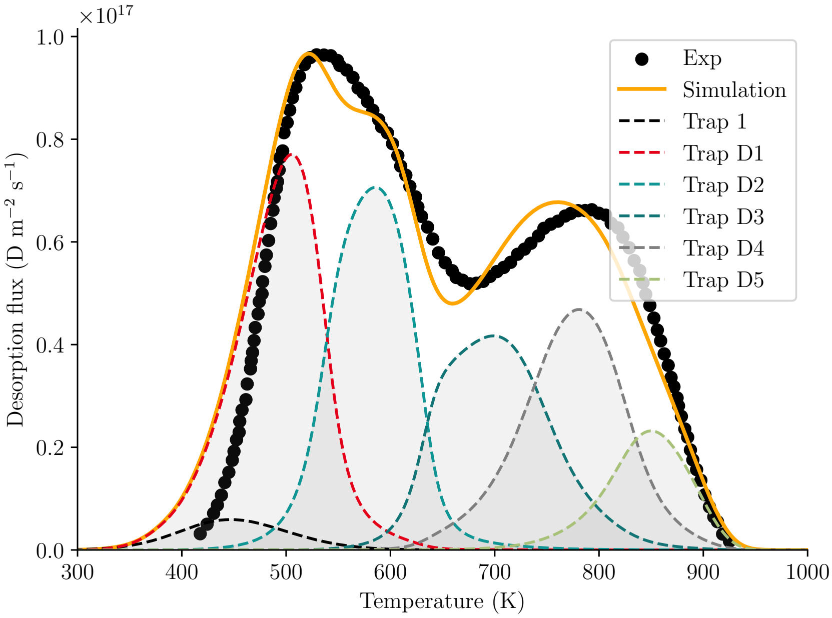

Figure D.8: TDS data for tungsten sample damaged to 2.5 dpa, fitted using one intrinsic trap and five extrinsic traps

APPENDIX E

Analytical model: Cylindrical permeation barrier

$$a_0 = \frac{\beta(c_0 - c_1)}{\ln\left(\frac{1+\gamma+\gamma'}{\gamma+\gamma'}\right) + \ln\left(\frac{(\gamma+\gamma')((1+2\gamma+\gamma')}{(\gamma')(1+\gamma+\gamma')}\right)} \tag{E.1}$$

$$a_1 = \alpha \cdot a_0 = a_3 \tag{E.2}$$

$$a_2 = a_0 \tag{E.3}$$

$$b_1 = \frac{c_0\left[\ln\left(\frac{\gamma+\gamma'}{\gamma+\gamma'+1}\right) - \alpha\beta\ln\left(\frac{\gamma+\gamma'+1}{L(\gamma+\gamma')(2\gamma+\gamma'+1)}\right)\right] + \alpha\beta c_1\ln\left(r_0\right)}{\alpha\beta\ln\left(\frac{\gamma'(\gamma+\gamma'+1)}{(\gamma+\gamma')(2\gamma+\gamma'+1)}\right) + \ln\left(\frac{\gamma+\gamma'}{\gamma+\gamma'+1}\right)} \tag{E.4}$$

$$\begin{aligned} b_2 = {} & \frac{\beta c_0\left[\alpha\beta\ln\left(\frac{\gamma+\gamma'+1}{2\gamma+\gamma'+1}\right) - \ln\left(L\left(\gamma+\gamma'+1\right)\right)\right]}{\alpha\beta\ln\left(\frac{\gamma'(\gamma+\gamma'+1)}{(\gamma+\gamma')(2\gamma+\gamma'+1)}\right) + \ln\left(\frac{\gamma+\gamma'}{\gamma+\gamma'+1}\right)} \\ & + \frac{\beta c_1\left[\alpha\beta\ln\left(\frac{\gamma'}{\gamma+\gamma'}\right) + \ln\left(L\left(\gamma+\gamma'\right)\right)\right]}{\alpha\beta\ln\left(\frac{\gamma'(\gamma+\gamma'+1)}{(\gamma+\gamma')(2\gamma+\gamma'+1)}\right) + \ln\left(\frac{\gamma+\gamma'}{\gamma+\gamma'+1}\right)} \end{aligned} \tag{E.5}$$

$$b_3 = \frac{c_1\left[\alpha\beta\ln\left(\frac{r_0(1+\gamma+\gamma')}{(\gamma+\gamma')}\right) + \ln\left(\frac{\gamma+\gamma'}{1+\gamma+\gamma'}\right)\right] - \alpha\beta c_0\ln(L(1+2\gamma+\gamma'))}{\alpha\beta\ln\left(\frac{\gamma'(1+\gamma+\gamma')}{(\gamma+\gamma')\cdot(1+2\gamma+\gamma')}\right) + \ln\left(\frac{\gamma+\gamma'}{1+\gamma+\gamma'}\right)} \tag{E.6}$$

Appendix F

Macroscopic boundary condition for permeation barriers

A recombination flux is a boundary condition that prescribes the flux at the surface based on a defined recombination coefficient and the square of the mobile population.

$$-D\boldsymbol{\nabla} c_\mathrm{m} \cdot \mathbf{n} = K_\mathrm{r} c_\mathrm{m}^2 \tag{F.1}$$

This models the formation of diatomic particles from two monoatomic particles diffusing in the bulk material. By leveraging this boundary condition, one can effectively simulate the behaviour of permeation barriers without the need for explicit barrier modelling or complex interface modifications.

The method for emulating permeation barriers using the recombination flux boundary condition is grounded in the fundamental definition of the PRF, which quantifies the flux reduction across a given boundary. The recombination flux boundary condition prescribes the flux at the surface as a function of a defined recombination coefficient and the square of the mobile population, modelling the formation of diatomic particles from two monoatomic particles diffusing in bulk. By artificially modifying the recombination coefficient, a specific PRF can be enforced, effectively emulating the behaviour of a permeation barrier. This approach allows for controlling the flux reduction at the boundary without explicitly modelling the barrier, providing a flexible and efficient method for permeation barrier simulation in various material systems.

$$-D\boldsymbol{\nabla} c_\mathrm{m} \cdot \mathbf{n} = K_\mathrm{r,eff} c_\mathrm{m}^2 \tag{F.2}$$

where:

$$K_\mathrm{r,eff} = \frac{K_\mathrm{r}}{\mathrm{PRF}} \tag{F.3}$$

This condition can emulate a PRF at a cooling channel's interface with the coolant. Consider the following domain:

A recombination flux was applied at the cooling surface, Γ_i, where $K_\mathrm{r} = 1.41 \times 10^{-26} \exp\left(0.257/k_\mathrm{B}T\right)$ was the recombination coefficient expressed in $[\mathrm{m^4\,s^{-1}}]$ [202]. A second boundary condition, fixing the concentration on the outer boundaries, Γ_o, at a concentration of $10^{18}\,\mathrm{m^{-3}}$.

The resulting PRF using this method is directly proportional to the modification factor applied to the recombination coefficient as expected (See figure F.2). This proportionality provides a straightforward and effective means of enforcing a PRF at a given boundary. By

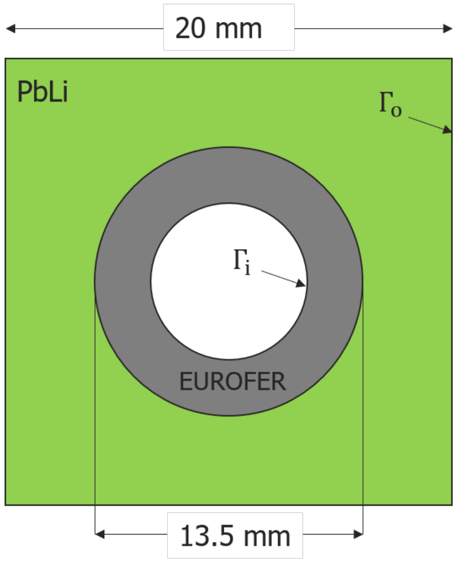

Figure F.1: 2D pipe geometry comprised of a 13.5 mm outer diameter Eurofer pipe (8 mm inner diameter) ■ within a 20 mm^2 PbLi 🟩 domain

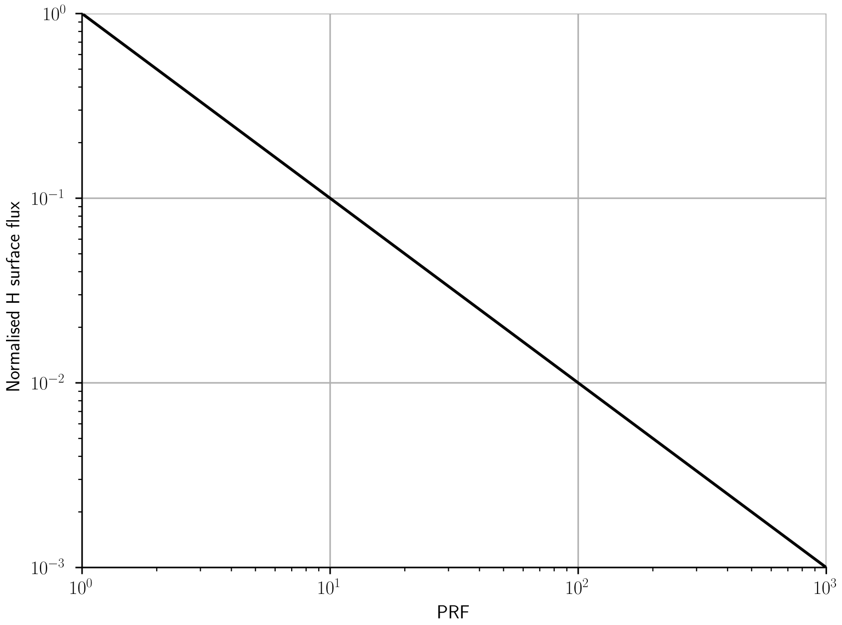

Figure F.2: Measured PRF compared to a recombination flux boundary condition against an enforced PRF value

adjusting the recombination coefficient, the flux reduction across the boundary can be precisely controlled, simulating the presence of a permeation barrier without explicitly needing to model the barrier. This method is particularly suitable when a recombination flux is enforced as a standard boundary condition, simplifying the implementation and ensuring consistent results.

However, this method is only appropriate when a recombination flux is the default boundary condition. A different approach is needed in cases where a vacuum is modelled, typically by setting a fixed concentration of zero at the boundary to emulate instantaneous recombination. To enforce a PRF in such scenarios, one can follow a similar procedure, testing over a range of values to deduce a behaviour law. The flux can still be enforced in this modified approach, but a standard coefficient value would be employed instead of using an Arrhenius law for the recombination coefficient. A behaviour law developed through this method would be geometry-dependent, necessitating evaluation on a case-by-case basis. This dependency arises because the fixed concentration boundary condition interacts with the domain geometry, affecting the overall transport behaviour. In contrast, when a recombination flux is enforced as the standard condition, the provided method for implementing a PRF remains geometry-independent. This independence from geometry makes the method robust and versatile for emulating a permeation barrier on a boundary, ensuring reliable performance across various applications and material systems.

Bibliography

[1] K. Tokimatsu *et al.*, “Energy analysis and carbon dioxide emission of Tokamak fusion power reactors,” *Fusion Engineering and Design*, vol. 48, no. 3, pp. 483–498, Sep. 2000. Available: https://www.sciencedirect.com/science/article/pii/S0920379600001575 (Cited on page 5.)

[2] L. L. Lucas and M. P. Unterweger, “Comprehensive Review and Critical Evaluation of the Half-Life of Tritium,” *Journal of Research of the National Institute of Standards and Technology*, vol. 105, no. 4, pp. 541–549, 2000. Available: https://www.ncbi.nlm.nih.gov/pmc/articles/PMC4877155/ (Cited on pages 5 and 14.)

[3] H. Günther and V. Müller, “Einstein’s Energy–Mass Equivalence,” in *The Special Theory of Relativity: Einstein’s World in New Axiomatics*, H. Günther and V. Müller, Eds. Singapore: Springer, 2019, pp. 97–105. Available: https://doi.org/10.1007/978-981-13-7783-9_7 (Cited on page 6.)

[4] M. P. Fewell, “The atomic nuclide with the highest mean binding energy,” *American Journal of Physics*, vol. 63, no. 7, pp. 653–658, Jul. 1995. Available: https://doi.org/10.1119/1.17828 (Cited on page 6.)

[5] A. Köhn-Seemann and J. Hillairet, “alfkoehn/fusion_plots: Second release of the fusion plot package (new plots added),” Jun. 2021. Available: https://zenodo.org/records/4946068 (Cited on pages 7 and 8.)

[6] B. L. Cohen, “The Disposal of Radioactive Wastes from Fission Reactors,” *Scientific American*, vol. 236, no. 6, pp. 21–31, 1977, publisher: Scientific American, a division of Nature America, Inc. Available: https://www.jstor.org/stable/24954067 (Cited on page 6.)

[7] C. Kittel and H. Kroemer, *Thermal physics*, 2nd ed. San Francisco: W.H. Freeman, 1980, oCLC: 5171399. Available: http://catdir.loc.gov/catdir/enhancements/fy1011/79016677-t.html (Cited on page 7.)

[8] B. W. Carroll and D. A. Ostlie, *An Introduction to Modern Astrophysics*, Sep. 2017, iSBN: 9781108380980 Publisher: Cambridge University Press. Available: https://www.cambridge.org/highereducation/books/an-introduction-to-modern-astrophysics/140DDF8A480C3841DCCD76D66984D858 (Cited on page 7.)

[9] F. F. Chen, *Introduction to Plasma Physics and Controlled Fusion*. Cham: Springer International Publishing, 2016. Available: http://link.springer.com/10.1007/978-3-319-22309-4 (Cited on pages 8 and 9.)

[10] M. Michell Waldrop, “Can the dream of fusion power be realized?” *Canary Media*, Jan. 2024. Available: https://www.canarymedia.com/articles/nuclear/can-the-dream-of-fusion-power-be-realized (Cited on page 10.)

[11] T. Tone, Y. Seki, and H. Iida, *Design study of a tokamak power reactor*. International Atomic Energy Agency (IAEA): IAEA, 1983, iNIS Reference Number: 53051776. (Cited on page 9.)

[12] L. Spitzer, Jr., “The Stellarator Concept,” *The Physics of Fluids*, vol. 1, no. 4, pp. 253–264, Jul. 1958. Available: https://doi.org/10.1063/1.1705883 (Cited on page 9.)

[13] J. P. Freidberg, *Plasma Physics and Fusion Energy*. Cambridge: Cambridge University Press, 2007. Available: https://www.cambridge.org/core/books/plasma-physics-and-fusion-energy/CD7B530D2889F70446F34E14EE0EF703 (Cited on page 10.)

[14] G. McCracken and P. Stott, *Fusion: The Energy of the Universe*. Academic Press, 2013, google-Books-ID: e6jEZfO2gO4C. (Cited on pages 10, 11, 19 and 20.)

[15] S. E. Wurzel and S. C. Hsu, “Progress toward fusion energy breakeven and gain as measured against the Lawson criterion,” *Physics of Plasmas*, vol. 29, no. 6, p. 062103, Jun. 2022. Available: https://doi.org/10.1063/5.0083990 (Cited on pages 10, 11 and 12.)

[16] R. G. Mills, “Lawson Criteria,” *IEEE Transactions on Nuclear Science*, vol. 18, no. 4, pp. 205–207, Aug. 1971, conference Name: IEEE Transactions on Nuclear Science. Available: https://ieeexplore.ieee.org/abstract/document/4326341 (Cited on page 12.)

[17] A. B. Zylstra *et al.*, “Burning plasma achieved in inertial fusion,” *Nature*, vol. 601, no. 7894, pp. 542–548, Jan. 2022, publisher: Nature Publishing Group. Available: https://www.nature.com/articles/s41586-021-04281-w (Cited on page 12.)

[18] J.-L. Miquel, C. Lion, and P. Vivini, “The Laser Mega-Joule : LMJ & PETAL status and Program Overview,” *Journal of Physics: Conference Series*, vol. 688, no. 1, p. 012067, Mar. 2016, publisher: IOP Publishing. Available: https://dx.doi.org/10.1088/1742-6596/688/1/012067 (Cited on page 12.)

[19] “DEMO.” Available: https://euro-fusion.org/programme/demo/ (Cited on page 13.)

[20] G. Federici *et al.*, "European DEMO design strategy and consequences for materials," *Nuclear Fusion*, vol. 57, no. 9, p. 092002, Jun. 2017, publisher: IOP Publishing. Available: https://dx.doi.org/10.1088/1741-4326/57/9/092002 (Cited on pages 13, 27 and 101.)

[21] E. Lewis, *Fundamentals of Nuclear Reactor Physics - 1st Edition*, 1st ed. Academic Press, Jan. 2008. Available: https://www.elsevier.com/books/fundamentals-of-nuclear-reactor-physics/lewis/978-0-12-370631-7 (Cited on page 14.)

[22] H. Smith, *1990 Recommendations of the International Commission on Radiological protection*, ser. Annals of the ICRP, 1993, vol. 21, no. 60. (Cited on page 15.)

[23] ——, *Annuals Limits on Intake of Radionuclides by Workers Based on the 1990 Recommendations*, ser. Annals of the ICRP, 1993, vol. 21, no. 61. (Cited on page 15.)

[24] I. A. E. Agency, "Safe Handling of Tritium Review of Data and Experience," International Atomic Energy Agency, Text, 1991, iSBN: 9789201253910 Publication Title: Safe Handling of Tritium Review of Data and Experience. Available: https://www.iaea.org/publications/1428/safe-handling-of-tritium-review-of-data-and-experience (Cited on page 15.)

[25] A. d. s. nucléaire, "Exposure of a worker in excess of the statutory dose limit." Available: https://www.french-nuclear-safety.fr/asn-informs/news-releases/exposure-of-a-worker-in-excess-of-the-statutory-dose-limit (Cited on page 15.)

[26] T. Honda *et al.*, "Analyses of loss of vacuum accident (LOVA) in ITER," *Fusion Engineering and Design*, vol. 47, no. 4, pp. 361–375, Jan. 2000. Available: https://www.sciencedirect.com/science/article/pii/S0920379699000678 (Cited on page 15.)

[27] J. Roth *et al.*, "Tritium inventory in ITER plasma-facing materials and tritium removal procedures," *Plasma Physics and Controlled Fusion*, vol. 50, no. 10, p. 103001, Aug. 2008. Available: https://dx.doi.org/10.1088/0741-3335/50/10/103001 (Cited on page 15.)

[28] G. De Temmerman *et al.*, "Efficiency of thermal outgassing for tritium retention measurement and removal in ITER," *Nuclear Materials and Energy*, vol. 12, pp. 267–272, Aug. 2017. Available: https://www.sciencedirect.com/science/article/pii/S2352179116301284 (Cited on page 15.)

[29] R. Arredondo *et al.*, "Preliminary estimates of tritium permeation and retention in the first wall of DEMO due to ion bombardment," *Nuclear Materials and Energy*, vol. 28, p. 101039, Sep. 2021. Available: https://www.sciencedirect.com/science/article/pii/S2352179121001125 (Cited on pages 15 and 86.)

[30] M. Shimada and R. J. Pawelko, "Tritium permeability measurement in hydrogen-tritium system," *Fusion Engineering and Design*, vol. 129, pp. 134–139, Apr. 2018. Available: https://www.sciencedirect.com/science/article/pii/S0920379618301340 (Cited on page 15.)

[31] X. Lefebvre *et al.*, "Preliminary results from a detritiation facility dedicated to soft housekeeping waste," *Fusion Engineering and Design*, vol. 87, no. 7, pp. 1040–1044, Aug. 2012. Available: https://www.sciencedirect.com/science/article/pii/S0920379612001366 (Cited on page 15.)

[32] M. Utili *et al.*, "Design of the Test Section for the Experimental Validation of Antipermeation and Corrosion Barriers for WCLL BB," *Applied Sciences*, vol. 12, no. 3, p. 1624, Jan. 2022, number: 3 Publisher: Multidisciplinary Digital Publishing Institute. Available: https://www.mdpi.com/2076-3417/12/3/1624 (Cited on pages 16 and 118.)

[33] R. A. Causey and W. R. Wampler, "The use of silicon carbide as a tritium permeation barrier," *Journal of Nuclear Materials*, vol. 220-222, pp. 823–826, Apr. 1995. Available: https://linkinghub.elsevier.com/retrieve/pii/0022311594006237 (Cited on page 16.)

[34] M. Utili *et al.*, "Development of anti-permeation and corrosion barrier coatings for the WCLL breeding blanket of the European DEMO," *Fusion Engineering and Design*, vol. 170, p. 112453, Sep. 2021. Available: https://www.sciencedirect.com/science/article/pii/S0920379621002295 (Cited on pages 16, 89 and 129.)

[35] M. Abdou *et al.*, "Physics and technology considerations for the deuterium–tritium fuel cycle and conditions for tritium fuel self sufficiency," *Nuclear Fusion*, vol. 61, no. 1, p. 013001, Nov. 2020, publisher: IOP Publishing. Available: https://iopscience.iop.org/article/10.1088/1741-4326/abbf35/meta (Cited on page 18.)

[36] H. Chen *et al.*, "Tritium fuel cycle modeling and tritium breeding analysis for CFETR," *Fusion Engineering and Design*, vol. 106, pp. 17–20, May 2016. Available: https://www.sciencedirect.com/science/article/pii/S0920379616301922 (Cited on page 18.)

[37] M. Coleman, Y. Hörstensmeyer, and F. Cismondi, “DEMO tritium fuel cycle: performance, parameter explorations, and design space constraints,” *Fusion Engineering and Design*, vol. 141, pp. 79–90, Apr. 2019. Available: https://www.sciencedirect.com/science/article/pii/S092037961930167X (Cited on page 18.)

[38] S. Meschini *et al.*, “Modeling and analysis of the tritium fuel cycle for ARC- and STEP-class D-T fusion power plants,” *Nuclear Fusion*, vol. 63, no. 12, p. 126005, Sep. 2023, publisher: IOP Publishing. Available: https://dx.doi.org/10.1088/1741-4326/acf3fc (Cited on page 18.)

[39] W. Holtslander, R. Osborne, and T. Drolet, “Recovery of tritium from CANDU reactors, its storage and monitoring of its migration in the environment,” Canada, Tech. Rep., 1979, aECL–6544 INIS Reference Number: 11523342. (Cited on page 19.)

[40] J. Shimwell and R. Delaporte-Mathurin, “XSPlot - Neutron cross section plotter for isotopes,” Aug. 2021. Available: https://github.com/openmc-data-storage/isotope-xs-plotter (Cited on pages 19 and 20.)

[41] R. J. Pearson, A. B. Antoniazzi, and W. J. Nuttall, “Tritium supply and use: a key issue for the development of nuclear fusion energy,” *Fusion Engineering and Design*, vol. 136, pp. 1140–1148, Nov. 2018. Available: https://linkinghub.elsevier.com/retrieve/pii/S092037961830379X (Cited on page 19.)

[42] T. Giegerich *et al.*, “Development of a viable route for lithium-6 supply of DEMO and future fusion power plants,” *Fusion Engineering and Design*, vol. 149, p. 111339, Dec. 2019. Available: https://www.sciencedirect.com/science/article/pii/S092037961930835X (Cited on page 20.)

[43] F. Hernández and P. Pereslavtsev, “First principles review of options for tritium breeder and neutron multiplier materials for breeding blankets in fusion reactors,” *Fusion Engineering and Design*, vol. 137, pp. 243–256, Dec. 2018. Available: https://linkinghub.elsevier.com/retrieve/pii/S0920379618306392 (Cited on page 20.)

[44] R. Delaporte-Mathurin, “Hydrogen transport in tokamaks : Estimation of the ITER divertor tritium inventory and influence of helium exposure,” thesis, Paris 13, Oct. 2022, publication Title: http://www.theses.fr. Available: http://www.theses.fr/2022PA131054 (Cited on pages 21, 22, 39 and 44.)

[45] J.-F. Coeurjolly, “Estimating the Parameters of a Fractional Brownian Motion by Discrete Variations of its Sample Paths,” *Statistical Inference for Stochastic Processes*, vol. 4, no. 2, pp. 199–227, May 2001. Available: https://doi.org/10.1023/A:1017507306245 (Cited on page 21.)

[46] G. R. Longhurst, “The soret effect and its implications for fusion reactors,” *Journal of Nuclear Materials*, vol. 131, no. 1, pp. 61–69, Mar. 1985. Available: https://www.sciencedirect.com/science/article/pii/0022311585904258 (Cited on pages 21 and 22.)

[47] E. Martínez *et al.*, “Thermal gradient effect on helium and self-interstitial transport in tungsten,” *Journal of Applied Physics*, vol. 130, no. 21, p. 215904, Dec. 2021. Available: https://doi.org/10.1063/5.0071935 (Cited on pages 21 and 22.)

[48] A. Krom, “Hydrogen transport near a blunting crack tip,” *Journal of the Mechanics and Physics of Solids*, vol. 47, no. 4, pp. 971–992, Feb. 1999, publisher: Pergamon. Available: https://www.sciencedirect.com/science/article/pii/S0022509698000647 (Cited on page 21.)

[49] A. Paul *et al.*, “Fick’s Laws of Diffusion,” in *Thermodynamics, Diffusion and the Kirkendall Effect in Solids*, A. Paul *et al.*, Eds. Cham: Springer International Publishing, 2014, pp. 115–139. Available: https://doi.org/10.1007/978-3-319-07461-0_3 (Cited on page 21.)

[50] L.-F. Wang *et al.*, “Molecular dynamics studies of hydrogen diffusion in tungsten at elevated temperature: Concentration dependence and defect effects,” *International Journal of Hydrogen Energy*, vol. 45, no. 1, pp. 822–834, Jan. 2020. Available: https://www.sciencedirect.com/science/article/pii/S0360319919339989 (Cited on page 22.)

[51] D. Kato *et al.*, “Super-saturated hydrogen effects on radiation damages in tungsten under the high-flux divertor plasma irradiation,” vol. 55, no. 8, p. 083019, Jul. 2015, publisher: IOP Publishing. Available: https://doi.org/10.1088/0029-5515/55/8/083019 (Cited on page 22.)

[52] Y.-N. Liu *et al.*, “Hydrogen diffusion in tungsten: A molecular dynamics study,” *Journal of Nuclear Materials*, vol. 455, no. 1, pp. 676–680, Dec. 2014. Available: https://www.sciencedirect.com/science/article/pii/S0022311514005911 (Cited on page 22.)

[53] X. W. Zhou *et al.*, “Molecular Dynamics Simulations of Hydrogen Diffusion in Aluminum,” *The Journal of Physical Chemistry C*, vol. 120, no. 14, pp. 7500–7509, Apr. 2016, publisher: American Chemical Society. Available: https://doi.org/10.1021/acs.jpcc.6b01802 (Cited on page 22.)

[54] F. Montupet-Leblond *et al.*, “Permeation and trapping of hydrogen in Eurofer97,” *Nuclear Materials and Energy*, vol. 29, p. 101062, Dec. 2021. Available: https://www.sciencedirect.com/science/article/pii/S2352179121001290 (Cited on pages 22, 23, 31, 55, 65, 66 and 67.)

[55] A. Drexler *et al.*, “Microstructural based hydrogen diffusion and trapping models applied to Fe–C X alloys,” *Journal of Alloys and Compounds*, vol. 826, no. 154057, Jun. 2020. Available: https://doi.org/10.1016/j.jallcom.2020.154057 (Cited on page 22.)

[56] G. Alefeld *et al.*, Eds., *Hydrogen in Metals I*, ser. Topics in Applied Physics. Berlin, Heidelberg: Springer, 1978, vol. 28. Available: http://link.springer.com/10.1007/3-540-08705-2 (Cited on pages 22 and 23.)

[57] J. Hou *et al.*, “Predictive model of hydrogen trapping and bubbling in nanovoids in bcc metals,” *Nature Materials*, vol. 18, no. 8, pp. 833–839, Aug. 2019, publisher: Nature Publishing Group. Available: https://www.nature.com/articles/s41563-019-0422-4 (Cited on pages 23, 98 and 99.)

[58] A. D. Backer *et al.*, “Hydrogen accumulation around dislocation loops and edge dislocations: from atomistic to mesoscopic scales in BCC tungsten,” *Physica Scripta*, vol. 2017, no. T170, p. 014073, Nov. 2017, publisher: IOP Publishing. Available: https://dx.doi.org/10.1088/1402-4896/aa9400 (Cited on pages 23 and 98.)

[59] N. Fernandez, Y. Ferro, and D. Kato, “Hydrogen diffusion and vacancies formation in tungsten: Density Functional Theory calculations and statistical models,” *Acta Materialia*, vol. 94, pp. 307–318, Aug. 2015. Available: https://www.sciencedirect.com/science/article/pii/S1359645415003043 (Cited on pages 23, 65 and 98.)

[60] G.-H. Lu, H.-B. Zhou, and C. S. Becquart, “A review of modelling and simulation of hydrogen behaviour in tungsten at different scales,” vol. 54, no. 8, p. 086001, Jul. 2014, publisher: IOP Publishing. Available: https://doi.org/10.1088/0029-5515/54/8/086001 (Cited on page 23.)

[61] K. Heinola *et al.*, “Hydrogen interaction with point defects in tungsten,” *Physical Review B*, vol. 82, no. 9, p. 094102, Sep. 2010, publisher: American Physical Society. Available: https://link.aps.org/doi/10.1103/PhysRevB.82.094102 (Cited on pages 23, 65, 98 and 99.)

[62] H.-B. Zhou *et al.*, “Investigating behaviours of hydrogen in a tungsten grain boundary by first principles: from dissolution and diffusion to a trapping mechanism,” *Nuclear Fusion*, vol. 50, no. 2, p. 025016, Jan. 2010. Available: https://dx.doi.org/10.1088/0029-5515/50/2/025016 (Cited on page 23.)

[63] O. V. Ogorodnikova, “Fundamental aspects of deuterium retention in tungsten at high flux plasma exposure,” *Journal of Applied Physics*, vol. 118, no. 7, p. 074902, Aug. 2015. Available: https://doi.org/10.1063/1.4928407 (Cited on pages 23 and 99.)

[64] A. J. Kumnick and H. H. Johnson, “Deep trapping states for hydrogen in deformed iron,” *Acta Metallurgica*, vol. 28, no. 1, pp. 33–39, Jan. 1980. Available: https://www.sciencedirect.com/science/article/pii/0001616080900383 (Cited on page 23.)

[65] E. A. Hodille *et al.*, “Modelling tritium adsorption and desorption from tungsten dust particles with a surface kinetic model,” *Nuclear Fusion*, vol. 61, no. 8, p. 086030, Jul. 2021, publisher: IOP Publishing. Available: https://dx.doi.org/10.1088/1741-4326/ac0f37 (Cited on page 23.)

[66] P. Alnot, A. Cassuto, and D. A. King, “Adsorption and desorption kinetics with no precursor trapping: Hydrogen and deuterium on W {100},” *Surface Science*, vol. 215, no. 1, pp. 29–46, May 1989. Available: https://www.sciencedirect.com/science/article/pii/0039602889906973 (Cited on page 23.)

[67] P. W. Tamm and L. D. Schmidt, “Interaction of H2 with (100)W. II. Condensation,” *The Journal of Chemical Physics*, vol. 52, no. 3, pp. 1150–1160, Feb. 1970. Available: https://doi.org/10.1063/1.1673110 (Cited on page 23.)

[68] D. F. Johnson and E. A. Carter, “Hydrogen in tungsten: Absorption, diffusion, vacancy trapping, and decohesion,” *Journal of Materials Research*, vol. 25, no. 2, pp. 315–327, Feb. 2010. Available: https://doi.org/10.1557/JMR.2010.0036 (Cited on pages 23 and 65.)

[69] M. Ajmalghan *et al.*, “Surface coverage dependent mechanisms for the absorption and desorption of hydrogen from the W(1 1 0) and W(1 0 0) surfaces: a density functional theory investigation,” *Nuclear Fusion*, vol. 59, no. 10, p. 106022, Aug. 2019, publisher: IOP Publishing. Available: https://dx.doi.org/10.1088/1741-4326/ab33e7 (Cited on pages 23 and 99.)

[70] M. A. Pick and K. Sonnenberg, “A model for atomic hydrogen-metal interactions — application to recycling, recombination and permeation,” *Journal of Nuclear Materials*, vol. 131, no. 2, pp. 208–220, Apr. 1985. Available: https://www.sciencedirect.com/science/article/pii/0022311585904593 (Cited on page 23.)

[71] D. R. Morris *et al.*, "Henry's law constant for hydrogen in natural water and deuterium in heavy water," *Physical Chemistry Chemical Physics*, vol. 3, no. 6, pp. 1043–1046, Jan. 2001, publisher: The Royal Society of Chemistry. Available: https://pubs.rsc.org/en/content/articlelanding/2001/cp/b007732l (Cited on page 24.)

[72] M. Vadrucci *et al.*, "Hydrogen permeation through Pd–Ag membranes: Surface effects and Sieverts' law," *International Journal of Hydrogen Energy*, vol. 38, no. 10, pp. 4144–4152, Apr. 2013. Available: https://www.sciencedirect.com/science/article/pii/S0360319913002000 (Cited on page 24.)

[73] D. T. Wadiak and T. K. Hight, "Diffusion and Chemical Reaction by the Finite Element Method," *Journal of Spacecraft and Rockets*, vol. 40, no. 4, pp. 584–590, Jul. 2003, publisher: American Institute of Aeronautics and Astronautics. Available: https://arc.aiaa.org/doi/10.2514/2.3980 (Cited on page 24.)

[74] S. P. K. Sternberg, "Dispersion Measurements in Highly Heterogeneous Laboratory Scale Porous Media," *Transport in Porous Media*, vol. 54, no. 1, pp. 107–124, Jan. 2004. Available: https://doi.org/10.1023/A:1025708313812 (Cited on page 25.)

[75] X. Fan and E. Suhir, Eds., *Moisture Sensitivity of Plastic Packages of IC Devices*. Boston, MA: Springer US, 2010. Available: http://link.springer.com/10.1007/978-1-4419-5719-1 (Cited on page 25.)

[76] F. P. Incropera and D. P. DeWitt, *Fundamentals of heat and mass transfer*, 5th ed. New York: J. Wiley, 2002, oCLC: 45951568. Available: http://catdir.loc.gov/catdir/toc/onix06/2001017854.html (Cited on pages 25 and 38.)

[77] R. A. Oriani, "Hydrogen Embrittlement of Steels," *Annual Review of Materials Research*, vol. 8, no. Volume 8,, pp. 327–357, Aug. 1978, publisher: Annual Reviews. Available: https://www.annualreviews.org/content/journals/10.1146/annurev.ms.08.080178.001551 (Cited on page 25.)

[78] S. K. Dwivedi and M. Vishwakarma, "Hydrogen embrittlement in different materials: A review," *International Journal of Hydrogen Energy*, vol. 43, no. 46, pp. 21 603–21 616, Nov. 2018. Available: https://www.sciencedirect.com/science/article/pii/S0360319918331306 (Cited on page 25.)

[79] X. Li *et al.*, "Review of Hydrogen Embrittlement in Metals: Hydrogen Diffusion, Hydrogen Characterization, Hydrogen Embrittlement Mechanism and Prevention," *Acta Metallurgica Sinica (English Letters)*, vol. 33, no. 6, pp. 759–773, Jun. 2020. Available: https://doi.org/10.1007/s40195-020-01039-7 (Cited on page 25.)

[80] L. M. Giancarli *et al.*, "Overview of the ITER TBM Program," *Fusion Engineering and Design*, vol. 87, no. 5, pp. 395–402, Aug. 2012. Available: https://www.sciencedirect.com/science/article/pii/S0920379611006090 (Cited on page 25.)

[81] P. Arena *et al.*, "The DEMO Water-Cooled Lead&ndash;Lithium Breeding Blanket: Design Status at the End of the Pre-Conceptual Design Phase," *Applied Sciences*, vol. 11, no. 24, p. 11592, Jan. 2021, number: 24 Publisher: Multidisciplinary Digital Publishing Institute. Available: https://www.mdpi.com/2076-3417/11/24/11592 (Cited on pages 25, 26, 60, 61 and 108.)

[82] C. Bachmann *et al.*, "Overview over DEMO design integration challenges and their impact on component design concepts," *Fusion Engineering and Design*, vol. 136, pp. 87–95, Nov. 2018. Available: https://www.sciencedirect.com/science/article/pii/S0920379617309997 (Cited on pages 25 and 26.)

[83] G. Federici *et al.*, "Overview of the design approach and prioritization of R&D activities towards an EU DEMO," *Fusion Engineering and Design*, vol. 109-111, pp. 1464–1474, Nov. 2016. Available: https://www.sciencedirect.com/science/article/pii/S0920379615303835 (Cited on page 26.)

[84] A. Tassone *et al.*, "Recent Progress in the WCLL Breeding Blanket Design for the DEMO Fusion Reactor," *IEEE Transactions on Plasma Science*, vol. 46, no. 5, pp. 1446–1457, May 2018, conference Name: IEEE Transactions on Plasma Science. Available: https://ieeexplore.ieee.org/document/8259041 (Cited on pages 26 and 29.)

[85] E. Martelli *et al.*, "Advancements in DEMO WCLL breeding blanket design and integration," *International Journal of Energy Research*, vol. 42, no. 1, pp. 27–52, 2018, _eprint: https://onlinelibrary.wiley.com/doi/pdf/10.1002/er.3750. Available: https://onlinelibrary.wiley.com/doi/abs/10.1002/er.3750 (Cited on pages 26 and 29.)

[86] G. Bongiovì *et al.*, "Multi-Module vs. Single-Module concept: Comparison of thermomechanical performances for the DEMO Water-Cooled Lithium Lead breeding blanket," *Fusion Engineering and Design*, vol. 136, pp. 1472–1478, Nov. 2018. Available: https://www.sciencedirect.com/science/article/pii/S0920379618304708 (Cited on page 26.)

[87] F. Edemetti *et al.*, "Thermal-hydraulic analysis of the DEMO WCLL elementary cell: BZ tubes layout optimization," *Fusion Engineering and Design*, vol. 160, p. 111956, Nov. 2020. Available:

https://www.sciencedirect.com/science/article/pii/S0920379620305044 (Cited on pages 26, 29, 30, 37, 59, 77, 78, 79, 80 and 89.)

[88] K. Ehrlich, E. E. Bloom, and T. Kondo, "International strategy for fusion materials development," *Journal of Nuclear Materials*, vol. 283-287, pp. 79–88, Dec. 2000. Available: https://www.sciencedirect.com/science/article/pii/S0022311500001021 (Cited on page 27.)

[89] J. R. Dunning *et al.*, "Interaction of Neutrons with Matter," *Physical Review*, vol. 48, no. 3, pp. 265–280, Aug. 1935, publisher: American Physical Society. Available: https://link.aps.org/doi/10.1103/PhysRev.48.265 (Cited on page 27.)

[90] M. R. Gilbert, J. Marian, and J. C. Sublet, "Energy spectra of primary knock-on atoms under neutron irradiation," *Journal of Nuclear Materials*, vol. 467, pp. 121–134, Dec. 2015. Available: https://www.sciencedirect.com/science/article/pii/S0022311515302129 (Cited on page 27.)

[91] K. Nordlund *et al.*, "Improving atomic displacement and replacement calculations with physically realistic damage models," *Nature Communications*, vol. 9, no. 1, p. 1084, Mar. 2018, bandiera_abtest: a Cc_license_type: cc_by Cg_type: Nature Research Journals Number: 1 Primary_atype: Research Publisher: Nature Publishing Group Subject_term: Metals and alloys;Nuclear physics;Theory and computation Subject_term_id: metals-and-alloys;nuclear-physics;theory-and-computation. Available: https://www.nature.com/articles/s41467-018-03415-5 (Cited on page 28.)

[92] J. Dark *et al.*, "Influence of hydrogen trapping on WCLL breeding blanket performances," *Nuclear Fusion*, vol. 61, no. 11, p. 116076, Oct. 2021, publisher: IOP Publishing. Available: https://doi.org/10.1088/1741-4326/ac28b0 (Cited on pages 27 and 31.)

[93] R. Delaporte-Mathurin *et al.*, "Fuel retention in WEST and ITER divertors based on FESTIM monoblock simulations," *Nuclear Fusion*, vol. 61, no. 12, p. 126001, Oct. 2021, publisher: IOP Publishing. Available: https://doi.org/10.1088/1741-4326/ac2bbd (Cited on page 27.)

[94] E. A. Hodille *et al.*, "Macroscopic rate equation modeling of trapping/detrapping of hydrogen isotopes in tungsten materials," *Journal of Nuclear Materials*, vol. 467, pp. 424–431, Dec. 2015. Available: http://www.sciencedirect.com/science/article/pii/S0022311515300660 (Cited on pages 27, 28, 31, 55, 66 and 67.)

[95] B. N. Sorbom *et al.*, "ARC: A compact, high-field, fusion nuclear science facility and demonstration power plant with demountable magnets," *Fusion Engineering and Design*, vol. 100, pp. 378–405, Nov. 2015. Available: https://www.sciencedirect.com/science/article/pii/S0920379615302337 (Cited on page 27.)

[96] G. S. Was *et al.*, "Emulation of neutron irradiation effects with protons: validation of principle," *Journal of Nuclear Materials*, vol. 300, no. 2, pp. 198–216, Feb. 2002. Available: https://www.sciencedirect.com/science/article/pii/S0022311501007516 (Cited on page 28.)

[97] M. H. J. t. Hoen *et al.*, "Reduced deuterium retention in self-damaged tungsten exposed to high-flux plasmas at high surface temperatures," *Nuclear Fusion*, vol. 53, no. 4, p. 043003, Mar. 2013, publisher: IOP Publishing. Available: https://doi.org/10.1088/0029-5515/53/4/043003 (Cited on pages 28, 98 and 99.)

[98] M. Shimada and B. J. Merrill, "Tritium decay helium-3 effects in tungsten," *Nuclear Materials and Energy*, vol. 12, pp. 699–702, Aug. 2017. Available: https://www.sciencedirect.com/science/article/pii/S2352179116302095 (Cited on page 28.)

[99] D. R. Mason *et al.*, "Parameter-free quantitative simulation of high-dose microstructure and hydrogen retention in ion-irradiated tungsten," *Physical Review Materials*, vol. 5, no. 9, p. 095403, Sep. 2021, publisher: American Physical Society. Available: https://link.aps.org/doi/10.1103/PhysRevMaterials.5.095403 (Cited on page 28.)

[100] M. Pečovnik, T. Schwarz-Selinger, and S. Markelj, "Experiments and modelling of multiple sequential MeV ion irradiations and deuterium exposures in tungsten," *Journal of Nuclear Materials*, vol. 550, p. 152947, Jul. 2021. Available: https://www.sciencedirect.com/science/article/pii/S0022311521001707 (Cited on pages 28, 55 and 95.)

[101] T. Schwarz-Selinger *et al.*, "Influence of the presence of deuterium on displacement damage in tungsten," *Nuclear Materials and Energy*, vol. 17, pp. 228–234, Dec. 2018. Available: https://www.sciencedirect.com/science/article/pii/S2352179118301273 (Cited on page 28.)

[102] T. Schwarz-Selinger, "A critical review of experiments on deuterium retention in displacement-damaged tungsten as function of damaging dose," *Materials Research Express*, vol. 10, no. 10, p. 102002, Oct. 2023, publisher: IOP Publishing. Available: https://dx.doi.org/10.1088/2053-1591/acfdf8 (Cited on pages 28, 92 and 96.)

[103] M. H. J. t. Hoen *et al.*, “Saturation of deuterium retention in self-damaged tungsten exposed to high-flux plasmas,” *Nuclear Fusion*, vol. 52, no. 2, p. 023008, Jan. 2012, publisher: IOP Publishing. Available: https://doi.org/10.1088/0029-5515/52/2/023008 (Cited on page 28.)

[104] M. Pečovnik *et al.*, “New rate equation model to describe the stabilization of displacement damage by hydrogen atoms during ion irradiation in tungsten,” *Nuclear Fusion*, vol. 60, no. 3, p. 036024, Feb. 2020, publisher: IOP Publishing. Available: https://doi.org/10.1088/1741-4326/ab680f (Cited on pages 28, 91 and 95.)

[105] A. Založnik *et al.*, “The influence of the annealing temperature on deuterium retention in self-damaged tungsten,” *Physica Scripta*, vol. T167, p. 014031, Jan. 2016, publisher: IOP Publishing. Available: https://doi.org/10.1088/0031-8949/t167/1/014031 (Cited on pages 28, 91 and 95.)

[106] F. Moro *et al.*, “Neutronic analyses in support of the WCLL DEMO design development,” *Fusion Engineering and Design*, vol. 136, pp. 1260–1264, Nov. 2018. Available: https://www.sciencedirect.com/science/article/pii/S0920379618304071 (Cited on pages 28, 29, 31, 37, 67, 68, 101 and 108.)

[107] U. Fischer *et al.*, “Required, achievable and target TBR for the European DEMO,” *Fusion Engineering and Design*, vol. 155, p. 111553, Jun. 2020. Available: https://www.sciencedirect.com/science/article/pii/S0920379620301010 (Cited on pages 28, 31 and 32.)

[108] ——, “Neutronics requirements for a DEMO fusion power plant,” *Fusion Engineering and Design*, vol. 98-99, pp. 2134–2137, Oct. 2015. Available: https://www.sciencedirect.com/science/article/pii/S092037961500112X (Cited on pages 29 and 31.)

[109] A. Del Nevo *et al.*, “WCLL breeding blanket design and integration for DEMO 2015: status and perspectives,” *Fusion Engineering and Design*, vol. 124, pp. 682–686, Nov. 2017. Available: https://www.sciencedirect.com/science/article/pii/S0920379617302235 (Cited on page 29.)

[110] ——, “Recent progress in developing a feasible and integrated conceptual design of the WCLL BB in EUROfusion project,” *Fusion Engineering and Design*, vol. 146, pp. 1805–1809, Sep. 2019. Available: https://www.sciencedirect.com/science/article/pii/S0920379619303503 (Cited on page 29.)

[111] G. Zhou *et al.*, “Design study on the new EU DEMO HCPB breeding blanket: Thermal analysis,” *Progress in Nuclear Energy*, vol. 98, pp. 167–176, Jul. 2017. Available: https://www.sciencedirect.com/science/article/pii/S0149197017300586 (Cited on page 29.)

[112] M. Rieth *et al.*, “EUROFER 97. Tensile, charpy, creep and structural tests,” Oct. 2003. Available: https://www.osti.gov/etdeweb/biblio/20448776 (Cited on page 29.)

[113] M. Eddahbi *et al.*, “Texture and mechanical properties of EUROFER 97 steel processed by ECAP,” *Materials Science and Engineering: A*, vol. 528, no. 18, pp. 5927–5934, Jul. 2011. Available: https://www.sciencedirect.com/science/article/pii/S0921509311004205 (Cited on page 29.)

[114] C. Ciurluini *et al.*, “Analysis of the thermal-hydraulic behavior of the EU-DEMO WCLL breeding blanket cooling systems during a loss of flow accident,” *Fusion Engineering and Design*, vol. 164, p. 112206, Mar. 2021. Available: https://www.sciencedirect.com/science/article/pii/S0920379620307547 (Cited on page 30.)

[115] M. Siccinio *et al.*, “Development of the plasma scenario for EU-DEMO: Status and plans,” *Fusion Engineering and Design*, vol. 176, p. 113047, Mar. 2022. Available: https://www.sciencedirect.com/science/article/pii/S0920379622000473 (Cited on page 30.)

[116] J. Reid *et al.*, “Comparison of waste due to irradiated steels in the ESFR and DEMO,” *EPJ Web of Conferences*, vol. 247, p. 18002, 2021, publisher: EDP Sciences. Available: https://www.epj-conferences.org/articles/epjconf/abs/2021/01/epjconf_physor2020_18002/epjconf_physor2020_18002.html (Cited on page 31.)

[117] “Roadmap.” Available: https://euro-fusion.org/eurofusion/roadmap/ (Cited on page 31.)

[118] R. Boullon *et al.*, “Development of a WCLL DEMO First Wall design module in the SYCOMORE system code interfaced with the neutronic one,” *Fusion Engineering and Design*, vol. 153, p. 111514, Apr. 2020. Available: http://www.sciencedirect.com/science/article/pii/S0920379620300624 (Cited on page 31.)

[119] F. Gabriel *et al.*, “A 2D finite element modelling of tritium permeation for the HCLL DEMO blanket module,” *Fusion Engineering and Design*, vol. 82, no. 15, pp. 2204–2211, Oct. 2007. Available: https://www.sciencedirect.com/science/article/pii/S0920379607004061 (Cited on page 31.)

[120] A. Tassone and G. Caruso, “Computational MHD analyses in support of the design of the WCLL TBM breeding zone,” *Fusion Engineering and Design*, vol. 170, p. 112535, Sep. 2021. Available: https://www.sciencedirect.com/science/article/pii/S0920379621003112 (Cited on page 31.)

[121] R. Testoni *et al.*, “Tritium transport model at breeder unit level for HCLL breeding blanket,” *Fusion Engineering and Design*, vol. 146, pp. 2319–2322, Sep. 2019. Available: https://www.sciencedirect.com/science/article/pii/S0920379619305137 (Cited on page 31.)

[122] A. Ying *et al.*, “Breeding blanket system design implications on tritium transport and permeation with high tritium ion implantation: A MATLAB/Simulink, COMSOL integrated dynamic tritium transport model for HCCR TBS,” *Fusion Engineering and Design*, vol. 136, pp. 1153–1160, Nov. 2018. Available: http://www.sciencedirect.com/science/article/pii/S0920379618303879 (Cited on page 31.)

[123] Y. Xu *et al.*, “Transport parameters and permeation behavior of hydrogen isotopes in the first wall materials of future fusion reactors,” *Fusion Engineering and Design*, vol. 155, p. 111563, Jun. 2020. Available: http://www.sciencedirect.com/science/article/pii/S0920379620301113 (Cited on page 31.)

[124] R. Frauenfelder, “Solution and Diffusion of Hydrogen in Tungsten,” *Journal of Vacuum Science and Technology*, vol. 6, no. 3, pp. 388–397, May 1969. Available: https://avs.scitation.org/doi/10.1116/1.1492699 (Cited on pages 31, 64, 65 and 66.)

[125] A. Aiello, A. Ciampichetti, and G. Benamati, “Determination of hydrogen solubility in lead lithium using sole device,” *Fusion Engineering and Design*, vol. 81, no. 1, pp. 639–644, Feb. 2006. Available: https://www.sciencedirect.com/science/article/pii/S092037960500565X (Cited on pages 31, 65, 66, 87 and 88.)

[126] Z. Chen *et al.*, “Deuterium transport and retention properties of representative fusion blanket structural materials,” *Journal of Nuclear Materials*, vol. 549, p. 152904, Jun. 2021. Available: https://linkinghub.elsevier.com/retrieve/pii/S0022311521001288 (Cited on pages 31, 64, 65, 66 and 67.)

[127] R. Delaporte-Mathurin *et al.*, “Parametric study of hydrogenic inventory in the ITER divertor based on machine learning,” *Scientific Reports*, vol. 10, no. 1, p. 17798, Oct. 2020, number: 1 Publisher: Nature Publishing Group. Available: https://www.nature.com/articles/s41598-020-74844-w (Cited on pages 31 and 70.)

[128] J. Shimwell *et al.*, “Multiphysics analysis with CAD-based parametric breeding blanket creation for rapid design iteration,” *Nuclear Fusion*, vol. 59, no. 4, p. 046019, Mar. 2019. Available: https://iopscience.iop.org/article/10.1088/1741-4326/ab0016 (Cited on pages 31, 68 and 69.)

[129] S. Noce *et al.*, “Neutronics analysis and activation calculation for tungsten used in the DEMO divertor targets: A comparative study between the effects of WCLL and HCPB blanket, different W compositions and chromium,” *Fusion Engineering and Design*, vol. 169, p. 112428, Aug. 2021. Available: https://www.sciencedirect.com/science/article/pii/S0920379621002040 (Cited on pages 31 and 108.)

[130] L. Candido *et al.*, “A novel approach to the study of magnetohydrodynamic effect on tritium transport in WCLL breeding blanket of DEMO,” *Fusion Engineering and Design*, vol. 167, p. 112334, Jun. 2021. Available: https://www.sciencedirect.com/science/article/pii/S0920379621001101 (Cited on pages 31, 32, 61, 64, 66, 68 and 105.)

[131] F. R. Urgorri *et al.*, “Tritium transport modeling at system level for the EUROfusion dual coolant lithium-lead breeding blanket,” *Nuclear Fusion*, vol. 57, no. 11, p. 116045, Aug. 2017, publisher: IOP Publishing. Available: https://doi.org/10.1088/1741-4326/aa7f9d (Cited on page 31.)

[132] P. A. Di Maio *et al.*, “On the effect of stiffening plates configuration on the DEMO Water Cooled Lithium Lead Breeding Blanket module thermo-mechanical behaviour,” *Fusion Engineering and Design*, vol. 146, pp. 2247–2250, Sep. 2019. Available: https://www.sciencedirect.com/science/article/pii/S092037961930496X (Cited on page 31.)

[133] X. Zhao *et al.*, “3D tritium transport analysis for WCCB blanket based on COMSOL,” *Fusion Engineering and Design*, vol. 151, p. 111405, Feb. 2020. Available: https://www.sciencedirect.com/science/article/pii/S0920379619309019 (Cited on page 31.)

[134] G. A. Esteban *et al.*, “Hydrogen transport and trapping in ODS-EUROFER,” *Fusion Engineering and Design*, vol. 82, no. 15, pp. 2634–2640, Oct. 2007. Available: http://www.sciencedirect.com/science/article/pii/S0920379607000580 (Cited on pages 31 and 65.)

[135] Y. Charles, J. Mougenot, and M. Gaspérini, “Modeling hydrogen dragging by mobile dislocations in finite element simulations,” *International Journal of Hydrogen Energy*, vol. 47, no. 28, pp. 13 746–13 761, Apr. 2022. Available: https://www.sciencedirect.com/science/article/pii/S036031992200711X (Cited on page 31.)

[136] G. Holzner *et al.*, “Solute diffusion of hydrogen isotopes in tungsten—a gas loading experiment,” *Physica Scripta*, vol. 2020, no. T171, p. 014034, Mar. 2020, publisher: IOP Publishing. Available: https://dx.doi.org/10.1088/1402-4896/ab4b42 (Cited on pages 32, 64, 65, 97 and 102.)

[137] D. Knighton, *Fluvial Forms and Processes: A New Perspective*, 2nd ed. London: Routledge, Nov. 1998. (Cited on page 38.)

[138] L. F. Moody, "Friction Factors for Pipe Flow," *Transactions of the American Society of Mechanical Engineers*, vol. 66, no. 8, pp. 671–678, Dec. 2022. Available: https://doi.org/10.1115/1.4018140 (Cited on page 38.)

[139] A. Tassone, G. Caruso, and A. Del Nevo, "Influence of PbLi hydraulic path and integration layout on MHD pressure losses," *Fusion Engineering and Design*, vol. 155, p. 111517, Jun. 2020. Available: https://www.sciencedirect.com/science/article/pii/S092037962030065X (Cited on pages 38 and 70.)

[140] D. Martelli, A. Venturini, and M. Utili, "Literature review of lead-lithium thermophysical properties," *Fusion Engineering and Design*, vol. 138, pp. 183–195, Jan. 2019. Available: https://www.sciencedirect.com/science/article/pii/S0920379618307361 (Cited on pages 38, 62, 63 and 64.)

[141] P. Tolias, "Analytical expressions for thermophysical properties of solid and liquid tungsten relevant for fusion applications," *Nuclear Materials and Energy*, vol. 13, pp. 42–57, Dec. 2017. Available: https://www.sciencedirect.com/science/article/pii/S2352179117300388 (Cited on pages 38, 63 and 64.)

[142] A. McNabb and P. K. Foster, "A New Analysis of the Diffusion of Hydorgen in Iron and Ferritic Steels," *Transactions of The Society for Modeling and Simulation International*, vol. 227, pp. 618–627, 1963. (Cited on pages 39 and 55.)

[143] G. R. Longhurst, "TMAP7 User Manual," Idaho National Lab. (INL), Idaho Falls, ID (United States), Tech. Rep. INEEL/EXT-04-02352, Dec. 2008. Available: https://www.osti.gov/biblio/952013 (Cited on page 42.)

[144] D. Matveev *et al.*, "Reaction-diffusion modeling of hydrogen transport and surface effects in application to single-crystalline Be," *Nuclear Instruments and Methods in Physics Research Section B: Beam Interactions with Materials and Atoms*, vol. 430, pp. 23–30, Sep. 2018. Available: http://www.sciencedirect.com/science/article/pii/S0168583X18303537 (Cited on pages 42 and 55.)

[145] E. Hodille, "Study and modeling of the deuterium trapping in ITER relevant materials," Ph.D. dissertation, Aix-Marseille, Nov. 2016. Available: https://tel.archives-ouvertes.fr/tel-01477426 (Cited on page 42.)

[146] K. Schmid, U. von Toussaint, and T. Schwarz-Selinger, "Transport of hydrogen in metals with occupancy dependent trap energies," *Journal of Applied Physics*, vol. 116, no. 13, p. 134901, Oct. 2014. Available: https://doi.org/10.1063/1.4896580 (Cited on page 42.)

[147] L. Candido *et al.*, "An integrated hydrogen isotopes transport model for the TRIEX-II facility," *Fusion Engineering and Design*, vol. 155, p. 111585, Jun. 2020. Available: http://www.sciencedirect.com/science/article/pii/S0920379620301332 (Cited on pages 42 and 68.)

[148] S. Benannoune *et al.*, "Multidimensional finite-element simulations of the diffusion and trapping of hydrogen in plasma-facing components including thermal expansion," *Physica Scripta*, vol. 2020, no. T171, p. 014011, Feb. 2020, publisher: IOP Publishing. Available: https://dx.doi.org/10.1088/1402-4896/ab4335 (Cited on page 42.)

[149] stephen dixon, "aurora-multiphysics/achlys: Isotope self-diffusion," Dec. 2021. Available: https://zenodo.org/records/6412090 (Cited on page 42.)

[150] R. Delaporte-Mathurin *et al.*, "FESTIM: An open-source code for hydrogen transport simulations," *International Journal of Hydrogen Energy*, vol. 63, pp. 786–802, Apr. 2024. Available: https://www.sciencedirect.com/science/article/pii/S0360319924010218 (Cited on pages 42, 43, 52, 56, 57 and 58.)

[151] ——, "Influence of interface conditions on hydrogen transport studies," *Nuclear Fusion*, vol. 61, no. 3, p. 036038, 2021. Available: http://iopscience.iop.org/article/10.1088/1741-4326/abd95f (Cited on pages 43 and 99.)

[152] "Homepage - Titans Project," Dec. 2022. Available: https://titans-project.eu/ (Cited on page 43.)

[153] G. Ferrero, "Verification, validation, and cross-comparison of Tritium transport codes FESTIM, MHIMS, and mHIT," *Submitted to International Journal of Hydrogen Energy*, 2024. (Cited on page 43.)

[154] A. Logg, K.-A. Mardal, and G. Wells, Eds., *Automated Solution of Differential Equations by the Finite Element Method: The FEniCS Book*, ser. Lecture Notes in Computational Science and Engineering. Berlin, Heidelberg: Springer, 2012, vol. 84. Available: https://link.springer.com/10.1007/978-3-642-23099-8 (Cited on pages 45 and 46.)

[155] P. G. Ciarlet, *The Finite Element Method for Elliptic Problems*, ser. Classics in Applied Mathematics. Society for Industrial and Applied Mathematics, Jan. 2002. Available: https://epubs.siam.org/doi/book/10.1137/1.9780898719208 (Cited on page 45.)

[156] “Detailed Explanation of the Finite Element Method (FEM).” Available: https://www.comsol.com/multiphysics/finite-element-method (Cited on page 47.)

[157] T. J. R. Hughes, *The Finite Element Method: Linear Static and Dynamic Finite Element Analysis.* Courier Corporation, May 2012, google-Books-ID: cHH2n_qBK0IC. (Cited on page 47.)

[158] D. C. Brydges and G. Slade, “A Renormalisation Group Method. I. Gaussian Integration and Normed Algebras,” *Journal of Statistical Physics*, vol. 159, no. 3, pp. 421–460, May 2015. Available: https://doi.org/10.1007/s10955-014-1163-z (Cited on page 48.)

[159] Z. Kalogiratou and T. E. Simos, “Newton–Cotes formulae for long-time integration,” *Journal of Computational and Applied Mathematics*, vol. 158, no. 1, pp. 75–82, Sep. 2003. Available: https://www.sciencedirect.com/science/article/pii/S0377042703004795 (Cited on page 49.)

[160] Z. Yang *et al.*, “Using Gauss-Jacobi quadrature rule to improve the accuracy of FEM for spatial fractional problems,” *Numerical Algorithms*, vol. 89, no. 3, pp. 1389–1411, Mar. 2022. Available: https://doi.org/10.1007/s11075-021-01158-x (Cited on page 49.)

[161] “The Finite Element Method: Its Basis and Fundamentals,” in *The Finite Element Method: its Basis and Fundamentals (Seventh Edition)*, O. C. Zienkiewicz, R. L. Taylor, and J. Z. Zhu, Eds. Oxford: Butterworth-Heinemann, Jan. 2013, p. i. Available: https://www.sciencedirect.com/science/article/pii/B9781856176330000198 (Cited on page 50.)

[162] S. C. Eisenstat, H. C. Elman, and M. H. Schultz, “Variational Iterative Methods for Nonsymmetric Systems of Linear Equations,” *SIAM Journal on Numerical Analysis*, vol. 20, no. 2, pp. 345–357, Apr. 1983, publisher: Society for Industrial and Applied Mathematics. Available: https://epubs.siam.org/doi/10.1137/0720023 (Cited on page 50.)

[163] M. S. Alnaes *et al.*, “The FEniCS Project,” 2015, doi.org/10.11588/ans.2015.100.20553. (Cited on pages 50 and 52.)

[164] Z. Liu *et al.*, “A multi-domain decomposition strategy for the lattice Boltzmann method for steady-state flows,” *Engineering Applications of Computational Fluid Mechanics*, vol. 10, no. 1, pp. 72–85, Jan. 2016, publisher: Taylor & Francis _eprint: https://doi.org/10.1080/19942060.2015.1092743. Available: https://doi.org/10.1080/19942060.2015.1092743 (Cited on pages 51, 139 and 140.)

[165] U. Ayachit, *The paraview guide: a parallel visualization application.* Kitware, Inc., Jan. 2015, archive Location: world. Available: https://dl.acm.org/doi/abs/10.5555/2789330 (Cited on pages 52 and 53.)

[166] C. Geuzaine and J.-F. Remacle, “Gmsh: A 3-D finite element mesh generator with built-in pre- and post-processing facilities,” *International Journal for Numerical Methods in Engineering*, vol. 79, no. 11, pp. 1309–1331, 2009, _eprint: https://onlinelibrary.wiley.com/doi/pdf/10.1002/nme.2579. Available: https://onlinelibrary.wiley.com/doi/abs/10.1002/nme.2579 (Cited on page 53.)

[167] “Coreform Cubit,” Orem, UT, Mar. 2024. (Cited on page 53.)

[168] “Salome,” Jul. 2023. (Cited on pages 53 and 142.)

[169] N. Schlömer, “meshio: Tools for mesh files,” Jan. 2024. Available: https://zenodo.org/records/1288334 (Cited on page 53.)

[170] S. Balay *et al.*, “PETSc Web page,” 2015. Available: http://www.mcs.anl.gov/petsc (Cited on page 53.)

[171] Hunter, J. D., “Matplotlib: A 2D graphics environment,” *Computing in Science & Engineering*, vol. 9, no. 3, pp. 90–95, 2007. (Cited on page 53.)

[172] C. R. Harris *et al.*, “Array programming with NumPy,” *Nature*, vol. 585, no. 7825, pp. 357–362, Sep. 2020, publisher: Nature Publishing Group. Available: https://www.nature.com/articles/s41586-020-2649-2 (Cited on page 53.)

[173] “On the Gibbs Phenomenon and Its Resolution | SIAM Review.” Available: https://epubs.siam.org/doi/10.1137/S0036144596301390 (Cited on page 54.)

[174] L. Simoni *et al.*, “An integrated experimental and modeling approach to determine hydrogen diffusion and trapping in a high-strength steel,” *International Journal of Hydrogen Energy*, vol. 46, no. 50, pp. 25 738–25 751, Jul. 2021. Available: https://www.sciencedirect.com/science/article/pii/S0360319921018334 (Cited on page 55.)

[175] D. Matveev *et al.*, “CRDS modelling of deuterium release from co-deposited beryllium layers in temperature programmed and laser induced desorption experiments,” *Physica Scripta*, vol. 2020, no. T171, p. 014053, Mar. 2020, publisher: IOP Publishing. Available: https://dx.doi.org/10.1088/1402-4896/ab5569 (Cited on page 55.)

[176] M. J. Simmonds *et al.*, “TMAP modeling of D release from baked multi-layer Be–D co-deposits,” *Physica Scripta*, vol. 2020, no. T171, p. 014043, Mar. 2020, publisher: IOP Publishing. Available: https://dx.doi.org/10.1088/1402-4896/ab4de4 (Cited on page 55.)

[177] S. Markelj *et al.*, “Deuterium transport and retention in the bulk of tungsten containing helium: the effect of helium concentration and microstructure,” *Nuclear Fusion*, vol. 60, no. 10, p. 106029, Sep. 2020, publisher: IOP Publishing. Available: https://dx.doi.org/10.1088/1741-4326/abadae (Cited on page 55.)

[178] M. Shimada and C. N. Taylor, “Improved tritium retention modeling with reaction-diffusion code TMAP and bulk depth profiling capability,” *Nuclear Materials and Energy*, vol. 19, pp. 273–278, May 2019. Available: https://www.sciencedirect.com/science/article/pii/S2352179118302758 (Cited on page 55.)

[179] M. Pečovnik *et al.*, “Influence of grain size on deuterium transport and retention in self-damaged tungsten,” *Journal of Nuclear Materials*, vol. 513, pp. 198–208, Jan. 2019. Available: https://www.sciencedirect.com/science/article/pii/S0022311518307256 (Cited on page 55.)

[180] E. A. Hodille *et al.*, “Simulations of atomic deuterium exposure in self-damaged tungsten,” *Nuclear Fusion*, vol. 57, no. 5, p. 056002, Mar. 2017. (Cited on pages 55, 95 and 96.)

[181] R. D. Smirnov, J. Guterl, and S. I. Krasheninnikov, “Modeling of Multispecies Dynamics in Fusion-Related Materials with FACE,” *Fusion Science and Technology*, vol. 71, no. 1, pp. 75–83, Jan. 2017, publisher: Taylor & Francis _eprint: https://doi.org/10.13182/FST16-125. Available: https://doi.org/10.13182/FST16-125 (Cited on page 55.)

[182] O. V. Ogorodnikova, J. Roth, and M. Mayer, “Deuterium retention in tungsten in dependence of the surface conditions,” *Journal of Nuclear Materials*, vol. 313-316, pp. 469–477, Mar. 2003. Available: https://www.sciencedirect.com/science/article/pii/S0022311502013752 (Cited on page 55.)

[183] M. J. Simmonds *et al.*, “Expanding the capability of reaction-diffusion codes using pseudo traps and temperature partitioning: Applied to hydrogen uptake and release from tungsten,” *Journal of Nuclear Materials*, vol. 508, pp. 472–480, Sep. 2018. Available: https://www.sciencedirect.com/science/article/pii/S0022311517315301 (Cited on page 55.)

[184] E. A. Hodille *et al.*, “Retention and release of hydrogen isotopes in tungsten plasma-facing components: the role of grain boundaries and the native oxide layer from a joint experiment-simulation integrated approach,” *Nuclear Fusion*, vol. 57, no. 7, p. 076019, May 2017, publisher: IOP Publishing. Available: https://dx.doi.org/10.1088/1741-4326/aa6d24 (Cited on pages 55, 74 and 99.)

[185] P. Calderoni *et al.*, “Measurement of tritium permeation in flibe (2LiF–BeF2),” *Fusion Engineering and Design*, vol. 83, no. 7, pp. 1331–1334, Dec. 2008. Available: https://www.sciencedirect.com/science/article/pii/S0920379608000926 (Cited on page 55.)

[186] S. Fukada and A. Morisaki, “Hydrogen permeability through a mixed molten salt of LiF, NaF and KF (Flinak) as a heat-transfer fluid,” *Journal of Nuclear Materials*, vol. 358, no. 2, pp. 235–242, Nov. 2006. Available: https://www.sciencedirect.com/science/article/pii/S0022311506004089 (Cited on page 55.)

[187] “Exact solutions,” in *Verification and Validation in Scientific Computing*, C. J. Roy and W. L. Oberkampf, Eds. Cambridge: Cambridge University Press, 2010, pp. 208–248. Available: https://www.cambridge.org/core/books/verification-and-validation-in-scientific-computing/exact-solutions/DFB030CD8A8334FA13DF3B2A627964E4 (Cited on page 55.)

[188] B. van der Schaaf *et al.*, “The development of EUROFER reduced activation steel,” *Fusion Engineering and Design*, vol. 69, no. 1, pp. 197–203, Sep. 2003. Available: https://www.sciencedirect.com/science/article/pii/S0920379603003375 (Cited on page 62.)

[189] M. Gorley *et al.*, “The EUROfusion materials property handbook for DEMO in-vessel components—Status and the challenge to improve confidence level for engineering data,” *Fusion Engineering and Design*, vol. 158, p. 111668, Sep. 2020. Available: https://www.sciencedirect.com/science/article/pii/S0920379620302167 (Cited on pages 62, 63 and 64.)

[190] F. Reiter, “Solubility and diffusivity of hydrogen isotopes in liquid Pb17Li,” *Fusion Engineering and Design*, vol. 14, no. 3, pp. 207–211, Apr. 1991. Available: https://www.sciencedirect.com/science/article/pii/0920379691900039 (Cited on pages 64, 65, 66, 73 and 87.)

[191] M. Utili *et al.*, “Design of a multipurpose laboratory scale apparatus for the investigation of hydrogen isotopes in PbLi and permeation technologies,” *Fusion Engineering and Design*, vol. 87, no. 7, pp. 1342–1346, Aug. 2012. Available: https://www.sciencedirect.com/science/article/pii/S0920379612002165 (Cited on page 64.)

[192] G. A. Esteban *et al.*, "Hydrogen isotope diffusive transport parameters in pure polycrystalline tungsten," *Journal of Nuclear Materials*, vol. 295, no. 1, pp. 49–56, May 2001. Available: https://www.sciencedirect.com/science/article/pii/S002231150100486X (Cited on page 65.)

[193] A. Aiello *et al.*, "Hydrogen Isotopes Permeability in Eurofer 97 Martensitic Steel," *Fusion Science and Technology*, vol. 41, no. 3P2, pp. 872–876, May 2002. Available: https://doi.org/10.13182/FST41-872 (Cited on page 65.)

[194] P. Fauvet and J. Sannier, "Hydrogen behaviour in liquid 17Li83Pb alloy," *Journal of Nuclear Materials*, vol. 155-157, pp. 516–519, Jul. 1988. Available: https://www.sciencedirect.com/science/article/pii/0022311588903017 (Cited on page 65.)

[195] Y. Shibuya *et al.*, "Isothermal release of tritium from neutron-irradiated Li17Pb83," *Journal of Nuclear Materials*, vol. 150, no. 3, pp. 286–291, Nov. 1987. Available: https://www.sciencedirect.com/science/article/pii/0022311587900067 (Cited on page 65.)

[196] T. Terai *et al.*, "Diffusion coefficient of tritium in molten lithium-lead alloy (Li17Pb83) under neutron irradiation at elevated temperatures," *Journal of Nuclear Materials*, vol. 187, no. 3, pp. 247–253, May 1992. Available: https://www.sciencedirect.com/science/article/pii/002231159290504E (Cited on page 65.)

[197] Y. Edao, H. Noguchi, and S. Fukada, "Experiments of hydrogen isotope permeation, diffusion and dissolution in Li–Pb," *Journal of Nuclear Materials*, vol. 417, no. 1, pp. 723–726, Oct. 2011. Available: https://www.sciencedirect.com/science/article/pii/S0022311510009487 (Cited on page 65.)

[198] Y. C. Chan and E. Veleckis, "A thermodynamic investigation of dilute solutions of hydrogen in liquid Li-Pb alloys," *Journal of Nuclear Materials*, vol. 123, no. 1, pp. 935–940, May 1984. Available: https://www.sciencedirect.com/science/article/pii/0022311584901983 (Cited on pages 65 and 87.)

[199] R. Schumacher and A. Weiss, "Hydrogen Solubility in the Liquid Alloys Lithium-Indium, Lithium-Lead, and Lithium-Tin," *Berichte der Bunsengesellschaft für physikalische Chemie*, vol. 94, no. 6, pp. 684–691, 1990, _eprint: https://onlinelibrary.wiley.com/doi/pdf/10.1002/bbpc.19900940612. Available: https://onlinelibrary.wiley.com/doi/abs/10.1002/bbpc.19900940612 (Cited on pages 65 and 87.)

[200] G. Alberro *et al.*, "Experimental determination of solubility values for hydrogen isotopes in eutectic Pb–Li," *Fusion Engineering and Design*, vol. 98-99, pp. 1919–1923, Oct. 2015. Available: https://www.sciencedirect.com/science/article/pii/S0920379615300119 (Cited on pages 65 and 87.)

[201] R. Delaporte-Mathurin *et al.*, "RemDelaporteMathurin/h-transport-materials: Patch 0.16.1," Jun. 2024. Available: https://zenodo.org/records/12189551 (Cited on pages 65 and 87.)

[202] H.-D. Liu *et al.*, "Effect of tungsten deposition thickness on hydrogen isotope permeation through RAFM steel," *Journal of Nuclear Materials*, vol. 545, p. 152647, Mar. 2021. Available: https://www.sciencedirect.com/science/article/pii/S0022311520312551 (Cited on pages 70 and 163.)

[203] J. Denis *et al.*, "Dynamic modelling of local fuel inventory and desorption in the whole tokamak vacuum vessel for auto-consistent plasma-wall interaction simulations," *Nuclear Materials and Energy*, vol. 19, pp. 550–557, May 2019. Available: https://www.sciencedirect.com/science/article/pii/S235217911830262X (Cited on page 70.)

[204] J. F. Ziegler, M. D. Ziegler, and J. P. Biersack, "SRIM – The stopping and range of ions in matter (2010)," *Nuclear Instruments and Methods in Physics Research Section B: Beam Interactions with Materials and Atoms*, vol. 268, no. 11, pp. 1818–1823, Jun. 2010. Available: https://www.sciencedirect.com/science/article/pii/S0168583X10001862 (Cited on pages 70, 96 and 97.)

[205] T. Pomella Lobo, S. Pestchanyi, and I. A. Maione, "A reduced-order model to estimate first wall particle and heat fluxes for systems codes," *Fusion Engineering and Design*, vol. 204, p. 114491, Jul. 2024. Available: https://www.sciencedirect.com/science/article/pii/S0920379624003442 (Cited on page 70.)

[206] E. A. Hodille *et al.*, "Modelling of hydrogen isotopes trapping, diffusion and permeation in divertor monoblocks under ITER-like conditions," *Nuclear Fusion*, vol. 61, no. 12, p. 126003, Oct. 2021, publisher: IOP Publishing. Available: https://dx.doi.org/10.1088/1741-4326/ac2abc (Cited on page 71.)

[207] K. Schmid, T. Schwarz-Selinger, and R. Arredondo, "Influence of hydrogen isotopes on displacement damage formation in EUROFER," *Nuclear Materials and Energy*, vol. 34, p. 101341, Mar. 2023. Available: https://www.sciencedirect.com/science/article/pii/S2352179122002228 (Cited on pages 74 and 95.)

[208] A. Hollingsworth *et al.*, "Comparative study of deuterium retention and vacancy content of self-ion irradiated tungsten," *Journal of Nuclear Materials*, vol. 558, p. 153373, Jan. 2022. Available: https://www.sciencedirect.com/science/article/pii/S0022311521005936 (Cited on page 74.)

[209] J. S. Gaffney and N. A. Marley, “Chapter 8 - Thermodynamics and Energy Balance,” in *General Chemistry for Engineers*, J. S. Gaffney and N. A. Marley, Eds. Elsevier, Jan. 2018, pp. 241–281. Available: https://www.sciencedirect.com/science/article/pii/B9780128104255000084 (Cited on page 77.)

[210] E. B. Entry, “STEAM TABLES,” in *Thermopedia*. Begel House Inc., Feb. 2011. Available: https://www.thermopedia.com/content/1150/ (Cited on page 78.)

[211] R. A. Causey, “Hydrogen isotope retention and recycling in fusion reactor plasma-facing components,” *Journal of Nuclear Materials*, vol. 300, no. 2-3, pp. 91–117, Feb. 2002, publisher: North-Holland. Available: https://www.sciencedirect.com/science/article/pii/S0022311501007322 (Cited on page 89.)

[212] E. A. Hodille *et al.*, “Stabilization of defects by the presence of hydrogen in tungsten: simultaneous W-ion damaging and D-atom exposure,” *Nuclear Fusion*, vol. 59, no. 1, p. 016011, Nov. 2018, publisher: IOP Publishing. Available: https://doi.org/10.1088/1741-4326/aaec97 (Cited on page 91.)

[213] M. Pečovnik *et al.*, “Effect of D on the evolution of radiation damage in W during high temperature annealing,” *Nuclear Fusion*, vol. 60, no. 10, p. 106028, Sep. 2020, publisher: IOP Publishing. Available: https://doi.org/10.1088/1741-4326/abaff6 (Cited on pages 91, 94, 98, 99 and 102.)

[214] M. Dürrschnabel *et al.*, “New insights into microstructure of neutron-irradiated tungsten,” *Scientific Reports*, vol. 11, no. 1, p. 7572, Apr. 2021, number: 1 Publisher: Nature Publishing Group. Available: https://www.nature.com/articles/s41598-021-86746-6 (Cited on page 92.)

[215] M. Shimada *et al.*, “Irradiation effect on deuterium behaviour in low-dose HFIR neutron-irradiated tungsten,” *Nuclear Fusion*, vol. 55, no. 1, p. 013008, Dec. 2014, publisher: IOP Publishing. Available: https://doi.org/10.1088/0029-5515/55/1/013008 (Cited on page 92.)

[216] J. Dark *et al.*, “Modelling neutron damage effects on tritium transport in tungsten,” *Nuclear Fusion*, vol. 64, no. 8, p. 086026, Jun. 2024, publisher: IOP Publishing. Available: https://dx.doi.org/10.1088/1741-4326/ad56a0 (Cited on pages 93 and 134.)

[217] E. Markina *et al.*, “Recovery temperatures of defects in tungsten created by self-implantation,” *Journal of Nuclear Materials*, vol. 463, pp. 329–332, Aug. 2015. Available: https://www.sciencedirect.com/science/article/pii/S0022311514009465 (Cited on page 94.)

[218] E. A. Hodille *et al.*, “Molecular dynamics simulation of beryllium oxide irradiated by deuterium ions: sputtering and reflection,” *Journal of Physics: Condensed Matter*, vol. 31, no. 18, p. 185001, Mar. 2019, publisher: IOP Publishing. Available: https://dx.doi.org/10.1088/1361-648X/ab04d7 (Cited on page 96.)

[219] R. Delaporte-Mathurin *et al.*, “Parametric optimisation based on TDS experiments for rapid and efficient identification of hydrogen transport materials properties,” *Nuclear Materials and Energy*, p. 100984, Mar. 2021. Available: https://www.sciencedirect.com/science/article/pii/S2352179121000661 (Cited on page 97.)

[220] A. Moitra and K. Solanki, “Adsorption and penetration of hydrogen in W: A first principles study,” *Computational Materials Science*, vol. 50, no. 7, pp. 2291–2294, May 2011. Available: https://www.sciencedirect.com/science/article/pii/S0927025611001352 (Cited on page 99.)

[221] O. V. Ogorodnikova *et al.*, “The influence of radiation damage on the plasma-induced deuterium retention in self-implanted tungsten,” *Journal of Nuclear Materials*, vol. 415, no. 1, Supplement, pp. S661–S666, Aug. 2011. Available: https://www.sciencedirect.com/science/article/pii/S0022311510008305 (Cited on page 99.)

[222] M. Shimada *et al.*, “The deuterium depth profile in neutron-irradiated tungsten exposed to plasma,” *Physica Scripta*, vol. T145, p. 014051, Dec. 2011, publisher: IOP Publishing. Available: https://doi.org/10.1088/0031-8949/2011/t145/014051 (Cited on pages 99 and 100.)

[223] A. Mannheim, J. A. W. van Dommelen, and M. G. D. Geers, “Modelling recrystallization and grain growth of tungsten induced by neutron displacement defects,” *Mechanics of Materials*, vol. 123, pp. 43–58, Aug. 2018. Available: https://www.sciencedirect.com/science/article/pii/S0167663617308529 (Cited on page 99.)

[224] W. Pantleon, “Thermal stability of the microstructure in rolled tungsten for fusion reactors,” *Physica Scripta*, vol. 96, no. 12, p. 124036, Oct. 2021, publisher: IOP Publishing. Available: https://dx.doi.org/10.1088/1402-4896/ac2854 (Cited on page 99.)

[225] M. Zibrov *et al.*, “Vacancy cluster growth and thermal recovery in hydrogen-irradiated tungsten,” *Journal of Nuclear Materials*, vol. 531, p. 152017, Apr. 2020. Available: https://www.sciencedirect.com/science/article/pii/S0022311519312395 (Cited on page 99.)

[226] H. Watanabe *et al.*, “Microstructure and thermal desorption of deuterium in heavy-ion-irradiated pure tungsten,” *Journal of Nuclear Materials*, vol. 455, no. 1, pp. 51–55, Dec. 2014. Available: https://www.sciencedirect.com/science/article/pii/S0022311514001871 (Cited on page 99.)

[227] G. H. Vineyard, “Frequency factors and isotope effects in solid state rate processes,” *Journal of Physics and Chemistry of Solids*, vol. 3, no. 1, pp. 121–127, Jan. 1957. Available: https://www.sciencedirect.com/science/article/pii/0022369757900598 (Cited on page 102.)

[228] E. A. Hodille *et al.*, “Kinetic model for hydrogen absorption in tungsten with coverage dependent surface mechanisms,” *Nuclear Fusion*, vol. 60, no. 10, p. 106011, Sep. 2020, publisher: IOP Publishing. Available: https://dx.doi.org/10.1088/1741-4326/aba454 (Cited on page 102.)

[229] R. Bonifetto *et al.*, “Conceptual design of a PAV-based tritium extractor for the WCLL breeding blanket of the EU DEMO: Effects of surface-limited vs. diffusion-limited modeling,” *Fusion Engineering and Design*, vol. 167, p. 112363, Jun. 2021. Available: https://www.sciencedirect.com/science/article/pii/S0920379621001393 (Cited on page 115.)

[230] K. Forcey and A. Perujo, “Tritium permeation barriers in contact with liquid lithium-lead eutectic (Pb17Li),” *Journal of Nuclear Materials*, vol. 218, no. 2, pp. 224–230, Feb. 1995. Available: https://linkinghub.elsevier.com/retrieve/pii/002231159400434X (Cited on page 118.)

[231] T. Hernández *et al.*, “Study of deuterium permeation, retention, and desorption in SiC coatings submitted to relevant conditions for breeder blanket applications: thermal cycling effect under electron irradiation and oxygen exposure,” *Journal of Nuclear Materials*, vol. 557, p. 153219, Dec. 2021. Available: https://www.sciencedirect.com/science/article/pii/S0022311521004426 (Cited on page 118.)

[232] L.-M. Luo *et al.*, “Preparation technologies and performance studies of tritium permeation barriers for future nuclear fusion reactors,” *Surface and Coatings Technology*, vol. 403, p. 126301, Dec. 2020. Available: https://linkinghub.elsevier.com/retrieve/pii/S0257897220309701 (Cited on page 118.)

[233] D. Stöver *et al.*, “Status of tritium permeation barrier development on austenitic structural alloys,” *Journal of Nuclear Materials*, vol. 123, no. 1-3, pp. 1541–1546, May 1984. Available: https://linkinghub.elsevier.com/retrieve/pii/0022311584902988 (Cited on page 118.)

[234] P. Pardo *et al.*, “A review on high temperature thermochemical heat energy storage,” *Renewable and Sustainable Energy Reviews*, vol. 32, pp. 591–610, 2014. Available: https://www.sciencedirect.com/science/article/pii/S1364032113008289 (Cited on page 118.)

[235] L. Liu *et al.*, “Present status and prospects of nanostructured thermal barrier coatings and their performance improvement strategies: A review,” *Journal of Manufacturing Processes*, vol. 97, pp. 12–34, 2023. Available: https://www.sciencedirect.com/science/article/pii/S1526612523004085 (Cited on page 118.)

[236] H. Li *et al.*, “Failure mechanisms and surface treatment processes of thermal barrier coatings: Review,” *Chinese Journal of Aeronautics*, 2024. Available: https://www.sciencedirect.com/science/article/pii/S100093612400270X (Cited on page 118.)

[237] L. Wang *et al.*, “Modeling of thermal properties and failure of thermal barrier coatings with the use of finite element methods: A review,” *Journal of the European Ceramic Society*, vol. 36, no. 6, pp. 1313–1331, May 2016. Available: https://www.sciencedirect.com/science/article/pii/S0955221915302971 (Cited on page 118.)

[238] A. Meurer *et al.*, “SymPy: symbolic computing in Python,” *PeerJ Computer Science*, vol. 3, p. e103, Jan. 2017. Available: https://doi.org/10.7717/peerj-cs.103 (Cited on pages 120 and 122.)

[239] E. Serra *et al.*, “Hydrogen Permeation Measurements on Alumina,” *Journal of the American Ceramic Society*, vol. 88, no. 1, pp. 15–18, 2005, _eprint: https://onlinelibrary.wiley.com/doi/pdf/10.1111/j.1551-2916.2004.00003.x. Available: https://onlinelibrary.wiley.com/doi/abs/10.1111/j.1551-2916.2004.00003.x (Cited on page 124.)

[240] J. Konys *et al.*, “Corrosion behavior of EUROFER steel in flowing eutectic Pb–17Li alloy,” *Journal of Nuclear Materials*, vol. 329-333, pp. 1379–1383, Aug. 2004. Available: https://www.sciencedirect.com/science/article/pii/S0022311504003514 (Cited on page 129.)

[241] R. Nishio *et al.*, “Reduction of MHD pressure drop by electrical insulating oxide layers in liquid breeder blanket of fusion reactors,” *Nuclear Materials and Energy*, vol. 34, p. 101382, Mar. 2023. Available: https://www.sciencedirect.com/science/article/pii/S2352179123000212 (Cited on page 129.)

[242] A. Aiello, A. Ciampichetti, and G. Benamati, “An overview on tritium permeation barrier development for WCLL blanket concept,” *Journal of Nuclear Materials*, vol. 329, pp. 1398–1402, Aug. 2004,

patent Number: B Place: Amsterdam Publisher: Elsevier Science Bv WOS:000223505200101. Available: http://www.webofscience.com/wos/alldb/full-record/WOS:000223505200101 (Cited on page 129.)

[243] J. Schöberl, "NETGEN An advancing front 2D/3D-mesh generator based on abstract rules," *Computing and Visualization in Science*, vol. 1, no. 1, pp. 41–52, Jul. 1997. Available: https://doi.org/10.1007/s007910050004 (Cited on page 145.)

[244] A. Blishchik, M. van der Lans, and S. Kenjereš, "An extensive numerical benchmark of the various magnetohydrodynamic flows," *International Journal of Heat and Fluid Flow*, vol. 90, p. 108800, Aug. 2021. Available: https://www.sciencedirect.com/science/article/pii/S0142727X21000308 (Cited on page 151.)

[245] J. C. R. Hunt, "Magnetohydrodynamic flow in rectangular ducts," *Journal of Fluid Mechanics*, vol. 21, no. 4, pp. 577–590, Apr. 1965, publisher: Cambridge University Press. Available: https://www.cambridge.org/core/journals/journal-of-fluid-mechanics/article/magnetohydrodynamic-flow-in-rectangular-ducts/D20116052C5908335E39D2CB5D0F4608 (Cited on page 152.)

[246] J. A. Shercliff, "Steady motion of conducting fluids in pipes under transverse magnetic fields," *Mathematical Proceedings of the Cambridge Philosophical Society*, vol. 49, no. 1, pp. 136–144, Jan. 1953, publisher: Cambridge University Press. Available: https://www.cambridge.org/core/journals/mathematical-proceedings-of-the-cambridge-philosophical-society/article/steady-motion-of-conducting-fluids-in-pipes-under-transverse-magnetic-fields/4C3BA0B8DF0F9A19CAD1B3DBDF23A990 (Cited on pages 152 and 153.)